Stress-induced protein dynamics and growth arrest in *C. elegans* during development

Cover: "Wormoboros", door Sarah de Buck

Stress-induced protein dynamics and growth arrest in *C. elegans* during development

Proefschrift

ter verkrijging van

de graad van doctor aan de Universiteit Leiden,

op gezag van rector magnificus prof.dr.ir. H. Bijl,

volgens besluit van het college voor promoties

te verdedigen op vrijdag 16 mei 2025

klokke 10:00 uur

door

Burak Demirbas

geboren te Vlaardingen

in 1995

Promotor:

Prof. dr. R. M. H. Merks

Co-promotor:

Dr. J. S. van Zon (AMOLF, the Netherlands)

Promotiecommissie:

Prof. dr. A. H. Meijer

Prof. dr. Prof. H. P. Spaink

Prof. dr. P. R. ten Wolde (AMOLF, the Netherlands)

Dr. M. Olmedo (University of Seville, Spain)

Dr. M. J. Rodriguez-Colman (UMC Utrecht, the Netherlands)

Table of contents

Chapter 1

General introduction

"It is, however, in the life of animals, so simple and easy to survey, that the vanity and nothingness of the strivings of the whole phenomenon can be grasped. The diversity of organisations, the perfection of the means by which each one is adapted to its environment and its prey, contrast vividly with the absence of any enduring goal; instead of this goal there is a moment of pleasure, so fleeting, which is inseparable from need, countless prolonged sufferings, an incessant struggle, bellum omnium, in which each is both hunter and prey, tumult, privation, misery and fear, shouts and screams, this is what appears to us; and so it will continue, in secula seculorum, or until the crust of the planet again bursts open."
-Arthur Schopenhauer (1)

"Imagine to yourselves a being like Nature, boundlessly extravagant, boundlessly indifferent, without purpose or consideration, without pity or justice, at once fruitful and barren and uncertain…"
-Friedrich Nietzsche (2)

On the suffering of animals

The natural environment of animals is an ever-shifting, and very often harsh place. Animals are confronted with fluctuations in their environment that are difficult to predict, and with environmental stresses such as low food availability, excesses of temperature, osmotic pressure, and toxins. And it is not enough to merely survive: during development into adults, animals are in constant competition with each other for resources that allow them to reproduce earlier and more frequently than others, a battle of all against all. How do animals not only persevere in these conditions, but also grow and reproduce? More concretely, in this thesis we ask two questions. First, how do developing animals deal with small deviations from their optimal environment? And second, how do they handle extreme deviations that cause stress and cellular damage?

During development animals must carry out a great number of processes, such as cell divisions, formation of distinct organs and tissues, and transcription and translation of particular genes. This is greatly complicated by the fact that these processes must be coordinated in space, across cells, and in time, meaning that these developmental events must often be completed in a specific order and at specific times. However, the environment forms an obstacle to robustly accomplishing this, as the overall rate of development in animals is affected by environmental factors such as the amount of available food, diet, temperature, etc. When these factors deviate from an optimum, or when they change during the course of development, animals must compensate for this by adjusting the timing of individual developmental events. Little is currently known about the mechanisms that regulate this tight coordination.

When environmental factors become extreme relative to the optimum, resulting in stress and damage to the organism, animals must deal with this by activating stress response pathways. Over millions of years, animals have evolved specialized pathways that are able to combat many of the stressors they encounter, for example by producing specialized proteins that can counter the negative effects of a given stress. So why do animals not simply keep these pathways continuously activated? Because doing so would mean using resources that could otherwise have been used to grow and to reproduce, to outcompete their competitors in the evolutionary arms race. This means animals must constantly make an active choice when to induce these pathways, and for how long. How the dynamics of this stress response unfold in the face of an environment that is unpredictable, and continuously changing, remains an open question (3, 4).

Environment-dependent development

The environment has a great deal of influence on the development of animals. For instance, temperature affects sex differentiation during embryonic development in many amphibians, with for example high temperature leading to sex ratios biased towards more males (5). While the environment impacts processes in embryos, environmental effects are particularly strong for post-embryonic development, that is development after birth or hatching. For example, in fruit flies there is an optimal developmental temperature "window" where development functions best, resulting in adult animals with the highest weight, wing and tibial length, and ovariole number (6). In humans, environmental factors such as nutrition during early development can influence the age at which puberty starts by several years (7), with delay of puberty seen following malnutrition (8). Dietary and environmental changes in the West have furthermore likely resulted in the increasingly prevalent occurrence of precocious puberty, with one study finding that the onset of puberty in girls decreased by ~1 year in a 15-year time span between 1991-1993 and 2006-2008, in Denmark (9, 10).

So far, the impact of the environment has been mostly measured on the whole-organism level, using features such as weight and length (6, 8), or timing of large-scale morphological changes during development (9, 11). At the same time, we have an increasingly complete understanding of development on the micro-scale: many of the genes and cellular processes involved in animal development have been identified (12, 13). Yet, how the impact of the environment on organ- or organismal level development is coupled to or emerges from dynamics on the cellular level is so far poorly understood. Advancing our knowledge of the connections between the cellular and organ(ismal) level therefore necessitates a different experimental approach than those previously employed that focus exclusively on organism-level features.

Insulin signaling

Insulin signaling plays a central role in cellular stress response during a wide array of stresses, such as oxidative stress, starvation (nutrient depletion), or osmotic stress (14–16). Components of the insulin signaling pathway are well conserved among metazoans (multicellular animals) (17). The main effector of insulin signaling is the transcription factor FOXO, which is found in almost all eukaryotes except plants (18), and works by binding to the DNA, thereby either allowing or blocking transcription of target genes. FOXO is responsible for regulating many cellular processes such as cell cycle arrest, apoptosis, and the expression of hundreds of stress-response genes (19–21). In mammals, there are four FOXO paralogs, namely FOXO1, FOXO3, FOXO4, and FOXO6, with partly overlapping functions, and different, tissue-specific expression patterns (18). Besides regulating processes at the cellular level, insulin signaling and FOXO also work at the organ- or even body-wide level. During

development, insulin-like growth factors (IGFs) regulate the insulin pathway to control the rate of organ- and body growth (22). Moreover, in adults insulin itself functions to maintain body-wide blood glucose homeostasis (23). More in general, insulin signaling is also implicated in various diseases such as diabetes, obesity, and cancer (24–26). Given the fact that there is currently a worldwide epidemic in cases of diabetes (27), and because FOXO is an important potential target of chemotherapeutic drugs (28, 29), understanding insulin signaling and FOXO is extremely relevant for improving human health. Insulin signaling is also known to regulate longevity in humans (17). For these reasons, the insulin signaling pathway has been widely studied.

Normally, animals produce insulins that bind to insulin receptors on cell-surfaces, initiating a signaling cascade that phosphorylates FOXO, causing it to be sequestered in the cytoplasm, where it is inactive, as it cannot access the DNA (30). When environmental conditions become extreme, inducing a stress response, insulin levels fall, causing insulin signaling to decrease and FOXO to translocated to the cell nucleus (30). There, it binds to DNA and helps maintain cellular homeostasis by regulating processes that address cellular damage, or in the case of severe cellular damage, causes cell cycle arrest or apoptosis in cells, thereby maintaining organismal homeostasis (31, 32). It is likely important that this process is coordinated between all the cells of a developing animal: if some parts of an animal arrest cell growth while others do not, this could lead to an animal growing out of proportion. For example, disrupting insulin signaling in mice result in smaller animals, and stress during development in fruit flies results in FOXO-mediated growth arrest, but in both cases the adult animals are still in proportion, suggesting coordination across the whole body (33, 34). However, little is known about how the cellular dynamics of insulin signaling, particularly that of FOXO nuclear translocation, relate to growth and development on the whole-body level.

The elegant roundworm

A key obstacle for understanding the impact of the environment on development – both for mild changes in external conditions and those that induce a stress-mediated insulin response – is linking responses at the cell-level to those of whole body. There are several reasons for this. First, in organisms that are non-transparent, such as humans, it is difficult to image the inside of cells in real time. Second, in animal studies it can be difficult to track individual animals over extended periods without drug-induced or mechanical immobilization, which can affect the natural processes that occur inside cells. Furthermore, because the body of even simple model organisms like fruit flies consist of more than 500,000 cells (35), it can be extremely challenging to see how processes in one cell or one tissue affect the wider body.

Here, we attempt to overcome these issues by studying the development of the small nematode, or roundworm, *Caenorhabditis elegans* ("elegant rod-like thing"), as it offers a number of important advantages compared to other animal models for development. First, it is small and simple, measuring ~0.2-1 mm in length, and has a relatively simple body plan, consisting of ~1,000 cells in the adult stage. Second, its body is fully transparent at all stages of development, in principle allowing observation of all cellular processes using fluorescence microscopy. Third, after hatching from the egg, it develops rapidly, through four larval stages that last 39-75 hours in total (36), into adulthood, following an almost stereotypical program of cell divisions during development, which have been fully mapped (30). This means that there are distinct, well-understood, individual developmental events that can be studied at the cell level, and can be related relatively easily to the whole-body level. Finally, many mutants and genetic manipulation techniques exist that make it possible to visualize and perturb the fundamental processes that underlie its expression, such as cell division and gene expression (37).

Furthermore, despite being an invertebrate, and thus evolutionarily very far removed from humans, *C. elegans* has an insulin signaling pathway surprisingly similar to that found in mammals, with the *C. elegans* insulin/IGF-1 signaling (IIS) pathway sharing many of its components with other animals, including humans (17). In contrast to mammals, *C. elegans* only contains a single version of the FOXO gene, called DAF-16 - albeit with various isoforms that are expressed in a tissue-specific manner - for which human FOXO3 is the closest ortholog (18, 30). The impact of *C. elegans* insulin signaling studies on understanding human diseases underscores its relevance as a model system for understanding biomolecular pathways shared with humans (38). So, *C. elegans* is also an excellent model organism specifically for studying the insulin signaling stress response.

Fluorescent timelapse microscopy of individual animals

Our work focuses on *C. elegans* post-embryonic development, meaning developmental processes that occur after hatching in growing larvae. Because C. *elegans* larvae are highly mobile, it poses challenges for performing time-lapse microscopy, as animals will move away from the microscope's field of view. This is a particular issue when following cell-level dynamics in time, as a microscope with a resolution high enough to image cells will necessarily have a limited field of view. To solve this, we employ custom-fabricated microchambers to trap *C. elegans*, enabling time-lapse microscopy of molecular and cellular dynamics in individual animals with high spatial and temporal resolution (39). Furthermore, we can control several environmental factors, such as temperature, osmolarity, and diet within the chambers. While similar setups have been utilized to observe individual worms (40, 41), our approach aims to

bridge the gap between (transcription factor localization, gene expression) dynamics at the single-cell level and the whole-body level, which remains largely unexplored.

As *C. elegans* is transparent, fluorescence microscopy can be used to follow the level and localization of genes of interest. In this microscopy technique, genes are tagged with a fluorescent reporter, such as GFP, that is excited by laser stimulation. In the case of development, we used this technique to measure the level of *wrt-2*, a developmental gene that peaks once during every larval stage, over the course of larval development. When studying insulin signaling and stress, we used a strain with fluorescently labelled DAF-16/FOXO to measure its translocation to the nucleus. Through this approach, we aim to elucidate the timing of developmental events when the overall rate of development is altered, and the interplay between single-cell DAF-16/FOXO translocation dynamics and whole-body responses during stress.

Quantitative analysis and mathematical modeling

In this thesis, we employ a quantitative approach to biology. Biological processes are inherently dynamic and complex, involving processes that occur across various scales of time and space. Quantification allows for the testing of specific hypotheses regarding the timing, coordination, and regulation of developmental events. For instance, understanding the dynamics of nuclear translocation or the synchronization of cellular events necessitates high-resolution temporal data. Without such precise data, it is challenging to draw meaningful conclusions about the underlying mechanisms and their regulatory networks. Furthermore, biological systems exhibit considerable variability, not only between different organisms but also within the same organism over time. A quantitative approach allows accounting for this variability. By measuring exact times of developmental events and other key metrics in individual organisms, we can uncover patterns that might be obscured by averaging data across populations.

A commonly used tool in biology for grasping the complexity of development and stress signaling is mathematical and computational modeling. Models allow us to better understand biological systems for a number of reasons. First, models can have striking explanatory power, especially for emergent dynamical phenomena such as monostability, bistability and oscillations (42, 43), where small changes in parameters can lead to profound differences in dynamics. Such unexpected changes in dynamics cannot be as easily explained through more qualitative models, such as the more classical biology approach of drawing a pathway of interactions. In addition, mathematical and computational modeling allow us to make precise, quantitative predictions about dynamical systems that can be tested experimentally, to see whether causal explanations proposed by the model are correct. Crucially, as discussed above,

these predictions are often not obvious, as they emerge from the complex interactions between simpler components of the modeled biological system.

For these reasons, various mathematical models were used in this thesis. In the case of animals adjusting developmental rates in response to variable environments, little is known about the mechanisms that tightly coordinate developmental events. Hence, here we used a simple phenomenological model, which describes development very generally. Nevertheless, we found that all variations in timing we observed for the different conditions and mutants examined could be explained by essentially the same simple mathematical model, providing a unified framework to understand the observed changes in timing. The insulin signaling pathway, on the other hand, has been well studied, especially in *C. elegans* (30). Hence, in this case we employed a more detailed, but still minimal, mechanistic model, using the current knowledge about interactions among components of the IIS pathway. Here, the model allowed us to identify possible molecular mechanisms underlying the dynamics of DAF-16/FOXO, and generated predictions that we subsequently verified experimentally. It is important to emphasize that no model perfectly captures the system it represents, and we therefore advocate for a pluralistic approach to mathematical modeling (44).

Thesis summary and outlook

In chapter 1, we present a novel approach utilizing time-lapse microscopy to track and analyze the timing of key cellular events during *C. elegans* larval development, from hatching to adulthood. Specifically, we focus on monitoring oscillatory gene expression, hypodermal stem cell divisions, and cuticle shedding in individual animals under various environmental conditions. Our investigation unveils a surprising variability in the timing of these cellular events, even among genetically identical individuals subjected to identical conditions. Intriguingly, despite this variability, we observe a phenomenon which we term "temporal scaling", wherein events occur at consistent relative timings when measured against the overall duration of development in each individual (**Fig. 1**).

Furthermore, we uncover pervasive shifts in population-averaged timing when environmental variables such as temperature, diet, or genotype are manipulated. These shifts are separated into developmental "epochs", consecutive periods in which the timing of all developmental events was impacted by the same distinct change in developmental rate. Nonetheless, we find that these variations in timing can be explained by temporal scaling when appropriately rescaled by the duration of the respective epochs in each individual. Remarkably, our investigations extend to mutants lacking LIN-42/Period, a presumed core regulator of larval developmental timing, which exhibit severe delays, heterogeneous timing, and growth arrest. Despite these disruptions, timing still adheres to temporal scaling,

suggesting the existence of alternative mechanisms governing developmental timing. It has been proposed that the regulation of larval development timing likely involves timers reliant on protein degradation or oscillations (45, 46), yet these mechanisms alone do not inherently generate temporal scaling. Consequently, our findings impose significant constraints on models aiming to explain the timing dynamics of larval development in *C. elegans*.
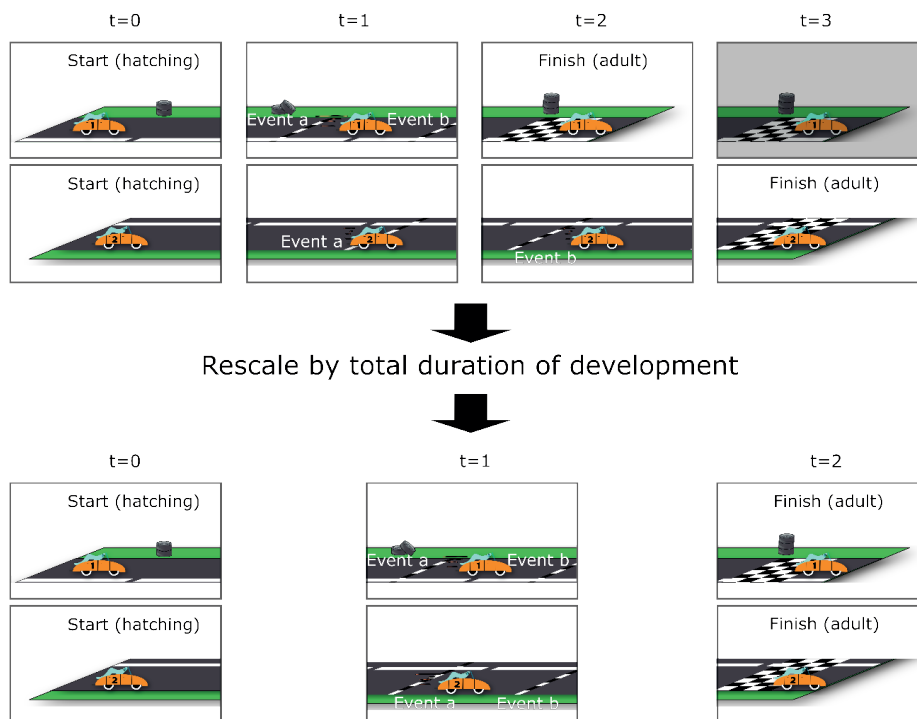
Figure 1 Cartoon showing the principle of developmental scaling. Individual, isogenic animals develop at varying developmental rates, and therefore pass developmental events ("event a", "event b", etc.) at different time points. But when the timing of these events is rescaled by the total time of development for each individual, the timing of these events becomes the same for each individual.

In **Chapter 2**, we investigate the dynamics of DAF-16, the ortholog of FOXO in *C. elegans,* with single-cell resolution across the entire organism. Surprisingly, our observations reveal that under conditions of constant stress leading to larval developmental arrest, DAF-16 translocates between the nucleus and cytoplasm in stochastic pulses that last on the order of hours (**Fig. 2**). Remarkably, while the timing of these pulses appears random, they exhibit strong synchronization in timing between cells throughout the organism. Furthermore, we find a correlation between DAF-16 pulse dynamics and body-wide growth, with temporally isolated translocation pulses causing transient reductions in growth rate and complete growth arrest

occurring only when pulses reach a certain frequency or duration threshold. This link between DAF-16 pulse dynamics and growth provides a compelling rationale for the observed synchrony, highlighting the necessity of tightly coordinated pulse dynamics across all cells to maintain uniform proportions during growth. Additionally, our investigations extend beyond *C. elegans* to mammalian cells, where we observe similar translocation pulses of FOXO3A under conditions of nutrient stress. These findings suggest that the long-range synchronization of FOXO translocation dynamics may constitute an integral aspect of growth control not only in simple organisms like *C. elegans* but also in more complex animals.
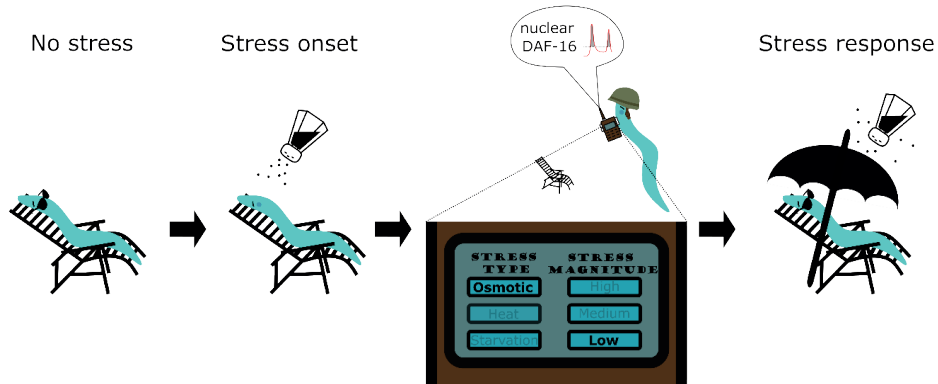
Figure 2 Cartoon schematically depicting the role of insulin signaling for animals under stress. Under stress, DAF-16 nuclear localization pulses occur, and worms switch on appropriate stress response genes to protect against particular stresses. The dynamics of DAF-16 localization depend on the type, and magnitude of stress.

Chapter 3 of this thesis is dedicated to the mathematical modeling of potential mechanisms underlying the DAF-16/FOXO nuclear localization pulses and their synchronization that we observed in **Chapter 2**. Presenting a set of coupled stochastic differential equations, we aim to elucidate the processes governing the generation and synchronization of DAF-16/FOXO pulses with a minimal model. We identify a model where oscillations and pulses in DAF-16/FOXO translocation dynamics originate from a negative feedback loop, where reduced insulin signaling and nuclear DAF-16/FOXO translocation result in excretion of ILPs, thereby increasing insulin signaling again. Moreover, this model also shows that this DAF-16/FOXO-induced ILP secretion can act as a synchronization mechanism. Here, ILPs released by one cell can impact insulin signaling in nearby cells, with the resulting coupling sufficient to reproduce the observed, strong body-wide synchrony of DAF-16/FOXO pulses. This model accurately replicates the dynamics of DAF-16/FOXO for osmotic, heat, and starvation stress, as well as the change in dynamics when stress magnitude is varied, and in mutant animals carrying an insulin receptor mutation. It also made several predictions, which we test experimentally. First, we predict that under heat stress, DAF-16/FOXO nuclear localization

should display hysteresis, meaning that the nuclear localization state of DAF-16/FOXO should depend on its past localization state. Indeed, we found that DAF-16/FOXO at 31°C was cytoplasmic when the temperature was upshifted from 20°C, but instead was predominantly nuclear at 31°C when shifting the temperature down from 33°C. Second, as our proposed synchronization mechanism of DAF-16/FOXO pulses relies on dynamic excretion of ILPs, it predicts that body-wide pulse dynamics, and potentially even pulse synchrony, should be impacted when the insulin pathway is mutated in a subset of cells, locking them for instance in a state of constant nuclear DAF-16/FOXO. We test this prediction using tissue-specific degradation of the insulin receptor DAF-2 and find a clear impact on pulse dynamics in surrounding wild-type cells, for animals under starvation. Finally, we use the results from these new experiments to theorize what alterations could be made to future iterations of the model (**Fig. 3**).
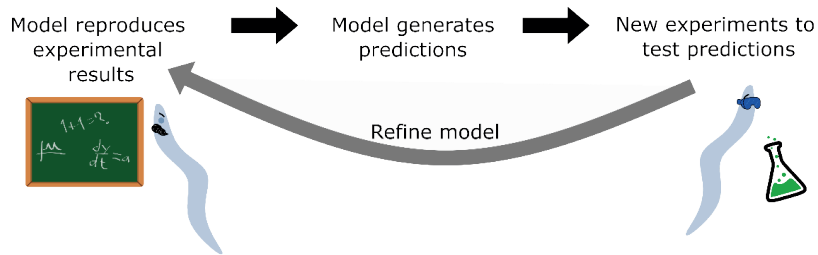
Figure 2 Cartoon depicting the procedure of mathematical modeling of the insulin signaling pathway. Our model reproduces the experimental findings from chapter 2, and makes novel predictions about DAF-16/FOXO dynamics. These predictions are then tested with new time-lapse experiments. Results from new experiments were used to make suggestions on how to improve future iterations of the model.

In conclusion, by using time-lapse microscopy and mathematical modeling to study molecular dynamics, we have aimed to elucidate the complex effects of the environment on *C. elegans* during development, with a particular focus on insulin signaling.

References

1.   A. Schopenhauer, "Supplements to The World as Will and Representation, chapter XXVIII" in *The World as Will and Representation, Vol. 2*, (Cambridge University Press).

2.   F. W. Nietzsche, *Beyond Good and Evil* (Project Gutenberg, 2003).

3.   M. O. Casanueva, A. Burga, B. Lehner, Fitness Trade-Offs and Environmentally Induced Mutation Buffering in Isogenic *C. elegans*. *Science* **335**, 82–85 (2012).

4.   M. Rodriguez, L. B. Snoek, J. A. G. Riksen, R. P. Bevers, J. E. Kammenga, Genetic variation for stress-response hormesis in *C. elegans* lifespan. *Exp. Gerontol.* **47**, 581–587 (2012).

5.   A. Ruiz-García, Á. S. Roco, M. Bullejos, Sex Differentiation in Amphibians: Effect of Temperature and Its Influence on Sex Reversal. *Sex. Dev.* **15**, 157–167 (2021).

6.   J. David, M.-F. Clavel, Influence de la température subie au cours du développement sur divers caractères biométriques des adultes de *Drosophila melanogaster* Meigen. *J. Insect Physiol.* **13**, 717–729 (1967).

7.   F. Darendeliler, IUGR: Genetic influences, metabolic problems, environmental associations/triggers, current and future management. *Best Pract. Res. Clin. Endocrinol. Metab.* **33**, 101260 (2019).

8.   H. Kulin, N. Bwibo, D. Mutie, S. Santner, The effect of chronic childhood malnutrition on pubertal growth and development. *Am. J. Clin. Nutr.* **36**, 527–536 (1982).

9.   L. Aksglaede, K. Sørensen, J. H. Petersen, N. E. Skakkebæk, A. Juul, Recent Decline in Age at Breast Development: The Copenhagen Puberty Study. *Pediatrics* **123**, e932–e939 (2009).

10.   F. M. Biro, *et al.*, Onset of Breast Development in a Longitudinal Cohort. *Pediatrics* **132**, 1019–1027 (2013).

11.   S. G. Kuntz, M. B. Eisen, *Drosophila* embryogenesis scales uniformly across temperature in developmentally diverse species. *PLoS Genet.* **10**, e1004293 (2014).

12.   A. E. Rougvie, Control of developmental timing in animals. *Nat. Rev. Genet.* **2**, 690–701 (2001).

13.   M. Mallo, C. R. Alonso, The regulation of Hox gene expression during animal development. *Development* **140**, 3951–3963 (2013).

14.   G. J. P. L. Kops, *et al.*, Forkhead transcription factor FOXO3a protects quiescent cells from oxidative stress. *Nature* **419**, 316–321 (2002).

15.   S. Nemoto, M. M. Fergusson, T. Finkel, Nutrient Availability Regulates SIRT1 Through a Forkhead-Dependent Pathway. *Science* **306**, 2105–2108 (2004).

16.   S. T. Lamitina, K. Strange, Transcriptional targets of DAF-16 insulin signaling pathway protect *C. elegans* from extreme hypertonic stress. *Am. J. Physiol.-Cell Physiol.* **288**, C467–C474 (2005).

17.   J. Piñero González, O. Carrillo Farnés, A. T. R. Vasconcelos, A. González Pérez, Conservation of key members in the course of the evolution of the insulin signaling pathway. *Biosystems* **95**, 7–16 (2009).

18.   B. F. Santos, I. Grenho, P. J. Martel, B. I. Ferreira, W. Link, FOXO family isoforms. *Cell Death Dis.* **14**, 702 (2023).

19.   R. H. Medema, G. J. P. L. Kops, J. L. Bos, B. M. T. Burgering, AFX-like Forkhead transcription factors mediate cell-cycle regulation by Ras and PKB through p27kip1. *Nature* **404**, 782–787 (2000).

20.   S. S. Lee, S. Kennedy, A. C. Tolonen, G. Ruvkun, DAF-16 Target Genes That Control *C. elegans* Life-Span and Metabolism. *Science* **300**, 644–647 (2003).

21.   D. Accili, K. C. Arden, FoxOs at the Crossroads of Cellular Metabolism, Differentiation, and Transformation. *Cell* **117**, 421–426 (2004).

22.   C. G. T. Tahimic, Y. Wang, D. D. Bikle, Anabolic effects of IGF-1 signaling on the skeleton. *Front. Endocrinol.* **4**, 6 (2013).

23.   J. H. Koeslag, P. T. Saunders, E. Terblanche, A reappraisal of the blood glucose homeostat which comprehensively explains the type 2 diabetes mellitus–syndrome X complex. *J. Physiol.* **549**, 333–346 (2003).

24.   A. R. Saltiel, New perspectives into the molecular pathogenesis and treatment of type 2 diabetes. *Cell* **104**, 517–529 (2001).

25.   M. F. White, Insulin Signaling in Health and Disease. *Science* **302**, 1710–1711 (2003).

26.   Y. Poloz, V. Stambolic, Obesity and cancer, a case for insulin signaling. *Cell Death Dis.* **6**, e2037–e2037 (2015).

27.   E. Standl, K. Khunti, T. B. Hansen, O. Schnell, The global epidemics of diabetes in the 21st century: Current situation and perspectives. *Eur. J. Prev. Cardiol.* **26**, 7–14 (2019).

28.   A. R. Gomes, J. J. Brosens, E. W.-F. Lam, Resist or die: FOXO transcription factors determine the cellular response to chemotherapy. *Cell Cycle* **7**, 3133–3136 (2008).

29.   S. Yao, L. Y.-N. Fan, E. W.-F. Lam, The FOXO3-FOXM1 axis: A key cancer drug target and a modulator of cancer drug resistance. *Semin. Cancer Biol.* **50**, 77–89 (2018).

30.   C. T. Murphy, P. J. Hu, "Insulin/insulin-like growth factor signaling in *C. elegans*" in *WormBook: The Online Review of C. Elegans Biology [Internet]*, (WormBook, 2018).

31.   T. Gui, B. M. T. Burgering, FOXOs: masters of the equilibrium. *Febs J.* **289**, 7918–7939 (2022).

32.   M. J. Rodriguez-Colman, T. B. Dansen, B. M. T. Burgering, FOXO transcription factors as mediators of stress adaptation. *Nat. Rev. Mol. Cell Biol.* **25**, 46–64 (2024).

33.   J. M. Kramer, J. T. Davidge, J. M. Lockyer, B. E. Staveley, Expression of *Drosophila* FOXO regulates growth and can phenocopy starvation. *BMC Dev. Biol.* **3**, 5 (2003).

34.   J. Baker, J.-P. Liu, E. J. Robertson, A. Efstratiadis, Role of Insulin-like Growth Factors in Embryonic and Postnatal Growth.

35.   H. Li, *et al.*, Fly Cell Atlas: A single-nucleus transcriptomic atlas of the adult fruit fly. *Science* **375**, eabk2432 (2022).

36.   Hermaphrodite Introduction. Available at: https://www.wormatlas.org/hermaphrodite/introduction/Introframeset.html [Accessed 24 June 2024].

37.   A. K. Corsi, B. Wightman, M. Chalfie, A Transparent Window into Biology: A Primer on *Caenorhabditis elegans*. *Genetics* **200**, 387–407 (2015).

38.   M. Rodriguez, L. B. Snoek, M. D. Bono, J. E. Kammenga, Worms under stress: *C. elegans* stress response and its relevance to complex human disease and aging. *Trends Genet.* **29**, 367–374 (2013).

39.   N. Gritti, S. Kienle, O. Filina, J. S. van Zon, Long-term time-lapse microscopy of *C. elegans* post-embryonic development. *Nat. Commun.* **7**, 12500 (2016).

40.   W. Keil, L. M. Kutscher, S. Shaham, E. D. Siggia, Long-Term High-Resolution Imaging of Developing *C. elegans* Larvae with Microfluidics. *Dev. Cell* **40**, 202–214 (2017).

41.   K. Stojanovski, H. Großhans, B. D. Towbin, Coupling of growth rate and developmental tempo reduces body size heterogeneity in *C. elegans*. *Nat. Commun.* **13**, 3132 (2022).

42.   J. T. Mettetal, D. Muzzey, J. M. Pedraza, E. M. Ozbudak, A. van Oudenaarden, Predicting stochastic gene expression dynamics in single cells. *Proc. Natl. Acad. Sci.* **103**, 7304–7309 (2006).

43.   M. B. Elowitz, S. Leibler, A synthetic oscillatory network of transcriptional regulators. *Nature* **403**, 335–338 (2000).

44.   L. Gyllingberg, A. Birhane, D. J. T. Sumpter, The lost art of mathematical modelling. *Math. Biosci.* **362**, 109033 (2023).

45.   M. W. Meeuse, *et al.*, Developmental function and state transitions of a gene expression oscillator in *Caenorhabditis elegans*. *Mol. Syst. Biol.* **16**, e9498 (2020).

46.   C. Tsiairis, H. Großhans, "Gene expression oscillations in *C. elegans* underlie a new developmental clock" in *Current Topics in Developmental Biology*, Nematode Models of Development and Disease., S. Jarriault, B. Podbilewicz, Eds. (Academic Press, 2021), pp. 19–43.

Chapter 2

Temporal scaling in *C. elegans* larval development

Olga Filina[1], Burak Demirbas[1], Rik Haagmans[1] and Jeroen S. van Zon[1]

[1]AMOLF, Science Park 104, 1098 XG Amsterdam, the Netherlands

Abstract

It is essential that correct temporal order of cellular events is maintained during animal development. During post-embryonic development, the rate of development depends on external conditions, such as food availability, diet and temperature. How timing of cellular events is impacted when the rate of development is changed at the organism-level is not known. We used a novel time-lapse microscopy approach to simultaneously measure timing of oscillatory gene expression, hypodermal stem cell divisions and cuticle shedding in individual *C. elegans* larvae, as they developed from hatching to adulthood. This revealed strong variability in timing between isogenic individuals under the same conditions. However, this variability obeyed 'temporal scaling', meaning that events occurred at the same time when measured relative to the total duration of development in each individual. We also observed pervasive changes in timing when temperature, diet or genotype were varied, but with larval development divided in 'epochs' that differed in how event timing was impacted. Yet, these variations in timing were still explained by temporal scaling when time was rescaled by the duration of the respective epochs in each individual. Surprisingly, timing obeyed temporal scaling even in mutants lacking *lin-42/Period*, presumed a core regulator of timing of larval development, that exhibited strongly delayed, heterogeneous timing. However, shifting conditions mid-development perturbed temporal scaling and changed event order in a highly condition-specific manner, indicating that a complex machinery is responsible for temporal scaling under constant conditions.

Introduction

Numerous cellular events that occur during animal development, such as cell division, cell movement and gene expression, must be tightly coordinated in time to allow formation of a functional organism with a correctly established body plan. However, despite our increasing understanding of the regulation of developmental timing[1-3], how cells in developing organisms measure time and execute events in the correct temporal order remains poorly understood. Moreover, the rate of post-embryonic development in animals is affected by external conditions, such as food availability, diet and temperature. For example, severe dietary restriction extends the duration of larval development in the nematode worm *C. elegans* as much as ten-fold, without apparent defects in development[4]. How the timing of individual developmental events is adjusted in response to such changes in the organism-level rate of development is not known.

This question about developmental timing has a parallel in the context of spatial patterning during development. It has been shown that spatial gene expression patterns often scale with organ or embryo size, i.e. with the spatial pattern adjusted in each individual organ or embryo so that the spatial features occurred at the same position relative to its overall size[5-8]. For example, in *Drosophila* embryos gap genes are expressed in bands along the anteroposterior body axis[9, 10]. These bands have highly stereotypical positions relative to the embryo's size, even though this size shows significant variability between individuals[6]. Moreover, embryos of closely related species that vary greatly in size exhibit the same number of bands with similar position relative to the size of the embryo[6]. Here, we examine whether, analogous to scaling of spatial patterns in development, the timing of development exhibits temporal scaling, meaning that, when the organism-level rate of development is changed, the timing of individual events is adjusted so that they still occur at the same time, when measured relative to the total duration of development. Such a mechanism would ensure the correct synchrony of developmental events even when organism-level timing is changed in an unpredictable manner by shifts in external conditions.

Due to its invariant cell lineage and highly stereotypical development, *C. elegans* is an ideal model for studying developmental timing. Its postembryonic development consists of four larval stages (L1-L4) that are separated by a molting event, where a new cuticle is synthesized and the old cuticle shed[11]. After the final L4 molt, animals enter adulthood. There is a clear periodic aspect to *C. elegans* development, with molts occurring every 8-10 hours at 25°C. Moreover, larval stages are accompanied by oscillatory expression of ~20% of genes, with peaks occurring once per larval stage[12-14].

Molecular mechanisms that have been proposed for regulation of developmental timing include oscillators, that encode time in periodic changes in protein level, and 'hourglass' mechanisms, that record time in the steady accumulation or degradation of proteins[15]. Developmental timing has been extensively studied in *C. elegans*, leading to the discovery of heterochronic genes[2, 3]. Heterochronic genes such as *lin-14* and *lin-28* show expression levels that decrease during larval development, suggestive of an hourglass mechanism[16, 17]. Indeed, mutations that perturb the *lin-14* and *lin-28* temporal expression patterns lead to timing defects, with the identity of events in one larval stage switched with those of a later stage or repeated in subsequent stages[18]. At the same time, these mutations otherwise have only limited impact on developmental timing on the organism level, e.g. the duration of larval stages. In contrast, the heterochronic gene *lin-42* is expressed in an oscillatory manner during development, peaking once every larval stage. In *lin-42* mutants, developmental timing is severely perturbed, with strong animal-to-animal variability in larval stage duration[19]. The body-wide, oscillatory expression dynamics of *lin-42,* together with its impact on larval stage duration, makes *lin-42* an interesting candidate for a global regulator of developmental timing. Intriguingly, *lin-42* is a homolog of Period, an important component of the circadian clock in *Drosophila* and higher organisms[20]. Hence, it has been speculated that *lin-42* forms part of an oscillator-based timer that allows cells and organs to read out developmental time[11].

How timing of individual events is impacted by changes in the organism-level rate of development is poorly characterized. Timing of *C. elegans* larval development is often measured at the population level, by examining the developmental stage of animals sampled from age-synchronized populations. This approach has limited time resolution and does not allow measuring timing of multiple events within the same individual. The latter is a particular problem for mutants such as *lin-42*, where developmental synchrony between individual animals is lost. However, the alternative approach of following individual animals was until recently performed by hand, limiting the number of animals that could be examined. We have recently developed a novel microscopy approach that allows automated imaging of individual *C. elegans* larvae during their entire development and at single-cell resolution[21], making it possible to measure timing of cellular events in many individual larvae. Here, we used this approach to simultaneously measure the timing of three recurring developmental events (oscillatory expression of a molting cycle gene, hypodermal stem cell divisions and cuticle shedding) in individual *C. elegans* larvae, both upon changes in environmental conditions (temperature and diet) and in mutants that increased the duration of larval development up to ~3-fold.

Our measurements uncovered strong variability in event timing between individuals, as compared to duration of larval development, even in isogenic animals under identical

environmental conditions. Strikingly, this variability obeyed temporal scaling, meaning that events occurred at the same time when rescaled by the total duration of development in each individual. Moreover, changes in average timing between populations that differ in genotype or environmental conditions were not always explained by a simple change in the overall rate of development of the organism. Instead, we found larval development is divided into distinct epochs, which are sequences of events that, upon variation in conditions or genotype, exhibit changes in timing that are identical, and differ from changes in timing observed for events in other epochs. Yet, this variation in timing between populations also obeys temporal scaling, provided that event times were rescaled by the duration of individual epochs, rather than total duration of development. Surprisingly, we found this was even the case for *lin-42* mutants, suggesting that, while *lin-42* is crucial for setting the duration of larval stages, it is dispensable for controlling event timing relative to each larval stage. However, condition shifts during larval development perturbed temporal scaling and inverted event order, in a manner that depended on the type of shift. This hints that a complex machinery, potentially requiring coordination of different timing mechanisms, is responsible for temporal scaling under constant conditions.

Overall, our results show that the broad variation observed between individuals, environmental conditions and genotypes in the timing of cellular events during *C. elegans* post-embryonic development can be captured by the simple concept of temporal scaling, thereby revealing a precise adaptation of cell-level timing to changes in the organism-level rate of development. These observations raise the important question how temporal scaling is implemented by the molecular mechanisms that control timing of larval development.

Results

To examine how developmental timing is coordinated at the organism-level in developing *C. elegans* larvae, we measured the timing of multiple developmental events that occurred frequently during larval development: seam cell divisions, oscillatory gene expression and ecdysis. Seam cells are hypodermal stem cells that divide asymmetrically once every larval stage, yielding one hypodermal cell and one seam cell (Fig. 1A,D)[22]. Seam cells V1-V4 and V6 undergo an additional symmetric division at the start of L2, doubling their number. Oscillatory gene expression is a pervasive phenomenon in *C. elegans*, with thousands of gene transcripts oscillating during development with the periodicity of the molting cycle[12-14]. We focused on *wrt-2*, a hedgehog-like protein expressed in seam cells, that peaks in expression once every larval stage[12, 21] (Fig. 1B,D). Ecdysis is the shedding of the old cuticle at the end of each larval stage (Fig. 1C,D). By focusing on these three events, we captured

qualitatively different developmental processes, while their repetitive nature allowed us to capture many events in a single experiment.

To accurately measure timing of individual events, we used a novel time-lapse microscopy approach to follow the full ~40 h of post-embryonic development of individual *C. elegans* larvae with single-cell resolution[21]. Briefly, embryos were placed inside hydrogel chambers filled with sufficient *E. coli,* as food source, to sustain development into adulthood, while constraining animals to the field of view of the microscope at each stage. By capturing fluorescence and transmitted light images with fast exposure time, we could image developmental dynamics in individual cells inside moving larvae, without immobilization.

To visualize seam cell divisions, we used the strain *heIs63[wrt-2p::H2B::GFP,wrt-2p::PH::GFP]*, with GFP targeted to the nucleus and membrane of seam cells[23]. Since seam cells divisions occurred close in time, we defined the time of each round of divisions as the average time at which V1-V6 cells have divided. Because the *heIs63* reporter is under control of the *wrt-2* promoter, it enabled simultaneous measurement of oscillatory *wrt-2* expression. Fluorescent images were analyzed automatically using custom-written software to extract the mean GFP fluorescence intensity of seam cells. The time of expression peaks was extracted from the fluorescence profiles, by fitting their dynamics with a combination of Gaussian functions and a linear offset (Fig. 1B, SI appendix, section S4). Finally, the time of the ecdysis was defined as the time when the shed cuticle was first visible in the transmitted light image (Fig. 1C). For details on data acquisition and analysis, see SI appendix, sections 1-3.

Scaling of developmental timing in individual animals

We first quantified developmental timing, i.e. the time of seam cell division, *wrt-2* expression peaks and ecdysis relative to hatching, under standard conditions: wild-type animals fed *E. coli* OP50 at 23°C (Fig. 1E,F). Individual animals showed strong variability in the total duration of development (~40 h), defined as the time between hatching and L4 ecdysis, with a ~10 h difference observed between the first and last animal to enter adulthood. We observed similar variability in the timing of all measured events (Fig. 1F). The variability in timing was uncorrelated with position of each animal in the microchamber array (SI appendix, Fig. S1A-G), ruling out that it represented systematic variation due to spatial gradients in temperature and/or chemical environment. Moreover, we found similar timing variability in populations propagated by picking single individuals for 5-11 generations (Fig. S1H), indicating that it did not result from underlying genetic variation between individuals. We therefore concluded that this variability in timing is intrinsic.

For some events, such as the second seam cell division and the first ecdysis, the magnitude of the variability was larger than the average difference in timing. However, we found that the

stereotypical event order was maintained in almost all individuals (Fig. S2A), even for events that took place close together in time, raising the question how this correct event order was maintained. Interestingly, the variability in timing was strongly correlated: when we plotted event times t_a and t_b measured in the same animal against each other, for different pairs of events a, b, all data points clustered along a line (Fig. 1G, Fig. S3A). This strong correlation was even present for event pairs widely separated in time, e.g. Division 1 and Peak 4.

A simple argument could explain this observation. As measure of developmental progression, we first defined the developmental phase $\phi_a = \langle t_a^S \rangle / \langle T^S \rangle$, where $\langle t_a^S \rangle$ and $\langle T^S \rangle$ are the population-averaged time of event a and duration of development under standard conditions (23°C), respectively, with $\phi = 0$ and 1 corresponding to hatching and adulthood. When we assumed that for any event a the event time t_a, measured in an individual animal, scales with the total duration of development T for that animal, $t_a = \phi_a \cdot T$, even as the duration T varies significantly between individuals, then the time at which two events a and b occur within the same individual is related by $t_b = \frac{\phi_b}{\phi_a} t_a$, independent of total duration of development T in that individual. As a result, measurements for individual animals will be clustered along a line of constant $\frac{t_b}{t_a}$, as observed experimentally.

Upon inspection, data for different event pairs scattered around this scaling line (Fig. 1G, Fig. S3A), although some event pairs exhibited more variation around this line than others. To quantify how closely the experimental data for each event pair adhered to the above scaling relationship, we first fitted the data for each event pair to a line of the form $t_b = s_{a,b} \cdot t_a$ (Fig. 1G) and then calculated for each data point the distance λ to this fitted line (Fig. S3A). The standard deviation σ_λ then measured the quality of scaling, with $\sigma_\lambda = 0$ corresponding to all data points exactly on the scaling line. While event pairs that included Division 1, Peak 4 or Ecdysis 4 appeared to exhibit a comparatively lower quality of scaling, we found $\sigma_\lambda < 1$hr for all event pairs (Fig. S3C), which was small compared to overall differences in timing observed between individuals.
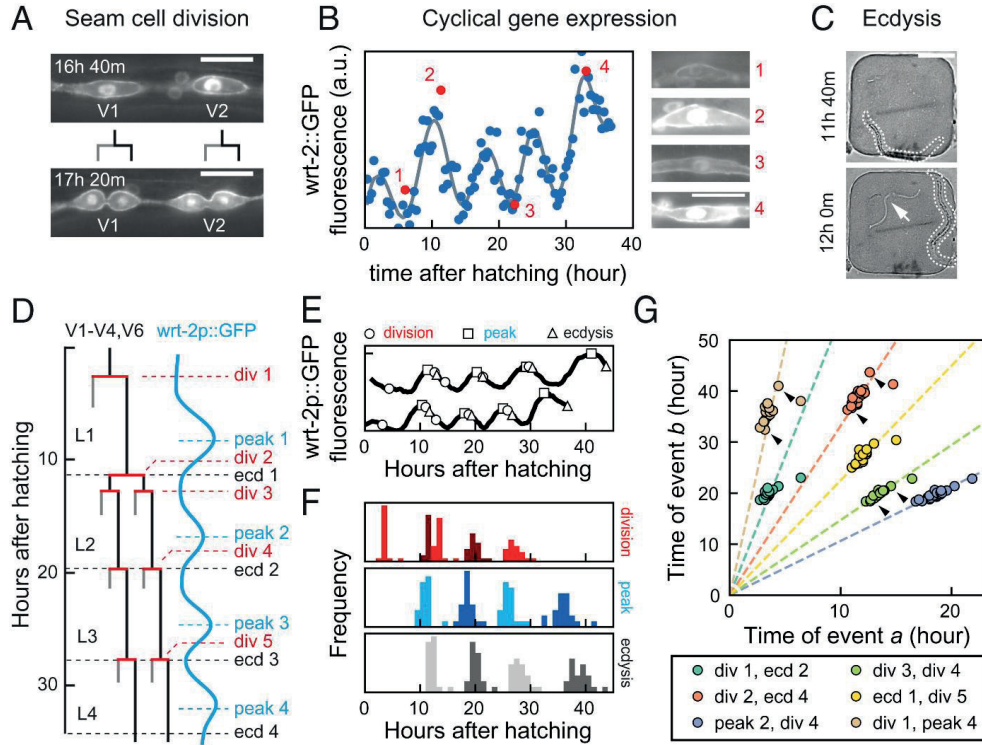
Figure 1. Scaling of developmental timing in individual animals. (A)-(C) Measuring timing of seam cell division, oscillatory gene expression and ecdysis. **(A)** Seam cells divide once or twice every larval stage into hypodermal (grey line) or seam cell (black line) daughters. V1-V6 seam cell division timing was determined using the *wrt-2p::GFP::PH; wrt-2p::GFP::H2B* fluorescent reporter (*wrt-2p::GFP*). Scale bar: 15 µm. **(B)** Oscillatory *wrt-2* expression was visualized in seam cells of *wrt-2p::GFP* animals (panels 1-4, showing posterior V3 seam cell). Time of each *wrt-2* peak was determined from the fluorescence averaged over V1-V6 seam cells (circles) by fitting (grey line, SI Appendix, section S4). Numbers indicate the time points in the side panels. Scale bar: 15 µm. **(C)** Ecdysis time was determined by the emergence of the larva (outlined) from the cuticle (arrow). Scale bar: 100 µm. **(D)** Overview of seam cell divisions, *wrt-2* peaks and ecdysis events during larval development. The V5 lineage lacks Division 2. **(E)** Example of variability in timing between two wild-type animals. Markers indicate the timing of divisions (circles), peaks (squares) and ecdyses (triangles). Tracks are running averages with 2 h window size of the data as shown in (B), shifted along the vertical axis for clarity. **(F)** Distribution of events times for standard conditions, wild-type animals fed *E. coli* OP50 diet at 23˚C (n=21). **(G)** Measured times of event pairs a, b for animals in (F). Markers represent single animals. Arrows indicate the examples in (E). Times of event pairs show temporal scaling, i.e. they cluster along lines of constant $\frac{t_b}{t_a}$, even as individual event times t_a and t_b vary between individuals. Dashed lines are fits $t_b = s_{a,b} \cdot t_a$.

We could reproduce these observations with a simple, phenomenological model. We assumed that development proceeded with average rate $1/\langle T \rangle$ and each event a occurred at a specific

average phase ϕ_a, but with animal-to-animal variation in T, that remained constant throughout development, and variability in ϕ that was uncorrelated between different events (SI appendix, section S5). If the variability in ϕ was sufficiently small, data for event pairs clustered along lines (Fig. S3G,H), indicating temporal scaling, with few changes to event order (Fig. S2C). Increasing variability in ϕ reduced the quality of scaling and caused changes in event order, with events taking place close together in time impacted most strongly.

Overall, our results show that the measured changes in timing between individuals can be fully explained by simple rescaling with the total duration of development in each individual. This means that if an animal executed e.g. its first seam cell division earlier than the rest of the population, it was highly likely to be similarly early in executing all subsequent events for the rest of larval development. This explains how animals maintain correct event order despite the observed variability in timing of individual events.

Scaling of developmental timing upon changes in temperature

Changes in environmental conditions typically change the duration of development, yet how timing of cell-level events is adjusted to such changes is an open question. To address this, we first measured event timing in individual animals maintained at different temperatures, as the duration of larval development increases with decreasing temperatures[24]. As expected, we observed that as temperature was reduced from the standard temperature of 23°C to 19°C and 15°C, the duration of larval development increased from 39±2 to 57±1 and 105±2 h, respectively. Likewise, we found that as temperature decreased, individual events were delayed more strongly relative to standard conditions (Fig. 2A).

To examine the impact of changing temperatures on average event timing, we examined the time evolution of the developmental phase ϕ. Our earlier definition ensured that under standard conditions (23°C) ϕ increases with constant rate $1/\langle T^S \rangle$ (Fig. 2B). If the total duration of development increases or decreases, e.g. due to shifting environmental conditions, $\phi(t)$ will change, so that the same developmental phase ϕ is reached at a different time t compared to standard conditions. When we measured the average time of each seam cell division, *wrt-2* peak and ecdysis for 19°C and 15°C, we found that, while the phase indeed increased at a lower rate compared to 23°C, its increase was still linear in time (Fig. 2B), meaning that all measured differences in average timing were explained by a constant change in the organism-level rate of development, $1/\langle T \rangle$.
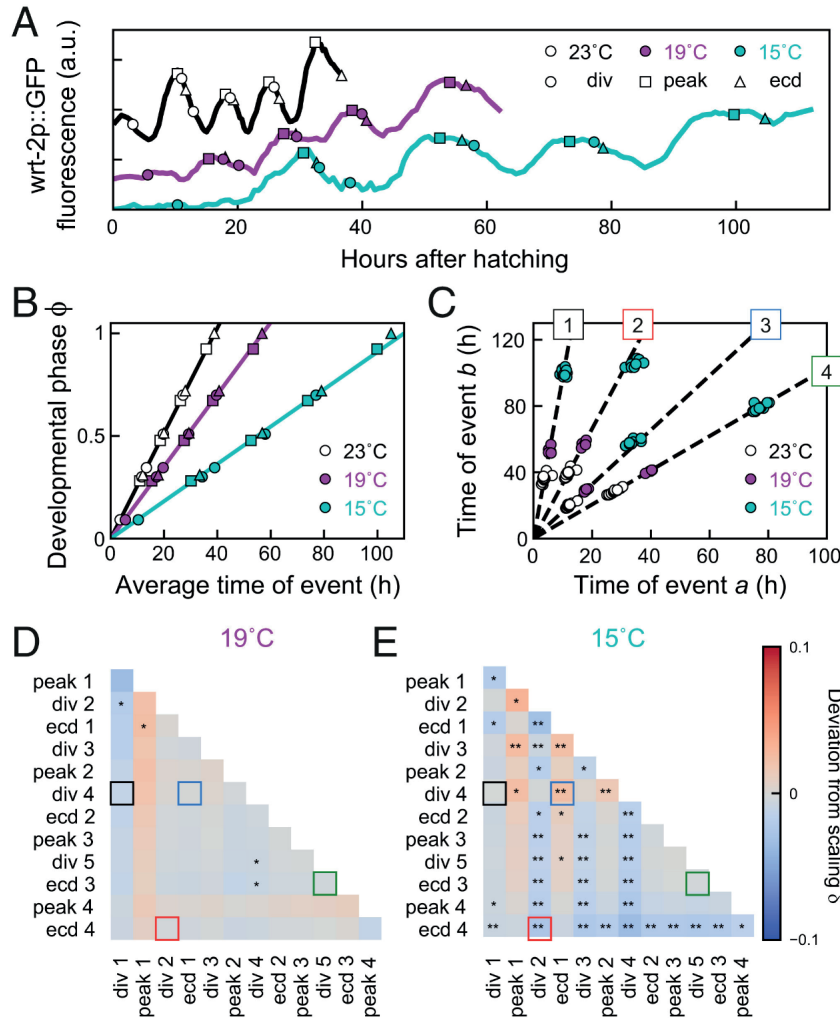
Figure 2. Temporal scaling of developmental timing at different temperatures. (A) Examples of timing in individual animals at standard conditions (23˚C, black), 19˚C (magenta) and 15˚C (cyan). **(B)** Developmental phase as function of time for different temperatures. Developmental progression is modeled as the time evolution of a developmental phase ϕ. Each developmental event a occurs at a specific phase $\phi_a = \langle t_a^S \rangle / \langle T^S \rangle$, where $\langle t_a^S \rangle$ and $\langle T^S \rangle$ are the population-averaged time of event a and of total duration of development under standard conditions. The phase for standard conditions (black line) increases linearly with rate $1/\langle T^S \rangle$. Markers indicate events as in (A). For 19˚C or 15˚C, the phase increases linearly with the average measured event times, albeit at lower rate compared to 23˚C. Solid lines are fits to the 'Uniform' model (defined in Fig. 3). **(C)** Measured times for different event pairs: (1) Division 1 and 4, (2) Division 2 and Ecdysis 4, (3) Ecdysis 1 and Division 4, and (4) Division 5 and Ecdysis 3. Lines are a linear fit to data for standard conditions. Event pair times for different temperatures cluster along the same line. i.e. all events occurred at the same time relative to the total duration of development. **(D),(E)** Deviation from scaling δ for development at (D) 19˚C and (E) 15˚C. In addition, stars indicate the probability that data for standard conditions and 19˚C or 15˚C observe the same scaling relation, as assessed by a Kolmogorov-

Smirnov (K-S) test: **:P<0.001, *:P<0.01, and N.S. otherwise. At 19˚C, temporal scaling was observed for all event pairs, while some significant deviations were seen at 15˚C. Colored squares correspond to event pairs in (C).

When we examined event times in individuals, we found similar variability in timing for animals at 19˚C and 15˚C compared to 23˚C. Moreover, times of event pairs still clustered along lines (Fig. 2C), meaning that variability in timing between individuals was explained by temporal scaling also for these conditions, even though the deviations away from the scaling line were generally stronger than seen for 23˚C (Fig. S3B): the quality of scaling was decreased for all event pairs, in particular at 15˚C. Interestingly, this increase in variability away from the scaling line was accompanied by more frequent changes in event order (Fig. S2B), with most animals at 15˚C reversing order of seam cell divisions and ecdysis in the L1 and L2 larval stages. This result argues against a mechanism that controls event order by causally linking subsequent events, for instance with initiation of seam cell divisions required to trigger the subsequent ecdysis. Finally, we found that, although timing of all events was delayed for 19˚C and 15˚C compared to 23˚C, event pairs clustered along the same line, independent of temperature. This indicates that temporal scaling can not only explain variability in timing between individuals, but also changes in timing between development under different environmental conditions. In the latter case, this means that events occurred at the same relative time, when rescaled with the population-averaged duration of development observed for each temperature, even as development at 15˚C was slowed ~3-fold compared to 23˚C.

We could reproduce these observations in our mathematical model, using the simplest assumption that the observed changes in timing resulted only from a uniformly lowered rate of development ('Uniform' model, Fig. 3A), as seen experimentally (Fig. 2B). Indeed, stochastic simulations showed that the times of event pairs for the 'Uniform' model clustered along the same scaling line as for standard conditions, even though the average times for the 'Uniform' model were significantly delayed (Fig. 3B-D). To test this systematically for all event pairs, we defined the deviation of scaling δ as the signed angle between the lines that fit the data for standard and perturbed conditions (Fig. 3C), with $\delta>0$ meaning that the line for perturbed conditions has a higher slope than for standard conditions. Here, we used the difference between angles rather than slopes, as the slope diverges when the first event *a* occurs close to hatching, $t_a \approx 0$. For the 'Uniform' model, we found that $\delta=0$ for all event pairs (SI appendix, section S6).
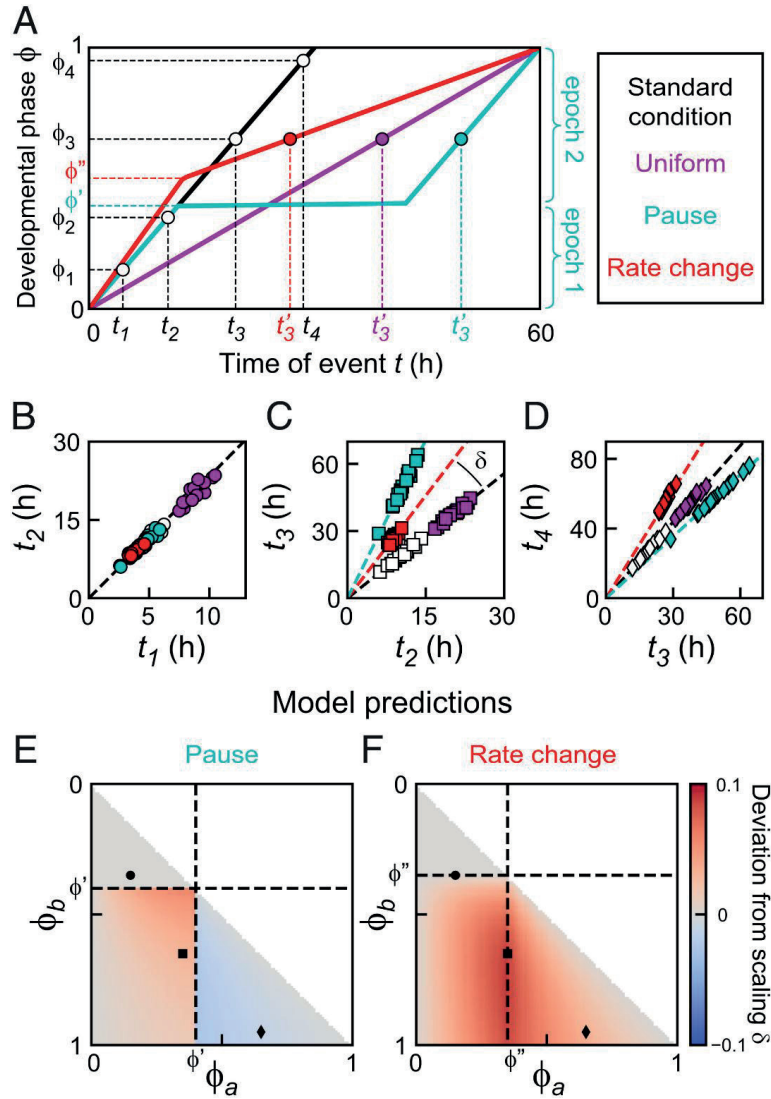
Figure 3. Timing models. (A) Developmental phase versus time for three different models that generate the same increase in duration of development: a uniform lower developmental rate (magenta), a single pause at ϕ' (cyan) or a single change in developmental rate at ϕ'' (red) (SI appendix, section S5, parameters chosen for clarity). For the 'Pause' and 'Rate change' models, the discontinuity in developmental rate results in two epochs of constant developmental rate, as illustrated for the 'Pause' model. (B)-(D) Simulated event times for the event pairs indicated in (A). Color indicates the timing model. For all models, event pair times cluster along a line, i.e. they occur at the same time when rescaled by each individual's duration of development. For the 'Uniform' model, times of event pairs lie along the scaling line for standard conditions (dashed line), i.e. they occur at the same time when rescaled by total duration of development. Other models generally deviate from this scaling line. The deviation from scaling δ is defined as the signed angle between these two lines, as indicated in (C). (E)-(F) Predicted values of δ for different events pairs a and b for the 'Pause' (E) and 'Rate change' (F) model, based on measured parameters (SI

Appendix, sections S6,8). Markers are the event pairs in (B)-(D). The timing models in (A) can be distinguished by measuring δ.

Next, we tested whether this held for our experimental observations. For each event pair a and b measured in the same individual, we calculated the angle $\theta=\arctan\frac{t_b}{t_a}$ and the deviation from scaling as $\delta=\langle\theta^P\rangle-\langle\theta^S\rangle$, the difference between the average angle for standard (S, 23°C) and perturbed (P, 19°C or 15°C) conditions, with $\delta\approx0$ indicating that the data for standard and perturbed conditions clustered along the same line. In addition, we also used the two-sample Kolmogorov-Smirnov test to estimate the probability that the θ distributions measured for standard and perturbed conditions were drawn from the same distribution. This analysis showed that most event pairs at 15°C and 19°C (Fig. 2D,E) lie along the same line as data for 23°C, i.e. changes in timing between temperatures are fully captured by temporal scaling with duration of development. At 15°C, we observed significant deviations from scaling only for event pairs that included Divisions 2-4 or Ecdysis 4. Interestingly, these deviations are consistent with the permutations in event order for 15°C (Fig. S2B), indicating that these permutations reflected changes in timing of seam cell divisions, not ecdyses.

Impact of changes in diet on developmental timing differs between epochs

To test whether temporal scaling is also observed under qualitatively different changes in environmental conditions, we studied the impact of changes in food uptake and diet on timing of individual events. Total duration of development can be changed by providing animals with other food than *E. coli* OP50[25-27]. Here, we used two different approaches. To mimic reduced food uptake, we fed the standard diet, E. coli OP50, to *eat-2(ad1113)* mutants that exhibit a 5-fold decrease in pharyngeal pumping and hence ingest bacteria at a lower rate[28]. In addition, we grew wild-type animals on a diet of E. coli HB101, which was reported to have faster larval development[25].

The total duration of development was slightly different in *eat-2* mutants (40±2h) and wild-type animals on HB101 (38±1h), compared to standard conditions of wild-type animals on OP50 (39±2h, Fig. 4A). However, we observed more complex changes in timing when we examined the average timing of seam cell divisions, *wrt-2* peaks and ecdyses (Fig. 4B). For *eat-2* mutants, the developmental phase increased linearly with time, with a lower rate compared to standard conditions, consistent with the 'Uniform' model. However, for animals fed HB101 the increase of phase in time did not appear to be linear. Instead, development was separated into multiple epochs, i.e. sequences of events that differed in how their timing was impacted by changing diet. Events in the first epoch (hatching to Division 3) occurred with the same timing as under standard conditions. In the second epoch (Peak 2 to Ecdysis 3) the phase increased

at the same rate, but with a ~2h pause compared to standard conditions. In comparison, events in the third epoch (Peak 4 and Ecdysis 4) were executed much earlier. This shows that the reported earlier entry into adulthood on HB101[28] did not reflect a general speed-up in larval development, but a more complex combination of pausing and acceleration.
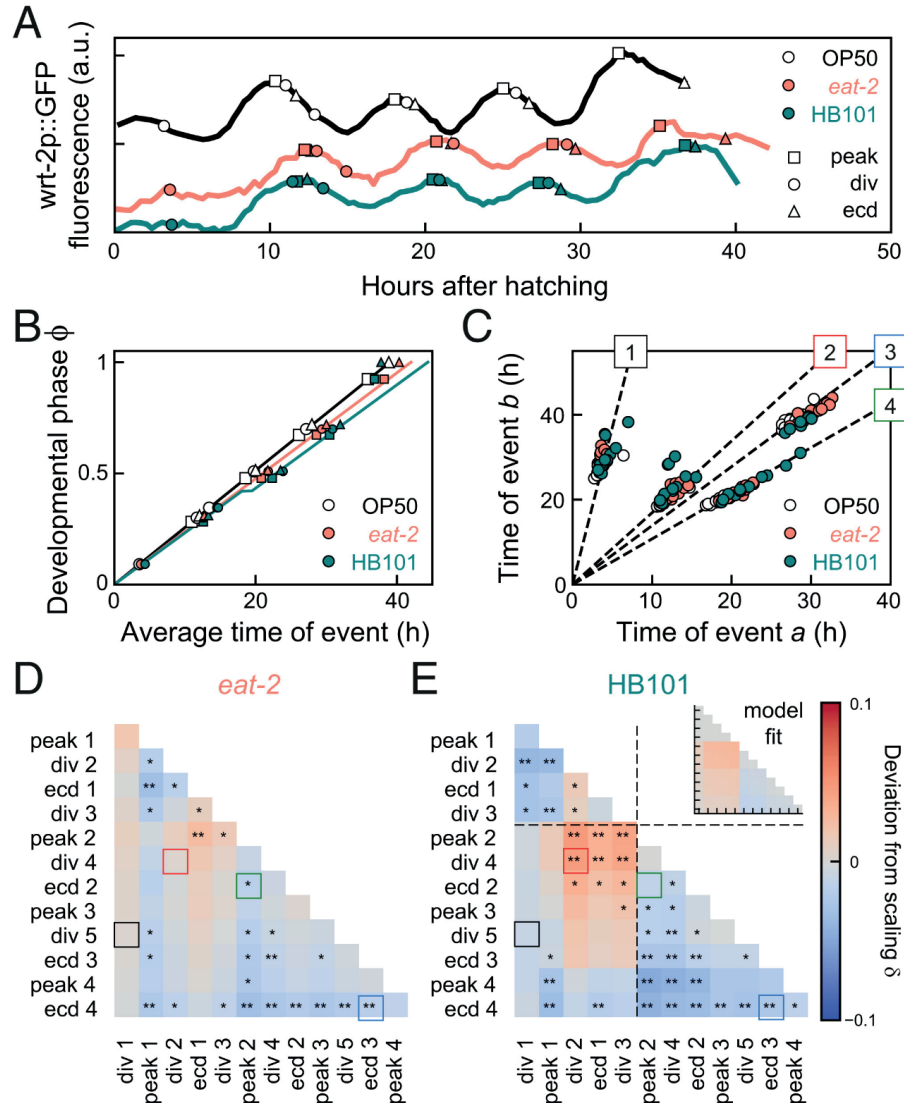
Figure 4. Temporal scaling for changes in diet. (A) Developmental timing in individual animals under standard conditions (black) and two conditions that exhibit slower development: wild-type on *E. coli* HB101 (green) and *eat-2* mutants, that have reduced food uptake, on *E. coli* OP50 (orange). **(B)** Developmental phase versus time. Solid lines are best fits to the 'Uniform' model (*eat-2* mutants, orange line) and the 'Pause' model (HB101 diet, green line) with a ~2 h pause between division 3 and peak 2. **(C)** Measured times for event pairs: (1) Division 1 and 5, (2) Division 2 and 4, (3) Peak 2 and Ecdysis 2, and (4) Ecdysis 3 and 4. Lines are the fit for standard conditions. For

(2) and (3), animals on HB101 deviate from this scaling line. **(D),(E)** Deviation from scaling for (D) *eat-2* mutants and (E) animals fed HB101. Stars indicate the probability that the data observes the scaling relation for standard conditions: **:P<0.001, *:P<0.01, and N.S. otherwise (K-S test). Lines in (E) indicate the fitted pause time. Inset shows best fit to the 'Pause' model. Animals on HB101 exhibit systematic deviations from scaling that match the 'Pause' model in sign and magnitude.

The comparatively small differences between standard conditions and animals fed HB1010 raised the question whether the data for HB101 was indeed not explained by a simple rescaling of time, as for changes in temperature, but required a more complex timing model. We focused on the apparent delay between epochs 1 and 2, and ignored the changes in timing of epoch 3, as the small number of events in that epoch made it difficult to constrain timing models. We constructed a phenomenological model analogous to the 'Uniform' model, that incorporated the pause separating epochs 1 and 2 ('Pause' model, Fig. 3A, SI appendix, section S5). Stochastic simulations of the 'Pause' model (Figs. 3B-D) showed that times of event pairs still clustered along a line, reflecting temporal scaling between individuals. However, this line deviated from the scaling line for standard conditions. Interestingly, the experiments reproduced these simulation results. Data for both *eat-2* mutants and fed HB101 still clustered along a line (Fig. 4C), consistent with temporal scaling between individuals, although compared to standard conditions the quality of scaling was decreased (Fig. S3E) and we observed more frequent permutations of event order for events that occurred close in time (Fig. S2D). However, for animals fed HB101, but not for *eat-2* mutants, some event pairs exhibited small, but systematic deviations from the scaling line for standard conditions (e.g. event pairs 2 and 3 in Fig. 4C), as seen in the 'Pause' model.

When we calculated the deviation from scaling δ between the 'Standard condition' and 'Pause' models, we found that it exhibited a specific pattern (Fig. 3E): while timing of event pairs that both occurred before the developmental pause matched the line for standard conditions, event times clustered along a line with higher slope ($\delta > 0$) when one event occurred before and the other after the pause, with stronger deviations if both events were close to the pause. When both events occurred after the pause, event times clustered along lines with lower slope ($\delta < 0$), with stronger deviations when events occurred farther apart in development. When we calculated δ for all experimentally measured event pairs, we found a clear difference between *eat-2* mutants and animals fed HB101 (Fig. 4D,E). Whereas for *eat-2* mutants we found $\delta \approx 0$ for most event pairs, animals fed HB101 showed significant deviations from scaling that resembled, both in magnitude and sign, those predicted by the 'Pause' model.

We then compared the performance of the 'Uniform' and 'Pause' models in reproducing the experimental data as follows (SI appendix, section S7): we used least-squares fitting to obtain values for the magnitude and timing of the pause that minimized the difference in δ between

experiments and the 'Pause' model (Fig. 4E, inset). The resulting fit accurately reproduced δ for events for epochs 1 and 2, but underestimated δ for Peak 4 and Ecdysis 4, confirming that they form a separate epoch. Next, we fitted the remaining free parameter, the developmental rate $1/\langle T \rangle$, to minimize the difference in the average event time as function of developmental phase (Fig. 4B). Notably, this curve provided an excellent fit to the data in epochs 1 and 2, even though the qualitative shape of this curve depended only on the timing and magnitude of the pause, and was thus fully determined by the fit to δ. A similar fit of the data in Figs. 4B,D,E to the 'Uniform' model showed that, while data for *eat-2* mutants was best fit by the 'Uniform' model, the 'Pause' model formed a much better fit for animals fed HB101 (Fig. S4).

The timing of the pause at the mid-L2 larval stage was notable, as it coincided with the developmental window during which animals, if deprived of food, decide whether to enter dauer, a stress-resistant arrested state[29, 30]. We therefore examined if the pause reflected a transient activation of the dauer regulatory machinery, potentially induced by nutrient stress due to the HB101 diet. DAF-2/Insulin signaling controls dauer entry and is triggered by nutrient stress[31]. As measure of insulin activity, we monitored nuclear translocation of DAF-16, as DAF-16 enters the nuclei of many cells both during food deprivation and in dauer [31]. We confirmed our time-lapse imaging approach could detect DAF-16 nuclear translocation in time, as we observed a strong increase in nuclear DAF-16 in the late-L2 stage of *daf-2* mutants that enter dauer even with food present[32] (Fig. S5A-C). When we examined wild-type animals fed OP50 or HB101, we found that DAF-16 was almost always cytoplasmic, with no difference between the two diets (Fig. S5D-F), indicating that the pause in animals fed HB101 was not due to different insulin signaling activity. Insulin signaling activity also controls developmental rate[33], raising the possibility that the variability in timing we observed might result from variation in insulin signaling between individuals. However, our data does not support this, as we observed no correlation between DAF-16 nuclear localization and ecdysis time in individual animals (Fig. S5G).

Perturbed developmental timing and growth in *lin-42* mutants

For wild-type animals on HB101 we observed deviations from temporal scaling even as diet had only minor impact on total duration of development. To seek stronger perturbations of developmental timing and, potentially, temporal scaling, we measured event timing in mutants of the heterochronic gene *lin-42*, for the following reasons. First, *lin-42* plays an important role in molting, with mutants showing longer larval stages, strongly reduced synchrony between individuals in progression through larval stages and frequent developmental arrest, with all these phenotypes increasing in severity as development proceeds[19, 34, 35]. Second, *lin-42* mutants exhibit heterochronic phenotypes in multiple organs[19, 20, 36, 37], indicating a body-wide role for *lin-42*. In addition, *lin-42* is expressed in oscillatory manner, peaking once every

larval stage[20]. This, together with the homology of *lin-42* to the circadian clock gene *Period*, led to the speculation that *lin-42* acts as a global developmental timer[11, 19]. Finally, *lin-42* regulates the expression of many miRNAs, including those involved in timing through the heterochronic pathway and binds to the promoter of many genes[38-40]. Because of this wide-ranging impact on developmental timing and gene expression, *lin-42* appeared to us a prime candidate also for a core component of a potential scaling mechanism. Hence, we examined whether *lin-42(0)* animals displayed stronger deviations from temporal scaling than observed under changes in diet.

We used the *lin-42(ox461)* allele that deletes the entire *lin-42* locus and shows the strongest perturbation of molting cycle progression[34]. Indeed, developmental progression varied strongly between individuals, with animals arresting at different stages of development and frequently skipping seam cell divisions (Fig. S6A). Most animals skipped the L4 seam cell division and ecdysis, a heterochronic phenotype observed before[19]. Moreover, the timing of larval development was highly delayed and variable, as seen e.g. by comparing the time of the L3 ecdysis (42±8h for *lin-42(0),* compared to 28±1h for wild-type animals). In addition, *lin-42(0)* animals showed reduced growth, as measured by the increase of body length and width over time in individual animals (Fig. 5A,B, Fig. S6B,C). In particular, we observed a fraction of animals that stopped growing completely between the L2 and L4 larval stage, with some reaching body lengths of only 0.3mm, compared to 0.9mm for wild-type animals. Surprisingly, all animals that arrested growth appeared to otherwise continue development: they underwent multiple rounds of ecdysis, seam cell divisions and *wrt-2* expression peaks (Fig. 5C). After molting, *lin-42(0)* animals often remain stuck in their old cuticle, and it was suggested that this interferes with the ability to feed[34]. However, we observed growth arrest also in animals that appear to shed their cuticle normally. Moreover, growth-arrested animals also displayed pharyngeal pumping, suggesting that growth arrest was not simply caused by inability to take up food.
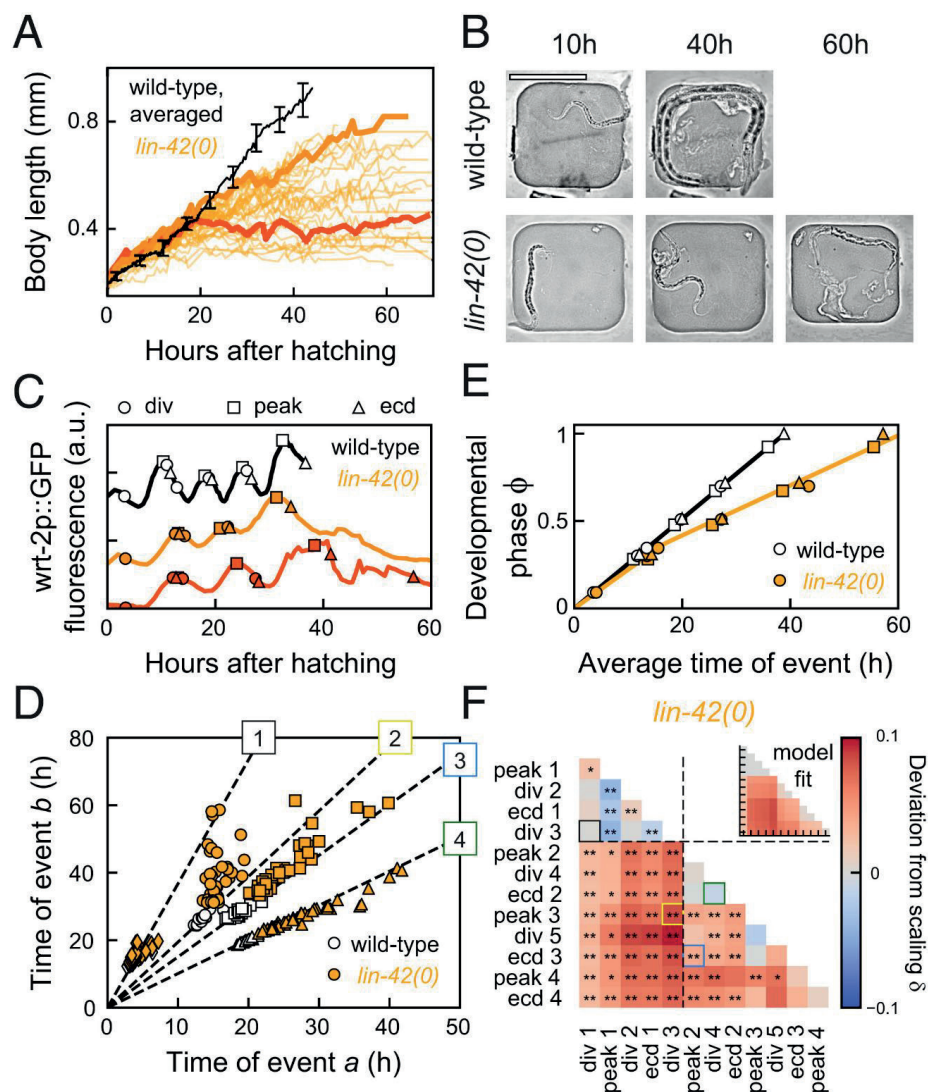
Figure 5. Growth arrest and temporal scaling in lin-42(0) animals. (A) Body length versus time for standard conditions (black, averaged, error bars are S.E.M) and *lin-42(0)* animals (orange lines, individual animals). *lin-42(0)* animals exhibited either reduced growth or complete growth arrest (final body length <0.5mm) from the mid-L2 stage, ~20 h after hatching. Thick lines highlight individuals with reduced (light orange) and arrested growth (dark orange). **(B)** Images of a wild-type (top) and growth-arrested *lin-42(0)* larva (bottom) at different times after hatching. Scale bar: 200 µm. **(C)** Timing in a wild-type larva (black), and in a slow-growing (light orange) and growth-arrested (dark orange) *lin-42(0)* animal, corresponding to the individuals highlighted in (A). The growth-arrested animal executed most events that occur after mid-L2, i.e. development was not arrested. **(D)** Measured times for event pairs: (1) Division 1 and 3, (2) Division 3 and Peak 3, (3) Peak 2 and Ecdysis 3, and (4) Division 4 and Ecdysis 2. Lines are fits for standard conditions. *lin-42(0)* animals show strong variability in timing between individuals, and for event pairs (2) and (3) exhibit clear deviations from the scaling line. **(E)** Developmental phase versus time in wild-type (black) and *lin-42(0)* animals (orange). Orange line is the best fit to the 'Rate change' model, with wild-type

developmental rate until mid-L2, and ~2-fold decreased afterwards. **(F)** Deviation from scaling in *lin-42(0)* mutants. Stars indicate probability that *lin-42(0)* data observes the same scaling relation as wild-type: **:P<0.001, *:P<0.01, and N.S. otherwise (K-S test). Inset shows best fit to 'Rate change' model. The data matches the 'Rate change' model, with lines indicating the fitted rate change time.

Temporal scaling explains most variability in timing of *lin-42* mutants

We then asked whether the increased variability in development of lin-42(0) mutants reflected errors in control of developmental timing. When we compared times of event pairs between individuals, variability in timing was indeed dramatically increased compared to wild-type animals (Fig. 5D). Yet, surprisingly, for many event pairs the data clustered along a line, indicating that this variability in timing scaled between individuals. Indeed, the quality of scaling was comparable to other conditions we examined (Fig. S3F), with strongly reduced quality only seen for events that occurred in L4, a stage rarely reached by most *lin-42(0)* animals, and in pairs where one event occurred before Peak 2 and the other event after. Moreover, we found that event order was well maintained (Fig. S2E). Growth-arrested animals did not develop more slowly, and their developmental timing did not exhibit stronger deviations from temporal scaling (Fig. S4D-F), suggesting that timing of development was largely independent of physical growth. Together, these results suggested that the strongly increased variability in timing was not due to intrinsic errors in timing, corresponding to changes in the developmental phase ϕ, but rather because of increased variability in the overall rate of development, $1/\langle T \rangle$, between individuals.

To test this hypothesis, we first measured the evolution of the developmental phase in *lin-42(0)* animals (Fig. 5E). We found that development separated into two epochs that differed in changes to timing: in the first epoch (hatching to Division 3), developmental phase increased at the same rate as in wild-type animals, while in the second epoch (from Peak 2 onwards) the phase still increased linearly but with a strongly decreased rate compared to wild-type animals. We then used the same procedure as above to fit our experimental data to a model ('Rate change', Fig. 3A, SI appendix, section S5) that incorporated the observed change in developmental rate. First, we calculated the deviation from scaling δ between the data for wild-type and *lin-42(0)* animals (Fig. 5F). Next, we fitted δ, as predicted by the 'Rate change' model, to the experimental data, thereby obtaining values for two model parameters, the developmental phase at which the rate change occurred and the ratio of the two developmental rates. The resulting fit accurately reproduced the experimental observations (Fig. 5F, inset), outperforming other models (Fig. S4A). This showed that the measured deviations from scaling were fully explained by the observed change in developmental rate. Finally, we obtained the value of the remaining free parameter, the developmental rate of the first epoch, by fitting the

phase evolution of the 'Rate change' model to that measured experimentally, with again good agreement between model and experimental (Fig. 5E). Overall, these results show that most differences in timing between *lin-42(0)* mutants and wild-type animals are explained by the change in developmental rate in the mid-L2 stage, combined with strongly increased variability in total duration of development between individuals.

However, a subset of event pairs exhibited timing that deviated strongly from temporal scaling, as measured by the scaling quality (Fig. S3F). The hallmark of scaling is that if an individual executes one event early compared to the population, then all subsequent events are equally early. Event pairs that showed low scaling quality often violated this rule. For example, some animals that were among the first to execute Division 3 exhibited an exceptionally late Peak 3, resulting in many points away from the scaling line (Fig. 5D, event pair 2). In general, the duration of the first and second epoch were often poorly correlated in *lin-42(0)* animals, in particular compared to standard conditions and wild-type animals fed HB101 (Fig. S7A-C). Simulations showed that this comparatively weak correlation reproduced the observed deviations from scaling (Fig. S7D-G). This suggested that the lack of scaling for these event pairs did not represent timing errors, but rather reduced correlation between the developmental rates of the two epochs.

Loss of epochal organization upon shifts in conditions

We found that upon a constant change in external conditions, either all events changed timing in the same manner (temperature, *eat-2* mutants), or all events within an epoch did (HB101 diet, *lin-42(0)* mutants). These coordinated changes in timing ensured that event order was largely maintained, even as the timing of individual events was shifted by many hours. This observation raised the question whether such coordinated changes in timing between events in an epoch is seen for all condition changes. We addressed this by examining the impact of a qualitatively different kind of condition change, namely shifting external conditions mid-development.

We first subjected animals to a shift in temperature from 19 to 23˚C in the L2 larval stage. The rate of development increased notably after the shift to higher temperature (Fig. 6A,C). We tested whether changes in average timing were simply described by development at the rate observed for 19˚C prior to the shift, and the rate for 23˚C after. Indeed, when we used the measured rates for 19 and 23˚C and the observed shift time, the 'Rate change' model accurately captured the measured average timing for most events, without any free fitting parameters (Fig. 6C). However, a clear exception was the timing of Peak 4. Whereas this peak always preceded Ecdysis 4 by 3 h at 23˚C, upon temperature shift, this order was reversed

with Peak 4 now observed 1 h after Ecdysis 4 (Fig. S2). Other events also showed reversals in order, but these occurred much closer in time than Peak 4 and Ecdysis 4. When we compared the deviation from scaling between standard conditions and the temperature shift experiment, we found that it strongly resembled the prediction by the 'Rate change' model (Fig. 6E). The only exception formed event pairs that included Peak 4, consistent with the delayed timing of Peak 4 relative to Ecdysis 4.
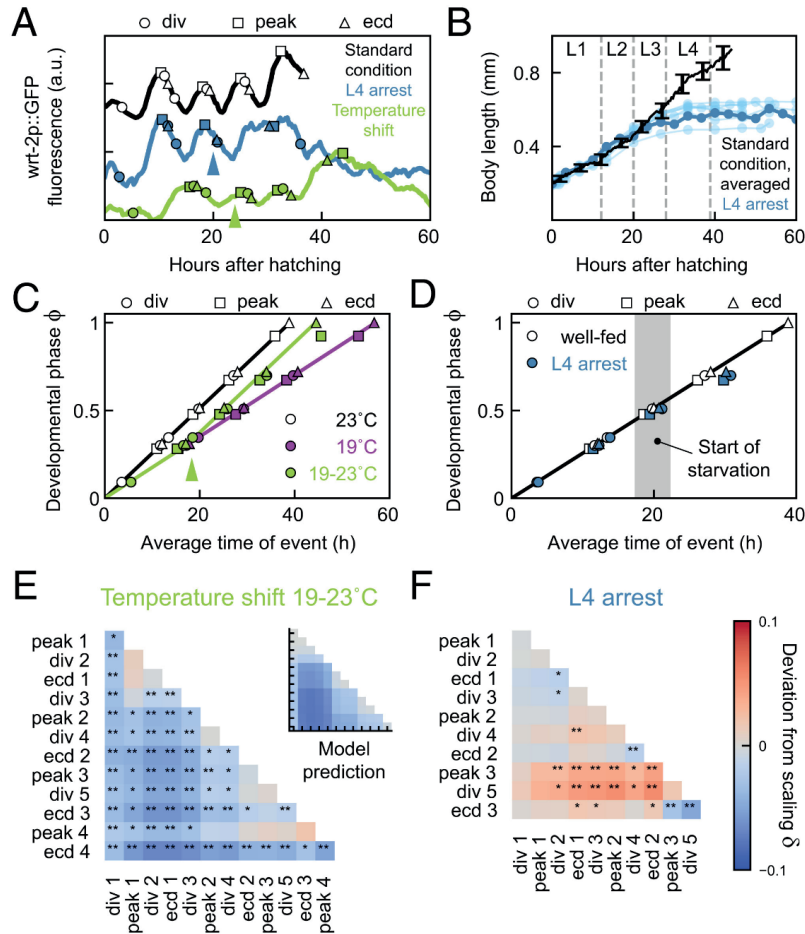
Figure 6. Loss of epochal organization upon condition shifts. (A) Developmental timing in a larva at standard conditions (black) and in animals shifted in temperature (green) or food abundance (blue). Arrows indicate time of the shift from 19 to 23˚C (green) or full depletion of food (blue). **(B)** Body length versus time for standard conditions (black, average, error bars are S.E.M.) and animals shifted to no food (blue). Dark blue line corresponds to the individual in (A). Grey lines indicate average ecdysis time for standard conditions. Animals arrest growth directly after depleting food in L3. **(C)** Developmental phase versus time in animals at 23˚C (black) and 19˚C (magenta), and in animals shifted from 19 to 23˚C (green). Arrow indicates the average time of the temperature shift. Green

line is the 'Rate change' model, assuming that development progresses at the 19˚C rate prior to the average shift time, and the 23˚C rate after. **(D)** Developmental phase versus time in well-fed animals (black) and animals shifted to no food (blue). Grey area indicates the time range at which the food supply was depleted. **(E)**,**(F)** Deviation from scaling for animals subjected to shift in temperature (E) or food abundance (F). Stars indicate probability that the data observes the same scaling relation as standard conditions: **:P<0.001, *:P<0.01, and N.S. otherwise (K-S test). Inset in (E) shows the prediction of the 'Rate change' model shown in (C).

Next, we subjected animals to a shift in food abundance. We loaded microchambers with a reduced amount of OP50. Under these conditions, animals developed with normal body growth and timing for early larval development (Fig. 6B, D), but fully depleted their food supply around the L2 ecdysis, which was accompanied by immediate halting of body length extension. Similar to our observations in *lin-42(0)* mutants, we found that development proceeded even after growth arrested, as all L3-specific events (Peak 3, Division 5 and Ecdysis 3) were executed. However, we did not observe any subsequent L4-specific events (Peak 4 and Ecdysis 4), consistent with larvae entering starvation-induced L4 arrest[41]. The timing of the L3 events was delayed compared to standard conditions (Fig. 6A,C), but with clear differences between events. The time of Peak 3 was delayed, both because it started later, but also due to its increased duration. Division 5 was similarly delayed. However, Ecdysis 3 occurred with a timing much closer to that for standard conditions. As a result, the order of events was shifted, so that Ecdysis 3 typically preceded Peak 3 and Division 5 (Fig. S2). This was further confirmed when we examined the deviation from scaling (Fig. 6F). Whereas the deviation was strong for event pairs including Peak 3 and Division 5, the deviation was much weaker for Ecdysis 3, meaning that the timing of Ecdysis 3 was close to that expected for animals on standard conditions.

Our observation that, under a constant change in diet or genotype, events were linked in epochs that changed their timing in a coordinated manner, suggested that these events were intrinsically linked in their timing: for example, they might all be controlled by a single timer. However, our observation here that this epochal organization is not maintained under shifts in conditions, implies that timing of these events is controlled by independent timers and, hence, that their organization in epochs seen under other conditions reflects a precise synchronization in timing.

Discussion

By performing time-lapse imaging on individual *C. elegans* larvae, we found that timing of seam cell divisions, *wrt-2* gene expression oscillations and ecdysis varied widely, not only when genotype or environmental conditions were changed, but even between genetically identical individuals under the same conditions. Surprisingly, we found that all this variation in timing could be explained to a great extent by simple, phenomenological timing models that relied on the concept of 'temporal scaling'.

In these models, the complexity of developmental progression is reduced to the evolution of a developmental phase in time (Fig. 3). Animal-to-animal variability arises because each animal proceeds through its phase evolution at an intrinsically different rate, giving rise to the strongly correlated variability we measured for timing of event pairs. As a result, timing between individuals exhibits temporal scaling, i.e. events occur at the same time when measured relative to the total duration of development in each individual. Varying conditions or genotype results in changes to the evolution of developmental phase. While in some cases (changes in temperature, impaired food uptake in *eat-2* mutants) the rate of phase evolution changed uniformly for all events, in other cases (HB101 diet, *lin-42(0)* mutants) larval development was divided in multiple epochs that differed in how the evolution of phase is impacted. In the latter case, changes in timing between animals of different genotype or raised under different conditions could not be explained by simple rescaling with total duration of development. However, event timing did exhibit temporal scaling, when taking into account these epochs, i.e. events occur at the same time when measured relative to the duration of each epoch. While these phenomenological models do not provide a molecular mechanism for temporal scaling, they reveal a remarkably simple organization that unifies the pervasive variation in timing seen in our experiments.

It is striking that isogenic animals under identical environmental conditions showed substantial variability in developmental timing. It is unlikely that this reflects systematic variation in environmental conditions, such as temperature, between animals in our experiment setup or genetic variation (Fig. S1). Similar individual variability was observed recently in the timing of lethargus, as measured by behavioral assays with a similar level of environmental control[42, 43]. Overall, these results suggest that this variability in timing is intrinsic, reflecting a variation in developmental rate between individuals. What controls this variation? Recent work showed that animal-to-animal variability in timing of the L4 ecdysis, i.e. the transition into adulthood, correlated with age of the mother at fertilization[44], with embryos generated by older mothers developing more rapidly. This was linked to the amount of yolk proteins loaded in each embryo, which increased with the mother's age, suggesting that the rate of larval development is determined by the status of nutrient stores in the embryo. It is surprising, however, that this variation in rate persists throughout development, particularly as larvae depend for growth on feeding rather than internal stores. We observed that the rate of early-larval development was poorly predictive of the late-larval rate for animals at 15˚C and in *lin-42(0)* mutants (Fig. S7). For *lin-42*, this might reflect a role in maintaining the developmental rate at the embryo-set level, but could also reflect that the severity of the *lin-42(0)* phenotype, as it emerges in the mid-L2 stage, is independent of the early-larval developmental rate.

For wild-type animals fed HB101 and *lin-42(0)* mutants, we observed discontinuities in the developmental rate that separated larval development into multiple epochs (Figs. 4B, 5E). Interestingly, even though the nature of the discontinuity differed, with a pause for HB101 diet and a rate change for *lin-42(0)* mutants, in both cases the transition between the first and second epoch occurred at the mid-L2 larval stage. At this developmental stage, animals may decide to enter the stress-resistant dauer state if the environment is crowded or deprived of food [29, 30], raising the question whether the change in developmental rate we observed reflected transient activation of dauer decision-making machinery. However, we found that activity of the DAF-2/insulin pathway, a key regulator of entry into dauer[31], did not differ between animals fed OP50 or HB101 (Fig. S5). This implied that animals did not suffer from stress due to nutrient depletion, making it unlikely that the pause in animals fed HB101 was linked to dauer. We therefore prefer another explanation: *C. elegans* larvae also shift their metabolism between the L1 and L2 larval stage, from the glyoxylate cycle to the TCA cycle[45]. The glyoxylate cycle likely allows L1 larvae to use stored lipids as an energy source, potentially rendering their development less dependent on ingestion of food. As a consequence, shifts in diet (from *E. coli* OP50 to HB101) or inability to ingest or metabolize food in *lin-42(0)* mutants might only impact developmental timing substantially after shifting to the TCA cycle upon entering the L2 larval stage.

A limit of our study is that it does not provide a mechanistic explanation of temporal scaling. Based on its oscillatory expression and homology to the circadian clock protein Period, *lin-42* was proposed to be a core component of a clock controlling *C. elegans* larval development[11]. This hypothesis was supported by the strong loss of developmental synchrony between *lin-42(0)* individuals. However, we found that this perturbed timing resulted mainly from dramatically increased variability in developmental rate between individuals, while timing of individual events obeyed temporal scaling within each epoch. This result argues against a key role for *lin-42* in controlling temporal scaling. One attractive, alternative mechanism to regulate timing in a manner that is synchronized throughout the body and adapts to changes in rate of development under different conditions, is to couple developmental timing to physical growth. If each event occurred at a specific body size, it would explain temporal scaling, as changes in conditions that impact the body's growth rate would naturally lead to concomitant changes in developmental timing. Analogously, cell cycle timing in bacteria and yeast strongly depends on cell size and growth[46-49]. Indeed, progression of *C. elegans* larval development is tightly linked to body size[24], and under dietary conditions that caused slow growth, larval stages lengthened so that molts occurred at their stereotypical body size[4]. Moreover, conditions that do not allow growth, such as starvation, cause developmental arrest at the start of each larval stage[41, 50, 51]. It is therefore significant that both *lin-42(0)* mutants and wild-type animals

shifted to no food showed continued development without physical growth (Fig. 5C, 6A). In *lin-42(0)* mutants, timing is explained by temporal scaling for most animals and event pairs (Fig. 5E,F) and growth-arrested *lin-42(0)* individuals showed similar deviations from scaling as *lin-42(0)* animals that continued growing (Fig. S6D-F). Moreover, while wild-type animals shifted to no food showed specific changes in timing that altered the order of events occurring after the shift, the approximate timing of these events was still similar to that found in animals with plentiful food (Fig. 6D). Thus, our observation of continued development with approximately correct timing in growth-arrested animals rules out a mechanism where the execution of a specific event occurs only at a predetermined body size.

Recent studies examined the dependence of developmental timing in *C. elegans*, fly and frog embryos on temperature[52-55]. Specifically, Kurtz and Eisen found that timing of fruit fly development scaled uniformly with temperature[54], similar to our observations for *C. elegans* larval development. Intriguingly, in these studies the measured dependence of timing on temperature followed an Arrhenius equation[52-54], which is historically used to describe the temperature dependence of chemical reactions. Temporal scaling was hypothesized to arise because timing of all events follows the same Arrhenius equation, i.e. varies by the same factor for a given change in temperature. Because the rates of molecular processes are likely not only controlled by temperature but also by metabolite levels, such thermodynamic mechanisms might also generate temporal scaling upon changes in diet or food uptake, as we observed. However, more recent measurements disputed the key assumption that all processes follow the same Arrhenius equation[52, 53], raising the question whether thermodynamic mechanisms by themselves are sufficient to explain temporal scaling, or if additional active feedback or checkpoint mechanisms are still essential.

Epochs emerged from our data as sets of consecutive events that changed their timing in a coordinated manner upon a constant change in environment or genotype. In particular, events within such epochs generally did not exhibit changes in their relative order, apart from reversals of events that occurred close together in time (Fig. S2). Hence, our observation of epochs could indicate that these events were controlled by the same timer. This would predict that events in an epoch always show coordinated changes in time, regardless of the type of condition change. However, when we shifted conditions (temperature or food abundance) during larval development, we found that some events were strongly delayed or advanced relative to other events in the same epoch (Fig. 6). This implies that timing of events within an epoch can be controlled independently and that precise tuning and/or active synchronization of timing of each individual event is required to maintain relative order under constant environmental conditions. Whereas the loss of stereotypical order in these experiments did not appear to hamper development, similar loss of synchrony between seam cell divisions and the

molting cycle, induced by a nicotinic agonist, caused larval lethality[56], indicating that in general maintaining synchrony of developmental events is of vital importance.

One of the most enduring mysteries of development is how its timing is regulated. Whereas we have a deep understanding of how spatial patterns arise during development[8], our understanding of how events like cell division, cell movement or gene expression are controlled in time is still very limited. Post-embryonic development poses a particular challenge, as its rate of progression depends strongly on environmental conditions such as food availability. How timing is adapted on the cellular level in response to such organism-level changes is an open question. On the molecular level, developmental timing is thought to be controlled either by oscillators or 'hourglass' mechanisms. In *C. elegans*, there is evidence for hourglass mechanisms[16, 17] and oscillators[11, 14] controlling timing of larval development in parallel, although it remains unclear how they determine the exact time of cell-level events on the molecular level. A priori, the core characteristic of hourglass and oscillator mechanisms (their decay time and period, respectively) will each be impacted differently by changes in conditions. Temporal scaling is only observed when all decay times and periods are changed in the same way. Hence, our observation of temporal scaling puts strong constraints on possible models that explain developmental timing of *C. elegans* larval development.

Materials and Methods

Additional information on experimental methods, analysis and models is found in SI Appendix. Briefly, the following mutants and transgenes were used: *heIs63[Pwrt-2::GFP::PH; Pwrt-2::GFP::H2B; Plin-48::mCherry][23]*, *eat-2(ad1113)[28]*, *lin-42(ox461)*[34], *zIs356[Pdaf16::daf-16a/b-gfp; rol-6], stIs10131[elt-7p::H1-wCherry; unc-119(+)], daf-2(e1368)[32]*. For time-lapse experiments, we refer to standard conditions as *wrt2p::GFP* animals fed *E. coli* OP50 at 23˚C. For experiments in perturbed conditions we varied one experimental parameter (genotype, temperature or diet) while keeping the others unchanged. Division and ecdysis times were recorded by manual annotation, while peak times were determined by fitting to *wrt2-p::GFP* fluorescence intensity.

Author contributions to paper

O.F., B.D., and J.S.v.Z. designed research; O.F., B.D., and R.H. performed research; O.F., B.D., and J.S.v.Z. analyzed data; and O.F., B.D., and J.S.v.Z. wrote the paper.

Supplementary Information
1. Strains and experimental conditions

To monitor *wrt-2::GFP* expression in *eat-2* and *lin-42* mutants, these mutations were crossed into *heIs63*. The *eat-2* genotype was confirmed by measuring the rate of pharyngeal pumping, which is decreased 5-fold compared to wild-type animals. As *lin-42* constitutes a complex genetic locus encoding multiple isoforms, we chose to use the *lin-42(ox461)* allele that deletes the entire locus of *lin-42.* In addition, the *lin-42(ok2385)* allele that deletes the main isoform *lin-42a* and the overlapping exons of *lin-42b*, was analyzed and showed similar phenotypes as *lin-42(ox461)* (data not shown). For maintenance, all strains were cultured at 20˚C on NGM (Nematode growth medium) agar plates seeded with OP50 strain of *E. coli* bacteria, using standard *C. elegans* techniques. For the *E. coli* HB101 diet experiment in Fig. 4, animals were maintained on HB101 for 5-7 generations prior to the experiment.

2. Time-lapse microscopy

Custom time-lapse microscopy setup was used to monitor the entire development of individual *C. elegans*. Late-stage embryos were placed inside the 250x250x20 µm polyacrylamide microchambers (one embryo per chamber) filled with *E. coli* OP50 bacteria as food source. Nikon Ti-E inverted microscope with a large chip camera (Hamamatsu sCMOS Orca v2) and a 40x magnification objective (Nikon CFI Plan Fluor 40x, NA=1.3, oil immersion) were used for imaging. Transmission and fluorescence images were acquired with an LED light source (CoolLED pE-100 615nm) and a 488 nm laser (Coherent OBIS LS 488-100), respectively. Each chamber containing a single animal was imaged every 20-40 minutes during the entire larval development (40-100 hours depending on the genotype and temperature). A stack of 20-30 images in the Z-direction was acquired using short exposure times (1-10 ms), such that the motion of the animal was insignificant.

3. Temperature control and condition shifts

All experiments were performed in a temperature-controlled room with a constant temperature inside the sample of 23˚C. To perform an experiment at different temperature, an additional temperature control system was used. A thermoelectric chiller (Thermotek T257P) was used to cool the custom-made objective jacket by circulating an antifreeze fluid (a mixture of water and glycerin) between the chiller and the objective jacket. In order to calibrate the system, a thermocouple temperature sensor measuring 0.025 mm in diameter (RS Pro) was placed inside the sample in contact with the polyacrylamide hydrogel and connected to a digital thermometer (RS Pro). The temperature was then varied on the thermoelectric chiller while the resulting temperature inside the sample was being monitored. In this work, experiments were performed at 23, 19 or 15 ˚C. Temperature shifts were implemented by changing the

temperature of the chiller mid-experiment. As animals in different microchambers hatch at slightly different times, the time after hatching at which the shift in temperature was initiated varied between animals. For shifts in food supply, we loaded each chamber with reduced amounts of OP50. Full depletion of food occurred at different times after hatching for each animal and we only analyzed data for animals that entered L4 arrest.

4. Image analysis

Time-lapse image stacks were processed with custom Python software in order to obtain the precise timing of ecdysis events, seam cell divisions, and peaks in oscillatory *wrt-2* expression. For every animal, the times of hatching and ecdysis events were annotated based on visual inspection of transmitted light images. Hatching was defined as the time larvae first appears out of the egg shell, while ecdysis events were defined as the first appearance of the shed cuticle in the chamber (Fig. 1C). Times of seam cell divisions were annotated based on visual inspection of the *wrt-2p::GFP* fluorescence signal in the nucleus and the membrane of seam cells. Divisions of V1-V6 seam cells occur close together in time. We therefore defined the time of each round of divisions as the average time V1-V6 cells had divided or had started dividing, as determined by the formation of the metaphase plate. We only analyzed seam cells located on the side of the body closest to the objective.

To determine the time of peaks in oscillatory *wrt-2* expression, we first obtained *wrt-2p::GFP* expression profiles as a function of time for individual animals. For this, in every time frame we automatically segmented the region encompassing seam cells using a Watershed algorithm and calculated the average fluorescence intensity inside this region. Finally, to find the time of each peak (μ_i), we fitted the obtained oscillatory profiles with a combination of Gaussian functions and a linear offset using non-linear least-squares minimization (Fig. 1B):

$$f(x, m, b, A_i, \mu_i, \sigma_i) = mx + b + \sum_{i=1}^{n} \left[\frac{A_i}{\sigma_i \sqrt{2\pi}} e^{\left[-\frac{(x-\mu_i)^2}{2\sigma_i^2} \right]} \right] \qquad (1)$$

where *n* is the number of peaks, A_i, μ_i, σ_i are the amplitude, center and width of peak. Finally, we fitted the experimentally measured times for pairs of events a and b to a line function of the form $t_b = s_{a,b} \cdot t_a$ using non-linear least-squares minimization (Fig. 1G), using the Linear Model from the *lmfit* package in Python. To visualize *wrt-2p::GFP* expression dynamics, e.g. in Fig. 1E, we applied a Savitzky-Golay filter with window size of 2 h and polynomial order of 1 on the raw segmented data we show in Fig. 1B. To measure the animal's body length as a function of time (Fig. 5A), we manually annotated ~10 points along the anterior-posterior body axis and performed spline interpolation. Body length was defined as the length of the resulting spline curve.

5. Timing models and simulations

We model the progression of development as the evolution of a developmental phase ϕ, that increases from $\phi=0$ (start of larval development at hatching) to $\phi=1$ (entry into adulthood at the L4 ecdysis). The exact assignment of a phase to a particular developmental event is arbitrary. Here, we define the phase so that for standard conditions (wild-type animals at 23 ˚C) the phase increases linearly with time, $\frac{d\phi}{dt}$=const, and $\phi=1$ at time $t=T$, where T is the total duration of development at standard conditions. As a result, for standard conditions we use the following definition for the developmental phase of event a:

$$\phi_a = \frac{t_a}{T} \tag{2}$$

For other conditions or genotypes, the time evolution $\phi(t)$ of the developmental phase has a different form. As a result, the time of event a, occurring at a developmental phase ϕ_a is given by $t_a = f(\phi_a)$, where f is a monotonically increasing function that is specific for each condition or genotype. Expressions for $f(\phi)$ are discussed further below.

To incorporate animal-to-animal variability, we assumed two different sources of variability. First, there is an intrinsic variability in the stage ϕ_a at which each event a occurs, that is uncorrelated between different events occurring within the same animal. Second, we assumed variability in the total duration of development, T. This corresponds to an animal-to-animal variability in the global rate of development that impacts each event occurring within the same animal equally. Then, the event time $t_{a,i}$ for event a in animal i is given by:

$$t_{a,i} = \frac{f(\phi_a + \eta_{\phi,i})}{T}(T + \eta_{T,i}) \tag{3}$$

where T and ϕ_a correspond to the population average values, while η_T and η_ϕ are Gaussian noise sources with standard deviation σ_T and σ_ϕ, respectively.

The function $f(\phi)$ changes for differing environmental conditions or mutants that perturb the duration of development. In particular, we considered three different models, the 'Uniform', 'Pause', and 'Rate change' models (Fig. 3A). For the 'Uniform' model, event times are given by Eq. 2, but now with an increased duration of development T'. For the 'Pause' model, development occurs at the same rate as for standard conditions, but with a pause at developmental phase ϕ' that results in a total duration of development $T'=(1+\kappa)T$. This results in:

$$t_a = \begin{cases} T\phi_a & \phi_a < \phi' \\ T(\kappa + \phi_a) & \phi_a \geq \phi' \end{cases} \tag{4}$$

Finally, for the 'Rate change' model, the developmental rate differs between events occurring prior to a developmental phase ϕ'' and events occurring afterwards. This yields:

$$t_a = \begin{cases} T_1\phi_a & \phi_a < \phi'' \\ (T_1 - T_2)\phi'' + T_2\phi_a & \phi_a \geq \phi'' \end{cases} \tag{5}$$

where $1/T_1$ and $1/T_2$ correspond to the two developmental rates and the total duration of development is given by $T' = T_1\phi'' + T_2(1 - \phi'')$.

6. Calculation of deviation from scaling for timing models

For the 'Uniform', 'Pause' and 'Rate change' model, we calculate the deviation from scaling as follows. First, we use that fact that for events a and b that occur in the same animal, the total duration of development, T' , has the same value, to express t_b as function of t_a. For the 'Uniform' model, this yields:

$$t_b = \frac{\phi_b}{\phi_a} t_a \tag{6}$$

meaning that that event pairs lie along the scaling line as measured for individuals under standard conditions, and that the changes in timing can be fully captured by a simple rescaling of event times with the duration of development T' under non-standard conditions. In contrast, for the 'Pause' model, this yields:

$$t_b = \begin{cases} \dfrac{\phi_b}{\phi_a} t_a & t_a, t_b < t^* \\ \dfrac{\kappa + \phi_b}{\phi_a} t_a & t_a < t^*, t_b > t^* \\ \dfrac{\kappa + \phi_b}{\kappa + \phi_a} t_a & t_a, t_b > t^* \end{cases} \tag{7}$$

Here, pairs of time points for events a and b only lie along the scaling line for standard conditions when both events occur before the time of the delay, $t^* = T\phi'$. Otherwise, the slope of the line is different from wild-type conditions and depends explicitly on the delay parameter κ. Finally, for 'Rate change' model, corresponding to the *lin-42(ox461)* mutant, we have:

$$t_b = \begin{cases} \dfrac{\phi_b}{\phi_a} t_a & t_a, t_b < t^* \\ \left(\dfrac{\phi''}{\phi_a} + \rho\dfrac{\phi_b - \phi''}{\phi_a}\right) t_a & t_a < t^*, t_b > t^* \\ \dfrac{\phi'' + \rho(\phi_b - \phi'')}{\phi'' + \rho(\phi_a - \phi'')} t_a & t_a, t_b > t^* \end{cases} \tag{8}$$

where $t^* = T_1\phi''$ and $\rho = \frac{T_2}{T_1}$. Apart from the case when $t_a, t_b < t^*$, this expression depends explicitly on the parameters ϕ'' and ρ and does not lie along the same line event pairs for standard conditions. Finally, we calculate the deviation from scaling as:

$$\delta_{ab} = \text{atan}\left(s_{ab}^S\right) - \text{atan}\left(s_{ab}^P\right) \tag{9}$$

where $t_b = s_{ab} \cdot t_a$, with the slope s_{ab} given by Eqs. 6-8, and S and P denote standard and perturbed conditions, respectively.

7. Model fitting

We examined which of the three models, 'Uniform', 'Pause' or 'Rate change', provided the best fit to the experimental data for each mutant or condition examined, using the following procedure. The expression for the deviation from scaling in Eqs. 6-9 either does not depend on model parameters ('Uniform' model) or only on a subset of parameters (κ and ϕ' for the 'Pause' model and ρ and ϕ'' for the 'Rate change' model). Hence, we first fitted the models to the experimentally measured deviation from scaling, by minimizing the root mean square error (RMSE) of the difference between experiment and models summed over all event pairs (Supplementary Fig. 4B,C). Using the best-fit values of these parameters, we then obtained best-fit values for the remaining parameters (T for the 'Uniform' and 'Pause' models, T_1 for the 'Rate change' model) by minimizing the RMSE of the difference between the model and the measured average event times as function of developmental phase, using Eqs. 2, 4 and 5 (Supplementary Fig. 4D). For HB101, we excluded the last two events, Peak 4 and Ecdysis 4, that formed the third epoch. Their timing deviated strongly from that of the events directly preceding them, but the long delay between Ecdysis 3 and Peak 4 and the small number of events in this epoch made it challenging to constrain a timing model for this epoch. For least-squares fitting, we used the *lmfit* package in Python.

8. Model parameters

For the model results in Fig. 3A-D, we used the following parameters, chosen to emphasize and clarify the differences between models. For the 'Standard condition' model: T=30 h. For the 'Uniform' model: T'=60 h. For the 'Pause' model: κ=1 and ϕ'=0.4, resulting in a total duration of development of T'=60 h. For the 'Rate Change' model: T_1=25 h, T_2=95 h and ϕ''=0.5, also resulting in T'=60 h. For the stochastic simulations in Fig. 3C-D: σ_T=5 h and σ_ϕ=7·10^{-3}. For Figs. 2, 3E,F, 4 and 5, we used model parameters that were fitted to the experimental data, as outlined above. In Fig. 2, we used the following fitted parameter values: $T^{23°C}$=39 h, $T^{19°C}$=57 h, and $T^{15°C}$=110 h. In Fig. 4 and Fig. 3E, we used the following fitted parameter values: T^{eat-1}=42 h, T^{HB101}=43 h, κ_{HB101}=0.032 and ϕ'_{HB101}=0.42. In Fig. 5 and Fig.

3F, we used the following fitted parameters: T_1^{lin-42}=45 h, T_2^{lin-42}=70 h and ϕ''_{lin-42}=0.37. In Fig. 6C,E, we used T_1=45 h, T_2=70 h, as determined by the experiments in Fig. 2, and ϕ'' =0.3, corresponding to the average time after hatching at which the temperature shift was initiated.

9. Event order

We first determined the average time of each event, as measured under standard conditions (wild-type animals, fed OP50 and raised at 23°C). We then established the average event order as the sequence of events, as ordered by their average timing. To detect permutations of event order in individual animals (either raised under standard conditions, under different conditions or in mutants) as compared to the average event order, we followed the following procedure. We stepped through each event i in the order determined by the average event order and examined the relative timing of event $i+1$. If event $i+1$ precedes event i in this individual, we first swapped the order of these two events in the sequence of events recorder in this animal, then recorded this as a permutation of events i and $i+1$, and then restarted the procedure at the first event, $i=0$. Upon completion, this procedure has sorted the sequence of events recorded in this individual so that it is identical to the average event order, while recording all permutations between subsequent events i and $i+1$ that are required to achieve this. The frequency of such permutations within a population of animals under different conditions is presented in Supplementary Fig. 2. Note that changes in order of events that on average are not adjacent in time, e.g. the normal order (*a,b,c*) is changed into (*b, c,* a), are with this procedure recorded as two permutations, namely first swapping *a* and *b*, and second *b* and *c*. However, such more complex event reorderings occur relatively rarely.

10. Calculating the deviation from scaling for experimental data

We consider two different kinds of deviations from scaling. First, deviations from inter-individual scaling refer to the deviation of event times $t_{a,i}$ and $t_{b,i}$, measured in each animal i, from the scaling line with slope $s_{a,b}$ that is fitted to the data points for the entire population. The deviation from inter-individual scaling would be zero if all data points for event pairs a and b fall exactly on the line with slope $s_{a,b}$. Second, deviations from population-level scaling refer to differences in the fitted slopes $s_{a,b}^S$ and $s_{a,b}^P$, measured for the same event pair a and b under standard (S) and perturbed (P) conditions. The deviation from population-level scaling is zero when the data points for standard and perturbed condition are fitted by lines with the same slope. To quantify the deviation from inter-individual scaling, we calculated $\theta_i=\arctan\left(\frac{t_{b,i}}{t_{a,i}}\right)$. The angle made by the data point of animal i with the scaling line is then given by $\delta\theta_i=\theta_i - \arctan(s_{a,b})$. Next, we calculated the distance λ_i to the scaling line along a circle with radius $\left(t_{a,i}^2 + t_{b,i}^2\right)^{\frac{1}{2}}$ as $\lambda_i =$

$\delta\theta_i\left(t_{a,i}^2 + t_{b,i}^2\right)^{\frac{1}{2}}$. The deviation from inter-individual scaling is then given by the standard deviation $\sigma_\lambda = \sqrt{\langle\lambda_i - \langle\lambda_i\rangle\rangle}$ calculated over all individuals in the population. We calculated the deviation from population-level scaling as $\delta = \langle\theta_i^P\rangle - \langle\theta_i^S\rangle$. However, in particular for event pairs with small average event times $\langle t_{a,i}\rangle$ and $\langle t_{b,i}\rangle$, values of θ_i can vary substantially, leading to non-zero deviation δ for the typical number of animals analyzed for these experiments. Hence, we also estimate the probability that the two series θ_i^P and θ_i^S are sampled from the same distribution, using the two-sample Kolmogorov-Smirnov test (*ks_2samp* from the *scipy.stats* package in Python). We reported the P value, with high P meaning that the distributions of the two samples are likely the same, and, hence, obey the same temporal scaling relationship.
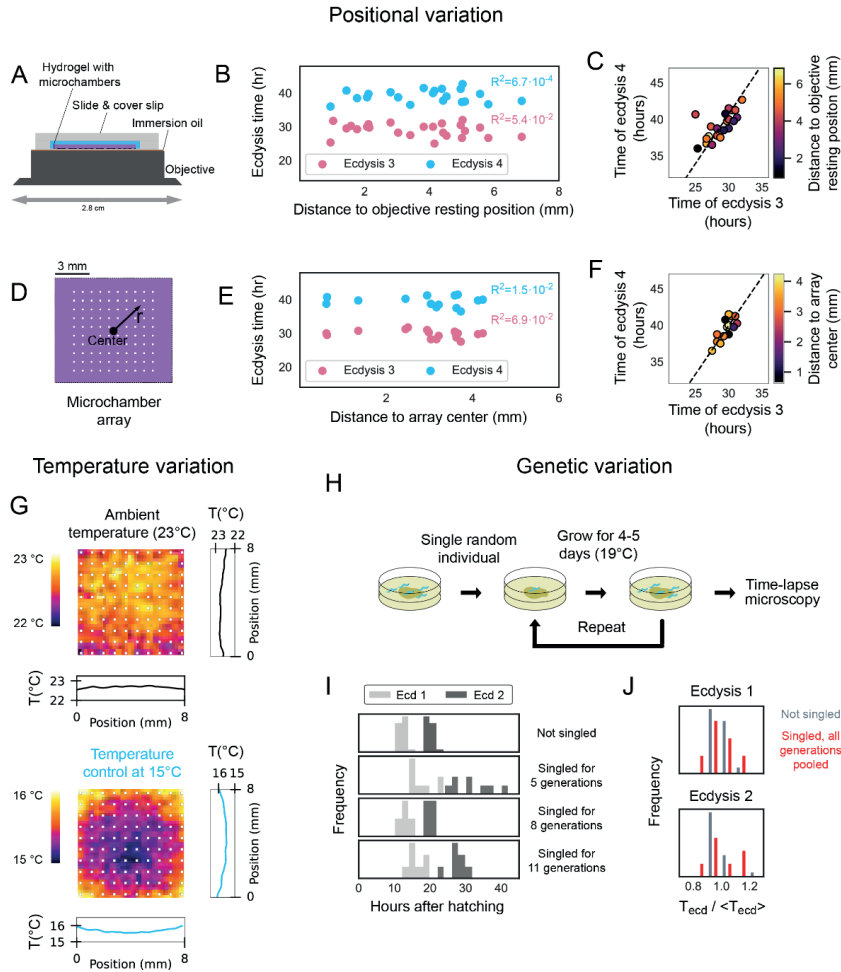
Figure S1 External sources of timing variability.

(A) Schematic cross-section of a sample (hydrogel between cover slip and microscopy slide) and objective during a typical experiment. All proportions are true to scale. Note the relatively large size of the microscope objective compared to the microchamber array. **(B)** Impact of sample position. Time of ecdysis measured in an individual animal, as function of the distance of its microchamber to center of the objective's resting position. The resting position is the location where the center of the objective is positioned between each imaging cycle, and varies between experimental batches. For both Ecdysis 3 and 4, the Pearson correlation R is small, indicating a poor correlation with distance to the objective's resting position. **(C)** Times of Ecdysis 3 and 4 plotted as event pairs, with marker colors indicating the distance to the objective's resting position. While event pairs exhibit scaling, no clear correlation is apparent between distance and early or late ecdysis timing. **(D)** Top view of the microchamber array. **(E),(F)** Same as (B),(C) but comparing to the distance *r* of each microchamber to the center of the microchamber array, as indicated in (D). Overall, the correlation of ecdysis timing with *r* is also weak (E), and does not explain the difference between early or late event timing (F). **(G)** Images of temperature distribution, measured by Forward

Imaging InfraRed (FLIR), of a microchamber array at ambient conditions (top, corresponding to the standard condition of 23°C) and with temperature control at 15°C (bottom). Graphs show the average temperature profile measured along the two axes. Temperature differences within the microchamber array are <1°C. **(H),(I),(J)** Impact of genetic variation. We propagated wild-type *C. elegans* populations as single animals (H), for either 5, 8 or 11 generations, to reduce any genetic variability, and measured ecdysis times (I). Animals that were propagated by singling showed delayed ecdysis times (dark grey) compared to wild-type animals (light grey), consistent with impact of accumulated deleterious mutations (Vassilieva et al., Evolution 2000). However, variability in ecdysis times was not reduced compared to wild-type animals (J), as singled animals showed a similar distribution of ecdysis times T_{ecd} relative to the population average $\langle T_{\text{ecd}} \rangle$ compared to non-singled animals. Here, times measured for animals singled 5, 8, and 11 generations were pooled together. This result shows that variability in timing is not due to genetic variability within the population.
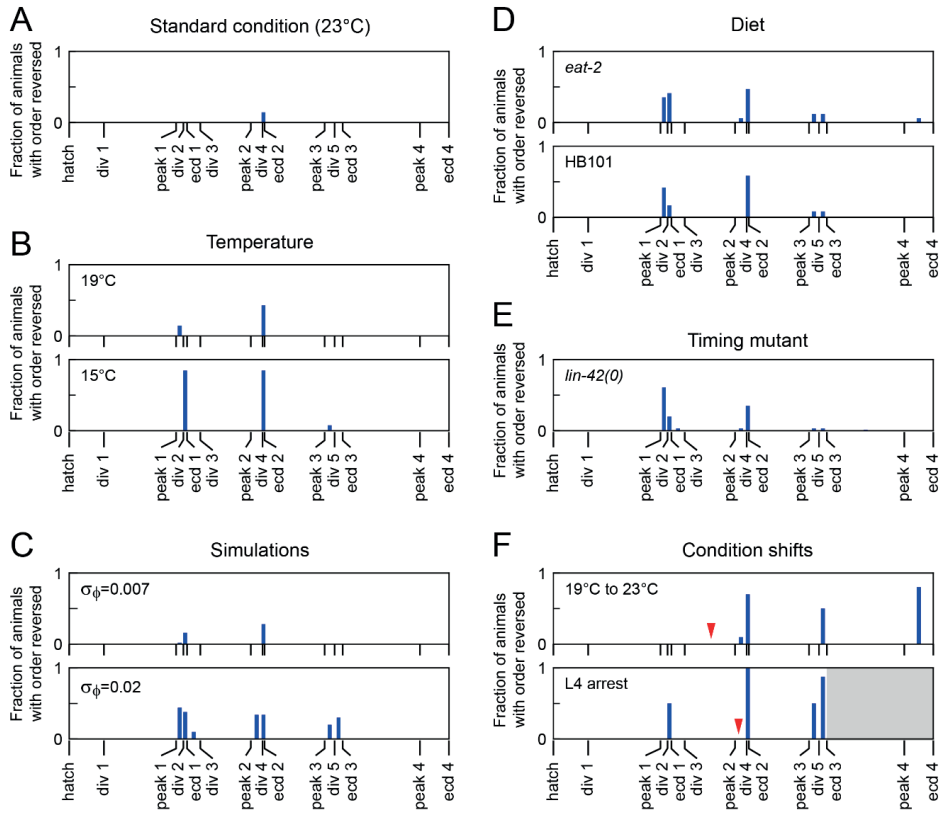
Figure S2. Event order.

(A) Fraction of animals with a measured event order that is permuted compared to the average event order, under standard conditions. Tick marks indicate the average time of each event, as measured under standard conditions. When the order of two events is reversed, e.g. Division 4 and Ecdysis 2, the fraction of animals that exhibited such a reversal is indicated by a bar placed between the corresponding tick marks. Overall, few animals have permutations in order compared to the average event order. **(B)** Permutations in event order upon changes in temperature. Tick marks correspond to average times measured under standard conditions. In particular for development at 15°C, reversals in order between seam cell divisions and ecdysis are frequent in the L1 and L2 larval stages. In general, reversals in event order are only seen in events that, on average, occur close together in time. **(C)** Permutation in event order in stochastic simulations of the timing model in Eq. 2 and 3 in the Methods, for increasing σ_ϕ, i.e. the variability in the developmental phase at which events are executed. For larger variability in phase, permutations of event order become more frequent, but impact more strongly those events that occur close together in time. **(D)**, **(E)** Permutations in event order upon changes in diet (D) and in *lin-42(0)* mutants (E). Tick marks correspond to average times measured under standard conditions. These animals occasionally show changes in event order that impact events that are non-adjacent in time, e.g. resulting in the permutated event order Division 5 - Ecdysis 3 - Peak 3. In our analysis, this is recorded as two order permutations, of Peak 3 and Division 5 and of Division 5 and Ecdysis 3. For *lin-42(0)* mutants, the decrease in permutations towards the end of larval development reflects the observation that many animals arrest before that stage. **(F)** Permutations in event order

for animals exposed to a shift in temperature (top, 19°C to 23°C) or a shift to starvation (bottom, L4 arrest). Markers correspond to the average observed timing of the shift. The grey area indicates events that do not take place as the starved animals arrest prior to Ecdysis 3 (L4 arrest).
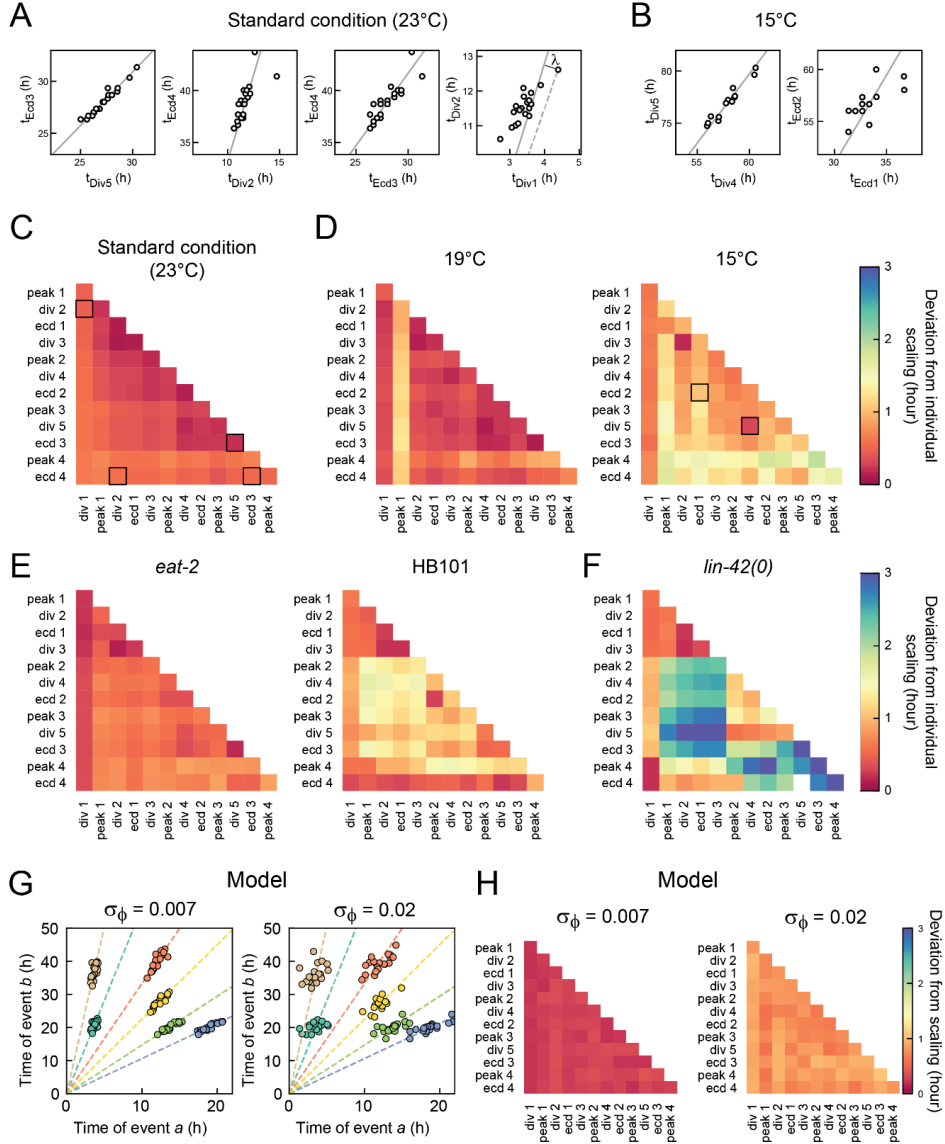
Figure S3. Quality of temporal scaling.

(A) Measured times for three different event pairs a, b under standard conditions (wild-type animals, on an *E. coli* OP50 diet at 23°C). Markers correspond to times measured in a single animal. Solid grey lines are fits of the form $t_b = s_{a,b} \cdot t_a$ to the data points for individual animals. The four event pairs are ordered by decreasing quality of scaling, i.e. larger variation of single-animal data around the fitted scaling lines. To quantify the scaling quality, we defined

$$\lambda_i^{a,b} = \left(\operatorname{atan}\left(t_{b,i}/t_{a,i}\right) - \operatorname{atan}\left(s_{a,b}\right) \right) \left(t_{a,i}^2 + t_{b,i}^2\right)^{\frac{1}{2}},$$

the distance between the data point of individual i and the scaling

line, as measured along a circle. **(B)** Times for event pairs measured at 15°C, ordered by decreasing scaling quality.

(C) Scaling quality, measured as the standard deviation $\sigma_\lambda^{a,b} = \sqrt{\langle \lambda_i^{a,b} - \langle \lambda_i^{a,b} \rangle \rangle}$ of the distance to the scaling line over all individuals in the population, shown here for all event pairs measured under standard conditions. Squares highlight the event pairs shown in (A). See Materials and Methods for full details. **(D), (E), (F)** Scaling quality for all events pairs measured (D) under different temperatures, (E) upon changes in diet and (F) in *lin-42(0)* mutants. Squares in (D) indicate event pairs shown in (B). **(G)** Simulated times of event pairs a, b in the stochastic timing model (Eqs. 2 and 3 in Methods). Data is shown for events with the same developmental phase as the events in Fig. 1G in the main text. Otherwise, simulation parameters were chosen to resemble the experimental data: we used standard deviations $\sigma_T = 3$h and $\sigma_\phi = 7 \cdot 10^{-3}$, meaning that common variability in the rate of development, $1/\langle T \rangle$, is stronger than variability in timing of each individual event. The simulated data closely resemble the experimental data in Fig. 1G, with times for event pairs a, b scattered along lines of $t_b = \frac{\phi_b}{\phi_a} t_a$ (dashed lines). Increased variability in developmental phase, $\sigma_\phi = 2 \cdot 10^{-2}$, resulted in weaker clustering along the scaling lines. **(H)** Deviation from inter-individual scaling for the parameters in (G). Data is shown for all events pairs in the experiments, with each event's average phase based on the experimentally measured value.
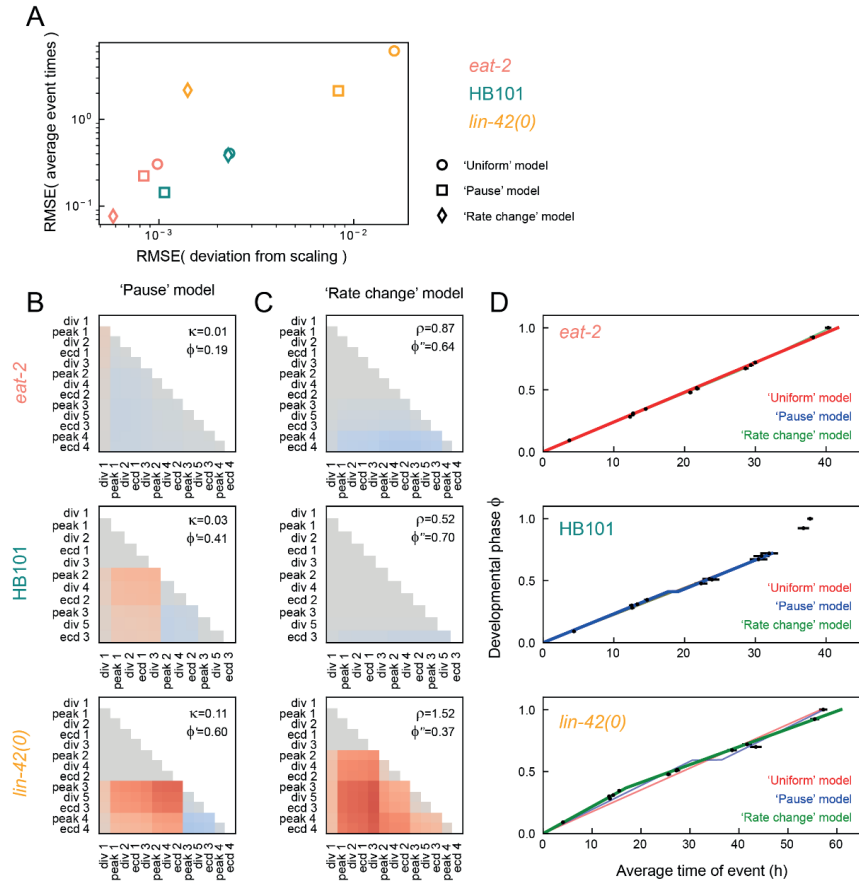
Figure S4. Model fits.

(A) Quality of fits to 'Uniform' (circle), 'Pause' (square) and 'Rate change' (diamond) models for the experimental timing data for *eat-2* (pink) and *lin-42(0)* (orange) mutants and wild-type animals fed an HB101 diet (teal). For each mutant or condition, the root mean square error (RMSE) of the best fit of each model to the experimental deviation from scaling data is plotted on the x-axis and the RMSE of the best fit to the average event times is plotted on the y-axis. For HB101 and *lin-42(0)*, a single model provided the best overall fit, i.e. the 'Pause' model for HB101 and the 'Rate change' model for *lin-42*(0). For *eat-2*, all three models fit the experimental data well. See Materials and Methods for details of the fitting procedure. **(B),(C)** Deviation of scaling predicted by the 'Pause' (B) and 'Rate change' (C) models for the best fit to the experimental data for *eat-2*, HB101 and *lin-42(0)*. The 'Uniform' model predicts zero deviation of scaling for all event pairs. For each model and mutant/condition, the values of the fitting parameters corresponding to the best fit are given. **(D)** Average event times. Experimentally measured average event times are shown as black markers, with error bars indicating the standard error. Lines indicate the predicted event times for the 'Uniform' (red), 'Pause' (blue) and 'Rate change' (green) models. Thick lines correspond to the model and parameter values used for the best-fitting model in the main text. For *eat-2*, we chose the 'Uniform' model as best-fitting model, as it performs approximately as well as the other two models but with fewer fitting parameters. This is supported by the observation that the best-fit of 'Pause' and 'Rate change' models exhibit either a small

delay, κ=0.01, or a weak change in developmental rate, ρ=0.87, resulting in an evolution of the developmental phase that is close to that of the 'Uniform' model.
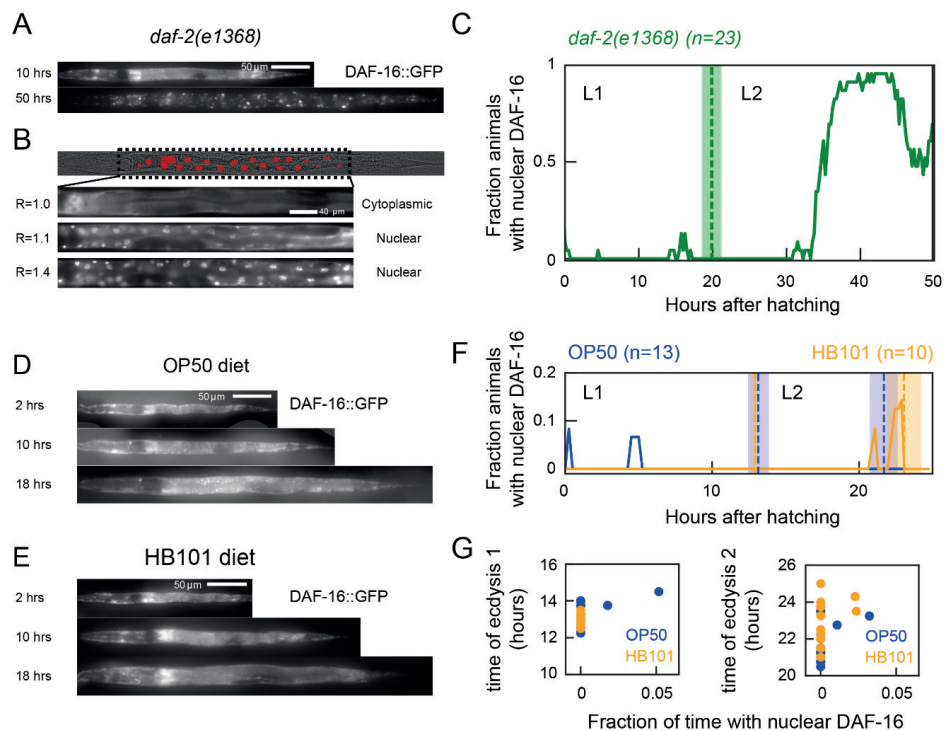
Fig. S5. Insulin signaling and developmental timing.

(A) Computationally straightened *daf-2(e1368)* animal carrying a DAF-16::GFP reporter, at different times after hatching. DAF-16 undergoes nuclear translocation, indicative of a change in insulin signaling, as *daf-2* animals enter dauer. **(B)** Quantification of DAF-16 nuclear localization. Top image shows a transmitted light image of a single, computationally straightened animal, with a fluorescent intestinal nuclear marker (*elt-7p::H1-wCherry*) superimposed in red. The nuclear marker is used to calculate the DAF-16 nuclear to cytoplasmic fluorescence ratio R. The bottom three images show DAF-16::GFP animals with increasing nuclear localization and the corresponding, measured values of R. Animals with clear cytoplasmic localization of DAF-16 have a ratio of R≈1. At a R=1.1, DAF-16 first shows visible nuclear localization, as seen by eye. Therefore, we classify animals with R≥1.1 as showing nuclear DAF-16 localization. **(C)** Fraction of *daf-2(e1368)* animals with nuclear DAF-16 (R≥1.1) during L1 and L2. Dashed lines and shaded area indicate the average and standard deviation of ecdysis time. As expected, DAF-16 becomes nuclear in almost all animals, as they enter dauer. **(D),(E)** DAF-16::GFP individuals fed (D) OP50 and (E) HB101 at different times after hatching. **(F)** Fraction of animals fed OP50 (blue) or HB101 (orange) with nuclear DAF-16 (R≥1.1) during L1 and L2. Dashed lines and shaded area are the average and standard deviation of ecdysis time. The late L2 ecdysis in animals fed HB101 indicates that the HB101-induced pause is also seen in DAF-16::GFP animals. Note the different scale of the y-axis compared to (C). In most animals, DAF-16 remains cytoplasmic at all times. Infrequent periods of nuclear localization typically reflect values close to the threshold of R=1.1. **(G)** Time of L1 (left) and L2 (right) ecdysis versus the fraction of time DAF-16 was nuclear from hatching to L1 or L2 ecdysis, respectively. Variability in ecdysis time between individuals was not explained by concomitant variation in insulin signaling, as measured by DAF-16 nuclear localization.
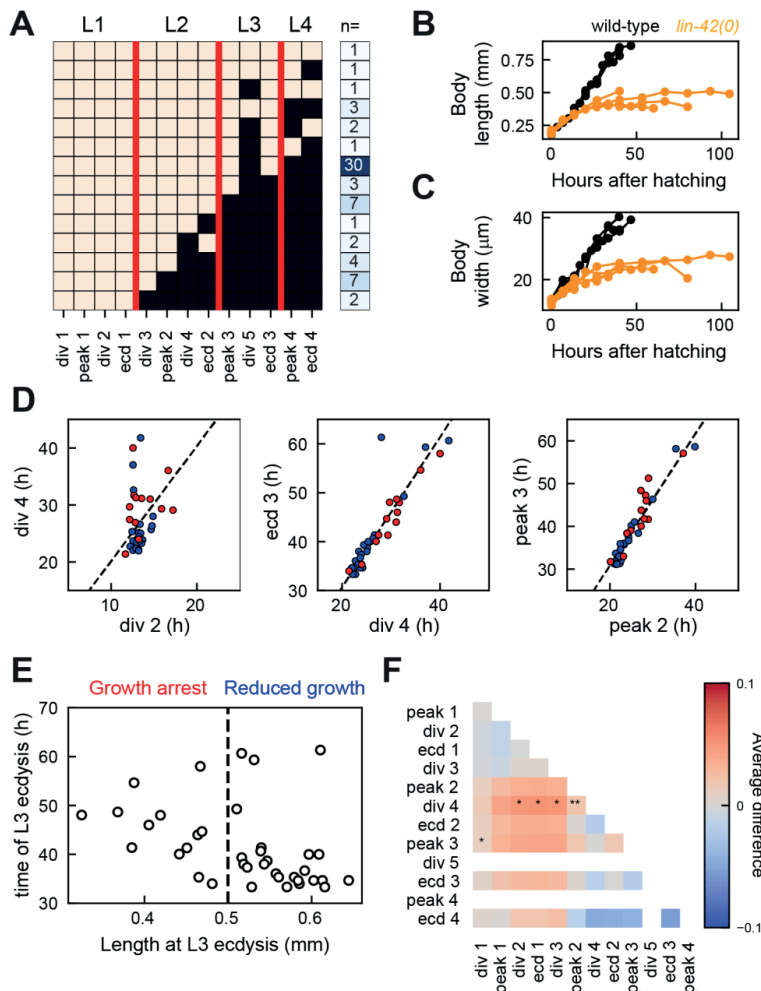
Fig. S6. Developmental progression and growth arrest in *lin-42(0)* mutants.

(A) Developmental progression in *lin-42(0)* animals. Bright squares indicate events that were executed, whereas dark squares are events that did not take place. Red lines separate the different larval stages. For each unique sequence of events recorded, we give the number of individuals n in which this sequence is observed. Of 65 animals, 4 reached adulthood (Ecdysis 4), 33 animals arrest in L3, and 21 animals arrest in L2. **(B)** Body length and **(C)** body width measured in the same individuals. Black and orange markers are wild-type animals and *lin-42(0)* animals, respectively. Animals exhibit a simultaneous arrest in extension of both body length and width. **(D)** Measured times for representative event pairs measured in *lin-42(0)* animals, with markers colored according to the growth phenotype as defined in panel (E). Lines are a linear fit to the data points. The deviation from scaling does not differ strongly between growth-arrested animals (red) and animals with reduced growth (blue). **(E)** Length at L3 ecdysis compared to time of L3 ecdysis in *lin-42(0)* animals. Based on this, we separated the population in growth-arrested animals (length < 0.5mm at L3 ecdysis) and animals with reduced growth (as compared to wild-type animals). Growth-arrested animals developed more slowly than animals with reduced growth, but a small number of animals with reduced growth also displayed very slow development (L3 ecdysis later than 50 h after hatching).

We scored the growth phenotype based on L3 characteristics, because most animals skip the L4 larval stage. **(F)** Difference in scaling between growth-arrested (GA) and reduce-growth (RG) animals. Color indicates the difference $\langle \theta^{GA} \rangle - \langle \theta^{RG} \rangle$ between the two populations, where, for each event pair a and b measured in an individual animal, the angle $\theta = \arctan \frac{t_a}{t_b}$. Stars indicate the probability that the distribution of θ is the same for growth-arrested and reduced-growth animals: **:P<0.001, *:P<0.01, and N.S. otherwise (K-S test). Overall, no significant differences in scaling were observed between growth-arrested and reduced-growth animals, indicating that growth-arrested animals do not display stronger breakdown of scaling. Empty squares reflect event pairs for which at least one of the two events did not occur in either growth-arrested or reduced-growth animals.
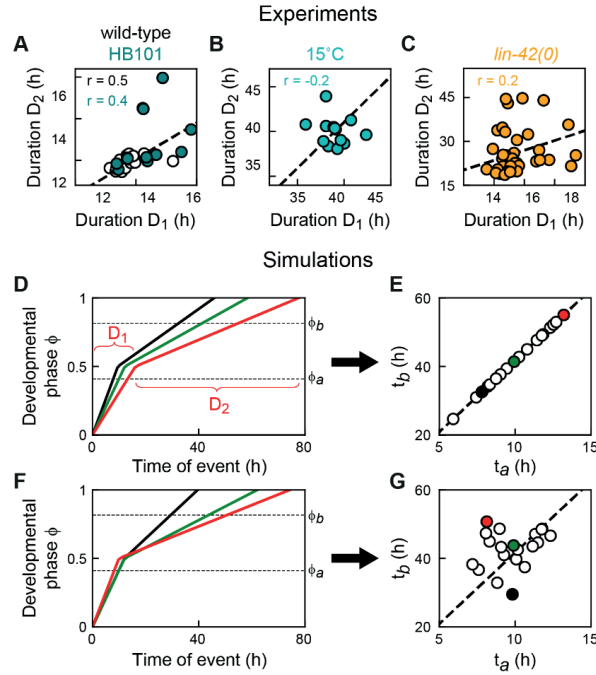
Fig. S7. Breakdown of inter-individual scaling.

(A),(B),(C) Experimentally measured correlation between the developmental duration D_1 and D_2 of development before and after the change in developmental rate, for development under standard conditions (A, wild-type at 23°C), animals fed HB101 (A), at 15°C (B) and in *lin-42(0)* mutants (C). The duration D_1 is defined at the time from hatching to the third seam cell division, while D_2 is given by the time from the third seam cell division to the third ecdysis. For D_2, we do not include the time from the third to fourth ecdysis, as this last part of larval development is often skipped in *lin-42* mutants. For each condition and genotype, r is the Pearson correlation coefficient. The correlation between D_1 and D_2 is much weaker for animals at 15°C and in *lin-42* mutants. **(D),(E)** Inter-individual variability in the 'Rate change' model. In this model, all individuals go through the same evolution of developmental phase ϕ but at a rate that differs between individuals (D). Hence, variability in the duration D_1 and D_2 of development before and after the change in developmental rate is strongly correlated within the same individual. As a consequence, times of events t_a and t_b, occurring at phase ϕ_a and ϕ_b, are clustered tightly along a line, indicating temporal scaling (E). The colored markers in (E) correspond to the individuals whose phase evolution is shown in (D). Model is given by Eqs. 3 and 5 in Methods, with T_1=25 h, T_2=95 h, ϕ''=0.5, σ_ϕ=7·10^{-3} and σ_T=15 h. Dashed line is Eq. 8. **(F),(G)** Breakdown of inter-individual scaling, when variability in durations D_1 and D_2 is not correlated within the same individual. As a result, individual animals show strong deviations from temporal scaling. Model is given by Eqs. 3 and 5, but T_1 and T_2 vary independently within the same individual, with σ_{T_1}=3 h and σ_{T_2}=15 h. This model result indicates that the lack of correlation between durations D_1 and D_2 observed in lin-42(0) mutants can explain the lack of inter-individual scaling seen in *lin-42(0)* mutants when comparing timing of events occurring before and after the change in developmental rate in Fig. 5E.

References

1. Ebisuya, M. and J. Briscoe, *What does time mean in development?* 2018. **145**(12).
2. Moss, E.G., *Heterochronic genes and the nature of developmental time.* Curr Biol, 2007. **17**(11): p. R425-34.
3. Rougvie, A.E., *Control of developmental timing in animals.* Development, 2001. **2**(9): p. 690-701.
4. Uppaluri, S. and C.P. Brangwynne, *A size threshold governs Caenorhabditis elegans developmental progression.* Proceedings of the Royal Society B: Biological Sciences, 2015. **282**(1813): p. 20151283.
5. Ben-Zvi, D., et al., *Scaling of the BMP activation gradient in Xenopus embryos.* Nature, 2008. **453**(7199): p. 1205-11.
6. Gregor, T., et al., *Diffusion and scaling during early embryonic pattern formation.* Proc Natl Acad Sci U S A, 2005. **102**(51): p. 18403-7.
7. Houchmandzadeh, B., E. Wieschaus, and S. Leibler, *Establishment of developmental precision and proportions in the early Drosophila embryo.* Nature, 2002. **415**(6873): p. 798-802.
8. Umulis, D.M. and H.G. Othmer, *Mechanisms of scaling in pattern formation.* Development, 2013. **140**(24): p. 4830-43.
9. Driever, W. and C. Nüsslein-Volhard, *A gradient of bicoid protein in Drosophila embryos.* Cell, 1988. **54**(1): p. 83-93.
10. Driever, W. and C. Nüsslein-Volhard, *The bicoid protein determines position in the Drosophila embryo in a concentration-dependent manner.* Cell, 1988. **54**(1): p. 95-104.
11. Monsalve, G.C. and A.R. Frand, *Toward a unified model of developmental timing: A "molting" approach.* Worm, 2012. **1**(4): p. 221-30.
12. Hendriks, G.J., et al., *Extensive oscillatory gene expression during C. elegans larval development.* Mol Syst Biol, 2014. **53**(3): p. 380-92.
13. Kim, D., D. Grün, and A. van Oudenaarden, *Dampening of expression oscillations by synchronous regulation of a microRNA and its target.* Mol Cell, 2013. **45**(11): p. 1337-44.
14. Meeuse, M.W. and Y.P. Hauser, *Developmental function and state transitions of a gene expression oscillator in Caenorhabditis elegans.* 2020. **16**(7): p. e9498.
15. Rensing, L., U. Meyer-Grahle, and P. Ruoff, *Biological timing and the clock metaphor: oscillatory and hourglass mechanisms.* Chronobiol Int, 2001. **18**(3): p. 329-69.
16. Moss, E.G., R.C. Lee, and V. Ambros, *The cold shock domain protein LIN-28 controls developmental timing in C. elegans and is regulated by the lin-4 RNA.* Cell, 1997. **88**(5): p. 637-46.
17. Ruvkun, G. and J. Giusto, *The Caenorhabditis elegans heterochronic gene lin-14 encodes a nuclear protein that forms a temporal developmental switch.* Nature, 1989. **338**(6213): p. 313-9.
18. Ambros, V. and H.R. Horvitz, *Heterochronic mutants of the nematode Caenorhabditis elegans.* Science, 1984. **226**(4673): p. 409-16.
19. Monsalve, G.C., C. Van Buskirk, and A.R. Frand, *LIN-42/PERIOD controls cyclical and developmental progression of C. elegans molts.* Curr Biol, 2011. **21**(24): p. 2033-45.
20. Jeon, M., et al., *Similarity of the C. elegans developmental timing protein LIN-42 to circadian rhythm proteins.* Science, 1999. **286**(5442): p. 1141-6.
21. Gritti, N., et al., *Long-term time-lapse microscopy of C. elegans post-embryonic development.* Nat Commun, 2016. **7**: p. 12500.
22. Sulston, J.E. and H.R. Horvitz, *Post-embryonic cell lineages of the nematode, Caenorhabditis elegans.* Dev Biol, 1977. **56**(1): p. 110-56.
23. Wildwater, M., et al., *Cell shape and Wnt signaling redundantly control the division axis of C. elegans epithelial stem cells.* Development, 2011. **138**(20): p. 4375-85.
24. Byerly, L., R.C. Cassada, and R.L. Russell, *The life cycle of the nematode Caenorhabditis elegans. I. Wild-type growth and reproduction.* Dev Biol, 1976. **51**(1): p. 23-33.

25. Avery, L. and B.B. Shtonda, *Food transport in the C. elegans pharynx.* J Exp Biol, 2003. **206**(Pt 14): p. 2441-57.

26. MacNeil, L.T., et al., *Diet-induced developmental acceleration independent of TOR and insulin in C. elegans.* Cell, 2013. **153**(1): p. 240-52.

27. Soukas, A.A., et al., *Rictor/TORC2 regulates fat metabolism, feeding, growth, and life span in Caenorhabditis elegans.* Genes Dev, 2009. **23**(4): p. 496-511.

28. Raizen, D.M., R.Y. Lee, and L. Avery, *Interacting genes required for pharyngeal excitation by motor neuron MC in Caenorhabditis elegans.* Genetics, 1995. **141**(4): p. 1365-82.

29. Cassada, R.C. and R.L. Russell, *The dauerlarva, a post-embryonic developmental variant of the nematode Caenorhabditis elegans.* Dev Biol, 1975. **46**(2): p. 326-42.

30. Golden, J.W. and D.L. Riddle, *The Caenorhabditis elegans dauer larva: developmental effects of pheromone, food, and temperature.* Dev Biol, 1984. **102**(2): p. 368-78.

31. Murphy, C.T. and P.J. Hu, *Insulin/insulin-like growth factor signaling in C. elegans.* WormBook, 2013: p. 1-43.

32. Kimura, K.D., et al., *daf-2, an insulin receptor-like gene that regulates longevity and diapause in Caenorhabditis elegans.* Science, 1997. **277**(5328): p. 942-6.

33. Ruaud, A.F., I. Katic, and J.L. Bessereau, *Insulin/Insulin-like growth factor signaling controls non-Dauer developmental speed in the nematode Caenorhabditis elegans.* Genetics, 2011. **187**(1): p. 337-43.

34. Edelman, T.L., et al., *Analysis of a lin-42/period Null Allele Implicates All Three Isoforms in Regulation of Caenorhabditis elegans Molting and Developmental Timing.* G3 (Bethesda), 2016. **6**(12): p. 4077-4086.

35. Olmedo, M., et al., *A high-throughput method for the analysis of larval developmental phenotypes in Caenorhabditis elegans.* Genetics, 2015. **201**(2): p. 443-448.

36. Abrahante, J.E., E.A. Miller, and A.E. Rougvie, *Identification of heterochronic mutants in Caenorhabditis elegans. Temporal misexpression of a collagen::green fluorescent protein fusion gene.* Genetics, 1998. **149**(3): p. 1335-51.

37. Tennessen, J.M., et al., *Novel heterochronic functions of the Caenorhabditis elegans period-related protein LIN-42.* Dev Biol, 2006. **289**(1): p. 30-43.

38. McCulloch, K.A. and A.E. Rougvie, *Caenorhabditis elegans period homolog lin-42 regulates the timing of heterochronic miRNA expression.* Proc Natl Acad Sci U S A, 2014. **111**(43): p. 15450-5.

39. Perales, R., et al., *LIN-42, the Caenorhabditis elegans PERIOD homolog, negatively regulates microRNA transcription.* PLoS Genet, 2014. **10**(7): p. e1004486.

40. Van Wynsberghe, P.M. and A.E. Pasquinelli, *Period homolog LIN-42 regulates miRNA transcription to impact developmental timing.* Worm, 2014. **3**(4): p. e974453.

41. Schindler, A.J., L.R. Baugh, and D.R. Sherwood, *Identification of late larval stage developmental checkpoints in Caenorhabditis elegans regulated by insulin/IGF and steroid hormone signaling pathways.* PLoS Genet, 2014. **10**(6): p. e1004426.

42. Faerberg, D.F., V. Gurarie, and I. Ruvinsky, *Inferring temporal organization of postembryonic development from high-content behavioral tracking.* Dev Biol, 2021. **475**: p. 54-64.

43. Mata-Cabana, A., et al., *Differential regulation of developmental stages supports a linear model for C. elegans postembryonic development.* bioRxiv, 2021.

44. Perez, M.F., et al., *Maternal age generates phenotypic variation in Caenorhabditis elegans.* Nature, 2017. **552**(7683): p. 106-109.

45. Wadsworth, W.G. and D.L. Riddle, *Developmental regulation of energy metabolism in Caenorhabditis elegans.* Dev Biol, 1989. **132**(1): p. 167-73.

46. Cooper, S. and C.E. Helmstetter, *Chromosome replication and the division cycle of Escherichia coli B/r.* J Mol Biol, 1968. **31**(3): p. 519-40.

47. Johnston, G.C., J.R. Pringle, and L.H. Hartwell, *Coordination of growth with cell division in the yeast Saccharomyces cerevisiae.* Exp Cell Res, 1977. **105**(1): p. 79-98.

48. Mitchison, J.M. and J. Creanor, *Further measurements of DNA synthesis and enzyme potential during cell cycle of fission yeast Schizosaccharomyces pombe.* Exp Cell Res, 1971. **69**(1): p. 244-7.
49. Robert, L., *Size sensors in bacteria, cell cycle control, and size control.* Front Microbiol, 2015. **6**: p. 515.
50. Baugh, L.R., *To grow or not to grow: nutritional control of development during Caenorhabditis elegans L1 arrest.* Genetics, 2013. **194**(3): p. 539-55.
51. Hu, P.J., *Dauer.* WormBook, 2007: p. 1-19.
52. Begasse, M.L., et al., *Temperature Dependence of Cell Division Timing Accounts for a Shift in the Thermal Limits of C. elegans and C. briggsae.* Cell Rep, 2015. **10**(5): p. 647-653.
53. Crapse, J., et al., *Evaluating the simple Arrhenius equation for the temperature dependence of complex developmental processes.* 2020.
54. Kuntz, S.G. and M.B. Eisen, *Drosophila embryogenesis scales uniformly across temperature in developmentally diverse species.* PLoS Genet, 2014. **10**(4): p. e1004293.
55. Chong, J., C. Amourda, and T.E. Saunders, *Temporal development of Drosophila embryos is highly robust across a wide temperature range.* J R Soc Interface, 2018. **15**(144).
56. Ruaud, A.F. and J.L. Bessereau, *Activation of nicotinic receptors uncouples a developmental timer from the molting timer in C. elegans.* Development, 2006. **133**(11): p. 2211-22.

Chapter 3

Body-wide communication by synchronized insulin signaling pulses

Burak Demirbas[1,2], Olga Filina[1,2], Timo Louisse[1], Yvonne Goos[1], María Antonia Sánchez-Romero[3], María Olmedo[4,*], Jeroen van Zon[1]

[1]AMOLF, Amsterdam, the Netherlands
[2]Equal contribution
[3]Department of Microbiology and Parasitology, University of Seville, Spain
[4]Department of Genetics, University of Seville, Spain

Abstract

Growth is strikingly uniform throughout the body, yet how this uniformity is achieved remains poorly understood. Insulin signaling is the core pathway regulating body growth, but the dynamics of insulin signaling across an organism has not been studied experimentally. By imaging C. elegans larvae in microchambers, we follow the key insulin signaling step, DAF-16/FOXO nuclear translocation, at cellular level throughout the body. We show that under constant stress, translocation occurs in stochastic pulses, but with each translocation pulse occurring near-simultaneously in all cells. Pulsatile insulin signaling impacts growth, with single short pulses directly causing a transient halt of body growth, and long or frequent pulses prompting full growth arrest. We thus identify organism-wide coordination of insulin signaling pulses as a mechanism to ensure uniformity of body growth, with implications for understanding tissue- and body-wide coordination of insulin-dependent processes also in humans.

Introduction

Insulin/insulin-like growth factor signaling (IIS) is the key pathway regulating body growth under normal [1-4] and stressed conditions [5-7]. Growth control occurs through FOXO transcription factors [8] that, upon loss of IIS activity, translocate to the nucleus, where they control downstream gene expression [1,9-12]. Growth uniformity is generally assumed to follow from body-wide spreading of insulins through passive mechanisms, such as release into the circulation and diffusion [13,14]. Tissue- or body-wide coordination is crucial also for other insulin-dependent processes, such as control of glucose metabolism by blood insulin[15], with impact on diabetes, obesity and longevity [16-19]. However, the dynamics of insulin signaling across an entire animal has not been studied experimentally.

To investigate organism-wide dynamics of DAF-16/FOXO, the sole C. elegans FOXO transcription factor (TF), we studied the *C. elegans* L1 arrest, a developmental arrest larvae enter when they encounter high stresses, including starvation, osmotic shock and heat, directly after hatching and that is under control of IIS [7,20-24] (Fig. 1A). Under unstressed conditions, high insulin-like peptide (ILP) levels activate the insulin receptor DAF-2, causing phosphorylation and cytoplasmic localization of DAF-16/FOXO [25-27]. Upon stress, low ILP levels result in DAF-2 inactivation, DAF-16/FOXO dephosphorylation and its subsequent translocation into in the nucleus, where it induces stress response genes [28-30] and regulators of cell proliferation [20], ultimately leading to developmental arrest. A puzzling result emerging from previous studies is that even under constant high stress, a substantial fraction (20-60%) of animals showed no or little nuclear DAF-16/FOXO [24,31,32], hinting at a so far unresolved variability in DAF-16/FOXO response between individual larvae.

Here, we show that insulin signaling propagates throughout the *C. elegans* body in highly synchronized yet stochastic pulses, that serve as a so far unknown form of body-wide communication setting growth state. By imaging *C. elegans* larvae locked in microchambers, we follow the key insulin signaling step, DAF-16/FOXO nuclear translocation, at cellular level throughout the body. Under constant stress, translocation is pulsatile, with dynamics depending on stress type and magnitude, while each translocation pulse occurs near-simultaneously in all cells. This synchronized pulsatile insulin signaling has major physiological implications, with single short pulses directly causing a transient halt of body growth, and long or frequent pulses prompting full growth arrest. The stochastic yet synchronized pulsing of DAF-16/FOXO excludes that coordination results simply from each cell responding independently to a spatially uniform stress, and instead implies active synchronization. Our findings raise urgent questions about the molecular basis of the underlying synchronizing signals. We speculate that this active mechanism of body-wide insulin communication is

important also in humans, for growth and for other insulin-dependent processes and diseases, including diabetes, obesity and longevity [16-19], that all hinge on tissue- or body-wide coordination.

Results

To investigate organism-wide dynamics of DAF-16/FOXO, the sole C. elegans FOXO transcription factor (TF), we studied the *C. elegans* L1 arrest, a developmental arrest larvae enter when they encounter high stresses, including starvation, osmotic shock and heat, directly after hatching and that is under control of insulin/insulin-like peptide signaling (IIS) [7,20-24] (**Fig. 1A**). Under unstressed conditions, high insulin-like peptide (ILP) levels activate the insulin receptor DAF-2, causing phosphorylation and cytoplasmic localization of DAF-16/FOXO [25-27]. Upon stress, low ILP levels result in DAF-2 inactivation, DAF-16/FOXO dephosphorylation and its subsequent translocation into in the nucleus, where it induces stress response genes [28-30] and regulators of cell proliferation [20], ultimately leading to developmental arrest. A puzzling result emerging from previous studies is that even under constant high stress, a substantial fraction (20-60%) of animals showed no or little nuclear DAF-16/FOXO [24,31,32], hinting at a so far unresolved variability in DAF-16/FOXO response between individual larvae.

Synchronized, stochastic DAF-16/FOXO nuclear translocation pulses

We visualized DAF-16/FOXO nuclear localization using a transgenic line expressing a functional DAF-16::GFP fusion protein that tags the DAF-16a/b isoforms [33] and is a standard reporter for studying DAF-16/FOXO activation [21,34-37]. When we examined a population of L1 larvae under starvation or 300 mM osmotic shock, DAF-16::GFP was nuclear in most animals, as expected, yet 20-40% of animals instead showed cytoplasmic localization (**Fig. 1B**), consistent with previous observations. Even for conditions that elicited a strong response (32°C heat shock or *daf-2(e1368)* mutants under starvation) still 5-10% of animals displayed cytoplasmic localization.

So far, DAF-16::GFP nuclear localization has only been studied by comparing static snapshots of animals under normal or stressed conditions. Instead, we performed time-lapse microscopy on animals hatched from eggs placed in 0.2x0.2 mm hydrogel microchambers [38] without food, allowing us to examine starvation-induced DAF-16/FOXO translocation dynamics in individual larvae (**SI Fig. 1A**). Upon hatching in absence of nutrients, DAF-16::GFP translocated from the cytoplasm to the nucleus within ~2 hr in most animals, as expected. Surprisingly, DAF-16::GFP typically moved back into the cytoplasm after ~1 hr (**Fig. 1C**) and continued to shuttle between the nucleus and the cytoplasm in pulses with ~2 hr duration, even

as starvation conditions were constant. Strikingly, even though timing and duration of DAF-16::GFP translocation pulses varied in time, DAF-16::GFP translocation was highly synchronized between *daf-16*-expressing cells throughout the body (**Fig. 1D**). We observed similar synchronized nuclear translocation pulses in a strain carrying a DAF-16::GFP endogenous CRISPR/Cas9 knock-in fusion (DAF-16::GFPsc) [39] (**Fig. 1E**), confirming that these translocation pulses were not an artefact of the DAF-16::GFP transgenic line.

We quantified DAF-16/FOXO nuclear translocation dynamics by measuring the ratio R between nuclear and cytoplasmic fluorescence (**SI Fig. 1B**, see **Methods** for details). We focused on intestinal cells, that form a stereotypical array along the antero-posterior (A-P) axis spanning approximately half the body length of L1 larvae. Most animals displayed initial oscillation-like translocation pulses (**Fig. 1F,G**), followed by more persistent DAF-16::GFP nuclear localization ($R>1$) as stress persisted, although brief pulses of translocation to the cytoplasm remained visible even at this stage. In general, R displayed clear variability between individual animals, in terms of both frequency and number of translocation pulses, underlining their stochastic nature. Yet, despite this individual variability, R dynamics always showed strong similarity between intestinal cells at markedly different positions along the A-P axis (**Fig. 1G**), revealing a degree of synchrony that was unexpected for an inherently stochastic process.

We observed no DAF-16::GFP translocation pulses when eggs hatched in microchambers filled with plentiful food (**SI Fig. 1C**), indicating that they are a specific response to starvation. In *daf-2(e1368)* animals, that carry a mutation in the ligand binding domain of the DAF-2 insulin receptor [40] and therefore displayed a higher fraction of animals with nuclear DAF-16 in population-level measurements (**Fig. 1B**), we found without food, DAF-16::GFP was localized primarily in the nucleus and exhibited infrequent ~1 hr pulses of translocation into the cytoplasm (**Fig. 1H**), indicating that DAF-16::GFP pulse dynamics was controlled by IIS. Overall, these measurements reveal that the animal-to-animal variability in DAF-16::GFP nuclear localization under constant stress, that was previously observed on the population level, in fact reflects stochastic DAF-16::GFP translocation pulses occurring with high internal synchrony within each individual.
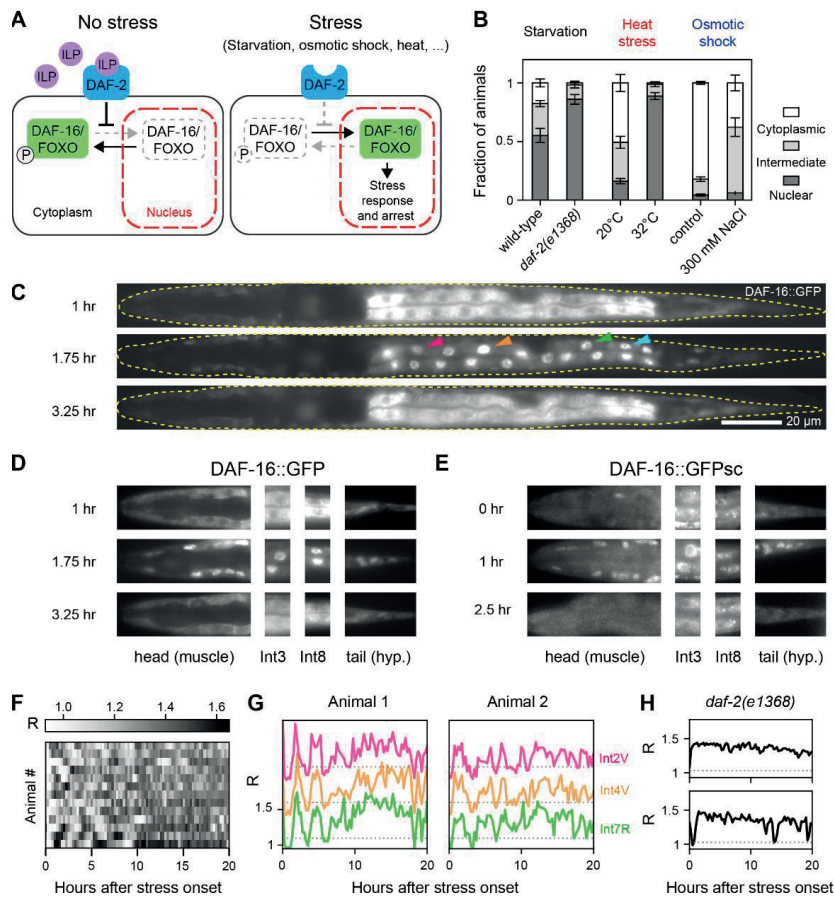
3

Figure 1. Stochastic, synchronized DAF-16/FOXO nuclear translocation pulses. (A) Schematic representation of the Insulin/insulin-like growth factor-1 signaling (IIS) pathway. **(B)** Fraction of L1 larvae with nuclear DAF-16::GFP localization for wild-type and *daf-2(e1368)* animals under starvation, and wild-type animals exposed to heat or osmotic shock. For each condition we performed 3 replicates of n>48 animals. Error bars are standard error of the mean (S.E.M.) over replicates. **(C)** Straightened fluorescence images of a starved L1 animal, carrying a DAF-16::GFP integrated transgene, showing alternating nuclear and cytoplasmic DAF-16 localization. Hours indicate time after hatching in microchambers without food. Dashed yellow line indicates animal's outline. Scale bar: 20 μm. Arrowheads indicate intestinal cells Int2D/V (magenta), Int4D/V (orange), Int7L/R (green) and Int8L/R (cyan), used for single-cell quantification. **(D),(E)** DAF-16::GFP nuclear translocation dynamics in head muscle cells, intestinal cells, or tail hypodermal cells upon constant starvation stress. Both for DAF-16::GFP (D) and a single-copy, endogenously-tagged DAF-16::GFPsc strain (E), translocation occurred in pulses that were synchronized between the different tissues. Scale bar: 20 μm. Images in (C)-(E) were computationally straightened for clarity. **(F)** Heatmaps of DAF-16::GFP nuclear localization R, calculated as the ratio of DAF-16::GFP intensity in the nucleus and cytoplasm, over time. Rows represent individual, starved animals. Color intensity corresponds to R, as averaged over all intestinal cells. **(G)** DAF-16::GFP nuclear localization R measured for different intestinal cells, for two starved individuals. Despite variability between individuals, R is synchronized between cells. Tracks are averaged over two cells at the same antero-posterior (A-P) location, e.g. Int2D and Int2V, and are shifted along the y-axis for clarity. Dashed line is R =1.03, corresponding to 105% of the average

DAF-16::GFP nuclear localization in non-stressed animals. **(H)** Nuclear localization R, averaged over all intestinal cells, for starved *daf-2(e1368)* mutants with constitutively low IIS activity.

Synchrony of DAF-16/FOXO translocation pulses is independent of stress type

We next asked if similar DAF-16::GFP nuclear translocation pulses were also seen for other types of stress. We exposed L1 larvae hatched in microchambers filled with food either to heat or osmotic shock (**SI Fig. 2A-D**, **Methods**), which are both known to induce DAF-16 nuclear translocation [21,33]. Interestingly, both stress treatments resulted in DAF-16::GFP translocation pulses but with qualitative differences in dynamics, as will be examined in more detail further below. In particular, compared to starvation (**Fig. 1F,G**), translocation pulses under osmotic shock appeared more variable, both in time and between individuals (**Fig. 2A**), while heat shock induced a single translocation pulse that varied much less between individuals (**SI Fig. 2E**). Nevertheless, for both stresses the dynamics of R was still highly synchronized between intestinal cells. This was particularly striking for animals under 200 mM NaCl osmotic shock, where translocation pulses were often infrequent and of short duration, yet simultaneous in all cells examined.

To put an upper bound on the degree of synchrony, we imaged DAF-16::GFP pulses with high, 30 s time resolution in animals under starvation stress and quantified R in the intestinal cells Int2-Int8, excluding the four Int1 and two Int9 cells where DAF-16::GFP was difficult to resolve in single cells (**Fig. 2B**). At this increased time resolution, we could observe gradual nuclear translocation of DAF-16::GFP over a ~20 min time interval. Moreover, we found that R displayed a shift in time between different cells, although the magnitude of the shift was small compared to the timescale of translocation. To quantify the shift, we cross-correlated R between each pair of cells (**Fig. 2C**). Here, the lag time at which the cross-correlation peaked represented an estimate of the delay in pulses between the two cells, with the error in the delay estimated through Monte-Carlo simulations (**SI Fig. 3A-D**).

We found that cells in close physical proximity within the body, such as Int2V and Int2D that have the same A-P position, showed no clear delay (**Fig. 2C-E**). However, we found that the cross-correlation showed a peak at positive lag time when we compared anterior cells to more posterior cells (**Fig. 2C**), with the magnitude of the delay increasing with the distance between the cells (**Fig. 2D,E**). Notably, the sign of the delay indicated an anterior-to-posterior order in DAF-16::GFP pulse dynamics, that was consistent between different animals, with pulse dynamics initiating in the Int2 cells ~3 min before the Int8 cells. When analysing high time resolution data obtained for osmotic shock, we found an equally strong synchronization, with delays between cells of <3 min (**Fig. 2E**). Intriguingly, the nature of the delay was more complex

than the simple anterior-to-posterior order seen for starvation, and instead reflected a partial dorsal-ventral ordering. For example, the anterior but ventral cells Int2V, Int3V and Int4V had pulse dynamics delayed compared to the more posterior but dorsal cells Int4D and Int5L (**SI Fig. 3E, F**). Overall, this suggests that the synchronizing mechanism depends at least partially on stress type.
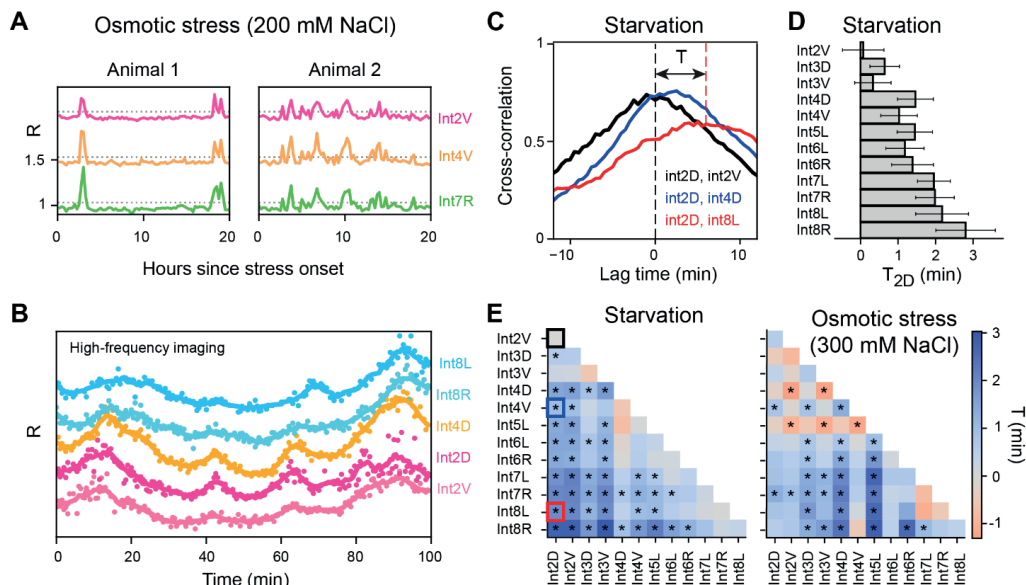

Figure 2. Synchrony of DAF-16/FOXO translocation dynamics in intestinal cells. (A) Synchronized DAF-16::GFP nuclear localization R in intestinal cells of animals exposed to 200 mM NaCl osmotic shock. **(B)** DAF-16::GFP nuclear localization R in intestinal cells of a starved L1 animal, imaged at 30-second time resolution (markers). Lines are data smoothed with a Savitzky-Golay (S-G) filter. Individual tracks are shifted along the y-axis for clarity. **(C)** Cross-correlation of R for int2D and intestinal cell pairs at the same (int2V) or increasing A-P distance (int4D and int8L, respectively). Data is for n=4 animals. The lag time T at which the cross-correlation peaks, corresponds to the average delay in R between cells. **(D)** Measured delay T_{2D} between Int2D and all other intestinal cells. Error bars are 95% confidence intervals of the peak centroid distributions obtained from Monte-Carlo simulations (*n*=4 animals). **(E)** Heatmap showing the delay T between all pairs of intestinal cells for starvation (left, *n*=4 animals) and osmotic shock (right, *n*=4). Squares denoted by * indicate a delay that is significantly different from 0 (*T*=0 lies outside 95% confidence interval). Outlined squares correspond to the curves in (C).

DAF-16/FOXO translocation dynamics encodes both stress type and magnitude

We then more systematically examined the differences in DAF-16::GFP translocation dynamics between different stresses. Given the observed synchrony between different intestinal cells, we here only compared R dynamics quantified over all intestinal cells. Differences in DAF-16::GFP translocation dynamics were already apparent when we compared population-averaged translocation dynamics, $\langle R \rangle$, between stresses (**Fig. 3A**): for 32°C heat shock, $\langle R \rangle$ exhibited a single translocation peak ~1.5 hrs after stress onset,

consistent with our observation of a single, stereotypical translocation pulse in individuals (**SI Fig. 2E**), followed by a more gradual increase in nuclear localization as stress persisted. A similar immediate peak in $\langle R \rangle$ was visible upon starvation, but here followed by additional peaks, consistent with our earlier observation of more regular, oscillation-like translocation pulses in individual animals (**Fig. 1F-G**). In contrast, no clear peaks in $\langle R \rangle$ were visible for 300 mM NaCl osmotic shock, as would in principle be expected for the random translocation pulses we observed in individuals (**Fig. 2A**).

To further differentiate R dynamics between starvation and osmotic shock, we determined the autocorrelation of R (**Fig. 3B**). Indeed, for starvation the autocorrelation in individual animals was oscillatory with exponentially decreasing envelope, a signature of stochastic oscillations. The population-averaged autocorrelation decayed more rapidly, showing only two peaks, at 2 and 4.25 hr, due to variation in pulse period and number of pulses between individuals. In contrast, the autocorrelation of R for osmotic shock showed simple exponential decay, both in individuals and averaged over all animals (**Fig. 3B**), consistent with random pulse dynamics.

Inspecting R dynamics in individuals highlighted the increased variability in number and duration of translocation pulses for osmotic shock, compared to starvation (**Fig. 1F, 3C**). For heat shock, we found that, even though the nature of the induced translocation dynamics was more stereotypical than for starvation or osmotic shock, substantial individual variability still remained. First, 6/21 animals failed to display a DAF-16::GFP pulse directly after shifting to 32°C. In addition, the gradual increase in $\langle R \rangle$ after the initial peak did not reflect a stereotypical increase in DAF-16::GFP nuclear localization in all individuals, but rather an increasing frequency and duration of pulses of increased nuclear localization that otherwise occurred stochastically within each individual.

In contrast to starvation, for osmotic and heat shock we could vary stress magnitude and examine the impact on DAF-16::GFP pulse dynamics. For osmotic shock, we hatched larvae in microchambers soaked with salt concentrations increasing from 200 to 400 mM NaCl. For 200 mM NaCl, we found that DAF-16::GFP displayed infrequent and short (<1 hr) pulses of nuclear localization, while increasing NaCl levels led to a proportional increase in the fraction of time DAF-16::GFP was nuclearly localized (**Fig. 3C**). This was due mainly to an increase in pulse duration (**Fig. 3D**), rather than pulse frequency (**SI Fig. 4A,B**), and occurred without any concomitant increase in pulse amplitude (**Fig. 3E**), i.e. the degree of nuclear enrichment.

For heat shock, we shifted hatched L1 larvae from 20°C to temperatures ranging from 31°C to 33°C. DAF-16::GFP dynamics displayed similar characteristics both for 31°C and 32°C heat shocks: most animals displayed a single transient pulse of strong nuclear translocation directly after the shift to high temperature, followed by dynamic pulse-like changes in nuclear DAF-

16::level (**Fig. 3F**). However, both the amplitude and duration of the initial translocation pulse increased with higher temperature (**Fig. 3G**, **SI Fig. 4C)**. In addition, the nuclear localization pulses that followed the initial pulse increased with temperature both in frequency and duration, resulting in a higher fraction of time ϕ that DAF-16::GFP was strongly nuclear (R >1.05, **Fig. 3H**). Following a 33°C heat shock, in contrast, we no longer observed a transient pulse, but found that DAF-16::GFP, after translocating, remained highly enriched in the nucleus for the duration of the experiment (**Fig. 3F**). In conclusion, for both osmotic and heat shock, higher stress magnitude was apparent through the increased fraction of time that DAF-16::GFP was nuclear.

Overall, this showed that DAF-16::GFP nuclear translocation dynamics was not only distinct for different types of stress (starvation, osmotic shock or heat shock), but also informed on stress magnitude. As DAF-16/FOXO mediates stress response primarily by binding to promoters of target genes and upregulating their expression [29,30,41], which crucially depends on DAF-16/FOXO nuclear localization, these observed differences in DAF-16/FOXO translocation dynamics thus likely impact stress response gene expression, in a manner that depends on stress type and magnitude.
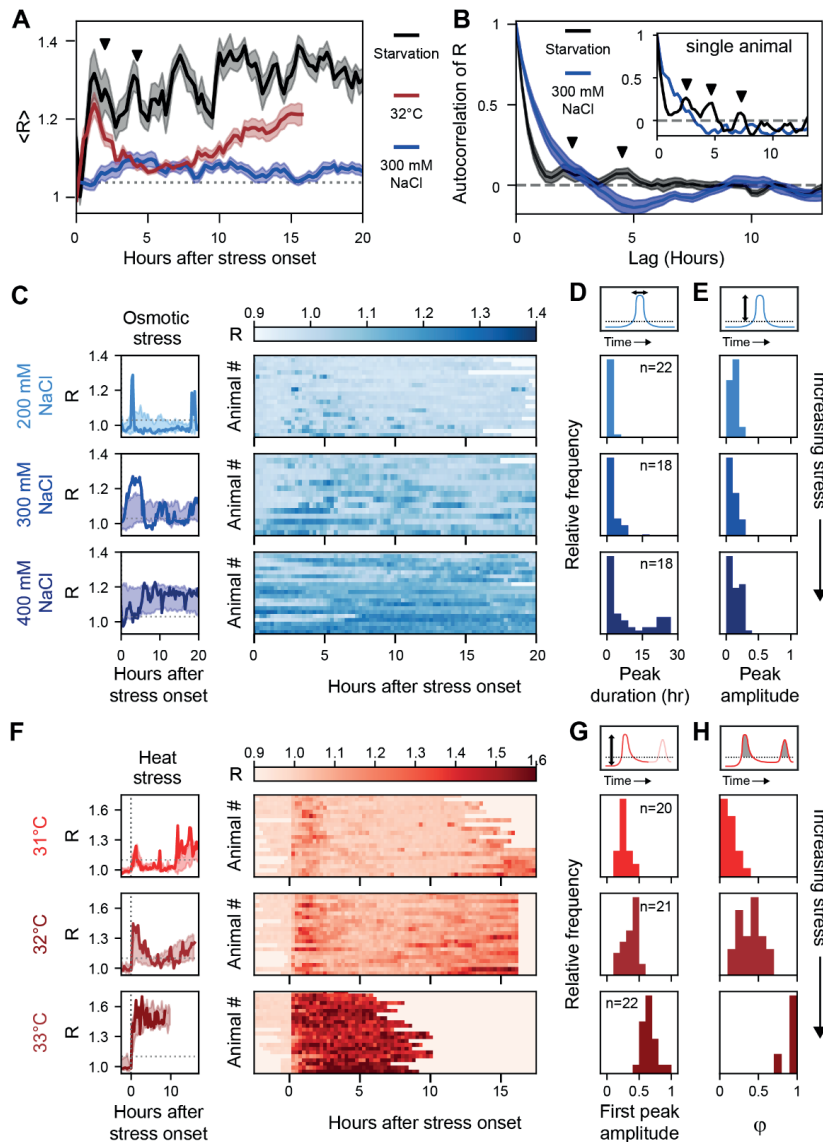
Figure 3. DAF-16/FOXO nuclear translocation dynamics depends on stress type and magnitude. (A) Population-averaged nuclear localization R for starvation (black, n=13), 300 mM osmotic shock (blue, n=18) and 32°C heat shock (red, n=21). Error bars are S.E.M. Arrowheads indicate the population-average oscillation period of DAF-16::GFP translocated as determined in (B). **(B)** Population-averaged autocorrelation of R for starvation (black, n=13) and 300 mM osmotic shock (blue, n=18). Inset shows autocorrelation for an individual animal. Error bars are S.E.M. Peaks in autocorrelation (indicated by arrows) correspond to oscillatory DAF-16::GFP translocation dynamics. **(C)** Individual tracks (left) and population view heatmaps (right) of R for increasing osmotic shock. Individual tracks (left) are compared with the standard deviation for the population (shaded regions). **(D),(E)** Distribution of peak duration (D) and peak amplitude (E) of DAF-16::GFP nuclear translocation pulses for osmotic shock. Increasing osmotic shock leads to more prolonged pulses without affecting amplitude. **(F)** Same as (C), but

for increasing heat shock. For 33°C heat shock, observation time is limited to ~10 h due to heat-induced shrinkage of the hydrogel microchambers. **(G)**,**(H)** Distribution of amplitude of the first DAF-16::GFP translocation peak (G) and fraction of time ϕ that DAF-16::GFP is strongly nuclear (H) for increasing heat shock.

DAF-16/FOXO pulses are causally linked to arrest of body growth

We then examined possible functional roles of DAF-16/FOXO translocation pulses, focusing on the most prominent feature of L1 arrest, namely the arrest of body growth [7,20]. IIS and DAF-16/FOXO have a well-established role in inducing cell cycle arrest during starvation [20,42]. However, this by itself does not explain growth arrest, as body growth in larvae is primarily driven by volume increase of a fixed number of cells, rather than by increasing cell number [43]. On the other hand, growth arrest does not simply reflect a lack of food: it is observed not only for starvation, but also for stresses such as heat or osmotic shock, where in principle sufficient food is present to support growth [21,44]. Therefore, we examined if body growth itself was also actively regulated by IIS and DAF-16/FOX.

As measure of body growth, we quantified the length of animals along their A-P axis as function of time, for unstressed and different stressed conditions. In the absence of stress, body length increased approximately linearly over the course of the L1 larval stage, as described previously [38,45,46], but such extension was absent upon starvation (**SI Fig. 5A,B**). While body growth was similarly arrested for 300 mM NaCl osmotic stress (**SI Fig. 5C**), we observed a surprising variability in growth arrest for 200 mM NaCl (**Fig. 4A**): some animals showed fully linear growth, albeit at lower rate than without stress, while others displayed complete growth arrest or intermediate growth. Strikingly, we found that the amount of growth depended on the number and duration of DAF-16::GFP pulses (**Fig. 4A, SI Fig. 5D**). Animals with approximately normal growth typically showed few or no DAF-16::GFP pulses, while fully arrested animals showed persistent DAF-16::GFP pulse trains. Moreover, especially for intermediate growth, individual pulses often coincided with a temporary halt in growth. This indicated that DAF-16::GFP translocation itself was directly linked to body growth.

To further examine the relation between DAF-16::GFP pulses and growth, we quantified each animal's average growth rate and compared it to the fraction of time ϕ that DAF-16::GFP was nuclear (defined as $R > 1.03$), for animals exposed to 200, 250 and 300 mM NaCl (**Fig. 4B**). The measured growth rate for animals under osmotic stress was always lower than for non-stressed animals, even when no DAF-16::GFP pulses were observed, and was negative for animals in 300 mM NaCl. Both observations likely reflected the known reduction in body volume induced by osmotic shock [47] that is independent of growth arrest. For frequent DAF-16::GFP pulses ($\phi > 0.2$), we found that animals ceased growth completely, consistent with

growth arrest. However, for few DAF-16::GFP pulses (ϕ<0.2), most animals showed persistent growth, with a rate that was largely independent of ϕ. Variability in growth arrest and intermediate growth phenotypes were seen at the border between these two regimes. Interestingly, while ϕ varied significantly between animals under the same osmotic stress conditions, the measured growth rates for animals under all osmotic stress conditions appeared to fall onto a single curve that only depended on ϕ, indicating that each animal's ϕ is a better predictor of growth rate than external stress conditions per se. Overall, these observations imply that animals integrate over DAF-16::GFP pulse dynamics, meaning that growth arrest is only enacted when the animal experiences a sufficient number of pulses, or pulses with sufficiently long duration, within a certain interval of time. This suggests that there is a direct causal link between DAF-16 pulses and growth arrest.

We observed similar patterns, with some differences, for heat shock (**Fig. 4C**). In contrast to osmotic shock, most animals at 31°C initially grew with a rate similar to unstressed animals, despite DAF-16::GFP exhibiting its first, transient translocation pulse. However, pulses in DAF-16::GFP nuclear enrichment occurring after ~5 hr typically coincided directly with cessation of growth (**Fig. 4C**, **SI Fig. 5E**). Consistently, the earlier occurrence of such nuclear enrichment pulses seen for animals on 32°C was accompanied by an earlier growth arrest. Finally, for 33°C, when DAF-16::GFP showed high nuclear enrichment in all animals, we observed full growth arrest immediately after onset of heat stress (**Fig. 4C**).

The striking coincidence of DAF-16::GFP nuclear translocation pulses and (transient) halt in growth (**Fig. 4A**, ϕ=0.1 and 0.18) strongly suggested that DAF-16 nuclear localization directly drove growth arrest. However, it could also be explained by an alternative hypothesis, namely that DAF-16::GFP nuclear translocation and growth arrest were controlled independently and in parallel by an upstream stress signal. To differentiate between these two scenarios, we placed animals carrying a *daf-16(mu86)* null allele under the same stress conditions. We found that *daf-16(mu86)* animals exposed to osmotic shock (250 or 300 mM NaCl) or heat shock (33°C) showed significantly higher growth than wild-type animals, which typically showed full growth arrest under these conditions (**Fig. 4D, E**). These results indicate that stress-induced growth arrest requires DAF-16 function and, thus, that the DAF-16 translocation pulses cause the growth arrest.
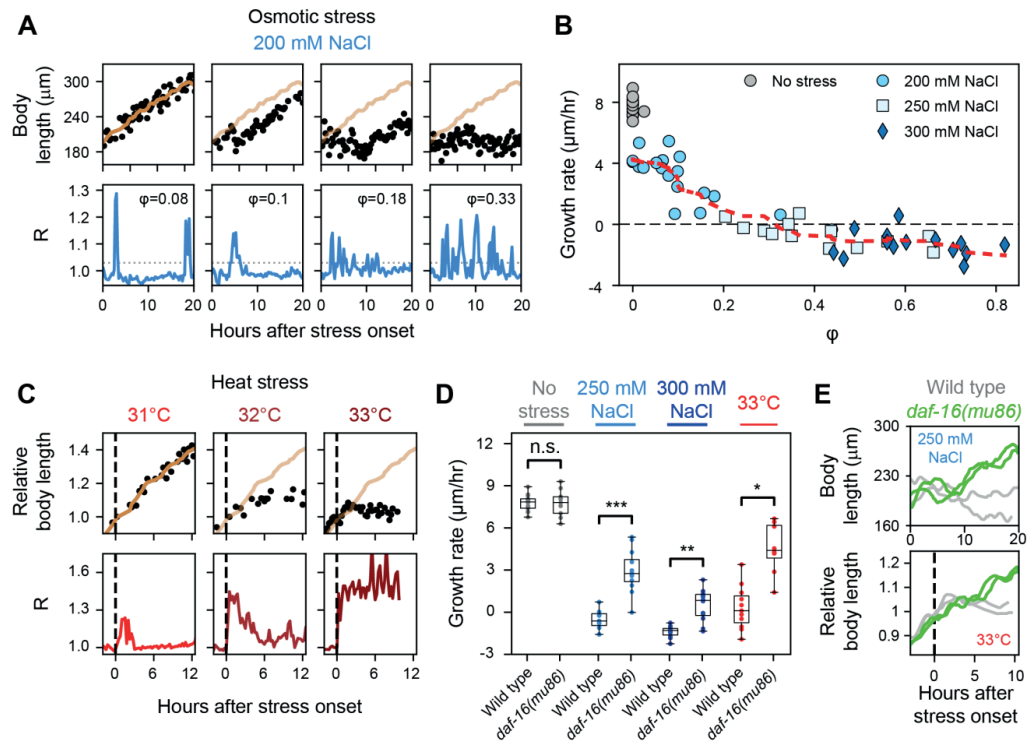
Figure 4. DAF-16/FOXO translocation pulses cause arrest of body growth. (A) Body length (top) and DAF-16::GFP nuclear localization (R, bottom) for individual animals under 200 mM NaCl osmotic shock, for increasing fractions of time ϕ that DAF-16::GFP was nuclear. Black markers are individual measurements. Orange line is length data for the animal with ϕ=0.08 smoothened with a S-G filter, shown for comparison. Sustained pulses or trains of shorter pulses correspond to times of reduced body growth. **(B)** Growth rate as function of ϕ for different magnitude of osmotic shock. Growth rate is defined as $\Delta L/\Delta T$, where ΔL is the change in body length over the measured time interval ΔT. Each marker represents an individual animal. Red line is smoothed growth rate data (S-G filter). The apparent negative growth rate for ϕ>0.3 is due to osmotic-shock driven decrease in body volume that is independent of growth. **(C)** Same as (A) but for individuals under increasing heat shock. Dashed line is time of temperature shift. Body length is measured relative to length at time of heat shock, which in each individual occurs at a different time relative to hatching. **(D)** Boxplots comparing growth rate for wild-type and *daf-16(mu86)* animals under various stress conditions. *daf-16(mu86)* mutants sustain growth under all stress conditions, meaning that DAF-16 is required for reduced or arrested growth under osmotic stress or heat shock. *:$P<1\cdot10^{-3}$, **:$P<1\cdot10^{-4}$, ***:$P<1\cdot10^{-5}$, N.S.: not significant (Welch's t-test). (E) Body length for two wild-type (grey) and two *daf-16(mu86)* animals exposed to 250 mM NaCl (top) and 33°C (bottom). Length data was smoothened as in (A).

FOXO3A nuclear translocation pulses in human cells

Stochastic translocation pulses had so far not been observed for FOXO TFs in general, yet our findings suggest that such pulses are an inherent feature of insulin signaling. To investigate whether this is conserved across animals, we turned to human cell culture. DAF-16 has four homologs in humans, *FOXO1*, *FOXO3A*, *FOXO4* and *FOXO6.* Among these, FOXO3 is associated with longevity [16], and has been proposed to retain ancestral functions [8]. We therefore transfected the human osteosarcoma U2OS cell line with a plasmid carrying FOXO3A::GFP (**Methods**). We subjected the culture to serum starvation, a condition that activates FOXO3A [11], by transferring cells from 10 % FBS to 0 % FBS, and followed FOXO3A::GFP subcellular localization for ~20 hours. Indeed, we observed that in many cells FOXO3A translocated between the nucleus and cytoplasm in repeated pulses **(Fig. 5A,B)**. These pulses occurred at a slower pace than in *C. elegans*, with a ~5-10 h period. Unlike in the *C. elegans* experiments, which did not permit titration of the starvation signal, the media concentration of FBS could be systematically adjusted. This allowed us to investigate whether pulse dynamics depended on stress magnitude, by placing cells in 1% and 0.1% FBS. Indeed, we observed that 0.1% FBS reduced the amplitude of the pulses, and 1% FBS resulted in mostly cytoplasmic localization (**Fig. 5C**). These results suggest that, depending on the concentration of growth factors and nutrients, the pulses can be modulated to control the time that FOXO3A spends in the nucleus. Overall, our results indicate that pulsatile regulation by FOXO transcription factors might be a general feature of the insulin signaling pathway.
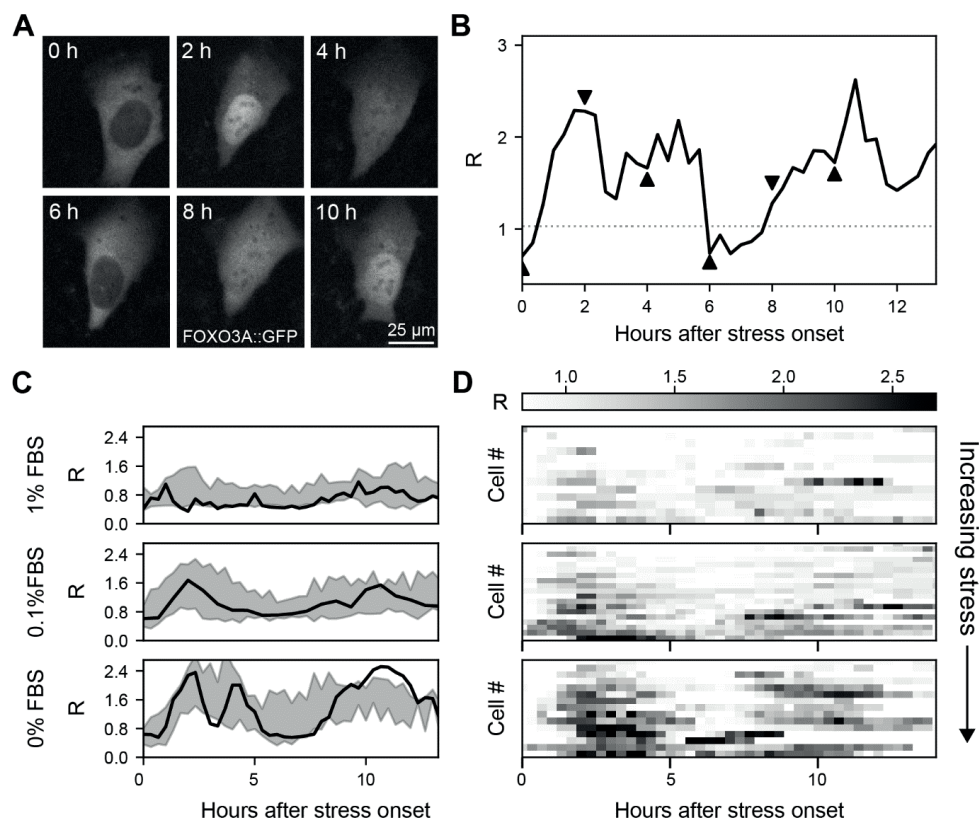
Figure 5. Stress-induced FOXO3A nuclear translocation pulses in human cells. (A) Fluorescence images of FOXO3A::GFP in a single U2OS cell under nutrient starvation (0% FBS in the medium), at different times since the start of the experiment. Scale bar: 25 μm. **(B)** FOXO3A::GFP nuclear localization R for the cell imaged in (A), with arrowheads indicating the time of each image. R =1 corresponds to equal FOXO3A::GFP intensity in nucleus and cytoplasm. **(C)** Individual cell tracks and (D) population-view heatmaps (right) of R, for increasing nutrient starvation (decreasing % FBS). Individual tracks are compared with the standard deviation for the cell population (shaded regions).

Discussion

FOXO TFs, including DAF-16/FOXO in *C. elegans*, are currently assumed to remain cytoplasmic under favorable conditions and become nuclearly localized upon unfavorable conditions, where they induce genes required for stress resistance and inhibit genes for proliferation and growth [10,20,33,48,48]. Here, our dynamic measurements of DAF-16/FOXO translocation dynamics during stress-induced L1 arrest revealed a strikingly different picture. We found that under constant stress (starvation, osmotic shock or heat), DAF-16/FOXO entered and exited the nucleus in distinct pulses that were highly synchronized between the different cells in the body (**Figs. 1,2**). While DAF-16/FOXO nuclear localization increased with

stress magnitude, DAF-16/FOXO pulse dynamics differed qualitatively between different types of stress at all stress magnitudes examined (**Fig. 2**). We observed similar nuclear translocation pulses of FOXO3A in a human cell line upon nutrient stress (**Fig. 5**), indicating that such pulses are a general feature of FOXO TFs. In general, these result show that studying FOXO translocation by examining single microscopy snapshots is insufficient and that, instead, dynamic measurements are essential.

A surprising aspect of DAF-16/FOXO translocation pulses is that they are inherently stochastic, with the incidence of an individual pulse typically difficult to predict, yet occurring simultaneously in all *daf-16* expressing cells throughout the body. Our results identified a function for such synchronized pulses, namely in coordinating body-wide growth. This is based on the close relationship observed between DAF-16/FOXO pulse dynamics and growth arrest (**Fig. 4**), especially for animals under osmotic stress: for short (< 0.5 h), isolated pulses animals did not show any growth arrest, while sufficiently persistent DAF-16/FOXO pulse trains resulted in complete lack of growth. This was further supported by our observation of intermediate cases, where an isolated DAF-16/FOXO pulse of longer duration (> 0.5 hr) caused an immediate, but transient growth arrest. Overall, these results suggest that cells integrated over DAF-16/FOXO pulses, so that growth arrest was only induced upon sustained DAF-16/FOXO nuclear localization and not induced by transient translocation pulses. This observed link between DAF-16/FOXO pulse dynamics and body-wide growth provides a compelling rationale for the observed synchrony: to maintain uniform proportions, (arrest of) cell volume growth and, hence, pulse dynamics, must be tightly synchronized between all cells.

The lack of observed growth arrest in *daf-16* loss-of-function mutants under osmotic stress and heat shock (**Fig. 4**) indicated that cessation of growth was a direct consequence of DAF-16/FOXO nuclear translocation. While the role of DAF-16/FOXO in *C. elegans* developmental arrest is well-established, it was so far only linked to arrest of the cell cycle [20,42] rather than of cell volume increase, which is the main driver of body growth [43]. Our finding that DAF-16/FOXO controls body-wide growth of *C. elegans* larvae is therefore novel. It also matches earlier results that *Drosophila* IIS regulates organ and cell size [3,51-53]. These previous studies left unaddressed how FOXO proteins control size. One proposed mechanism is that IIS impacts cell size through direct control of protein synthesis, by impacting proteins, such as initiation factors or ribosomal proteins, that set translation rates [52,53]. In the alternative mechanism, growth is controlled more indirectly, by FOXO inducing large-scale changes in gene expression, including of metabolic genes, and the resulting rerouting of metabolism impacting growth [41,54]. Our work now provides the first examination of IIS activity and body-wide growth at high time resolution. Strikingly, we observed several cases where DAF-16/FOXO nuclear translocation was rapidly (within 0.5 h) followed by full arrest in body length

extension, in particular for osmotic shock (**Fig. 4A, SI Fig. 5D**). In contrast, full induction of L1 arrest-specific gene expression, including many metabolic genes, was shown to require 3-6 h [41,55], too long to explain the rapid impact on growth we observed. Our results thus favor a mechanism where IIS controls growth directly, on timescales short compared to expression of metabolic genes.

Individual FOXO family members respond to multiple stresses, by inducing stress-specific gene-expression programs [10-12,48]. Indeed, in *C. elegans* the majority of genes expressed under osmotic shock were not induced under starvation [21], even though in both cases stress response is mediated by IIS and DAF-16/FOXO nuclear translocation. How a single signaling pathway, such as IIS, can respond to different stresses with a tailored gene expression response is an important, unresolved question. In general, it has been speculated that stress-specificity of FOXO-induced gene expression is achieved by interaction with other, stress-induced and stress-specific TFs [22,48,56,57]. In *C. elegans,* for example, the TFs HSF-1 and HCF-1 were proposed to direct DAF-16/FOXO to specifically induce expression of either heat-shock (HSF-1) or oxidative stress (HCF-1) response genes [58,59]. Our observation that DAF-16/FOXO translocation dynamics differed qualitatively between stress types (**Fig. 2**), ranging from stochastic oscillations (starvation) to random pulses (osmotic shock) or a single pulse of fixed duration (heat shock), now suggests an alternative mechanism for stress discrimination. Given that the ability of DAF-16/FOXO to induce gene expression depends crucially on its nuclear localization, differences in the duration or frequency of DAF-16/FOXO translocation between stresses will likely impact gene expression. Indeed, while novel for FOXO TFs, pulsatile translocation dynamics has been discovered in recent years more broadly in signaling networks linked to stress response [60,61]. Single-cell studies have shown that stress-specific differences in TF nuclear translocation dynamics are sufficient to induce expression of different genes [61,62]. For example, transient and sustained nuclear TF localization often leads to expression of distinct sets of genes [63,64], while changes in number and duration of TF translocation pulses can cause expression of different genes, depending on the nature of their promoters [65]. Hence, we speculate that the observed stress-specificity of translocation dynamics are key in explaining how a single FOXO TF, in this case DAF-16/FOXO, induces a stress response that is specific to stress type.

While pulses in nuclear translocation dynamics have been observed for pathways, such as Erk and P53, that govern developmental processes and stress response in animals [64,66], they have so far only been examined in isolated cells. Here, we used *C. elegans* to study, for the first time, TF translocation pulses on the cellular level, but within the context of the animal's body. Our observation that DAF-16/FOXO translocation pulses were variable between individual animals, yet strongly synchronized throughout the animal's body (**Figs. 1,2**) implies

the action of a synchronizing mechanism that coordinates dynamics between cells long after the shift to stressed conditions. Our measurements indicate that synchronization must be rapid, as delays in DAF-16/FOXO translocation between intestinal cells were of order 1-3 min (**Fig. 2**), much shorter than the ~20 min required for DAF-16/FOXO to transition between cytoplasmic and nuclear. Our data for starvation revealed that DAF-16/FOXO translocation occurred slightly earlier in anterior versus posterior intestinal cells, suggestive of a head-to-tail signal responsible for synchronization and consistent with proposed long-range signals emanating from head neurons that detect starvation [67]. However, synchronization could arise without long-range signals purely through local coupling between cells, as was demonstrated for example for the collective, wave-like gene expression oscillations in somitogenesis [68].

A compelling open question concerns the molecular identity of the synchronizing signal. An intriguing candidate are the insulin-like peptides (ILPs). While *C. elegans* has only a single insulin-like receptor, DAF-2, its genome encodes 40 ILPs that function as either agonists or antagonists of IIS [69]. ILPs are excreted by multiple tissues, including neurons, intestine and hypodermis [22]. Moreover, it was shown that DAF-16/FOXO activation by IIS in one tissue induced ILP expression that in turn impacted IIS in other tissues [70,71]. In principle such inter-tissue IIS interactions appear sufficiently complex to synchronize and possibly even generate DAF-16/FOXO translocation pulses, through body-wide modulation of ILP secretion. However, IIS-mediated changes in ILP expression were shown to require 1-6 h [70], which is relatively slow compared to the observed timescale of DAF-16/FOXO translocation pulses (<1 h). It will therefore be interesting to examine whether IIS can impact ILP excretion also on shorter timescales.

The molecular machinery of IIS is maintained from nematodes to mammals, with a conserved role in organizing body-wide responses. Our unexpected observation of nuclear translocation pulses both for DAF-16/FOXO in *C. elegans* and for FOXO3A in human cell lines indicate that such pulses are likely a broadly conserved feature of FOXO signaling. It will be important to establish whether FOXO translocation pulses, including long-range synchronization to ensure body-wide coordination, also function in higher organisms.

Acknowledgements

Author contributions to paper

O.F., B.D., M.O. and J.v.Z. conceived the research. O.F., B.D., M.O. and J.v.Z. wrote the manuscript with the input and discussion of all authors. O.F., B.D., T.L, Y.G and M.O. performed *C. elegans* experiments. M.A.S-R. performed cell culture experiments. O.F., B.D. and T.L. performed analysis of microscopy data. O.F. and B.D. developed Python scripts to perform most data analysis.

Materials and Methods

C. elegans experimental methods

Strains

Most strains were maintained on NGM seeded with OP50 at 20°C, only animals containing *daf-2(e1368)* were kept at 15°C. TJ356 *zIs356 [daf-16p::daf-16a/b::GFP + rol-6(su1006)]*, RW10131 *unc-119(ed3), zuIs178, stIs10024, stIs10131 [elt-7::H1-wCherry + unc-119(+)]*, DR1572 *daf-2(e1368)* , CF1038 *daf-16(mu86)* and OH16024 *daf-16(ot971[daf-16::GFP])* were obtained from CGC. Several lines were created by crossing: MOL193 *zIs356 [daf-16p::daf-16a/b::GFP + rol-6(su1006)], stIs10131 [elt-7::H1-wCherry + unc-119(+)]*, JVZ139 *daf-16(ot971[daf-16::GFP]), stIs10131 [elt-7::H1-wCherry + unc-119(+)]* and MOL232 *daf-2(e1368), zIs356 [daf-16p::daf-16a/b::GFP + rol-6(su1006)], stIs10131 [elt-7::H1-wCherry + unc-119(+)]*.

Microchamber fabrication

Microfabricated arrays of chambers were made from a master mold. Master molds were created using standard soft-lithography techniques. Briefly, SU-8 2025 epoxy resin (MicroChem) was first spin-coated on a silicon wafer to form a 20 μm layer. The SU-8 layer was exposed with ultraviolet-light through a foil mask (SELBA S.A.) containing the micropattern. To create polyacrylamide microchamber arrays from the master mold, a 10% dilution of 29:1 acrylamide/bis-acrylamide was mixed with 0.1% ammonium persulfate (Sigma) and 0.01% TEMED (Sigma) as polymerization initiators. The resulting aqueous solution was then poured in a cavity placed on top of the micropatterned silicon wafer. The cavity was closed with a silanized coverslip and sealed by mechanical clamping, allowing the solution to polymerize for 2 h. To remove the toxic unpolymerized acrylamide monomers, the resulting polyacrylamide microchamber arrays were washed at least three times for at least 3 h each in distilled water. Fewer or shorter washing steps often resulted in developmental arrest. Microchamber arrays could be stored in distilled water for ~15 days. Single microchamber arrays were placed in M9 buffer for 4 h directly before time-lapse imaging.

Sample preparation

To prepare the sample, a glass spacer with the same height as the polyacrylamide membrane was attached to a 76 × 26 × 1 mm microscope slide using high vacuum grease (Dow Corning). A single microchamber array was positioned with tweezers on the microscope slide, with the openings of the microchambers facing up. Excess liquid was removed with a tissue. With a pipette, drops of M9 buffer (~40 μL in total) were placed on the side and on the surface of the microchamber array, while preventing the liquid from filling the chambers. For all experiments

except starvation stress, under a dissection microscope, a drop of bacterial suspension containing a single late-stage embryo was transferred from a NGM agar plate seeded with OP50 bacteria into a microchamber, using an eyelash attached to a Pasteur pipette. To facilitate the release of the bacteria and embryo into the chamber, the eyelash was dipped briefly into the M9 drop before touching the microchamber. Once the egg was transferred, more bacterial suspension was added to the microchamber using the eyelash, until completely filled. For osmotic stress experiments, hydrogels were stored in 200, 300 or 400 mM NaCl solutions for at least one week prior to the experiment. For starvation experiments, eggs were isolated by bleaching to remove the bacteria and placed one by one inside different microchambers filled with liquid M9 media. For each experiment, ~10–20 chambers were loaded. Subsequently, tissue paper was used to remove all excess M9 buffer. Finally, a 25 × 75 mm #1 coverslip was lowered on the chambers to seal the sample, slow enough to avoid forming large air bubbles. The sample was placed on a custom fabricated holder and clamped to seal the chambers and avoid liquid evaporation during the duration of the experiment. Microchamber dimensions were 190 x 190 x 10 µm for heat stress and osmotic stress experiments, while 190 x 190 x 6 µm were used for starvation experiments.

Time-lapse microscopy

We performed time-lapse imaging on a Nikon Ti-E inverted microscope. Using a large chip camera (Hamamatsu sCMOS Orca v2), it was possible to fit single microchambers in the field of view of the camera while using a 60 x magnification objective (Nikon CFI Plan Fluor 60 x , NA=0.5-1.25, oil immersion). Transmission imaging was performed using a red LED (CoolLED pE-100 615 nm), while fluorescence images were acquired using a 488 nm laser (Coherent OBIS LS 488-100) and a 561 nm laser (Coherent OBIS LS 561-100). The laser beam was expanded from 0.7 to 36 mm through a telescope composed of two achromatic lenses of 10 and 500 mm focal lengths (Thorlabs AC080-010-A-ML and AC508-500-A). The expanded beam was then aligned through additional dielectric mirrors (Thorlab BB2-E02) to enter the back aperture of the microscope. A tube lens (300 mm focal length, Thorlabs AC508-300-A) was used to focus the beam in the back focal plane of the objective. For fluorescence microscopy, we used a dual band filter set (Chroma, 59904-ET). An XY-motorized stage (Micro Drive, Mad City Labs) was used to move between chambers, while a piezo Z-stage (Nano Drive 85, Mad City Labs) was used to move the sample in the Z direction. To optimize acquisition speed, we synchronized the camera, laser illumination and stage movement as follows: to operate the rolling-shutter camera in the global exposure mode, the laser beam was switched on (rise time <3 µs) once all the lines on the camera chip were active and switched off once the camera started reading out the chip. In order to rapidly acquire Z-stacks, we synchronized the piezo Z-stage and the camera, so that the stage moved to the new Z position

during the 10 ms that the camera read out the chip to its internal memory. The microscope and all its components were controlled with custom software implemented using a National Instruments card (PCIe-6323) installed on a computer with a solid-state drive (Kingston V300-120GB), an Intel Core i7 processor (3.50 GHz) and 16 GB of RAM. By using sufficiently high laser power (80–100 mW), we could use exposure times that were short enough (1–10 ms) that animal movement during acquisition was negligible. Acquiring a single imaging volume, typically consisting of 20 Z-slices in two channels, took <0.4 s. Some animal movements along the A–P axis was observed between Z-slices. Each chamber was imaged every 20 min for ~48 h. During imaging intervals, we used the Perfect Focus system of the microscope to prevent sample drift.

To achieve high-throughput analysis of DAF-16 fluorescence in intestinal cells, we performed simultaneous 2-color imaging of DAF-16::GFP and H1::mCherry, a protein fusion that localizes specifically to the nuclei of intestinal cells and thus constitutes a good nuclear marker. Z-stacks with ~9 images were collected every 15-minutes for most experiments. Cell synchronization experiments were performed with a 30 second time resolution. Hatching was defined as the first frame where the larvae appeared outside the egg shell. Times of hatching were manually annotated for each animal, and used as the start of time courses.

A temperature control system was used to maintain a constant temperature of 20 °C inside the sample. A thermoelectric chiller (Thermotek T257P) was used to cool the custom-made objective jacket by circulating an antifreeze fluid (a mixture of water and glycerin) between the chiller and the objective jacket. In order to calibrate the system, a thermocouple temperature sensor measuring 0.025 mm in diameter (RS Pro) was placed inside the sample in contact with the polyacrylamide hydrogel and connected to a digital thermometer (RS Pro). The temperature was then varied on the thermoelectric chiller while the resulting temperature inside the sample was being monitored. As animals in different microchambers hatch at slightly different times, the time after hatching at which the shift in temperature was initiated varied between animals. For the heat stress experiments, animals were allowed to hatch at 20 °C, followed by a sudden temperature increase to 31, 32 or 33 °C within 5 hours after hatching.

NaCl can possibly already permeate the egg shell 1 hour prior to hatching, due to softening of the egg shell [72], resulting in an onset of osmotic stress just before hatching. Indeed, at high salt concentrations we observed that a fraction of embryos (3/18 at 300 and 10/32 at 400 mM NaCl) did not hatch normally, in which case the cessation of embryonic motility was interpreted as hatching for analysis.

Segmentation of intestinal cell nuclei and cytoplasm

Custom Python software was used to calculate DAF-16::GFP fluorescence intensity in the nucleus and cytoplasm of intestinal cells. We processed the H1-wCherry signal (marker for intestinal nuclei) in order to obtain precise boundaries of each cell's nucleus. First, the image z-stack for each time point was reduced to the maximum intensity projection, and the worm was segmented from the background using the Otsu method. To speed up computation time, the projected image was cropped to a rectangular region encompassing only the worm, thus removing most background areas. Next, the edges of individual nuclei were detected from the image gradient, which was calculated using the Sobel filter. Finally, a watershed segmentation algorithm was applied to the image gradient to isolate and label the nuclei and to generate a binary mask (see Fig. S1B). For each individual nucleus, the focal plane with the maximum average fluorescence intensity was automatically detected, and selected as the optimal focal plane. To obtain the cytoplasmic region, the nuclear mask was first expanded by dilation (7 pixels) and subsequently subtracted from the expanded mask, resulting in a narrow ring surrounding the nucleus. Finally, for each cell the average fluorescence intensity inside the nuclear mask, I_{nucl}, and inside the cytoplasmic mask, I_{cyt}, was evaluated at the optimal focal plane. To analyze DAF-16::GFP in each cell independently, segmented cells were manually annotated. All time-lapse movies were carefully inspected by eye and showed no disagreement with DAF-16 localization trajectories obtained by automatic quantification.

Quantification of DAF-16 localization

DAF-16::GFP subcellular localization in intestinal cells was quantified as the ratio $R = \frac{I_{nucl}}{I_{cyt}}$. Since DAF-16 localization trajectories appeared almost identical in all intestinal cells at a 15-minute time resolution, they were averaged for the ease of analysis, unless otherwise stated. To perform quantitative analysis of pulsatile dynamics, we first needed to discriminate nuclear from cytoplasmic localization of DAF-16. For animals under starvation and osmotic stress we defined a threshold by calculating the average *R* of animals in the control condition (20°C *ad libitum* food in the absence of stress) and multiplying by a factor of 1.05. Due to the persistent nuclear localization of DAF-16 in animals under heat stress, we used a higher threshold of *R* =1.1.

Analysis of pulse characteristics

DAF-16 pulses under osmotic stress were characterized by their duration and amplitude. For each pulse, duration was defined as the time the *R(t)* value was uninterruptedly above the threshold (*R*>*R*control*1.05). Pulse amplitude was defined as the maximum *R(t)* value within each pulse. To differentiate true pulses from inherent variability and measurement noise, we only took pulses into account that lasted longer than a single time-point. Amplitude was defined

as the maximum R value during each uninterrupted pulse. The amplitude of the initial nuclear peak upon heat stress was characterized by finding the maximum $R(t)$ value within 3 hours after the onset of heat stress. The fraction of time DAF-16 is nuclear ϕ was calculated as the number of time points DAF-16 is nuclear versus the total number of time points after onset of heat stress.

Measurements of body length and growth analysis

We used body length over time as a proxy for growth. In order to measure body length of worms, ~10 points were manually placed along the worms' proximal-distal axis and a spline was fit through the points at each time point. The growth rate was defined as $\frac{\Delta L}{\Delta T}$, where ΔL is the change of body length measured over interval ΔT. Here, ΔT was the time between hatching and the end of the time-lapse movie, and varied in value between individuals depending e.g. on whether the animal's full body was in view for body length analysis. The reported fraction of time ϕ that DAF-16::GFP was nuclear was then determined over the same time interval. A Savitzky-Golay filter was used to smooth data for presentation, using a window length of 19, and a polynomial order of 3.

Monte Carlo simulation for determining lag time uncertainties

To detect potential cell-to-cell delays in DAF-16::GFP translocation dynamics, we computed cell-pair cross-correlations and quantified the lag time as the position of the cross-correlation maximum. The peak position is subject to uncertainties due to the propagation of measurement error, intrinsic cellular noise, and a finite sampling rate. Large uncertainties in the peak position challenge the fact that any observed lag is 'real', i.e. whether a non-zero lag is statistically significant. Uncertainties in the cross-correlation lag times were estimated using the following model-independent Monte Carlo simulation [73]. A random set of N points was selected from the original time series data (also consisting of N points/measurements), regardless of whether any point was previously chosen. Points that were selected multiple times were only included once, thus reducing the size of the original set by ~35%. The temporal order of the sampled points was retained by re-ordering them after the random selection. The set was generated for the time series of two different cells, i.e. the same time points were selected for both signals, which were then cross- correlated and lag time obtained as the cross-correlation maximum. This procedure was iterated 2000 times, leading to a distribution of lag times. The mean of the distribution was used as the delay between any given pair of cells, and the 95% confidence interval as its error. If the confidence interval for any given cell-pair lag time included the value zero, the DAF-16 dynamics delay between the cells was considered not significant. As an additional control, N data points were randomly extracted from the time series, but not temporally re-ordered, and signals were cross-correlated. The peak position histogram after

1000 iterations displayed a sharp peak at zero, which confirmed that the observed delays are not an artefact.

Human cells experimental methods

Construction of GFP-FOXO3a plasmid

A human FOXO3a cDNA (Genecopoeia, Product ID Z1129) was cloned into pEGFP-C1 (Clontech Laboratories) to generate the GFP-FOXO3A plasmid.

Cell culture

U20S H2B-RFP7 Hygroo-1 cells (a gift from Dr. Israel Salguero, a member of Dr. Steve Jackson's laboratory) were grown in in Dulbecco's modified Eagle medium (DMEM) supplemented with 10% fetal calf serum (FBS) and 2 mM L-glutamine (Sigma-Aldrich). Cells were maintained in a 5% CO_2 humidified atmosphere at 37°C. U20S cells were transiently transfected with GFP-FOXO3a expression plasmid.

Transient transfection of human epithelial cells

U2OS cells were transfected by electroporation using the GFP-FOXO3a expression plasmid. Briefly, approximately 10^7 cells were trypsinized, washed with cold PBS, and then resuspended in 200 µl of DMEM supplemented with 15 mM HEPES pH 7.4. 6 µg of plasmid DNA was mixed with H_2O and NaCl (final concentration of 200 mM) in 50 µl of final volume, and added to the cell suspension. The cell–DNA mixture was then incubated on ice for 10 min and electroporated using a Gene Pulser Xcell (BioRad) at a setting of 950 µF, 720 Ω and 240 V in 0.4-cm transfection cuvettes. Cells were incubated on ice for an additional 10 min, diluted 1:20 in DMEM supplemented with 10% FBS, and seeded into µ-slide 8 well plates (Ibidi). Transfected human cells were incubated at 37°C with 5% CO_2.

FBS starvation assay

24 hours after electroporation transfections, cells were washed twice PBS and incubated in a fresh medium without phenol red and supplemented with 2 mM glutamine (Sigma-Aldrich). Different amounts of FBS were added to the fresh medium when the effect of FBS was analyzed. After 15 minutes, 8-well plates containing epithelial cells expressing GFP-FOXO3a were placed in a fluorescence microscope equipped with an incubation system and images were captured.

Fluorescence microscopy.

Images were captured with a Zeiss Apotome fluorescence microscope equipped with a 10x Plan Apochromat objective and an incubation system that covers every requirement in the

cultivation and observation of living cells (37 °C; 5% CO_2). Pictures were taken at 20 or 40 min intervals using an Axiocam 506 camera, and the images were analyzed using ImageJ software (Wayne Rasband, Research Services Branch, National Institute of Mental Health, MD, USA).

Quantification of GFP-FOXO3a dynamics

GFP-FOXO3a nuclear localization was quantified using ImageJ (FIJI). We measured the mean fluorescence signal in regions of the same size, in the nucleus and cytoplasm. We calculated *R* as the ratio of the signal of the nucleus to that of the cytoplasm. The graphs show the values for 13-19 cells per condition, obtained in three independent experiments.

3

Supplementary Information
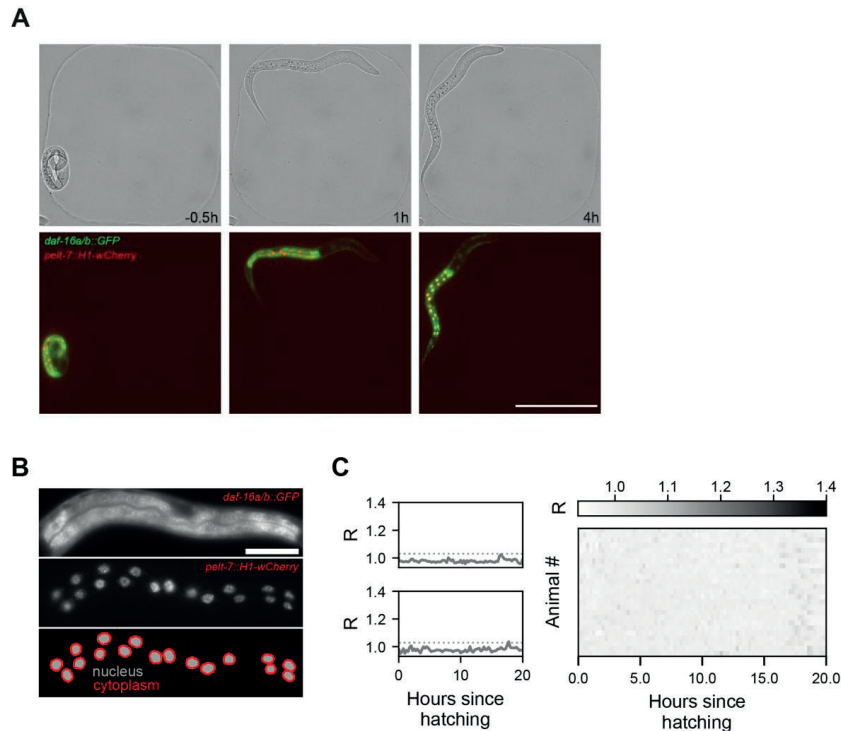
SI Figure 1. Automated quantification of DAF-16/FOXO pulse dynamics. (A) Single L1 larva imaged in a microchamber. Time is hours relative to hatching. Scale bar: 100 ⬚m. (B) Fluorescence images of DAF-16::GFP (top panel) and intestinal marker H1-wCherry (middle panel) in the intestinal cells of an L1 larva. Bottom panel shows the binary mask of the nuclei (gray) and cytoplasm (red) of the intestinal cells for which the DAF-16::GFP fluorescence intensity was calculated. Note that the cytoplasmic mask only covers a narrow strip of cytoplasm directly surrounding each nucleus. Scale bar: 20⬚m. (C) Individual tracks (left) and population view heatmaps (right) of DAF-16::GFP nuclear localization *R* averaged over all intestinal cells, for animals on food. DAF-16::GFP remains cytoplasmic at almost all times, as expected.
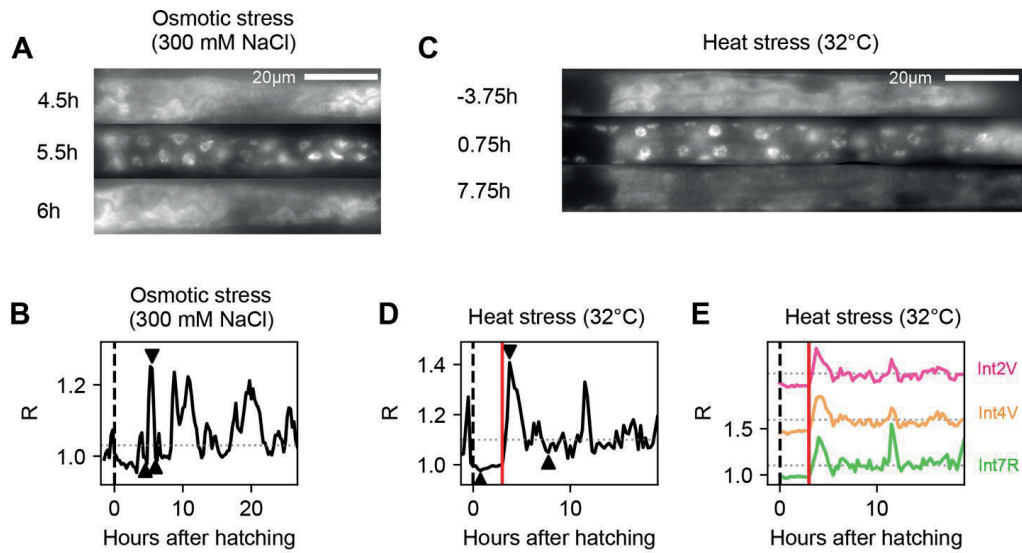
SI Figure 2. DAF-16/FOXO dynamics under osmotic and heat stress. (A) Fluorescence images of DAF-16::GFP in the intestinal cells of an L1 larva subject to osmotic stress (300 mM NaCl). Time is hours since the onset of osmotic shock at the time of hatching. Images were computationally straightened for clarity. Scale bar: 20 µm. (B) DAF-16::GFP nuclear localization R of the animal in (A), averaged over all intestinal cells. Arrowheads correspond to the time points in (A). (C) Fluorescence images of DAF-16::GFP in the intestinal cells of an L1 larva under 32°C heat shock. Time in hours relative to the onset of heat stress. Animals under heat shock are larger that animals under osmotic shock both because the former entered L1 arrest at the time of the temperature shift, rather than immediately upon hatching, and because animals shrink under osmotic shock. Scale bar: 20 µm. (D) DAF-16::GFP localization trajectory R for the animal in (C), averaged over all intestinal cells. Arrowheads correspond to the time points shown in (C), with the red line indicating the time of shift from 20°C to 32°C. (E) Same animal as (C) and (D), but here R is shown for individual intestinal cells. Trajectories are shifted for clarity.
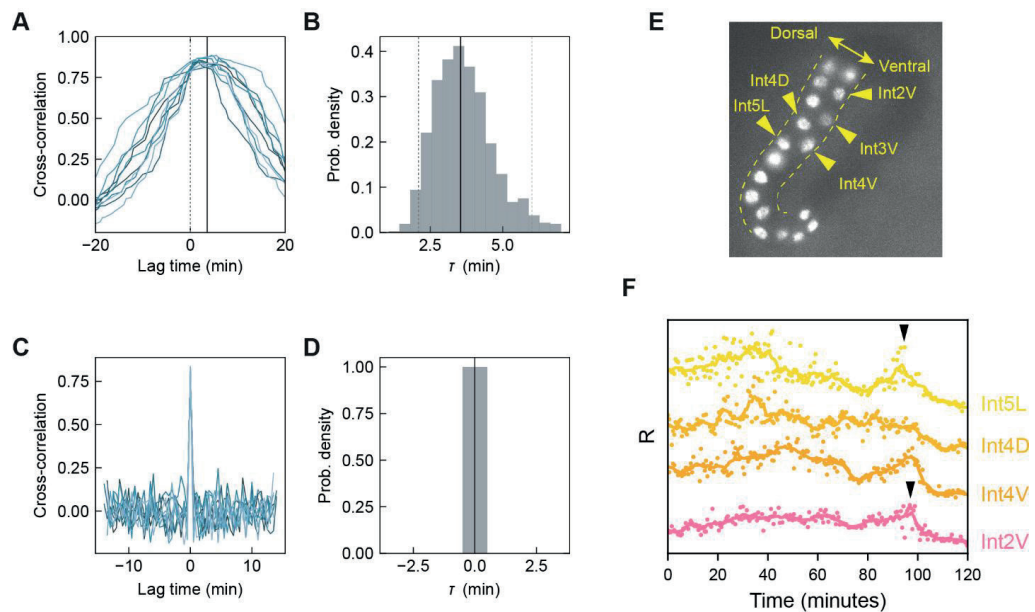
SI Figure 3. DAF-16/FOXO translocation delay between intestinal cells. (A) Cross-correlations of DAF-16::GFP localization trajectories between Int2V and Int8R cells. The 10 different curves are generated from 10 different subsets randomly sampled from a single worm using Monte Carlo simulations. The average peak position or delay (τ, solid black line) clearly differs from 0 (dashed gray line). **(B)** Distribution of peak positions or delays for 1000 cross-correlation random subsets. **(C)** Cross-correlations of scrambled DAF-16 localization trajectories (see **Methods**), between Int2V and Int8R. **(D)** Distribution of peak positions or delays for 1000 cross-correlation subsets of scrambled trajectories. For the scrambled data there is no delay, which indicates that the delay observed between cells with unshuffled data is not an artifact. **(E)** Example of an animal outlining dorsal location of Int4D, 5L and ventral location of Int2V, Int3V and Int4V. Fluorescence is an intestinal nuclear marker. Dashed lines indicate the relevant part of the body outline. **(F)** Example trajectories of nuclear localization R showing dorsal-ventral order in DAF-16::GFP translocation dynamics upon osmotic shock. Black arrow marks an example of a DAF-16::GFP nuclear translocation pulse that occurs in Int5L before Int2V.
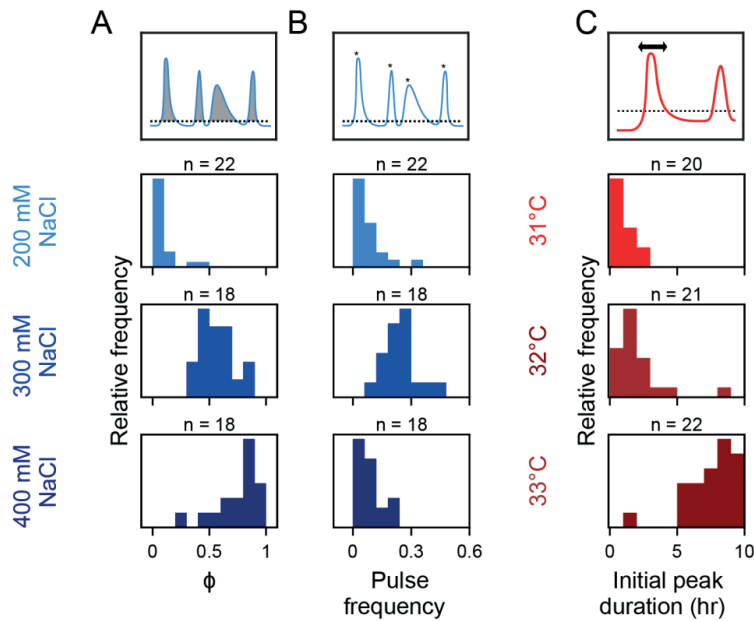
SI Figure 4. Quantification of pulse characteristics under osmotic and heat stress. (A), (B) Distributions of (A) the fraction of time ϕ that DAF-16::GFP is nuclear and (B) pulse frequency, both for increasing osmotic shock. **(C)** Distributions of peak duration of the first DAF-16::GFP translocation peak for increasing heat shock.
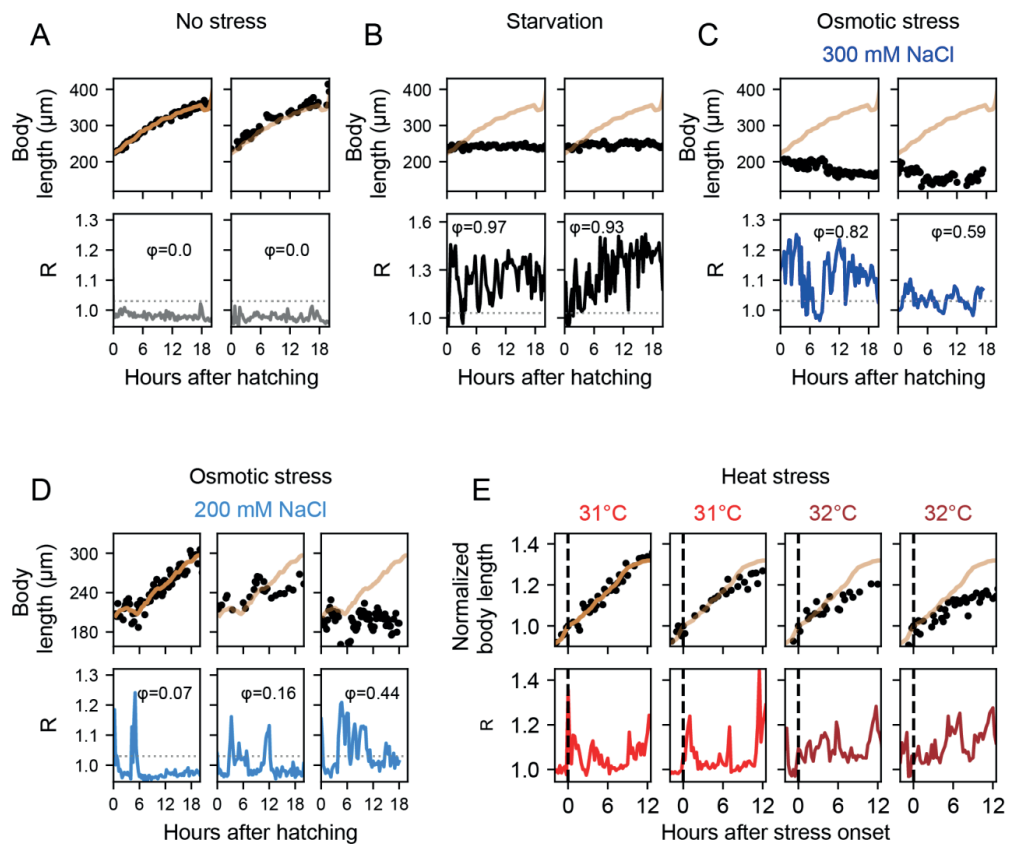
SI Figure 5. Growth arrest coincides with DAF-16/FOXO pulses. (A) Body length (top) and DAF-16::GFP nuclear localization (*R*, bottom) for two individuals in absence of stress. Animals grow at a constant rate, which decreases as they approach ecdysis. The smoothened length data (orange, Savitzky-Golay filter) of the animal in the left panel is also shown in the right panel for comparison. **(B),(C)** Same as (A), but under starvation (B) or osmotic stress (C). For starvation, animals do not show any growth. Under 300 mM NaCl osmotic shock, most animals at the end of imaging have not noticeably grown, and in many cases even shrunk. Orange line is length data for the unstressed animal in (A), shown here for comparison. **(D)** Individuals under 200 mM NaCl osmotic shock. Growth rate is linked to number and duration of DAF-16 pulses, with timing of growth arrest coinciding with DAF-16 pulses. Orange line is smoothened length data of the animal with □=0.07 and sustained growth, shown in other panels for comparison. **(E)** Individuals exposed to different heat stresses. Upon heat shock, animals do not arrest growth after the first DAF-16::GFP pulse, but only after secondary pulse(s). Orange line is smoothened length data of the animal with sustained growth in the left panel, shown in other panels for comparison.

3

References

1. Puig, O., et al., *Control of cell number by Drosophila FOXO: downstream and feedback regulation of the insulin receptor pathway.* Genes Dev, 2003. **17**(16): p. 2006-20.
2. Baker, J., et al., *Role of insulin-like growth factors in embryonic and postnatal growth.* Cell, 1993. **75**(1): p. 73-82.
3. Brogiolo, W., et al., *An evolutionarily conserved function of the Drosophila insulin receptor and insulin-like peptides in growth control.* Curr Biol, 2001. **11**(4): p. 213-21.
4. Liu, J.P., et al., *Mice carrying null mutations of the genes encoding insulin-like growth factor I (Igf-1) and type 1 IGF receptor (Igf1r).* Cell, 1993. **75**(1): p. 59-72.
5. Shingleton, A.W., et al., *The temporal requirements for insulin signaling during development in Drosophila.* PLoS Biol, 2005. **3**(9): p. e289.
6. Tennessen, J.M. and C.S. Thummel, *Coordinating growth and maturation - insights from Drosophila.* Curr Biol, 2011. **21**(18): p. R750-7.
7. Baugh, L.R., *To grow or not to grow: nutritional control of development during Caenorhabditis elegans L1 arrest.* Genetics, 2013. **194**(3): p. 539-55.
8. Gui, T. and B.M.T. Burgering, *FOXOs: masters of the equilibrium.* Febs j, 2022. **289**(24): p. 7918-7939.
9. Brunet, A., et al., *Akt promotes cell survival by phosphorylating and inhibiting a Forkhead transcription factor.* Cell, 1999. **96**(6): p. 857-68.
10. Kops, G.J., et al., *Forkhead transcription factor FOXO3a protects quiescent cells from oxidative stress.* Nature, 2002. **419**(6904): p. 316-21.
11. Nemoto, S., M.M. Fergusson, and T. Finkel, *Nutrient availability regulates SIRT1 through a forkhead-dependent pathway.* Science, 2004. **306**(5704): p. 2105-8.
12. Tran, H., et al., *DNA repair pathway stimulated by the forkhead transcription factor FOXO3a through the Gadd45 protein.* Science, 2002. **296**(5567): p. 530-4.
13. Tokarz, V.L., P.E. MacDonald, and A. Klip, *The cell biology of systemic insulin function.* J Cell Biol, 2018. **217**(7): p. 2273-2289.
14. Andersen, D.S., J. Colombani, and P. Léopold, *Coordination of organ growth: principles and outstanding questions from the world of insects.* Trends Cell Biol, 2013. **23**(7): p. 336-44.
15. Petersen, M.C. and G.I. Shulman, *Mechanisms of Insulin Action and Insulin Resistance.* Physiol Rev, 2018. **98**(4): p. 2133-2223.
16. Willcox, B.J., et al., *FOXO3A genotype is strongly associated with human longevity.* Proc Natl Acad Sci U S A, 2008. **105**(37): p. 13987-92.
17. Poloz, Y. and V. Stambolic, *Obesity and cancer, a case for insulin signaling.* Cell Death Dis, 2015. **6**(12): p. e2037.
18. Suh, Y., et al., *Functionally significant insulin-like growth factor I receptor mutations in centenarians.* Proc Natl Acad Sci U S A, 2008. **105**(9): p. 3438-42.
19. Gross, D.N., M. Wan, and M.J. Birnbaum, *The role of FOXO in the regulation of metabolism.* Curr Diab Rep, 2009. **9**(3): p. 208-14.
20. Baugh, L.R. and P.W. Sternberg, *DAF-16/FOXO regulates transcription of cki-1/Cip/Kip and repression of lin-4 during C. elegans L1 arrest.* Curr Biol, 2006. **16**(8): p. 780-5.
21. Burton, N.O., et al., *Insulin-like signalling to the maternal germline controls progeny response to osmotic stress.* Nat Cell Biol, 2017. **19**(3): p. 252-257.
22. Murphy, C.T. and P.J. Hu, *Insulin/insulin-like growth factor signaling in C. elegans.* WormBook, 2013: p. 1-43.
23. Ogg, S., et al., *The Fork head transcription factor DAF-16 transduces insulin-like metabolic and longevity signals in C. elegans.* Nature, 1997. **389**(6654): p. 994-9.
24. Weinkove, D., et al., *Long-term starvation and ageing induce AGE-1/PI 3-kinase-dependent translocation of DAF-16/FOXO to the cytoplasm.* BMC Biol, 2006. **4**: p. 1.
25. Paradis, S. and G. Ruvkun, *Caenorhabditis elegans Akt/PKB transduces insulin receptor-like signals from AGE-1 PI3 kinase to the DAF-16 transcription factor.* Genes Dev, 1998. **12**(16): p. 2488-98.

26. Rena, G., et al., *Phosphorylation of the transcription factor forkhead family member FKHR by protein kinase B.* J Biol Chem, 1999. **274**(24): p. 17179-83.
27. Lee, R.Y., J. Hench, and G. Ruvkun, *Regulation of C. elegans DAF-16 and its human ortholog FKHRL1 by the daf-2 insulin-like signaling pathway.* Curr Biol, 2001. **11**(24): p. 1950-7.
28. Furuyama, T., et al., *Identification of the differential distribution patterns of mRNAs and consensus binding sequences for mouse DAF-16 homologues.* Biochem J, 2000. **349**(Pt 2): p. 629-34.
29. Schuster, E., et al., *DamID in C. elegans reveals longevity-associated targets of DAF-16/FoxO.* Mol Syst Biol, 2010. **6**: p. 399.
30. Tepper, R.G., et al., *PQM-1 complements DAF-16 as a key transcriptional regulator of DAF-2-mediated development and longevity.* Cell, 2013. **154**(3): p. 676-690.
31. Kaplan, R.E.W., et al., *Food perception without ingestion leads to metabolic changes and irreversible developmental arrest in C. elegans.* BMC Biol, 2018. **16**(1): p. 112.
32. Mata-Cabana, A., et al., *Social Chemical Communication Determines Recovery From L1 Arrest via DAF-16 Activation.* Front Cell Dev Biol, 2020. **8**: p. 588686.
33. Henderson, S.T. and T.E. Johnson, *daf-16 integrates developmental and environmental inputs to mediate aging in the nematode Caenorhabditis elegans.* Curr Biol, 2001. **11**(24): p. 1975-80.
34. Alam, H., et al., *EAK-7 controls development and life span by regulating nuclear DAF-16/FoxO activity.* Cell Metab, 2010. **12**(1): p. 30-41.
35. Putker, M., et al., *Redox-dependent control of FOXO/DAF-16 by transportin-1.* Mol Cell, 2013. **49**(4): p. 730-42.
36. Riedel, C.G., et al., *DAF-16 employs the chromatin remodeller SWI/SNF to promote stress resistance and longevity.* Nat Cell Biol, 2013. **15**(5): p. 491-501.
37. Wolff, S., et al., *SMK-1, an essential regulator of DAF-16-mediated longevity.* Cell, 2006. **124**(5): p. 1039-53.
38. Gritti, N., et al., *Long-term time-lapse microscopy of C. elegans post-embryonic development.* Nat Commun, 2016. **7**: p. 12500.
39. Aghayeva, U., A. Bhattacharya, and O. Hobert, *A panel of fluorophore-tagged daf-16 alleles.* MicroPubl Biol, 2020. **2020**.
40. Kimura, K.D., et al., *daf-2, an insulin receptor-like gene that regulates longevity and diapause in Caenorhabditis elegans.* Science, 1997. **277**(5328): p. 942-6.
41. Hibshman, J.D., et al., *daf-16/FoxO promotes gluconeogenesis and trehalose synthesis during starvation to support survival.* Elife, 2017. **6**.
42. Schindler, A.J., L.R. Baugh, and D.R. Sherwood, *Identification of late larval stage developmental checkpoints in Caenorhabditis elegans regulated by insulin/IGF and steroid hormone signaling pathways.* PLoS Genet, 2014. **10**(6): p. e1004426.
43. Uppaluri, S., S.C. Weber, and C.P. Brangwynne, *Hierarchical Size Scaling during Multicellular Growth and Development.* Cell Rep, 2016. **17**(2): p. 345-352.
44. Muñoz, M.J. and D.L. Riddle, *Positive selection of Caenorhabditis elegans mutants with increased stress resistance and longevity.* Genetics, 2003. **163**(1): p. 171-80.
45. Stojanovski, K., H. Großhans, and B.D. Towbin, *Coupling of growth rate and developmental tempo reduces body size heterogeneity in C. elegans.* Nat Commun, 2022. **13**(1): p. 3132.
46. Uppaluri, S. and C.P. Brangwynne, *A size threshold governs Caenorhabditis elegans developmental progression.* Proc Biol Sci, 2015. **282**(1813): p. 20151283.
47. Lamitina, S.T., et al., *Adaptation of the nematode Caenorhabditis elegans to extreme osmotic stress.* Am J Physiol Cell Physiol, 2004. **286**(4): p. C785-91.
48. Calnan, D.R. and A. Brunet, *The FoxO code.* Oncogene, 2008. **27**(16): p. 2276-88.
49. Huang, H. and D.J. Tindall, *Dynamic FoxO transcription factors.* J Cell Sci, 2007. **120**(Pt 15): p. 2479-87.
50. Böhni, R., et al., *Autonomous control of cell and organ size by CHICO, a Drosophila homolog of vertebrate IRS1-4.* Cell, 1999. **97**(7): p. 865-75.

51.   Kramer, J.M., et al., *Expression of Drosophila FOXO regulates growth and can phenocopy starvation.* BMC Dev Biol, 2003. **3**: p. 5.
52.   Miron, M., et al., *The translational inhibitor 4E-BP is an effector of PI(3)K/Akt signalling and cell growth in Drosophila.* Nat Cell Biol, 2001. **3**(6): p. 596-601.
53.   Radimerski, T., et al., *dS6K-regulated cell growth is dPKB/dPI(3)K-independent, but requires dPDK1.* Nat Cell Biol, 2002. **4**(3): p. 251-5.
54.   Puigserver, P., et al., *Insulin-regulated hepatic gluconeogenesis through FOXO1-PGC-1alpha interaction.* Nature, 2003. **423**(6939): p. 550-5.
55.   Baugh, L.R., J. Demodena, and P.W. Sternberg, *RNA Pol II accumulates at promoters of growth genes during developmental arrest.* Science, 2009. **324**(5923): p. 92-4.
56.   Tissenbaum, H.A., *DAF-16: FOXO in the Context of C. elegans.* Curr Top Dev Biol, 2018. **127**: p. 1-21.
57.   Zhou, K.I., Z. Pincus, and F.J. Slack, *Longevity and stress in Caenorhabditis elegans.* Aging (Albany NY), 2011. **3**(8): p. 733-53.
58.   Hsu, A.L., C.T. Murphy, and C. Kenyon, *Regulation of aging and age-related disease by DAF-16 and heat-shock factor.* Science, 2003. **300**(5622): p. 1142-5.
59.   Li, J., et al., *Caenorhabditis elegans HCF-1 functions in longevity maintenance as a DAF-16 regulator.* PLoS Biol, 2008. **6**(9): p. e233.
60.   Levine, J.H., Y. Lin, and M.B. Elowitz, *Functional roles of pulsing in genetic circuits.* Science, 2013. **342**(6163): p. 1193-200.
61.   Purvis, J.E. and G. Lahav, *Encoding and decoding cellular information through signaling dynamics.* Cell, 2013. **152**(5): p. 945-56.
62.   Venkatachalam, V., A. Jambhekar, and G. Lahav, *Reading oscillatory instructions: How cells achieve time-dependent responses to oscillating transcription factors.* Curr Opin Cell Biol, 2022. **77**: p. 102099.
63.   Litvak, V., et al., *Function of C/EBPdelta in a regulatory circuit that discriminates between transient and persistent TLR4-induced signals.* Nat Immunol, 2009. **10**(4): p. 437-43.
64.   Murphy, L.O., et al., *Molecular interpretation of ERK signal duration by immediate early gene products.* Nat Cell Biol, 2002. **4**(8): p. 556-64.
65.   Hansen, A.S. and E.K. O'Shea, *Promoter decoding of transcription factor dynamics involves a trade-off between noise and control of gene expression.* Mol Syst Biol, 2013. **9**: p. 704.
66.   Purvis, J.E., et al., *p53 dynamics control cell fate.* Science, 2012. **336**(6087): p. 1440-4.
67.   Kang, C. and L. Avery, *Systemic regulation of starvation response in Caenorhabditis elegans.* Genes Dev, 2009. **23**(1): p. 12-7.
68.   Kageyama, R., et al., *Oscillatory gene expression and somitogenesis.* Wiley Interdiscip Rev Dev Biol, 2012. **1**(5): p. 629-41.
69.   Fernandes de Abreu, D.A., et al., *An insulin-to-insulin regulatory network orchestrates phenotypic specificity in development and physiology.* PLoS Genet, 2014. **10**(3): p. e1004225.
70.   Kaplan, R.E.W., et al., *Pervasive Positive and Negative Feedback Regulation of Insulin-Like Signaling in Caenorhabditis elegans.* Genetics, 2019. **211**(1): p. 349-361.
71.   Murphy, C.T., S.J. Lee, and C. Kenyon, *Tissue entrainment by feedback regulation of insulin gene expression in the endoderm of Caenorhabditis elegans.* Proc Natl Acad Sci U S A, 2007. **104**(48): p. 19046-50.
72.   Singh, R. and J. Sulston, *Some observations on moulting in Caenorhabditis elegans.* Nematologica, 1978. **24**(1): p. 63-71.
73.   Peterson, B.M., et al., *On Uncertainties in Cross-Correlation Lags and the Reality of Wavelength-dependent Continuum Lags in Active Galactic Nuclei.* Publications of the Astronomical Society of the Pacific, 1998. **110**(748): p. 660.

3

Chapter 4

A collective model of stress-specific, synchronized DAF-16/FOXO pulses in insulin signaling

Burak Demirbas[1] and Jeroen van Zon[1]

[1]AMOLF, Amsterdam, The Netherlands

"Treu die Natur und ganz!" - Wie fängt er's an:	"Completely true to nature!" - What a lie:
Wann wäre je Natur im Bilde *abgetan*?	How could nature ever be *constrained* into a picture?
Unendlich ist das kleinste Stück der Welt! -	The smallest bit of nature is infinite! -
Er malt zuletzt davon, was ihm *gefällt*.	And so he paints what he *likes* about it.
Und was gefällt ihm? Was er malen *kann*!	And what does he like? He likes what he *can* paint!

Friedrich Nietzsche, "Die fröhliche Wissenschaft"

Abstract

Proper functioning of multicellular organisms requires synchronized cellular states, vital in processes like circadian rhythms and stress responses. Insulin signaling is crucial in stress responses, developmental growth control, and diseases such as diabetes and cancer. We introduce a stochastic differential equation model to study the stress-dependent dynamics and synchronization of the transcription factor DAF-16/FOXO, the main effector of insulin signaling in C. elegans. Our model shows that stress-induced pulses can emerge through a relaxation oscillator mechanism driven by an insulin signaling-dependent feedback loop, with synchrony achieved via intercellular insulin-like peptide (ILP) exchange. Experimental validation shows that perturbing insulin signaling in specific tissues disrupts DAF-16/FOXO dynamics in the remaining tissues, as well as pulse synchrony, supporting our model's predictions.

Our findings suggest that the system's tuning near transitions between different dynamical regimes explains DAF-16/FOXO dynamics' stress specificity and the effects of insulin receptor mutations. The model predicts hysteresis in DAF-16/FOXO localization under heat stress, which we confirm experimentally. The study highlights the potential conservation of similar synchronization mechanisms in higher animals, informing stress response pathways and therapeutic strategies targeting DAF-16/FOXO in diseases.

Introduction

To ensure the proper functioning of multicellular organisms, body-wide synchronization of cell states is paramount. Perhaps the most famous example is the circadian rhythm, cellular oscillations with a period of 24 hours, where synchronization of circadian clocks between cells is crucial for animal health (1). Another, less understood example is the stress response, especially when environmental stresses necessitate organism-wide processes, such as growth arrest during development. Without synchronization, some parts of an organism might arrest growth while others continue, resulting in disproportional growth and developmental abnormalities. One of the key stress response pathways in animals is the insulin signaling pathway. It is highly conserved across species and plays pivotal roles in cellular stress response, growth control, longevity, and diseases such as diabetes, obesity, and cancer (2–5). For instance, genetically disrupting insulin signaling in mice results in smaller, but otherwise developmentally normal animals (6) while nutrient deprivation during development in fruit flies causes insulin signaling-mediated growth arrest (7). Remarkably, in both cases, the animals maintain their stereotypical body proportions, indicating effective coordination of growth across the entire body (6, 7). How the remarkable coordination of insulin signaling is achieved remains a critical question.

Dynamics of transcription factors (TF) play an important role in stress response signaling through pulsatile, or even oscillatory translocation to the nucleus upon stress induction, where they activate stress-response genes. Examples include Msn2/4 and Crz-1 in yeast, and NF-κB, p53 and FOXO in mammals (8–14). However, because in all cases the translocation have been studied either in individual cells (e.g. yeast) or in mammalian cell culture, it remains unknown how the translocation dynamics unfold at the organ- or even the whole-body level. Our recent findings where we examined individual *C. elegans* nematode animals trapped in microchambers revealed that the transcription factor DAF-16/FOXO, the primary effector of insulin/IGF-1 signaling (IIS) in *C. elegans*, exhibits translocation pulses that are not only highly stochastic but also remarkably synchronized throughout the organism's body (over distances of ~200 μm) (13). Furthermore, we showed that these pulses cause a body-wide arrest in growth, underscoring the significance of cell synchrony in maintaining proportional body development in organisms. While pulses observed in developmental signaling pathways like Erk show synchrony between adjacent cells in monolayers, it is typically limited to a few cells' distance (15). Other examples of synchronized pulsatile behavior are calcium and circadian oscillations, but in these cases the dynamics are relatively regular, i.e. less stochastic than DAF-16/FOXO pulses. In the case of circadian oscillators, where body-wide synchrony is observed, this synchrony also arises, at least in part, from their entrainment to external, environmental stimuli such as the day-night light cycles (16–20). Exploring the mechanisms

enabling entirely stochastic TF pulses to synchronize with body-wide synchrony, but without such external entrainment, thus likely requires novel mechanisms.

The insulin/insulin-like signaling (IIS) pathway in *C. elegans* is highly similar to that in higher animals, including humans (21). In the absence of stress, *C. elegans* neurons produce various insulin-like peptides (ILPs), which bind the insulin receptor DAF-2, ultimately activating the kinases AKT-1 and AKT-2 through a signaling cascade (21). In turn, these kinases phosphorylate the transcription factor DAF-16/FOXO, promoting its binding to 14-3-3 proteins, which blocks DAF-16/FOXO nuclear localization, thereby sequestering it in the cytoplasm (21). Upon exposure to stress (e.g. starvation, osmotic stress, or heat stress), ILP levels fall and IIS becomes inactive, leading to DAF-16/FOXO dephosphorylation and its translocation to the nucleus, where it induces the expression of hundreds of stress-response genes (21). However, this linear pathway structure is not sufficient to explain how DAF-16/FOXO translocation pulses are generated, nor how their synchrony is achieved. While it has been shown that DAF-16/FOXO up- or downregulates mRNA and/or protein levels of most ILPs and IIS components such as AKT-1 (22–24), their potential role in DAF-16/FOXO stochastic translocation pulses and their synchronization has never been explored.

Here, we introduce a minimal mathematical model aimed at identifying mechanisms underlying synchronized DAF-16/FOXO translocation pulses. This model has three novel elements. First, DAF-16/FOXO nuclear localization is bistable, meaning that for a given level of IIS activity, DAF-16/FOXO can be either fully phosphorylated and cytoplasmic, or fully dephosphorylated and nuclear, depending on the history of IIS activity (25, 26). Second, DAF-16 translocation increases IIS activation, either cell-autonomously by changing kinase activity, or through extracellular (autocrine) signaling by DAF-16-induced ILP secretion (22, 23, 27–29). This negative feedback loop generates pulses in DAF-16/FOXO translocation through a relaxation oscillator mechanism (57). Finally, when this negative feedback loop is predominantly extracellular, ILPs secreted by one cell can activate IIS in other cells (paracrine signaling), resulting in coupling of the IIS state between cells. Strikingly, our computational results show that this causes tight synchronization of DAF-16/FOXO pulses, even when pulse dynamics is highly stochastic.

Our model provides a potential mechanism for a so-far unexplained feature of our experimental observations, namely that different stresses (starvation, osmotic pressure, heat) elicited qualitatively different DAF-16/FOXO translocation dynamics (13). Specifically, it shows how stress type-specific modulation of feedback strength, and stress magnitude-dependent regulation of tonic ILP levels could lead to the observed qualitative differences in DAF-16/FOXO dynamics. Moreover, it also reproduces the quantitative changes in DAF-16/FOXO

dynamics both as stress magnitude (salt concentration, temperature) is varied, and when the insulin receptor is mutated.

In addition, our model also makes novel predictions that we verify experimentally. First, it predicts that DAF-16/FOXO translocation under heat stress should be hysteretic, meaning DAF-16/FOXO nuclear localization depends on heat stress history rather than on the current temperature by itself. Indeed, we find clear differences in DAF-16/FOXO translocation depending on whether we shift temperature up or down that match these predictions. Second, the predicted IIS-mediated cell-cell coupling that underlies synchronization in our model implies that DAF-16/FOXO translocation dynamics should be perturbed by fixing the IIS state in a subset of cells. We subsequently used tissue-specific downregulation of the insulin receptor DAF-2, resulting in constitutive nuclear DAF-16/FOXO in the targeted tissues, and found that it strongly impacted DAF-16/FOXO translocation dynamics and synchrony also in other tissues, as predicted.

Overall, the mathematical model we present here provides a compelling mechanism to explain IIS-dependent DAF-16/FOXO pulse dynamics with body-wide synchrony, with key aspects of the mechanism verified by novel experiments. Given the broad conservation of IIS and FOXO translocation dynamics from worms to humans, similar mechanisms might play an important role in the organ- or body-wide coordination of growth and other IIS-dependent processes also in higher animals.

Results

Model construction

DAF-16/FOXO phosphorylation. For simplicity, we do not explicitly model DAF-16/FOXO nuclear transport but instead assume it directly follows DAF-16/FOXO phosphorylation, i.e. dephosphorylated DAF-16/FOXO is always nuclear and vice versa. DAF-16/FOXO is phosphorylated by the kinases AKT-1 and AKT-2 at three phosphorylation sites, thereby sequestering DAF-16/FOXO in the cytoplasm through stimulation of its binding to 14-3-3 proteins (30–32). AKT-1/2 in turn is either active or inactive, being positively regulated by PDK-1, an upstream component of IIS (33, 34). In the absence of AKT-1/2 signaling, DAF-16/FOXO is rapidly dephosphorylated by the phosphatase PPTR-1/PP2A, promoting localization to the nucleus (35). Previous theoretical studies have shown that such a multi-step phosphorylation/dephosphorylation cascade can lead to bistability and hysteresis in phosphorylation level, provided that kinase and phosphatase modify their substrate according to a distributive mechanism and are present in concentrations that are limiting compared to the

substrate concentration (25, 36–40). Such bistability was shown to result in oscillations in the phosphorylation state, when coupled to negative feedback (26). Here, we use these results as basis for a simple model of DAF-16/FOXO phosphorylation and, hence, nuclear localization (**Fig. 1A, B, Supplemental Fig. 1**). For simplicity, we do not explicitly model multi-step phosphorylation, but instead use a phenomenological approximation constructed to reproduce bistable (de)phosphorylation dynamics, given by:

$$\frac{d}{dt}D = f_D\left[a(D_T - D) + \frac{D^2(D_T - D)}{D_T - a}\right] - \frac{b_D K D}{b + D} \tag{1}$$

where D is the level of DAF-16/FOXO that is dephosphorylated and, hence, nuclear, D_T is total DAF-16/FOXO, K is the level of activated kinases, f_D and b_D are rates that determine the (de)phosphorylation timescale, while a and b are effective parameters that control bistable behavior.

Feedback through kinase activity. We model two distinct mechanisms for DAF-16/FOXO-mediated negative feedback, either extracellularly through ILPs (P) being secreted and binding to the cell's insulin receptors, or intracellularly by DAF-16/FOXO (D) directly up- or downregulating activity of IIS pathway, for example by changing PDK-1 levels (**Fig. 1A**). While most *C. elegans* ILPs likely act as agonists, stimulating IIS binding the insulin receptor DAF-2, some ILPs, such as *daf-28*, might function as antagonists, by preventing agonistic ILPS from activating DAF-2 (21). For simplicity, we assume ILPs only act as agonists, described collectively as the ILP levels P_0 and P. Here, P_0 represents a basal ILP level due to tonic ILP secretion by stress-sensing neurons, which decreases upon exposure to stress (41), while P represent the level of ILPs secreted upon nuclear DAF-16/FOXO translocation. Both ILP pools are assumed to activate IIS, leading to downstream activation of the DAF-16/FOXO kinases AKT-1/2, described collectively as the level of activated kinases *K,* leading to:

$$\frac{d}{dt}K = f_K[P_0 + c_P P + c_D D](K_T - K) - b_K K \tag{2}$$

where P is the DAF-16/FOXO-dependent ILP level, P_0 is the DAF-16/FOXO-independent basal ILP level, K_T total kinase level, f_K and b_K describe kinase activation/deactivation dynamics, c_P the feedback strength for kinase activation of IIS by external ILPs and c_D for internal feedback. Finally, P_0 is a model parameter, whose value depends on the type and magnitude of stress, while P varies dynamically according to:

$$\frac{d}{dt}P = f_P D - b_P P \tag{3}$$

where f_P is the rate of ILP secretion induced by nuclear DAF-16/FOXO, and b_P the degradation rate in the extracellular environment.

Dimensionless parameters. We further simplified Eqs. (1)-(3) by employing the following dimensionless variables*: $d = \frac{D}{D_T}, k = \frac{K}{K_T}, p = P/P_{max}$ and $\tau = b_k t$, where d, k are the fraction of dephosphorylated DAF-16/FOXO and activated kinases, respectively, $P_{max} = \frac{f_P}{b_P} D_T$ is the maximum possible DAF-16/FOXO-dependent ILP level, and τ is time relative to kinase half-life. This yields the following set of dimensionless ODEs:

$$\frac{d}{d\tau} d = \zeta \left[\alpha(1 - d) + \frac{d^2(1 - d)}{1 - \alpha'} \right] - \chi \frac{kd}{\beta + d} \tag{4}$$

$$\frac{d}{d\tau} k = \gamma [\delta + \phi p + (1 - \phi)d](1 - k) - k \tag{5}$$

$$\frac{d}{d\tau} p = \epsilon(d - p) \tag{6}$$

where:

$$\zeta = \frac{f_D D_T}{b_K} \tag{7}$$

$$\gamma = \frac{f_K D_T}{b_K} \left(\frac{f_P}{b_P} c_P + c_D \right) \tag{8}$$

$$\chi = \frac{b_D K_T}{b_K D_T} \tag{9}$$

$$\delta = \frac{P_0}{\frac{f_P}{b_P} c_P + c_D} \tag{10}$$

$$\alpha = \frac{a}{D_T} \tag{11}$$

$$\phi = \frac{f_P c_P}{f_P c_P + b_P c_D} \tag{12}$$

$$\beta = \frac{b}{D_T} \tag{13}$$

$$\epsilon = \frac{b_P}{b_K} \tag{14}$$

Full stochastic, multicellular model. So far, we set up the equations for a single cell. Here, however, we propose that DAF-16/FOXO-induced ILPs can be shared between all cells (paracrine signaling). We assume that the secreted ILPs diffuse fast, and therefore do not model their diffusion explicitly. Instead, ILPs produced by any cell in our model instantly diffuse and mix, adding to a common pool shared by all cells. The effective ILP level felt by each cell is then the total produced and secreted ILP, divided by the number of cells N_{cells}. To model the stochastic dynamics of the system, we add to each equation a Gaussian noise term η with a time-averaged mean of zero, following Langevin dynamics (42). Hence, in the full stochastic, multicellular model we have for each cell i:

$$\frac{d}{d\tau}d_i = \zeta \left[\alpha(1 - d_i) + \frac{d_i^2(1 - d_i)}{1 - \alpha'} \right] - \chi \frac{k_i d_i}{\beta + d_i} + \sigma_d \eta_d^i(\tau) \qquad (15)$$

$$\frac{d}{d\tau}k_i = \gamma[\delta + \phi p + (1 - \phi)d_i](1 - k_i) - k_i + \sigma_k \eta_k^i(\tau) \qquad (16)$$

and for the shared ILP level:

$$\frac{d}{d\tau}p = \epsilon \left(\frac{1}{N_{cells}} \sum d_i - p \right) + \sigma_p \eta_p(\tau) \qquad (17)$$

where η is uncorrelated Gaussian noise with $< \eta_a^i(\tau) > = 0$ and $< \eta_a^i(\tau) \cdot \eta_b^j(\tau') > = \delta_{i,j}\delta_{a,b}\delta(\tau - \tau')$, and σ_j is a positive constant that denotes the magnitude of fluctuations per unit time (43).

Free parameters. The dimensionless model has eight free parameters, of which we constrain four: α, β, ζ, χ (with values set to 0.019, 4, 100, and 200, respectively), to support bistability as a function of activated kinase level k (**Fig. 1B**), with magnitude of ζ and χ, such that DAF-16/FOXO (de)phosphorylation is much faster than other reactions. The parameter ϕ indicates the relative importance of the external feedback, mediated through ILP secretion, and the internal feedback, by direct control of internal IIS regulators, with $\phi = 0$ corresponding to only internal feedback and $\phi = 1$ to only external feedback. The parameter γ represents the feedback strength, as it describes how strongly the kinases are activated by both external and internal feedback. The parameter δ represents the basal, stress-dependent ILP level that is independent of the IIS feedback loop. Finally, ϵ represents the rate of ILP degradation relative to rate of kinase deactivation, with $\epsilon > 1$ corresponding to ILP degradation faster than kinase deactivation.

Qualitatively different DAF-16/FOXO translocation dynamics regimes

Together, the parameters γ and δ represent parts of the model that connect to the known biology of *C. elegans* IIS upon entering stress. First, δ corresponds to the tonic level of ILP secreted by *C. elegans* sensory neurons, which is decreased upon exposure to stress (41, 44, 45). Whereas the human genome contains a single insulin and two insulin-like growth factor (IGF) genes (46, 47), and mice have two types of insulin (48), the *C. elegans* genome encodes for 40 different ILPs (21). However, fluorescent reporter gene experiments have shown that different types of stress lead to the expression of specific combinations of ILPs (49). Moreover, these ILPs function as either antagonists (e.g. INS-17, INS-18) or agonists (e.g. INS-3, INS-4), possibly also with different binding affinities to DAF-2 (41, 44, 45, 50, 51). Second, γ describes how cells respond internally both to external ILP levels and the internal feedback. The IIS response to external ILPs is known to depend on crosstalk with other signaling pathways that sense stress intracellularly, such as the AMPK and JNK signaling pathways (52–56). As a consequence, the cell's IIS response to the same external ILP level might depend on the exact stress experienced. Overall, this indicates that both γ and δ might depend on the exact stress type and magnitude. We therefore first examined the dynamics of the model when varying γ and δ.

The phase diagram (**Fig. 1C**) shows the dependence of DAF-16/FOXO dynamics on γ and δ. We first focus on the dynamics of the deterministic, one-cell model (N=1) and feedback exclusively through ILP secretion ($\phi = 1$). For high γ (strong response to ILP) and high δ (low stress and hence high basal ILP), the system is monostable, with DAF-16/FOXO phosphorylated and cytoplasmic (low d). For low γ and δ, the system is also monostable, but with DAF-16 dephosphorylated and nuclear (high d). At the interphase of these two regions of phase space, we observe more complex dynamics. For low γ and high δ, the model is bistable, with the steady-state level of d depending on the initial values of d, k, and p (**Fig. 1F,G**). Moreover, for high γ and low δ, nuclear DAF-16/FOXO levels exhibit oscillations (**Fig. 1H**). These oscillations arise through the following mechanism: nuclear DAF-16/FOXO induces secretion of ILPs (p), which leads to kinase activation (k), resulting in dephosphorylation and nuclear exit of DAF-16/FOXO, whereafter the ILP and subsequently kinase levels decrease until the cycle is reset and repeats, acting as a relaxation oscillator (57). For oscillations, the frequency of pulses generally decreases near the edge of the oscillatory region, and increases as δ is lowered, while the amplitude remains relatively constant (**Fig. 1D,E**). We see the same dynamical regimes for different values of ϵ and ϕ (**Supplemental Fig. 2**).

Stochastic DAF-16/FOXO translocation dynamics

The deterministic model shows oscillations and bistability, but not the discrete pulses in nuclear localization we observed in our experiments, e.g. for osmotic shock (13). Given that the experimentally observed pulses were stochastic in nature, we therefore next examine the impact of inherent fluctuations on the model dynamics (58), by adding a stochastic noise source to each of the non-dimensionalized ODEs. For γ and δ values in the middle of the oscillatory regime, this resulted in robust oscillations, that only differed little from the deterministic model (**Fig. 1H**). However, when we performed simulations for parameter values within the nuclear monostable regime, but close to the oscillatory regime, were the deterministic model exhibits strongly damped oscillations to the monostable nuclear state, this resulted in alternating pulses and 'plateaus', periods of persistent nuclear DAF-16/FOXO (**Fig. 1I**). In the bistable regime, adding fluctuations leads to stochastic transitions between the two bistable states, either nuclear or cytoplasmic DAF-16/FOXO, with the frequency of transitions, and therefore the average duration of individual pulses, depending on the values of γ and δ (**Fig. 1H, I**). These results suggest that DAF-16/FOXO nuclear translocation pulses could result from fluctuations acting on a system tuned close to transitions between oscillatory, bistable and monostable regimes.
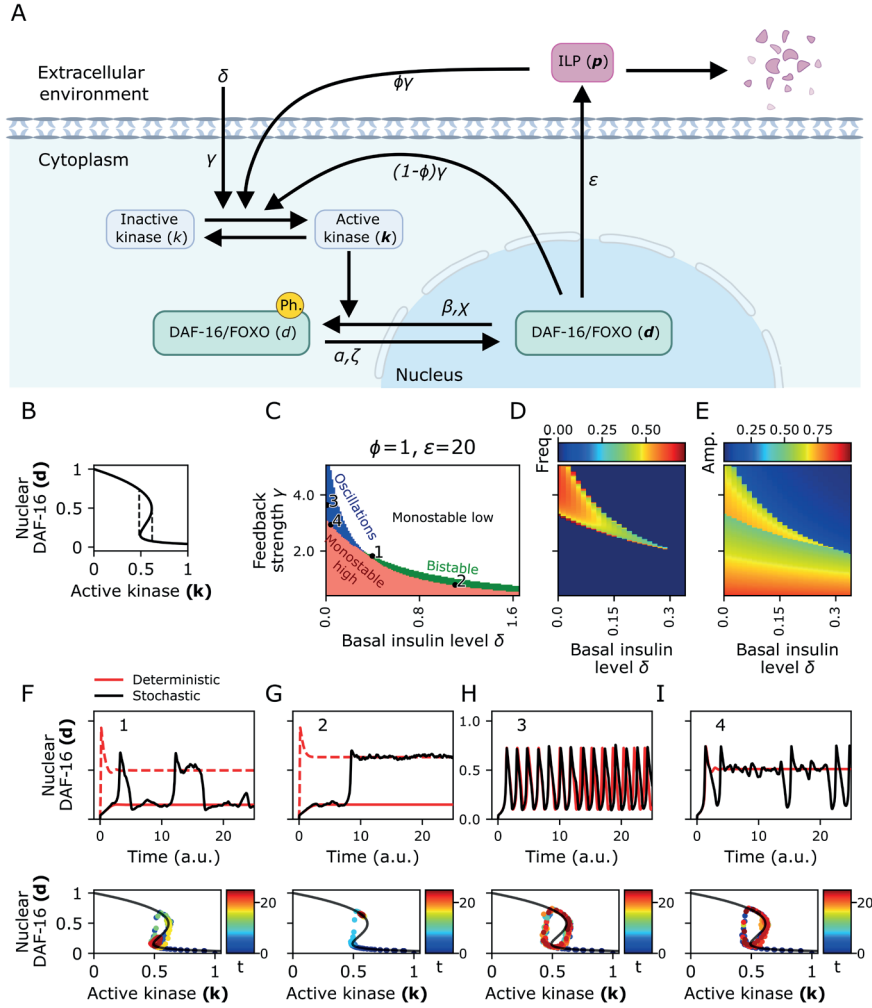
Figure 1. Oscillations and pulses in a minimal model of DAF-16/FOXO nuclear translocation dynamics. **A)** Schematic of the model, showing the dimensionless variables, their interactions, and the parameters. **B)** Steady state curve of *d* versus *k*, showing that nuclear DAF-16/FOXO is bistable for a range of values of the kinase. **C)** Phase diagram displaying the various types of qualitative dynamics the model produces: monostability with either nuclear or cytoplasmic DAF-16/FOXO, oscillations, or bistability. **D, E)** Heatmaps for frequency and amplitude corresponding to C). Within the oscillatory regime frequency varies, reaching a maximum when δ is zero. Amplitude in the oscillatory region is defined as the maximum peak value, and increases near the edge with the monostable region. In the monostable nuclear region, amplitude is the steady-state level of nuclear DAF-16/FOXO, and increases with decreasing γ. **F-I)** Top: Example tracks of simulations for various parts of the phase diagram, where red corresponds to a deterministic simulation and black to its stochastic version. Bottom: Nuclear DAF-16/FOXO versus active kinase level, with color indicating time, showing how the system traverses the bistable k-d landscape of B).

Stress-specific translocation dynamics as transitions between distinct dynamical regimes

Our previous experimental observations showed that DAF-16/FOXO translocation dynamics are stress-dependent, with starvation giving rise to stochastic oscillations, while osmotic stress-induced dynamics yield more stochastically timed pulses (13). Moreover, we also found quantitative changes in DAF-16/FOXO dynamics upon changing stress magnitude, e.g. increasing pulse frequency and duration for increasing osmotic shock. Based on the above results, we examined whether the experimentally observed changes in DAF-16/FOXO dynamics for different stress type and magnitude can be explained as transitions between the different dynamical regimes (oscillatory, monostable nuclear, bistable) we observe in the model (**Fig. 2A**).

First, we examined the transition from the monostable cytoplasmic regime through the oscillatory regime (high γ, **Fig. 2A, i**). As δ is decreased, corresponding to the onset of stress, the model produced dynamics that are characterized by a stochastic switching between oscillations and 'plateaus', periods of prolonged nuclear localization (**Fig. 2A, B**). This resembled our experimental observations of DAF-16/FOXO translocation dynamics under starvation (**Fig. 2C**). Moreover, the oscillatory nature of the model dynamics was also evident in the autocorrelation function, which displayed a peak at 2.5-3 hr. that corresponded to the average oscillation period, as was also seen in the experimental data (**Fig. 2L**). Our model predicts that DAF-16/FOXO should display more robust oscillations, without exhibiting plateaus, when δ is increased relative to complete starvation, as evidenced also by more a pronounced peak in the autocorrelation (**Fig. 2A, L, Supplemental Fig. 3A**). We therefore aimed to experimentally identify low food conditions corresponding to such low, but not minimal values of δ. We examined rare cases where larvae hatched in presence of an additional unviable egg that subsequently disintegrated (see **Materials and Methods**). We found that the larvae fed on the unviable egg, leading to slow body growth indicative of limited food (**Supplemental Fig. 3B, C, E**). In agreement with model predictions, this was accompanied by highly regular DAF-16/FOXO oscillations without clear plateaus as long as the food source lasted (**Supplemental Fig. 3D**), as evidenced also by an increased peak in the autocorrelation (**Fig. 2L**).

Next, we examined transitions from the monostable cytoplasmic to the monostable nuclear regime (low γ, **Fig. 2A**). In this case simulated tracks show stochastic pulses (**Fig. 2G**), corresponding to our experimental observations of DAF-16 dynamics under osmotic stress (**Fig. 2I**). Indeed, the autocorrelation calculated for model dynamics showed constant decay, consistent with stochastic pulses rather than oscillations and in agreement with experimental data (**Fig. 2L**). An important aspect of DAF-16 dynamics under osmotic stress is that average

pulse duration increases with increasing stress magnitude (NaCl concentration) (13). Here, we simulate an increasing level of osmotic stress by further decreases in δ (**Fig. 2A**). Indeed, we observe isolated pulses, with the average duration of pulses increasing with higher stress (**Fig. 2G, I, K**).

We also explored the impact of changing the feedback strength γ. For transitions to parameters around the oscillatory regime, corresponding to starvation stress, we found that lowering γ changed the dynamics so that DAF-16/FOXO remained nuclear significantly longer, with only infrequent transitions to the cytoplasmic state (**Fig. 2D, F**). In the model, lower γ means that more ILPs are required to achieve the same level of kinase activation and hence can experimentally be reproduced in the *daf-2(e1368)* mutant, where the insulin receptor DAF-2 shows strongly reduced activation (59). Indeed, in *daf-2(e1368)* animals under starvation, we observe similar dynamics as in the model, with a strong shift to nuclear DAF-16/FOXO and rare periods of cytoplasmic localization (**Fig. 2E,F**). When we lowered γ for transitions around the parameter regime corresponding to osmotic stress, we found that this increased pulse duration (**Fig. 2H**, **K**). We then performed experiments with *daf-2(e1368)* mutants on 200 mM NaCl stress, and observed a significant lengthening of DAF-16/FOXO translocation pulses (**Fig. 2J**, **K**), in accordance with our model prediction.
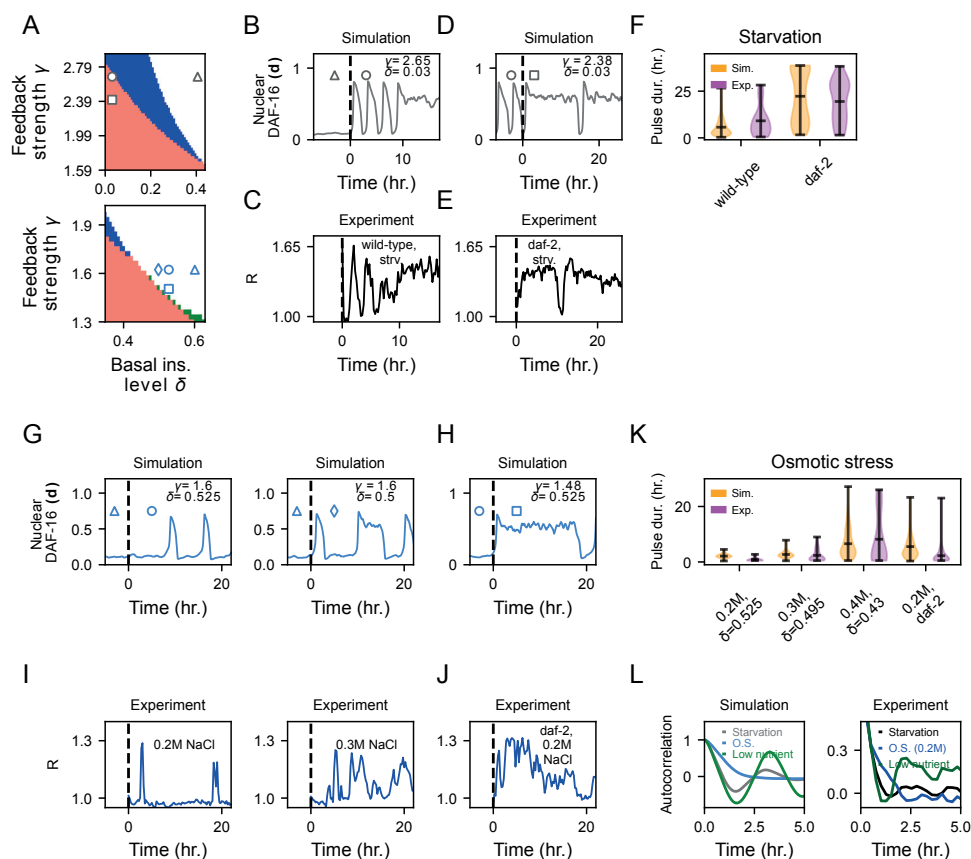
Figure 2 Transitions between dynamical regimes explains stress-dependent DAF-16/FOXO translocation dynamics. **A)** Zoomed in parts of the phase diagram for the deterministic model, with focus on the regimes corresponding to starvation-like (top) and osmotic stress-like dynamics (bottom) dynamics originate. Blue indicates oscillatory regime, white monostable cytoplasmic, red monostable nuclear, and green bistable. Grey symbols show the parameters used in the starvation simulations, while blue symbols indicate the parameters used for osmotic stress. **B)** Representative simulation tracks for γ=2.65, of the stochastic model, displaying starvation-like DAF-16 nuclear localization dynamics. Initially, the basal ILP level δ=0.4, in the monostable cytoplasmic regime corresponding to the absence of stress. For t<0, the value of δ is set sufficiently high to ensure a monostable nuclear DAF-16 state. At t=0, δ is lowered, corresponding to the onset of starvation, and DAF-16/FOXO alternates between pulses and prolonged periods of nuclear localization ("plateaus"). **C)** Same parameters as in B), but γ=2.38 to reproduce a mutant with reduced insulin receptor activation. Dynamics become overwhelmingly nuclear, with occasional excursions to the cytoplasm. **D)** Example track from a starvation experiment, corresponding to a single, wild-type individual. **E)** Example track from a starvation experiment, for an animal with the insulin receptor mutation *daf-2(e1368*) that reduces activity. **F)** Violin plots of individual pulse duration, comparison between simulation (orange, N=50 iterations) and experiment (magenta, N=14 and N=26 animals for wild-type and *daf-2(e1368)*). The model correctly reproduces the increase in pulse duration in the *daf-2(e1368)* mutant. Data in (D),(E) and (F) correspond to our previously published data (13). **G)** Representative simulation track for γ=1.6, displaying osmotic stress-like DAF-16 nuclear localization dynamics. At t=0, δ is decreased to represent onset of stress, with lower

values of δ corresponding to higher osmotic stress. **H)** Same parameters as in G) (left panel), but γ=1.48 to simulate reduced insulin receptor activity. **I)** Example experimental tracks for animals under low (left) and intermediate (right) osmotic stress, corresponding to 200 mM, and 300 mM NaCl, respectively. **J)** Example track from a 200 mM NaCl osmotic stress experiment, for a *daf-2(e1368)* mutant animal. **K)** Violin plots of individual pulse duration, comparison between simulation (N=50 iterations) and experiment (N=17, N=18, N=16, and N=15 animals for wild-type on 200, 300, 400 mM NaCl and *daf-2* (e1368) on 200 mM NaCl, resp.). Model correctly reproduces the increase in pulse duration when stress magnitude is increased, and when the insulin receptor is mutated. Wild-type data in I) and K) from our previous publication (13). **L)** Averaged autocorrelation of simulated and experimental DAF-16/FOXO nuclear localization tracks. Starvation leads to a peak at 2.5-3 hr., indicative of oscillatory translocation dynamics with this average period, both for experiments and simulations. This peak is more pronounced for the more robust oscillations seen for low nutrient conditions (δ=0.15 In the simulations), and is absent for osmotic shock, consistent with the more randomly timed pulsatile translocation dynamics seen for this stress.

Bistable DAF-16/FOXO localization for heat stress

While the model reproduced the experimentally observed DAF-16/FOXO dynamics specific to starvation and osmotic stress, none of the dynamical regimes directly reproduced the experimentally observed heat stress-specific dynamics of exhibiting only a single pulse lasting 2-4 hours (13), upon a simple change in the basal ILP level δ from non-stressed to stressed values. However, we found that the model could reproduce heat stress-like dynamics for more complex changes in δ. Specifically, we envisioned that heat stress corresponds to changes in δ close to the bistable regime ($\gamma = 0.6$). Here, for intermediate values of δ, DAF-16 nuclear localization shows bistability (**Fig. 1C, F, G, Fig. 3A**). However, instead of a simple change in δ upon entry into stress, as before, we assume that the change occurs in two steps. This is partly motivated by previous research which shows that the general heat stress response in *C. elegans* attenuates after 3-4 hours (60). Furthermore, when we exposed animals to repetitive 32°C pulses, during which DAF-16 typically reverts to cytoplasmic levels within 3-4 hours, we observed that animals consistently displayed robust DAF-16 localization after each subsequent heat pulse (**Supplemental Fig. 4**). Taken together, this suggests that the onset of heat stress is distinct from persistent heat stress, supporting our choice to partition the shift in δ into two parts.

Upon shift to heat stress temperature T, we shift from δ_U=2.4 corresponding to the unstressed condition of 20°C, to a lower, temperature-dependent, level δ_T. Second, after 2 hours, we shift to a higher, but still stressed level $\delta_{T,S}$, where it remains while heat stress persists (**Fig. 3B**):

$$\delta(t) = \begin{cases} \delta_U, & t \leq t_{HS} \\ \delta_T, & t_S > t > t_{HS} \\ \delta_{T,S} & t \geq t_S \end{cases}$$

For decreasing values of δ_T ($\delta_{32°C} < \delta_{31°C}$ chosen to represent dynamics at 31°C and 32°C heat stress), this yields a single pulse of nuclear DAf-16/FOXO, with amplitude higher for the

lower δ (**Fig. 3C**). Here, the increase in pulse amplitude for decreasing delta is determined by the upward curvature of the lower stable branch corresponding to low nuclear DAF-16/FOXO level (**Fig. 3A, B**), which in turn is determined by the parameters α, β, ζ and η (see **Supplemental Fig. 5**). The subsequent, steady state level of nuclear DAF-16/FOXO depends on the value of $\delta_{T,S}$, with $\delta_{32°C,S} < \delta_{31°C,S}$). This matches the experimental data for 31°C and 32°C, where we see an initial pulse, followed by a subsequent baseline of low, but persistent nuclear localization of DAF-16 (**Fig. 3D**).

A so far unexplained part of our experimental observations (13) is that for a 33°C heat shock we did not simply observe a single pulse with amplitude increased compared to 32°C, but rather persistent high levels of nuclear DAF-16/FOXO for entire duration of the experiments (>10 hours) (**Fig. 3D**). Our model, however, now provides an intuitive explanation. For further decrease in δ_T, as expected for stronger heat shock, the model enters the monostable nuclear regime, resulting in full nuclear localization of DAF-16/FOXO, and subsequently remains nuclear even when the model enters the bistable regime again once δ increase to the steady state level $\delta_{33°C,S}$ (**Fig. 3A-C**).

Our model thus indicates that the experimentally observed DAF-16/FOXO translocation dynamics upon exposure to heat stress reflects an underlying bistability in DAF-16/FOXO nuclear localization. Such a model crucially predicts that DAF-16/FOXO dynamics should be hysteretic, meaning that dynamics depend not only on the current value of δ, but also on how it changed in the past (**Fig. 3A**), reflecting the history of heat stress exposure. While shifting from 20°C to 31°C (δ_U to $\delta_{31°C}$) resulted in low DAF-16/FOXO nuclear localization both in the model and experiment (**Fig. 3C, D**), simulations predicted that shifting from 33°C to 31°C ($\delta_{33°C}$ to $\delta_{31°C}$), instead leads to prolonged periods of high nuclear DAF-16/FOXO, which ended by stochastic transitions to the state of cytoplasmic DAF-16/FOXO (**Fig. 3E, G**). To test this prediction, we performed new experiments, where larvae were subjected to 33°C for at least 4 hours, followed by a shift to constant 31°C. Strikingly, a substantial number of larvae had a persistently high DAF-16/FOXO nuclear level at 31°C, while others exhibited more rapid transitions to cytoplasmic DAF-16/FOXO (**Fig. 3F, G**), as predicted by the model. Finally, the bistable nature of DAF-16/FOXO nuclear localization was also apparent when measuring average levels of nuclear DAF-16/FOXO as function of temperature, both for upshifts from 20°C and downshifts from 33°C (**Fig. 3H**).
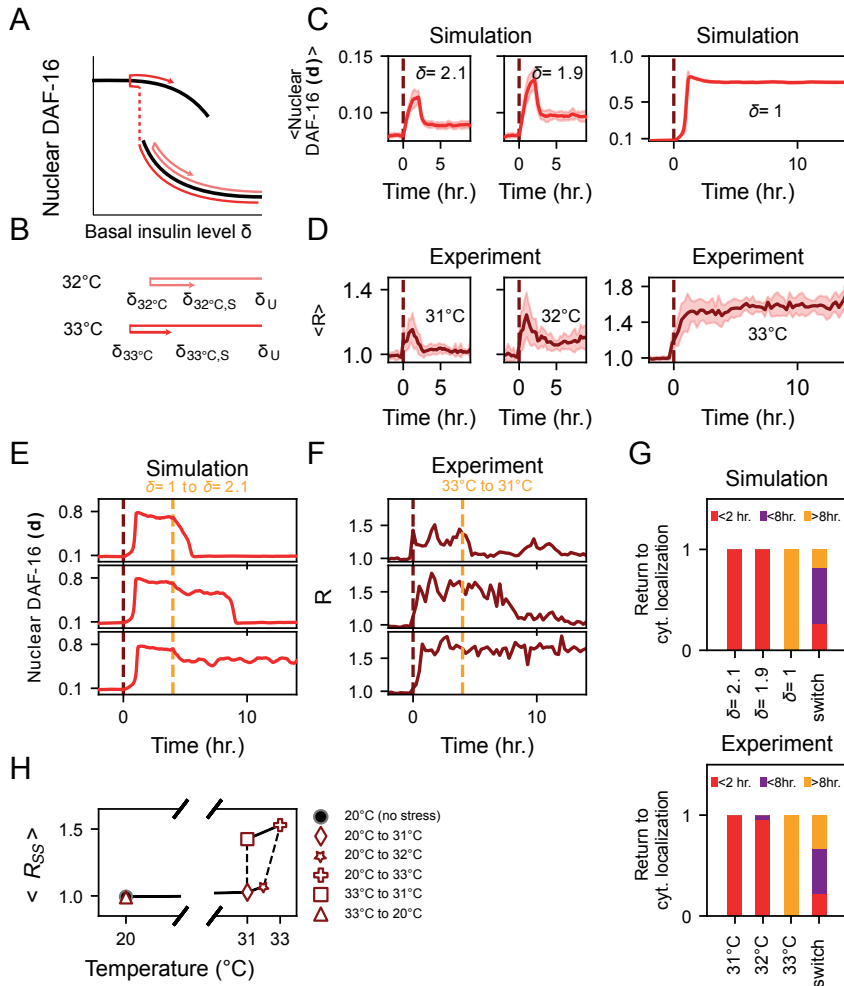
Figure 3 Bistable DAF-16/FOXO nuclear localization for heat stress. **A, B)** Cartoon diagram showing the proposed two-step adjustment of basal ILP level δ upon heat stress at temperature T. **C)** Average simulated nuclear DAF-16/FOXO levels for decreasing values of δ_T and $\delta_{T,S}$, corresponding to increasing heat shock (N=300 simulations). For δ_T<1.45, DAF-16/FOXO becomes constant nuclear, and remains nuclear for $\delta_{33°C}$=1, whereas for larger δ_T DAF-16/FOXO nuclear localization peaks before decreasing. Solid lines represent the mean value of nuclear DAF-16, while the shaded regions indicate standard deviation. **D)** Average experimental DAF-16/FOXO nuclear localization time traces for animals under 31°C, 32°C, and 33°C heat shock (N=20, 21 and 12 animals). **E)** Example simulation tracks of DAF-16/FOXO translocation dynamics for a downshift in heat stress from $\delta_{33°C}$ to $\delta_{31°C}$. **F)** Example experimental DAF-16/FOXO nuclear localization tracks for animals first subjected to 33°C heat stress for 4 hours, then shifted to 31°C heat stress. **G)** Bar plots of durations before DAF-16 returns to the cytoplasm, for simulated and experimental tracks, showing good correspondence between simulations and experiment. For 300 simulated tracks (top) and, from left to right, N=20, N=21, N=12, and N=12 animals (bottom). **H)** Average value of nuclear DAF-16 nuclear/cytoplasmic ratio R for N=20, N=21, and N=12 animals, for animals under 31°C, 32°C, and 33°C to 31°C, respectively, versus temperature (stress level). In all heat stress cases, the level of R was taken 4

hours after switching to the specified temperature, i.e. the "steady state" (SS) level of *R*. At 31°C, the value of nuclear/cytoplasmic DAF-16::GFP is bistable.

DAF-16/FOXO pulse synchronization by ILP exchange between cells

So far, we only considered dynamics for a single cell. However, for $\phi > 0$, the feedback loop relies, at least in part, on secretion of ILPs in the extracellular environment. ILPs secreted by one cell can in principle activate insulin receptors of another cell, suggesting a mechanism that couples the IIS state and, hence, DAF-16/FOXO localization between cells (**Fig. 4A**), potentially leading to synchronization. When we simulated N=20 cells, assuming a fully extracellular feedback loop ($\phi = 1$), we indeed found strong synchronization of DAF-16/FOXO pulse dynamics, both for the starvation (stochastic oscillations) and osmotic stress (random pulses) regimes (**Fig. 4B,C**).

We explored the impact on pulse synchronization of the two key parameters governing ILP exchange, namely the ILP coupling parameter ϕ, but also the ILP turnover ϵ. To simplify analysis, we focused on γ and δ in the oscillatory regime, rather than for starvation- or osmotic shock-like parameters. We systematically varied ϕ and ϵ, for cells starting with randomized initial conditions and quantified synchronization between cells using the Pearson correlation coefficient (PCC) (61). Here, low PCC indicates poor synchrony, while a PCC=1 indicates full synchrony (see **Materials and Methods**). As changing ϕ and ϵ affects the frequency of pulsing, even for the one-cell model, we adjusted the duration of each simulation so that the same number of oscillations occurred. Varying these parameters did not change the types of dynamical regimes (monostable states, bistability, and oscillations) of the system (**Supplemental Fig. 2**). For $\phi = 0$ there is no synchronization by definition, as evidenced by the low value of PCC≈0.4 (**Fig. 4D**) and the visibly uncorrelated dynamics between cells (**Fig. 4E**). Within stochastic simulations, increasing ϕ beyond a threshold value ($\phi \approx 0.2$) results in robust synchronization (PCC>0.7), after which increasing ϕ does not significantly improve synchronization (**Fig. 4D**). Full synchrony is observed after an initial period of asynchrony, due to the chosen random initial conditions (**Fig. 4F,G**). The number of cells does not affect synchrony (**Supplemental Fig. 6A-C**). Synchrony is hampered when the value of the cell-intrinsic noise parameters ($\sigma_{d,k}$) are large compared to the ILP noise (σ_p) (**Supplemental Fig. 6D-F**). In particular, for more stochastic dynamics, such as in the "starvation-like" and "osmotic stress-like" parameter regimes, the standard noise parameter values resulted in frequent loss of synchrony, which was circumvented by reducing the internal noise (to $\sigma_{d,k}$=0.001) and increasing the ILP noise (to σ_p=0.2) (**Fig. 4B, C, Supplemental Fig. 6I**). For all values of ϵ, the level of synchronization declines again for high ϕ values. For high ϕ and ϵ, this reduced synchrony was due to cells ceasing oscillations and becoming locked in opposing high and low

DAF-16/FOXO states, leading to decreased PCC (**Fig. 4D, H, I**). This occurred at a lower value for ϕ when ϵ was high, meaning good synchrony for a higher ILP turnover was only possible for intermediate values of ϕ (**Fig. 4D, J**). This resembled the phenomenon of "unstable synchronization" described previously for coupled hysteresis-based oscillators, where synchrony becomes unstable for large coupling strengths (62). Finally, overall synchronization is robust even when all parameter values (except the noise parameters) are randomly varied by 5% around their original value between cells (**Supplemental Fig. 6G, H**), indicating that synchrony occurs even when cells have different intrinsic IIS dynamics.
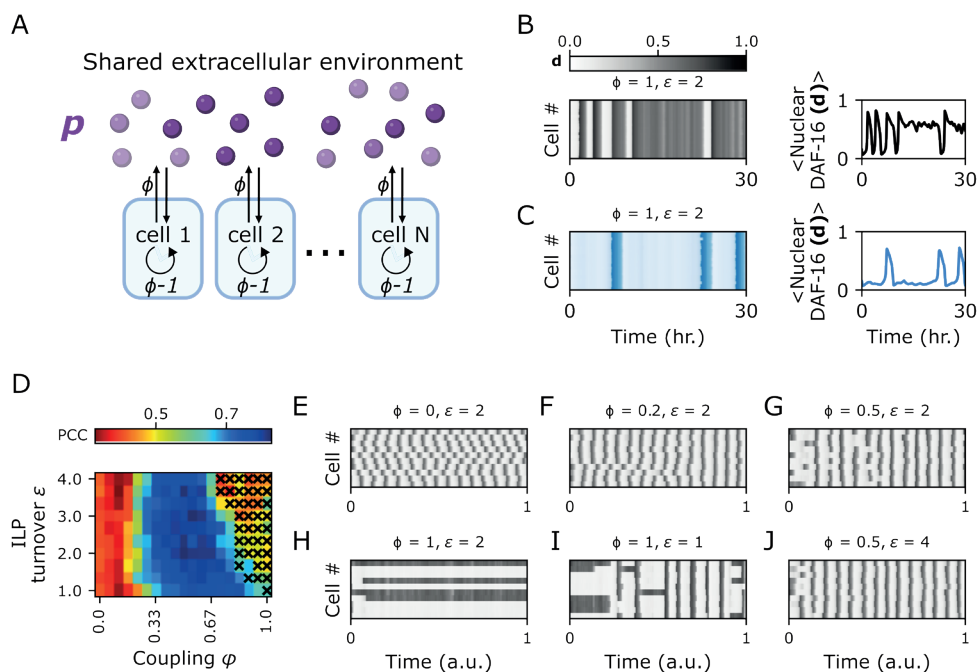
Figure 4. DAF-16/FOXO pulse synchronization by ILP exchange between cells. **A)** Schematic showing the interaction between ILP-secreting cells. ILP exchange between cells occurs when the DAF-16/FOXO negative feedback is fully externally ($\phi = 1$) or a combination of internal and external ($0 < \phi < 1$). **B, C)** Simulated example tracks for 20 coupled cells ($\phi = 1$), for the case of starvation-like (B) and osmotic stress-like (C) parameters. The panels on the right show the corresponding average levels of DAF-16/FOXO nuclear localization over time. Noise parameters are $\sigma_k = 0.001$, $\sigma_d = 0.001$, and $\sigma_p = 0.2$ **D)** Heatmap showing the level of synchrony (Pearson correlation coefficient) as the coupling parameter ϕ and ILP turnover ϵ are varied. Each value represents the average of 10 iterations, ran for an average of 20 oscillations, for 20 cells. For high values of ϕ and ϵ, the majority of iterations (>60%) resulted in cells locking in opposite nuclear localization states for more than 20% of total simulation time, indicated by crosses. Noise parameters are $\sigma_k = 0.02$, $\sigma_d = 0.001$, and $\sigma_p = 0.1$ **E-J)** Example tracks corresponding to the heatmap in C), for 20 cells, and varying values of ϕ and ϵ.

Experimental test of the collective synchronization model

A possible model to explain the body-wide synchronization of DAF-16/FOXO translocation pulses is that it merely reflects a passive read-out of ILPs excreted with some inherent dynamics by an independent external source, for example neurons (**Fig. 5A**). This matches the current view of FOXO translocation controlled by ILP levels and IIS activity through a largely linear pathway (21), without extracellular feedback loops. Here, we propose an alternative model where synchronized DAF-16/FOXO pulses originate collectively, without an external, time-varying ILP source, resulting from an IIS-mediated feedback loop that controls external ILP dynamics (**Fig. 5B**). We reasoned that these models can be differentiated experimentally by studying DAF-16/FOXO translocation dynamics in mosaic IIS mutants, where DAF-16/FOXO is constitutively nuclear in targeted tissues, independently from external ILP levels (**Fig. 5A, B**). For the "passive read-out" model, DAF-16/FOXO pulse dynamics would be unchanged in the remaining wild-type cells, as it depends only on externally controlled ILP levels. In contrast, for the "collective synchronization" model, mutant cells that, for example, have constitutive low IIS would continuously excrete ILPs, thereby perturbing IIS and DAF-16/FOXO translocation dynamics in the remaining wild-type cells. To systematically test the impact of mosaic IIS mutations, we first performed simulations.

To better understand the impact on the collective synchronization model, we first simulated IIS pathway mutations for the oscillatory regime (**Fig. 4D**). Specifically, we simulated *daf-2* reduction-of-function as we did previously, by decreasing γ such that DAF-16/FOXO becomes monostable nuclear. We performed simulations for various values of ϕ, and again normalized the duration of the simulation between them. We then varied the fraction of cells carrying the simulated mutation, and quantified the average pulse frequency for the remaining wild-type cells. For small fractions of mutated cells, or when $\phi=0$, we find that wild-type cells continue to exhibit synchronized oscillations (**Fig. 5C, D**). However, when $\phi>0$, the frequency decreases with increasing fraction of mutated cells (**Fig. 5C, E**). For high fractions of mutated cells, oscillations cease entirely (**Fig. 5C**). The drop-off in frequency and cessation of pulses occurs earlier for higher values of ϕ (**Fig. 5C, Supplemental Fig. 7A-C**). Moreover, increasing the fraction of mutated cells lead also caused a loss of synchronization, as shown by a lower PCC, with some cells remaining mostly in the monostable cytoplasmic state, while other cells displayed relatively desynchronized, stochastically timed pulses (**Fig. 5D, E**). Finally, we performed simulations that show this effect also occurs for starvation-like parameters (**Fig. 5G**).

We then tested these predictions. To perturb IIS in a subset of cells, we made use of the auxin-inducible degron (AID) system (63, 64). We used *daf-2::AID::mNG* animals where an AID tag

is attached to *daf-2* (65). Auxin-induced degradation requires TIR1, ensuring that DAF-2 degradation only occurs in the tissue in which TIR1 is expressed. First, we used a *rgef-1::TIR1* strain (65) to degrade DAF-2 specifically in the nervous system, causing nuclear localization of DAF-16/FOXO only in the neurons upon exposure to auxin (**Fig. 5F**), as expected. Under non-stressed conditions, DAF-16/FOXO remained cytoplasmic in all non-neuron cells, including the intestine (data not shown), while under starvation animals exhibited DAF-16/FOXO translocation pulses in the non-neuron cells. However, when we measured DAF-16/FOXO nuclear localization in the intestine, we found that pulses occurred at much reduced frequency compared to wild-type animals (**Fig. 5F, G, H, I**), in agreement with our simulations.

The collective synchronization model predicted that, as all cells contribute to synchronize DAF-16/FOXO translocation dynamics, similar phenotypes should be seen regardless of the tissue in which DAF-2 is depleted. We tested this using a *ges-1p::TIR1* strain (65), where DAF-2 is degraded specifically in the intestine. Indeed, upon auxin exposure DAF-16::GFP localized to the intestinal nuclei for the duration of the experiment (**Fig. 5J**). We found that this perturbed DAF-16/FOXO translocation dynamics in other cells, but in a more complex manner than seen for IIS perturbation in neurons. First, we found that many cells in the head (likely neurons and hypodermis), and in the mid-body hypodermis displayed constant DAF-16/FOXO nuclear localization, sometimes after exhibiting a single pulse (23/23 animals, **Fig. 5K, Supplemental Fig. 7D**). Moreover, this was typically accompanied by cells in the tail (likely hypodermal) that displayed persistent pulsing, representing a striking loss of synchrony for at least 30 minutes between different parts of the body (19/23 animals, **Fig. 5K, L**). In addition, loss of synchronization was also observed for cells within close proximity: for example, we found head neurons and mid-body hypodermal cells that show DAF-16/FOXO nuclear localization distinct from that of neighboring hypodermal cells (**Supplemental Fig. 7D, E**). Overall, such loss of synchrony was not observed for wild-type animals (0/14 animals). We further supported these observations by manually quantifying DAF-16/FOXO dynamics in individual tail cells. Whereas these cells showed synchronized dynamics in wild-type animals, we found a loss of synchrony in *ges-1p:TIR1;daf-2::AID* animals (**Fig. 5L**). Overall, this loss of synchrony following intestine-specific IIS perturbation reproduces our model predictions and furthermore reveals that different tissues contribute to body-wide DAF-16/FOXO dynamics in distinct manner.

Taken together, these results exclude the passive read-out model of synchronized DAF-16/FOXO dynamics, as it shows that DAF-16/FOXO translocation pulses in one tissue are dependent on IIS in other tissues. Instead, the observed change in pulse frequency and loss of synchrony upon perturbing IIS in subsets of cells strongly favor the collective synchronization model.
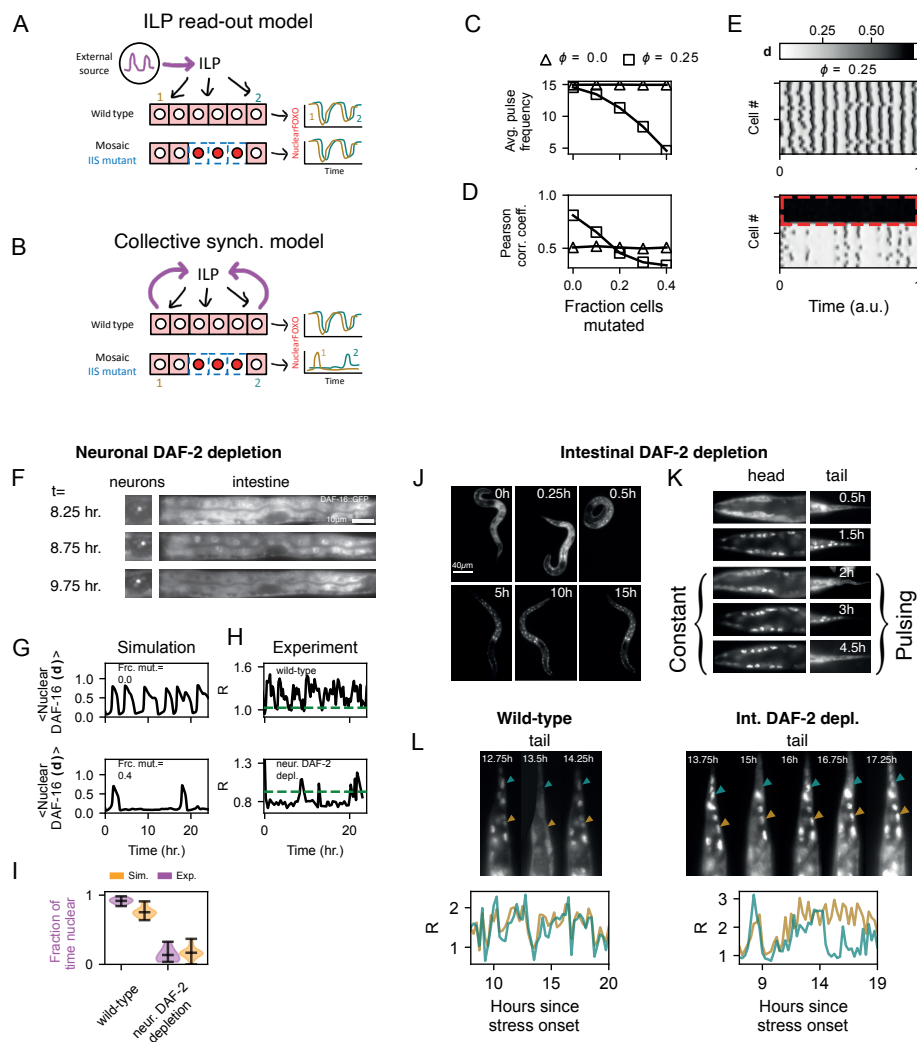
Figure 5. Changes in DAF-16/FOXO dynamics and synchrony loss upon tissue-specific IIS perturbation. **A, B)** Cartoon showing two possible mechanisms for body-wide synchronization of DAF-16/FOXO (red) dynamics. These mechanisms can be differentiated by IIS mosaic mutants, where IIS is perturbed only in a subset of cells. **C)** Average pulse duration and **D)** Pearson correlation coefficient (PCC) for stochastic simulations, as function of the fraction of cells with strongly reduced IIS activity (γ=1). For $\phi > 0$, increasing the number of IIS-perturbed cells decreases the average pulse frequency and reduces synchrony (lower PCC). Simulation for N=20 cells and in oscillatory regime (γ=4, δ=0.03). **E)** Example tracks corresponding to the simulations in C) and D), with no (top) or 40% (bottom) of cells with perturbed IIS. Red line indicates cells with perturbed IIS and, hence, constitutively nuclear DAF-16/FOXO, while in the other cells translocation dynamics has reduced frequency and synchrony. **F)** Fluorescent microscopy images of an *rgef-1p::tir1;daf-2::AID* animal (neuronal *daf-2* degradation) showing constant nuclear DAF-16::GFP in neurons (left) and a DAF-16::GFP translocation pulse in the intestine (right). **G)** Simulated example tracks (N=20 cells) showing a decrease in pulse frequency of DAF-16/FOXO translocation pulses when

40% of cells have perturbed IIS, for starvation-like parameters (γ=2.65,δ=0.03). **H)** Example tracks from experiments, showing DAF-16::GFP nuclear localization dynamics in individual animals. Top: wild-type animal under starvation. Bottom: *rgef-1p::tir1;daf-2::AID* animals (neuronal *daf-2* degradation) under starvation and exposed to 1 mM auxin. **I)** Comparison of DAF-16/FOXO dynamics for simulations in F) and experiments in G). Compared to wild-type animals (N=14), *rgef-1p::tir1;daf-2::AID* animals (N=7) showed reduced fraction of time with DAF-16/FOXO nuclear, consistent with the model prediction for IIS mosaic mutants. Simulations are for 30 iterations of the model, with 30 hours simulation time per iteration. **J), K)** Fluorescence microscopy images of *ges-1p::tir1;daf-2::AID* animals (intestinal *daf-2* degradation), under starvation and exposed to 1 mM auxin. DAF-16::GFP was constantly nuclear in intestinal cells (J), but exhibited nuclear translocation dynamics that was desynchronized between the head and the tail (K). **L)** DAF-16/FOXO nuclear localization quantified in two tail cells. In wild-type animals these cells exhibit synchronized dynamics, while in *ges-1p::tir1;daf-2::AID* animals (intestinal *daf-2* degradation), the same show loss of synchrony in nuclear localization.

Discussion

We have presented a stochastic differential equation model that replicates and predicts the stress-dependent dynamics of DAF-16 pulses and their synchronization. While DAF-16/FOXO dynamics have previously been modeled, these studies focused at most on an initial pulse of activity (66–68), or very long timescales (69). Our model, however, represents the first computational study of DAF-16/FOXO persistent pulsing/oscillations, and their synchronization, offering a novel perspective on synchronized pulsatile dynamics in living organisms in general. Given the critical role of cell state synchronization in maintaining animal health, particularly during stress and growth arrest, understanding the underlying mechanisms is of broad importance (1). In our model, stress-induced DAF-16/FOXO pulses emerge through a relaxation oscillator mechanism, that is driven by an IIS-dependent feedback loop which we propose here, and with body-wide synchrony arising through exchange of ILPs between cells. We validate key predictions of this model experimentally, by showing changed dynamics and loss of synchrony of DAF-16/FOXO translocation in mosaic IIS mutants, where IIS is perturbed only in specific tissues. These findings hold significance as insulin signaling is recognized to regulate body-wide growth arrest in model organisms like fruit flies and mice, as well as *C. elegans* itself, a process where coordination between cells is vital for maintaining proportionality in developing animals (6, 7, 13).

Our model suggests that the striking stress type- and magnitude-specificity of DAF-16/FOXO dynamics, as well as the effect of insulin receptor mutations, can be explained by the tuning of the system close to transitions between different dynamical regimes, i.e. monostable, bistable or oscillatory dynamics. Combined with stochastic noise, this induces randomly timed, rapid transitions in DAF-16/FOXO localization dynamics. This could potentially explain the significant

inter-individual variability in stress-induced DAF-16/FOXO dynamics that has been previously reported (13, 70). In addition, the model made a non-trivial prediction about DAF-16/FOXO dynamics: under heat stress, DAF-16/FOXO nuclear localization should display hysteresis, meaning that the nuclear localization state of DAF-16/FOXO depends on its past localization state. Indeed, we found that DAF-16/FOXO at 31°C was cytoplasmic when the temperature was upshifted from 20°C, but instead was predominantly nuclear at 31°C when shifting the temperature down from 33°C. Here, the experiments showed that there was significant variability between individuals in the timing of when DAF-16/FOXO returned to the cytoplasm. Previously, we found that variability in DAF-16 dynamics at least correlates with, and likely causes a variability in growth rate (13). Some organisms display such variability in what is called "bet-hedging", where switching between phenotypic states serves as a way to ensure some individuals in a given population always survive adverse conditions (71). Taken together, this suggests that the combination of proximity to transitions between dynamical regimes and stochasticity in insulin signaling may not be merely accidental, but may have evolved in order to allow bet hedging in response to stress. As animals cannot know the duration of a stress they enter, it may be beneficial to alternate states of strong and weak stress response stochastically, with some animals "betting" on a long-lasting stress, corresponding to frequent pulses/constant nuclear DAF-16 and slow growth/growth arrest (but a stronger activation of stress response genes), and others on a short-lasting stress, corresponding to isolated pulses/constant cytoplasmic DAF-16 and sustained growth (but a lowered chance of survival if a stress persists). Our model thus offers an insight into the mechanism that facilitates this possible bet hedging behavior in insulin signaling.

Previous research has highlighted the presence of FOXO-to-FOXO signaling, wherein the nuclear localization of DAF-16/FOXO induces nuclear DAF-16/FOXO localization in other tissues through ILPs (28). However, the real-time dynamics of this process have so far remained unexplored. Our computational and experimental investigation offers novel insights into this phenomenon from the perspective of protein dynamics at high temporal resolution. Specifically, we computationally demonstrate how insulins could facilitate dynamic cell-to-cell synchronization of DAF-16/FOXO pulses by being part of the negative feedback loop that generates these pulses. Although we propose ILPs serve as the communicator molecules in our model, it is still possible that other molecules play this role instead, or in conjunction with ILPs. For example, recent experiments have shown that tyramine, a neurohormone released during the *C. elegans* flight response, positively regulates the release of the ILP INS-3 in the intestine (41, 72). The question then is, to what extent is cell-cell coupling mediated by ILPs versus other factors, such as neurohormones. An interesting experiment would be to measure DAF-16/FOXO dynamics in mosaic mutants lacking functional ASNA-1, which positively

regulates insulin secretion in *C. elegans* and mammalian cells (73), in specific tissues. If cell-to-cell pulse synchronization is facilitated primarily through ILPs, we should expect that when ASNA-1 is depleted in, for example, the intestine, it would cause changes in DAF-16/FOXO dynamics and synchronization, similar to our experiments for mosaic *daf-2* mutants. Finally, other studies have reported FOXO-induced secretion of insulins from intestinal epithelial cells in rats (74, 75). Recent studies, including ours, have highlighted the presence of FOXO translocation pulses in mammalian cells, including humans (13, 14). Given these parallels, we hypothesize that the pulse generation and synchronization mechanisms elucidated in *C. elegans* may similarly operate in mammalian tissues. Our model could be used to predict and understand synchronization behavior of FOXO pulses in human cells, for example by studying FOXO dynamics in human intestinal organoids.

Our results support the idea of collective synchronization over an "ILP read out" model, suggesting that there is a DAF-16-dependent pool of ILPs (or some other messenger molecule) that facilitate the negative feedback/pulse generation. This model shows that collective, ILP-mediated pulsing can lead to good synchrony in DAF-16 pulsing between cells. A common occurrence that caused poor synchrony in the model was what we call "locking", where cells lock into opposite, non-oscillating states. This was especially common for more stochastic dynamics, such as for starvation and osmotic stress. We found that two factors helped reduce this occurrence. Firstly, an intermediate value of ϕ (**Fig. 4**). This is an argument that supports the idea that ϕ in reality is also smaller than 1, i.e. that there are both cell-internal, and external feedback loops driving the generation of DAF-16/FOXO pulses. Indeed, experiments from previous work show that FOXO pulses also occur in isolated mammalian cells, suggesting that cells can generate FOXO pulses without the context of other cells (13, 14). Secondly, the noise term for the ILPs being large relative to internal noise terms η_k and η_d helps reduce the occurrence of locking. This might suggest that in reality, most of the stochasticity in DAF-16/FOXO pulse dynamics comes from fluctuations in the ILP level, while cell-autonomous dynamics are relatively deterministic.

We have aimed to present a minimal model of DAF-16/FOXO pulses, and therefore greatly simplified the underlying complexity of the IIS. For example, we only included agonist ILPs in our model. In reality, some of the 40 *C. elegans* ILPs act as antagonists, meaning they positively regulate DAF-16 nuclear localization (27, 51). The model could be reformulated by replacing the DAF-16-dependent upregulation of agonist ILPs with DAF-16-dependent downregulation of antagonist ILPs as the pulse-generating negative feedback loop. We suspect that this would not qualitatively change the outcome of our model. A more complex addition would be to include both upregulation and downregulation, of both agonists and antagonists.

Our model predicts that when DAF-16/FOXO is constitutively nuclear in enough cells, the remaining cells will mostly exhibit cytoplasmic DAF-16/FOXO during starvation (**Fig. 5**). When we observed starved animals with neuronal DAF-2 degradation, and therefore permanently nuclear DAF-16 in neurons, we indeed observed a lowered frequency of pulsing in the remainder of the animals' cells (**Fig. 5**). However, in starved animals with DAF-2 degradation only in the intestine, other cells, particularly in the hypodermis and head, eventually showed mostly nuclear localization, in principle contradicting our model's prediction. Specifically, some cells locked into a nuclear state while others had decoupled pulses, for example in the tail. What is the cause of this discrepancy? As noted, we only included negative feedback through agonistic ILPs in the model for simplicity. Hence, forced nuclear localization in a subset of cells in the model drives the remaining wild-type cells to a monostable cytoplasmic state, but still close to a transition in dynamics, allowing occasional, stochastic, less synchronized pulses in some of those cells. We argue that in essence we see the same type of qualitative behavior in the intestinal DAF-2 degradation experiment: some (non-intestinal) cells show permanently nuclear DAF-16/FOXO (e.g. in the head and hypodermis, **Fig. 5K, Supplemental Fig. 7D**), but others decouple and occasionally pulse (e.g. in the tail, Fig. 5). This would be consistent with a model where the majority of the DAF-16-induced ILPs in the intestine are antagonistic in nature. Notably, some cells are more likely to assume the monostable nuclear state, such as those in the head and hypodermis, and some cells in the tail (**Fig. 5L**, **Supplemental Fig. 7D, E**). Biologically, it is plausible that the concentration of components of the IIS, such as DAF-2, vary from cell type to cell type, and that, in terms of our model, some are closer to parameter values corresponding to a transition between dynamical regimes (see, for example, **Supplemental Fig. 6H**). In short, our model qualitatively predicts the observed behavior, but needs modification to incorporate positive feedback mechanisms for accuracy. These results also shed new light on the brain-gut connection, which is being increasingly studied in *C. elegans* (41, 72), but remains poorly understood. Here, we demonstrate that the insulin signaling state in the neurons or intestine directly affects the dynamics of insulin signaling in the other tissue.

Another question is which cells are part of the "ILP pool". In our model we have assumed that all cells of the animal contribute to this pool. But it is also possible that in reality only a subset of cells, for example only the neurons and intestine, form this ILP pool, and the rest of the cells read out their effective/mean DAF-16/FOXO localization state. In effect, this would be a combination of the ILP read out and collective synchronization models. As we aimed for simplicity, we did not attempt to distinguish these complex possibilities in the model, but instead focused on excluding the case where it is only a simple ILP read out model. It's possible to

further explore this by systematically depleting DAF-2 in other tissues than neurons and the intestine.

Our results raise the general question whether other stress response signaling pathways are also synchronized *in vivo*. Oscillations of NF-κB do not generally appear synchronized, but can be entrained by a periodic stimulus, leading to synchronized pulses in cells in a cell culture (76–78). P53 pulses likewise generally appear asynchronous (12, 79, 80), but can also be synchronized through entrainment by periodically delivered double strand breaks (DSBs) (81). In both cases, therefore, these pulses at least appear to have the *ability* to synchronize, without a clear reason as to why. In both cases, these pathways are generally studied *in vitro* in cell cultures, therefore missing the context of a living animal. Or they are studied in fixed samples, missing a clear dynamic view. Taken together, this begs the question whether P53 and NF-κB pulses might actually be synchronized among cells *in vivo* . Our model can offer a starting point for investigating how synchronization could work in other stress response pathways, for example by generating hypotheses that can be tested in cell cultures. This could lead to a deeper understanding of stress signaling dynamics across different biological contexts.

Insulin signaling plays a key role in cancer, and DAF-16/FOXO is a promising target for chemotherapeutic drugs (5, 82–84). As the function of DAF-16/FOXO depends on its dynamic localization to the nucleus, having a quantitative understanding of the effects of drugs on DAF-16/FOXO dynamics could help increase their effectiveness. Furthermore, the response of cells to chemotherapeutic agents can be highly stochastic (85). Therefore, our model, which offers insights into the mechanism behind the stochastic dynamics of DAF-16, could be used to better understand the effects of chemotherapeutic agents on DAF-16/FOXO function. It would be interesting to measure the effect of common chemotherapeutic drugs at varying concentrations on DAF-16/FOXO dynamics and determine what kind of dynamical transitions they elicit.

4

Author contributions to the chapter

B.D. and J.v.Z. designed research. B.D. performed experiments and modeling. B.D. wrote the text. J.v.Z. reviewed and edited the text. J.v.Z. supervised the study.

Materials and methods

Model simulations and analysis of simulated tracks

The set of coupled differential equations were numerically solved using the Euler-Maruyama method in python, using custom written software (86).

The different dynamical regimes presented in **Fig. 1**, were classified as follows. We detected peaks in the deterministic simulations using the scipy signal package, and classified tracks with two or more peaks as oscillatory. Amplitude was defined as the maximum value of nuclear DAF-16 in the second half of the simulated track, in order to exclude values before a steady state is reached. Bistability was assessed by running each simulation twice, for different initial conditions, namely $d_0, k_0, p_0 = [0,1,1]$ and $d_0, k_0, p_0 = [1,0,0]$, and measuring the value of d at the end of the simulation. Where the simulated track was non-oscillatory, and not bistable, it was classified as either monostable high ($d_{end} > 0.2$) or monostable low $d_{end} \leq 0.2$. At the end of the simulation, we manually checked a number of parameter combinations to confirm that this procedure gave accurate results.

Analyzing synchrony in stochastic simulations

Measuring synchrony

Because the timing and duration of pulses in the stochastic simulations varies randomly, we used a statistical measure to quantify the degree of synchrony. We calculated the Pearson correlation coefficient for each possible pair of cells (without repletion) for each iteration of the stochastic simulation. We then took the average value for all possible combinations, for a given iteration. The presented values (PCC) are the average value for the total number of iterations (e.g. 10 iterations). A PCC of 1 means that there is perfect positive correlation, while a value of -1 corresponds to perfect anti-correlation, and 0 implies no correlation.

Normalization

Varying ϕ within the range of 0 to 1 introduces changes to the structure of the feedback loop, while variations in ϵ influence the time scale of the external feedback loop. Consequently, the

dynamics of a singular cell are contingent upon the values of these two parameters. This inherent dependence implies that direct comparisons cannot be drawn from simulations where ϕ and ϵ are systematically altered. To correct for this, we implement a normalization procedure by computing the frequency of the deterministic simulation for each unique parameter combination. Then, we adjust the time vector in subsequent simulations, thereby ensuring a consistent and normalized basis for the comparison of dynamic trajectories.

Detecting locking cells

During stochastic simulations with coupled cells ($\phi > 0$), cells sometimes assumed opposite, non-oscillatory nuclear DAF-16/FOXO states, which we dubbed "locking". This could occur at random times and cells could also "unlock", resuming synchronized pulses. Because of this, we used a heuristic method to automatically detect parameter combinations where locking occurred significantly more often than usual. For each iteration of a simulation for N cells, we calculated the fraction of time where the standard deviation between the cells exceeded 0.2. If this fraction exceeded 20% of the simulation time, it was defined as "locking". When 60% or more of the iterations were defined as locking for a given parameter combination, we placed a cross in the synchronization heatmaps to indicate high likelihood of locking.

Timelapse microscopy

Microchamber fabrication

Microfabricated arrays of chambers were made from a master mold. Master molds were created using standard soft-lithography techniques. Briefly, SU-8 2025 epoxy resin (MicroChem) was first spin-coated on a silicon wafer to form a 20 μm layer. The SU-8 layer was exposed with ultraviolet-light through a foil mask (SELBA S.A.) containing the micropattern. To create polyacrylamide microchamber arrays from the master mold, a 10% dilution of 29:1 acrylamide/bis-acrylamide was mixed with 0.1% ammonium persulfate (Sigma) and 0.01% TEMED (Sigma) as polymerization initiators. The resulting aqueous solution was then poured in a cavity placed on top of the micropatterned silicon wafer. The cavity was closed with a silanized coverslip and sealed by mechanical clamping, allowing the solution to polymerize for 2 h. To remove the toxic unpolymerized acrylamide monomers, the resulting polyacrylamide microchamber arrays were washed at least three times for at least 3 h each in distilled water. Fewer or shorter washing steps often resulted in developmental arrest. Microchamber arrays could be stored in distilled water for ~15 days. Single microchamber arrays were placed in M9 buffer for 4 h directly before time-lapse imaging.

Sample preparation

To prepare the sample, a glass spacer with the same height as the polyacrylamide membrane was attached to a 76 × 26 × 1 mm microscope slide using high vacuum grease (Dow Corning). A single microchamber array was positioned with tweezers on the microscope slide, with the openings of the microchambers facing up. Excess liquid was removed with a tissue. With a pipette, drops of M9 buffer (~40 μL in total) were placed on the side and on the surface of the microchamber array, while preventing the liquid from filling the chambers. For all experiments except starvation stress, under a dissection microscope, a drop of bacterial suspension containing a single late-stage embryo was transferred from a NGM agar plate seeded with OP50 bacteria into a microchamber, using an eyelash attached to a Pasteur pipette. To facilitate the release of the bacteria and embryo into the chamber, the eyelash was dipped briefly into the M9 drop before touching the microchamber. Once the egg was transferred, more bacterial suspension was added to the microchamber using the eyelash, until completely filled. For osmotic stress experiments, hydrogels were stored in 200, 300 or 400 mM NaCl solutions for at least one week prior to the experiment. For starvation experiments, eggs were isolated by bleaching to remove the bacteria and placed one by one inside different microchambers filled with liquid M9 media. For each experiment, ~10–20 chambers were loaded. Subsequently, tissue paper was used to remove all excess M9 buffer. Finally, a 25 × 75 mm #1 coverslip was lowered on the chambers to seal the sample, slow enough to avoid forming large air bubbles. In rare cases, two eggs ended up in a chamber instead of one. In cases where both eggs hatched, the chamber was not imaged (as it's not possible to distinguish the animals), and in cases where one egg hatched and the other disintegrated, the data was only exclusively used for the "low nutrient" analysis. The sample was placed on a custom fabricated holder and clamped to seal the chambers and avoid liquid evaporation during the duration of the experiment. Microchamber dimensions were 190 x 190 x 10 μm for heat stress and osmotic stress experiments, while 190 x 190 x 6 μm were used for starvation experiments.

Time-lapse microscopy

We performed time-lapse imaging on a Nikon Ti-E inverted microscope. Using a large chip camera (Hamamatsu sCMOS Orca v2), it was possible to fit single microchambers in the field of view of the camera while using a 60 x magnification objective (Nikon CFI Plan Fluor 60 x , NA=0.5-1.25, oil immersion). Transmission imaging was performed using a red LED (CoolLED pE-100 615 nm), while fluorescence images were acquired using a 488 nm laser (Coherent OBIS LS 488-100) and a 561 nm laser (Coherent OBIS LS 561-100). The laser beam was expanded from 0.7 to 36 mm through a telescope composed of two achromatic

lenses of 10 and 500 mm focal lengths (Thorlabs AC080-010-A-ML and AC508-500-A). The expanded beam was then aligned through additional dielectric mirrors (Thorlab BB2-E02) to enter the back aperture of the microscope. A tube lens (300 mm focal length, Thorlabs AC508-300-A) was used to focus the beam in the back focal plane of the objective. For fluorescence microscopy, we used a dual band filter set (Chroma, 59904-ET). An XY-motorized stage (Micro Drive, Mad City Labs) was used to move between chambers, while a piezo Z-stage (Nano Drive 85, Mad City Labs) was used to move the sample in the Z direction. To optimize acquisition speed, we synchronized the camera, laser illumination and stage movement as follows: to operate the rolling-shutter camera in the global exposure mode, the laser beam was switched on (rise time <3 µs) once all the lines on the camera chip were active and switched off once the camera started reading out the chip. In order to rapidly acquire Z-stacks, we synchronized the piezo Z-stage and the camera, so that the stage moved to the new Z position during the 10 ms that the camera read out the chip to its internal memory. The microscope and all its components were controlled with custom software implemented using a National Instruments card (PCIe-6323) installed on a computer with a solid-state drive (Kingston V300-120GB), an Intel Core i7 processor (3.50 GHz) and 16 GB of RAM. By using sufficiently high laser power (80–100 mW), we could use exposure times that were short enough (1–10 ms) that animal movement during acquisition was negligible. Acquiring a single imaging volume, typically consisting of 20 Z-slices in two channels, took <0.4 s. Some animal movements along the A–P axis was observed between Z-slices. Each chamber was imaged every 20 min for ~48 h. During imaging intervals, we used the Perfect Focus system of the microscope to prevent sample drift.

To achieve high-throughput analysis of DAF-16 fluorescence in intestinal cells, we performed simultaneous 2-color imaging of DAF-16::GFP and H1::mCherry, a protein fusion that localizes specifically to the nuclei of intestinal cells and thus constitutes a good nuclear marker. Z-stacks with ~9 images were collected every 15-minutes for most experiments. Hatching was defined as the first frame where the larvae appeared outside the egg shell. Times of hatching were manually annotated for each animal, and used as the start of time courses.

A temperature control system was used to maintain a constant temperature of 20 °C inside the sample. A thermoelectric chiller (Thermotek T257P) was used to cool the custom-made objective jacket by circulating an antifreeze fluid (a mixture of water and glycerin) between the chiller and the objective jacket. In order to calibrate the system, a thermocouple temperature sensor measuring 0.025 mm in diameter (RS Pro) was placed inside the sample in contact with the polyacrylamide hydrogel and connected to a digital thermometer (RS Pro). The temperature was then varied on the thermoelectric chiller while the resulting temperature

inside the sample was being monitored. As animals in different microchambers hatch at slightly different times, the time after hatching at which the shift in temperature was initiated varied between animals. For the heat stress experiments, animals were allowed to hatch at 20 °C, followed by a sudden temperature increase to 31, 32 or 33 °C within 5 hours after hatching.

Segmentation of intestinal cell nuclei and cytoplasm

Custom Python software was used to calculate DAF-16::GFP fluorescence intensity in the nucleus and cytoplasm of intestinal cells. We processed the H1-wCherry signal (marker for intestinal nuclei) in order to obtain precise boundaries of cells' nuclei. First, the image z-stack for each time point was reduced to the maximum intensity projection, and the worm was segmented from the background using the Otsu method. To speed up computation time, the projected image was cropped to a rectangular region encompassing only the worm, thus removing most background areas. Next, the edges of individual nuclei were detected from the image gradient, which was calculated using the Sobel filter. Finally, a watershed segmentation algorithm was applied to the image gradient to isolate and label the nuclei and to generate a binary mask (see Fig. S1B). For each individual nucleus, the focal plane with the maximum average fluorescence intensity was automatically detected, and selected as the optimal focal plane. To obtain the cytoplasmic region, the nuclear mask was first expanded by dilation (7 pixels) and subsequently subtracted from the expanded mask, resulting in a narrow ring surrounding the nucleus. Finally, for each cell the average fluorescence intensity inside the nuclear mask, I_{nucl}, and inside the cytoplasmic mask, I_{cyt}, was evaluated at the optimal focal plane. To analyze DAF-16::GFP in each cell independently, segmented cells were manually annotated. All time-lapse movies were carefully inspected by eye and showed no disagreement with DAF-16 localization trajectories obtained by automatic quantification.

Quantification of DAF-16 localization

DAF-16::GFP subcellular localization in intestinal cells was quantified as the ratio $R = \frac{I_{nucl}}{I_{cyt}}$. Since DAF-16 localization trajectories appeared almost identical in all intestinal cells at a 15-minute time resolution, they were averaged for the ease of analysis, unless otherwise stated. To perform quantitative analysis of pulsatile dynamics, we first needed to discriminate nuclear from cytoplasmic localization of DAF-16. For animals under starvation and osmotic stress we defined a threshold by calculating the average *R* of animals in the control condition (20°C ad libitum food in the absence of stress) and multiplying by a factor of 1.05. Due to the

persistent nuclear localization of DAF-16 in animals under heat stress, we used a higher threshold of R =1.1.

In the AID experiments a membrane marker for intestinal nuclei was not used, and quantification of DAF-16 nuclear localization was done manually. In this case, using custom software in Python, we drew ellipsoids around the nucleus and in the cytoplasm immediately adjacent to the nuclei, for the first (near the head) dorsal and first ventral cell in the animals' intestine. We measured the average fluorescence value inside the ellipsoids, and the *R* values presented in figure 5 are the ratio between these values. The threshold used to quantify pulse characteristics is the (manually) measured *R* value of animals carrying the neuron-specific TIR tag on food, in absence of stress (data not shown), multiplied by 1.05.

Analysis of pulse characteristics

For each DAF-16 pulse in animals under osmotic stress or starvation, pulse duration was defined as the time the R(t) value was uninterruptedly above the threshold (R>Rcontrol*1.05). To differentiate true pulses from inherent variability and measurement noise, we only took pulses into account that lasted longer than a single time-point.

Strains

Auxin-inducible degradation (AID) experiments

For the DAF-2 degradation experiments we made use of the *hqSi8 [rgef-1p::TIR1::mRuby::unc-54 3'UTR+Cbr-unc-119(+)] II* and *ieSi61 [ges-1p::TIR1::mRuby::unc-54 3' UTR + Cbr-unc-119(+)] II* strains (65), which we obtained from the Caenorhabditis Genetics Center (CGC), for neuron- and intestine-specific degradation of DAF-2, respectively. In these strains, a degron tag is inserted at the 3' end of the endogenous daf-2 gene locus, and TIR1 is expressed in a tissue-specific manner. Combined with auxin (3-Indoleacetic acid, Sigma Aldrich), this leads to degradation of DAF-2 specifically in tissues expressing TIR1. We crossed these strains with TJ356 *zIs356 [daf-16p::daf-16a/b::GFP + rol-6(su1006)]* animals for visualizing DAF-16::GFP dynamics.

The auxin was stored at -23°C, suspended in alcohol, and was diluted with M9 prior to use. Microchambers were soaked in 1 mM auxin in M9 solution for at least 3 hours prior to the start of experiments. This was sufficient to induce clear nuclear localization of DAF-16::GFP in neurons and intestine for the duration of the experiment.

Supplementary Information
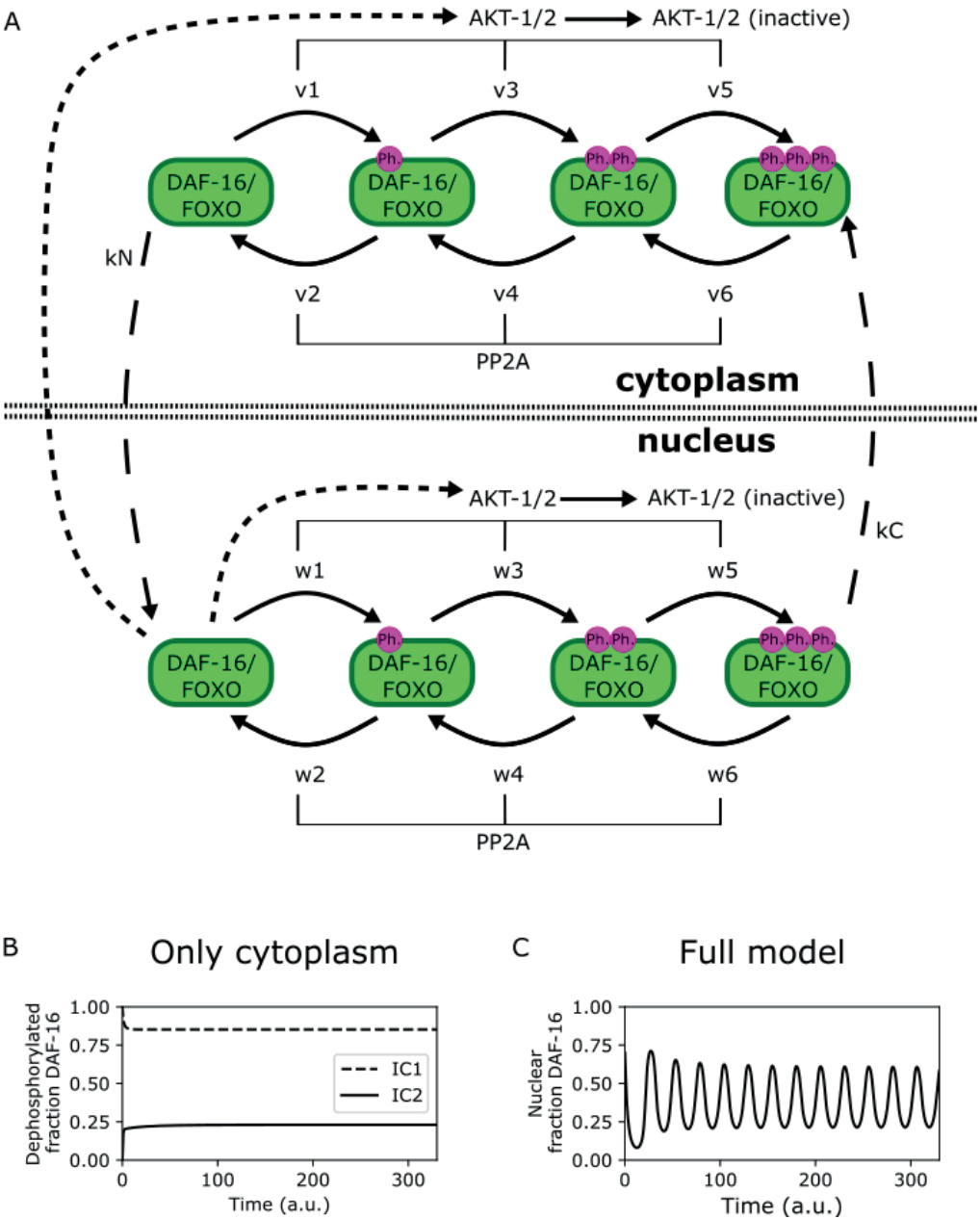
SI figure 1 Alternate model with explicit equations for each phosphorylation state and nuclear-cytoplasmic shuttling. This model shows the same qualitative behavior as the simpler, three-equation model used in this work. **A)** Schematic detailing the three-step phosphorylation and dephosphorylation cycle, in the cytoplasm and nucleus, as well as the translocation step. **B)** Example showing that bistability occurs, in a version of the model without negative feedback (only accounting for (de)phosphorylation of DAF-16/FOXO in the cytoplasm). **C)** Full model, incorporating negative feedback via upregulation of AKT-1/2, showing nuclear-cytoplasmic DAF-16 oscillations.
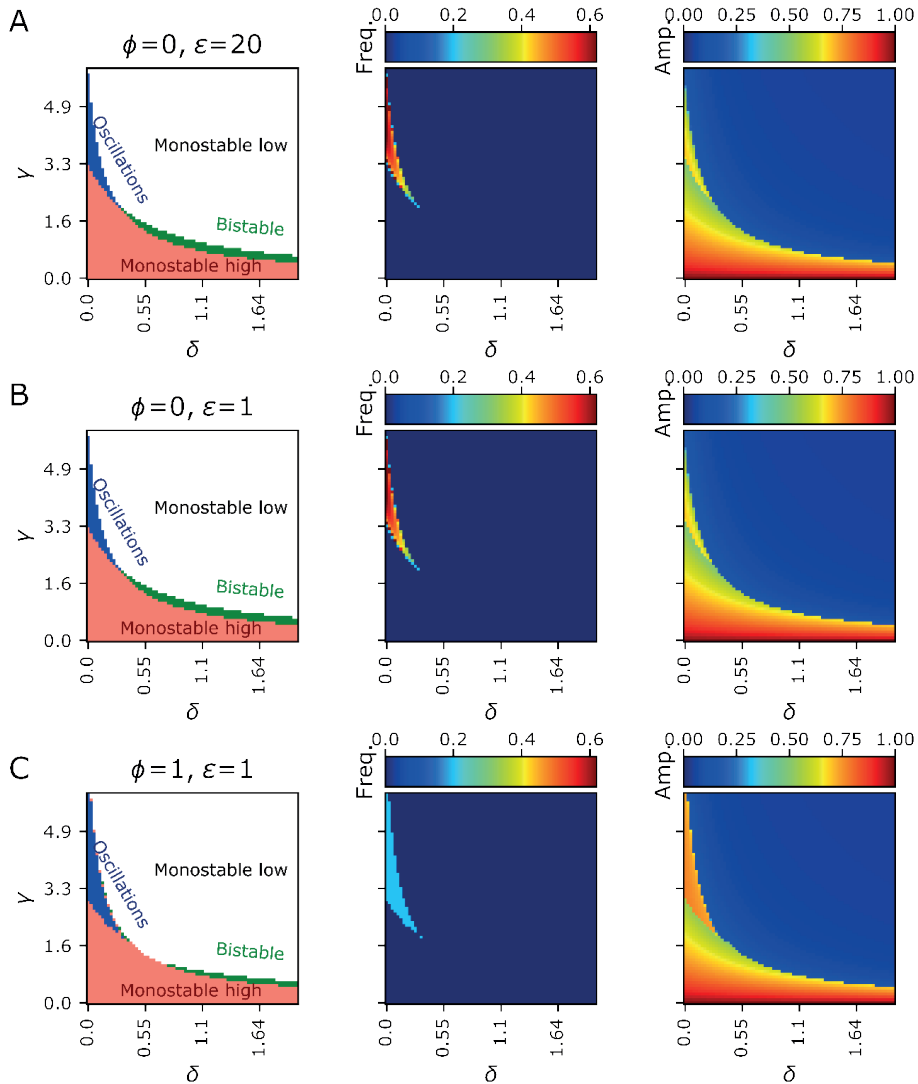
SI figure 2 Recreating the phase diagram in Figure 1 with alternate value of ϕ and ϵ. **A, B)** When there is no external feedback loop, the value of ϵ does not matter for DAF-16/FOXO dynamics. **C)** For $\phi = 1$, but a lower value of ϵ, the phase diagram shows the same types of dynamical regimes as in **Fig. 1**.

137
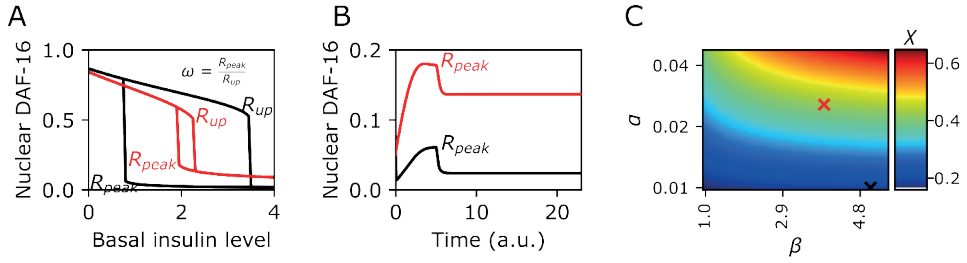
SI figure 3 Determining the maximum value of the initial peak for parameters corresponding to heat stress. **A)** Bistability diagram for various combinations of the parameters α and β. R_{peak} and R_{up} denote the maximum possible value of nuclear DAF-16/FOXO without jumping to the upper branch, and the lowest possible value on the upper branch, respectively. The ratio between these two, which we call ω, determines the amplitude of the initial peak relative to the maximum possible, steady state value. **B)** Example tracks corresponding to A), where δ is first decreased to a value just before jumping to the upper branch, and then increased again, to illicit the characteristic initial DAF-16/FOXO pulse under heat stress. **C)** Heatmap showing the value of ω for systematically varying α and β. Values were determined by assuming steady state in equation (4) and (5), plugging in values for α and β, and calculating the values of the peaks in the bistable diagram.
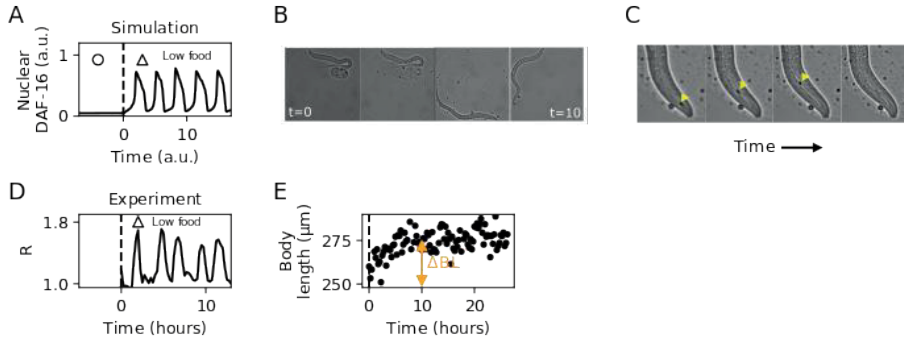
SI figure 4: A) Example of a stochastic simulation in the oscillatory regime, showing robust, repeated pulses. B) Film strip of an individual animal hatching with a secondary, unviable egg, which subsequently disintegrates. The remains of this egg are eaten by the healthy individual, over the course of ~10 hours. C) Zoomed-in view of animal from B) showing it ingesting remains of secondary egg. The frames shown are subsequent slices of a z-stack at one time point, with time between frames of 15ms. D) Example of experimental time trace of nuclear DAF-16::GFP, for one of three cases where an animal hatched with a secondary egg, showing robust oscillations during the first ~10 hours after hatching. E) Body length of the individual shown in B) over time. Note the increase from ~260 to ~275 μm, indicating that the animal is gaining nutrition from the consumed egg.
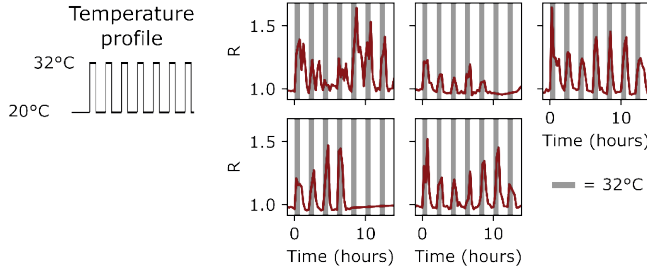
SI figure 5 DAF-16 nuclear ratio *R* time traces for five individuals. Animals were subjected to repeated heat pulses of 32°C lasting .75 hours, alternated with periods of 20°C lasting 1.25 hours. The timing of heat stress is indicated by the grey background. Animals almost always showed a robust peak of DAF-16::GFP nuclear localization at the onset of each new period of heat stress.
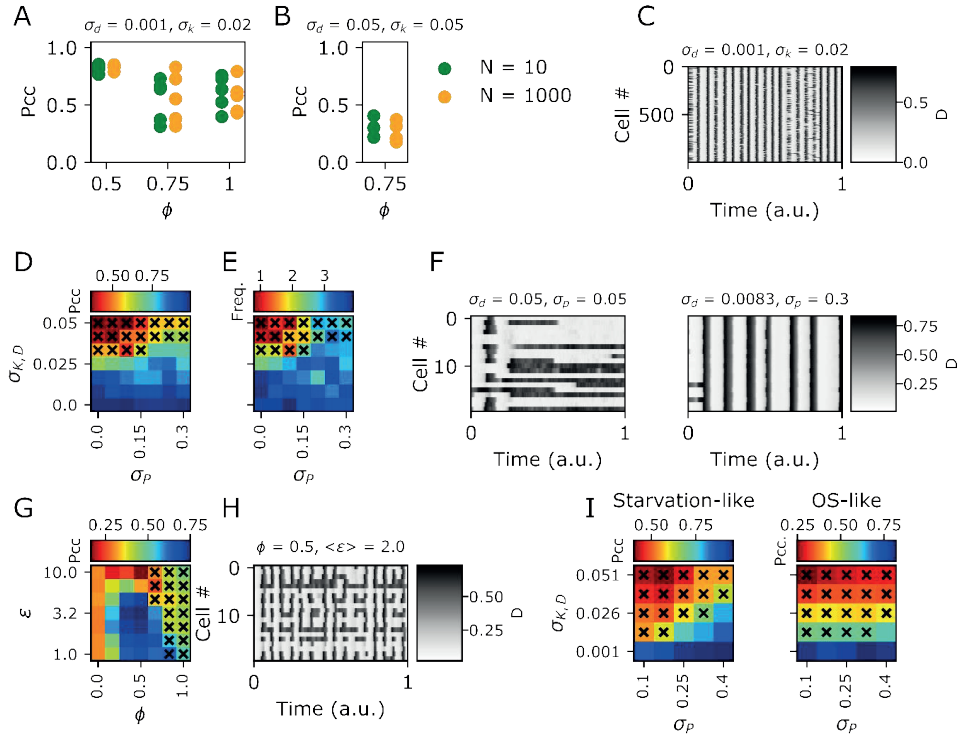
SI Figure 6 Effects of cell number, noise parameters, and random variation of parameters on synchronization. **A)** Pearson correlation coefficients for simulations with either N=10 or N=1000 cells, for various values of ϕ. Each dot represents one iteration. Noise parameters are the same used in Figure 4. **B)** Same as A), but with higher internal noise parameters σ_d and σ_k. In all cases, there is no significant difference in PCC between N=10 and N=1000 cells. **C)** Example of simulation with parameters from A), for N=1000 cells and ϕ=1. **D, E)** Heat maps of PCC and frequency of pulses as the noise parameters are varied, for N=10 cells. When internal noise values are low relative to σ_p, PCC values decrease dramatically due to the ubiquitous occurrence of locking. **F)** Example

tracks for N=20 cells, for various combinations of noise parameters. The example on the left shows poor synchronization (locking) as a consequence of relatively high internal noise, while the right example shows good synchronization. **G)** Pulses are still largely synchronized when all parameter values (except ϕ) by 5% around their original values for each cell. PCC values are overall lower, and locking occurs at lower values of ϕ, compared to the case where parameters are not varied between cells (see **Fig. 4**). **H)** Example tracks corresponding to G), for N=20 cells, showing good synchronization between cells. Note how some cells display consistent nuclear or cytoplasmic localization over time. **I)** Effect of noise parameters on starvation-like and osmotic stress-like dynamics. When cell-autonomous noise ($\sigma_{d,k}$) is large, synchronization is generally bad, largely due to occurrence of locking. This effect can (at least in the case of starvation-like dynamics) be 'rescued' by increasing ILP noise (σ_p) relative to cell-autonomous noise (see e.g. $\sigma_{k,d}$=0.026, σ_p=0.4). The PCC value for each parameter combination is the average of 30 iterations (with N=10 cells).
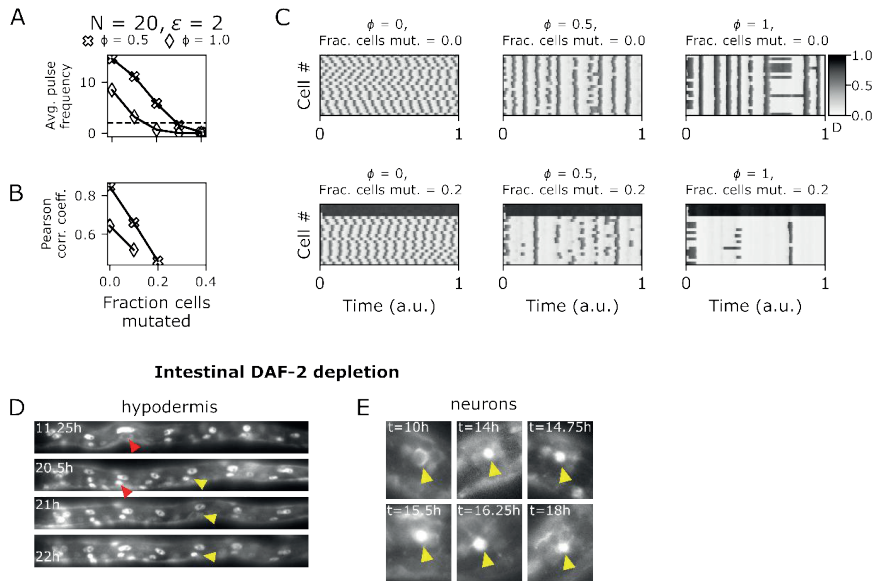
SI Figure 7 Mutating cells decreases the level of synchrony in the remaining cell population. **A)** Average frequency of pulses. Time normalized for different values of ϕ as described in Materials & Methods. Despite normalization, for ϕ = 1 the average frequency is lowered even when no cells are mutated, due to occurrence of locking. **B)** Average value of the PCC for 20 iterations, for varying values of ϕ and fractions of cells mutated. As the mutated fraction is increased, the PCC decreases. As N_muts is increased, pulsing effectively stops, and this data was then not used for the PCC plot (as PCC would simply go to 1). Dashed line in A) indicates threshold for including data for the PCC plot. **C)** Representative examples for various values of ϕ and fractions of mutated cells, for 20 cells. Top: when no cells are mutated, ϕ = 0.5 leads to better synchrony, while ϕ = 1 causes locking and therefore worse synchrony. Bottom: the topmost rows with constant nuclear DAF-16 represent the mutated cells. In the case of ϕ = 0, mutations in a subset of cells does not affect the dynamics, nor the synchrony of pulses. When cells are mutated for ϕ = 0.5, the overall dynamics of the system changes from robust oscillations to stochastic pulses, which are less synchronized. For ϕ = 1, pulse frequency becomes extremely low. Note the

many isolated pulses in the case of ϕ = 0.5. **D, E)** Additional example images of animals from the intestinal DAF-2 depletion experiment. **D)** Example of an animal, with focus on the hypodermis, where most hypodermal cells remain in the nuclear DAF-16 state for most of the experiment. However, one cell remains in the cytoplasmic state for longer (red arrows) before becoming nuclear, and another undergoes a short return to the cytoplasm (yellow arrows), decoupled from the surrounding cells. **E)** Focus on neurons in the animal's head. The cells start out in the cytoplasmic state (note the characteristic "honeycomb" structure), after which they become nuclear. Then, the cell indicated by the yellow arrow remains nuclear while surrounding cells return to the cytoplasmic state.

References

1. A. Patke, M. W. Young, S. Axelrod, Molecular mechanisms and physiological importance of circadian rhythms. *Nat Rev Mol Cell Biol* **21**, 67–84 (2020).
2. A. R. Saltiel, New perspectives into the molecular pathogenesis and treatment of type 2 diabetes. *Cell* **104**, 517–529 (2001).
3. D. J. Withers, M. White, Perspective: The Insulin Signaling System—A Common Link in the Pathogenesis of Type 2 Diabetes. *Endocrinology* **141**, 1917–1921 (2000).
4. M. F. White, Insulin Signaling in Health and Disease. *Science* **302**, 1710–1711 (2003).
5. Y. Poloz, V. Stambolic, Obesity and cancer, a case for insulin signaling. *Cell Death Dis* **6**, e2037–e2037 (2015).
6. J. Baker, J.-P. Liu, E. J. Robertson, A. Efstratiadis, Role of Insulin-like Growth Factors in Embryonic and Postnatal Growth.
7. J. M. Kramer, J. T. Davidge, J. M. Lockyer, B. E. Staveley, Expression of *Drosophila* FOXO regulates growth and can phenocopy starvation. *BMC Developmental Biology* **3**, 5 (2003).
8. N. Hao, E. K. O'Shea, Signal-dependent dynamics of transcription factor translocation controls gene expression. *Nat Struct Mol Biol* **19**, 31–39 (2012).
9. L. Cai, C. K. Dalal, M. B. Elowitz, Frequency-modulated nuclear localization bursts coordinate gene regulation. *Nature* **455**, 485–490 (2008).
10. D. E. Nelson, *et al.*, Oscillations in NF-κB Signaling Control the Dynamics of Gene Expression. *Science* **306**, 704–708 (2004).
11. G. Lahav, *et al.*, Dynamics of the p53-Mdm2 feedback loop in individual cells. *Nat Genet* **36**, 147–150 (2004).
12. J. E. Purvis, *et al.*, p53 Dynamics Control Cell Fate. *Science* **336**, 1440–1444 (2012).
13. B. Demirbas, *et al.*, Control of *C. elegans* growth arrest by stochastic, yet synchronized DAF-16/FOXO nuclear translocation pulses. [Preprint] (2023). Available at: http://biorxiv.org/lookup/doi/10.1101/2023.07.05.547674 [Accessed 8 March 2024].
14. K. A. Lasick, *et al.*, FOXO nuclear shuttling dynamics are stimulus-dependent and correspond with cell fate. *MBoC* **34**, ar21 (2023).
15. P. A. Gagliardi, *et al.*, Collective ERK/Akt activity waves orchestrate epithelial homeostasis by driving apoptosis-induced survival. *Developmental Cell* **56**, 1712-1726.e6 (2021).
16. S. O. Sage, D. J. Adams, C. Van Breemen, Synchronized oscillations in cytoplasmic free calcium concentration in confluent bradykinin-stimulated bovine pulmonary artery endothelial cell monolayers. *Journal of Biological Chemistry* **264**, 6–9 (1989).
17. M. Nivala, C. Y. Ko, M. Nivala, J. N. Weiss, Z. Qu, The emergence of subcellular pacemaker sites for calcium waves and oscillations. *The Journal of Physiology* **591**, 5305–5320 (2013).
18. D. Seppey, R. Sauser, M. Koenigsberger, J.-L. Bény, J.-J. Meister, Intercellular calcium waves are associated with the propagation of vasomotion along arterial strips. *Am J Physiol Heart Circ Physiol* **298**, H488-496 (2010).
19. S. Honma, The mammalian circadian system: a hierarchical multi-oscillator structure for generating circadian rhythm. *J Physiol Sci* **68**, 207–219 (2018).
20. S. Bernard, D. Gonze, B. Čajavec, H. Herzel, A. Kramer, Synchronization-Induced Rhythmicity of Circadian Oscillators in the Suprachiasmatic Nucleus. *PLoS Comput Biol* **3**, e68 (2007).
21. C. T. Murphy, P. J. Hu, "Insulin/insulin-like growth factor signaling in *C. elegans*" in *WormBook: The Online Review of C. Elegans Biology [Internet]*, (WormBook, 2018).
22. W.-J. Li, *et al.*, Insulin signaling regulates longevity through protein phosphorylation in *Caenorhabditis elegans*. *Nat Commun* **12**, 4568 (2021).
23. R. E. W. Kaplan, C. S. Maxwell, N. K. Codd, L. R. Baugh, Pervasive Positive and Negative Feedback Regulation of Insulin-Like Signaling in *Caenorhabditis elegans*. *Genetics* **211**, 349–361 (2019).
24. E. Schuster, *et al.*, DamID in *C. elegans* reveals longevity-associated targets of DAF-16/FoxO. *Mol Syst Biol* **6**, 399 (2010).
25. N. I. Markevich, J. B. Hoek, B. N. Kholodenko, Signaling switches and bistability arising from multisite phosphorylation in protein kinase cascades. *Journal of Cell Biology* **164**, 353–359 (2004).

26. V. Chickarmane, B. N. Kholodenko, H. M. Sauro, Oscillatory dynamics arising from competitive inhibition and multisite phosphorylation. *Journal of Theoretical Biology* **244**, 68–76 (2007).

27. S. B. Pierce, *et al.*, Regulation of DAF-2 receptor signaling by human insulin and ins-1, a member of the unusually large and diverse *C. elegans* insulin gene family. *Genes Dev.* **15**, 672–686 (2001).

28. C. T. Murphy, S.-J. Lee, C. Kenyon, Tissue entrainment by feedback regulation of insulin gene expression in the endoderm of *Caenorhabditis elegans*. *Proceedings of the National Academy of Sciences* **104**, 19046–19050 (2007).

29. D. Michaelson, D. Z. Korta, Y. Capua, E. J. A. Hubbard, Insulin signaling promotes germline proliferation in *C. elegans*. *Development* **141**, 237–237 (2014).

30. A. Brunet, *et al.*, Akt Promotes Cell Survival by Phosphorylating and Inhibiting a Forkhead Transcription Factor. *Cell* **96**, 857–868 (1999).

31. L. P. Van Der Heide, M. F. M. Hoekman, M. P. Smidt, The ins and outs of FoxO shuttling: mechanisms of FoxO translocation and transcriptional regulation. *Biochem J* **380**, 297–309 (2004).

32. K. Lin, H. Hsin, N. Libina, C. Kenyon, Regulation of the *Caenorhabditis elegans* longevity protein DAF-16 by insulin/IGF-1 and germline signaling. *Nat Genet* **28**, 139–145 (2001).

33. S. R. Datta, A. Brunet, M. E. Greenberg, Cellular survival: a play in three Akts. *Genes Dev.* **13**, 2905–2927 (1999).

34. A. Toker, A. C. Newton, Cellular Signaling: Pivoting around PDK-1. *Cell* **103**, 185–188 (2000).

35. A. Singh, *et al.*, Protein Phosphatase 2A Reactivates FOXO3a through a Dynamic Interplay with 14-3-3 and AKT. *MBoC* **21**, 1140–1152 (2010).

36. M. Thomson, J. Gunawardena, Unlimited multistability in multisite phosphorylation systems. *Nature* **460**, 274–277 (2009).

37. T. Suwanmajo, J. Krishnan, Mixed mechanisms of multi-site phosphorylation. *Journal of The Royal Society Interface* **12**, 20141405 (2015).

38. S. M. V. K, A. C. Ventura, S. D. Merajver, X. N. Lin, Multisite Phosphorylation Provides an Effective and Flexible Mechanism for Switch-Like Protein Degradation. *PLOS ONE* **5**, e14029 (2010).

39. F. Ortega, J. L. Garcés, F. Mas, B. N. Kholodenko, M. Cascante, Bistability from double phosphorylation in signal transduction. *The FEBS Journal* **273**, 3915–3926 (2006).

40. K. Takahashi, S. Tănase-Nicola, P. R. ten Wolde, Spatio-temporal correlations can drastically change the response of a MAPK pathway. *Proceedings of the National Academy of Sciences* **107**, 2473–2478 (2010).

41. T. Veuthey, S. Giunti, M. J. D. Rosa, M. Alkema, D. Rayes, The neurohormone tyramine stimulates the secretion of an Insulin-Like Peptide from the intestine to modulate the systemic stress response in *C. elegans*. [Preprint] (2024). Available at: https://www.biorxiv.org/content/10.1101/2024.02.06.579207v2 [Accessed 8 April 2024].

42. T. Schlick, "Molecular Dynamics: Further Topics" in *Molecular Modeling and Simulation: An Interdisciplinary Guide: An Interdisciplinary Guide*, T. Schlick, Ed. (Springer, 2010), pp. 463–517.

43. D. T. Gillespie, The mathematics of Brownian motion and Johnson noise. *American Journal of Physics* **64**, 225–240 (1996).

44. Y. Chen, L. R. Baugh, *Ins-4* and *daf-28* function redundantly to regulate *C. elegans* L1 arrest. *Developmental Biology* **394**, 314–326 (2014).

45. W. L. Hung, Y. Wang, J. Chitturi, M. Zhen, A *Caenorhabditis elegans* developmental decision requires insulin signaling-mediated neuron-intestine communication. *Development* **141**, 1767–1779 (2014).

46. G. I. Bell, *et al.*, Sequence of the human insulin gene. *Nature* **284**, 26–32 (1980).

47. A. Giustina, G. Mazziotti, E. Canalis, Growth Hormone, Insulin-Like Growth Factors, and the Skeleton. *Endocr Rev* **29**, 535–559 (2008).

48. B. M. Wentworth, I. M. Schaefer, L. Villa-Komaroff, J. M. Chirgwin, Characterization of the two nonallelic genes encoding mouse preproinsulin. *J Mol Evol* **23**, 305–312 (1986).

49. A. D. Ritter, *et al.*, Complex expression dynamics and robustness in *C. elegans* insulin networks. *Genome Res.* **23**, 954–965 (2013).

50. A. J. Varewijck, J. A. M. J. L. Janssen, Insulin and its analogues and their affinities for the IGF1 receptor. *Endocrine-Related Cancer* **19**, F63–F75 (2012).

51. Y. Matsunaga, K. Gengyo-Ando, S. Mitani, T. Iwasaki, T. Kawano, Physiological function, expression pattern, and transcriptional regulation of a *Caenorhabditis elegans* insulin-like peptide, INS-18. *Biochemical and Biophysical Research Communications* **423**, 478–483 (2012).

52. E. L. Greer, *et al.*, An AMPK-FOXO Pathway Mediates Longevity Induced by a Novel Method of Dietary Restriction in *C. elegans*. *Current Biology* **17**, 1646–1656 (2007).

53. E. L. Greer, *et al.*, The Energy Sensor AMP-activated Protein Kinase Directly Regulates the Mammalian FOXO3 Transcription Factor*. *Journal of Biological Chemistry* **282**, 30107–30119 (2007).

54. J. M. A. Tullet, *et al.*, DAF-16/FoxO Directly Regulates an Atypical AMP-Activated Protein Kinase Gamma Isoform to Mediate the Effects of Insulin/IGF-1 Signaling on Aging in *Caenorhabditis elegans*. *PLoS Genet* **10**, e1004109 (2014).

55. T. Mizuno, *et al.*, The *Caenorhabditis elegans* MAPK phosphatase VHP-1 mediates a novel JNK-like signaling pathway in stress response. *The EMBO Journal* **23**, 2226–2234 (2004).

56. S. W. Oh, *et al.*, JNK regulates lifespan in *Caenorhabditis elegans* by modulating nuclear translocation of forkhead transcription factor/DAF-16. *Proceedings of the National Academy of Sciences* **102**, 4494–4499 (2005).

57. S. H. Strogatz, *Nonlinear Dynamics and Chaos: With Applications to Physics, Biology, Chemistry, and Engineering*, 2nd Ed. (CRC Press, 2019).

58. A. Eldar, M. B. Elowitz, Functional roles for noise in genetic circuits. *Nature* **467**, 167–173 (2010).

59. K. D. Kimura, H. A. Tissenbaum, Y. Liu, G. Ruvkun, daf-2, an insulin receptor-like gene that regulates longevity and diapause in *Caenorhabditis elegans*. *Science* **277**, 942–946 (1997).

60. K. Jovic, *et al.*, Temporal dynamics of gene expression in heat-stressed *Caenorhabditis elegans*. *PLoS ONE* **12**, e0189445 (2017).

61. J. P. Buonaccorsi, J. S. Elkinton, S. R. Evans, A. M. Liebhold, Measuring and Testing for Spatial Synchrony. *Ecology* **82**, 1668–1679 (2001).

62. A. Kuznetsov, M. Kærn, N. Kopell, Synchrony in a Population of Hysteresis-Based Genetic Oscillators. *SIAM Journal on Applied Mathematics* **65**, 392–425 (2004).

63. L. Zhang, J. D. Ward, Z. Cheng, A. F. Dernburg, The auxin-inducible degradation (AID) system enables versatile conditional protein depletion in </i>C. elegans</i>. *Development* **142**, 4374–4384 (2015).

64. K. Nishimura, T. Fukagawa, H. Takisawa, T. Kakimoto, M. Kanemaki, An auxin-based degron system for the rapid depletion of proteins in nonplant cells. *Nat Methods* **6**, 917–922 (2009).

65. Y.-P. Zhang, *et al.*, Intestine-specific removal of DAF-2 nearly doubles lifespan in *Caenorhabditis elegans* with little fitness cost. *Nat Commun* **13**, 6339 (2022).

66. R. J. Wimmer, *et al.*, Mathematical modeling reveals modulation of both nuclear influx and efflux of Foxo1 by the IGF-I/PI3K/Akt pathway in skeletal muscle fibers. *American Journal of Physiology-Cell Physiology* **306**, C570–C584 (2014).

67. A. C. Dhadve, *et al.*, Decoding molecular interplay between RUNX1 and FOXO3a underlying the pulsatile IGF1R expression during acquirement of chemoresistance. *Biochimica et Biophysica Acta (BBA) - Molecular Basis of Disease* **1866**, 165754 (2020).

68. N. Shukla, S. Kadam, R. Padinhateeri, U. Kolthur-Seetharam, Continuous variable responses and signal gating form kinetic bases for pulsatile insulin signaling and emergence of resistance. *Proceedings of the National Academy of Sciences* **118**, e2102560118 (2021).

69. J. M. Wentz, A. R. Mendenhall, D. M. Bortz, Pattern Formation in the Longevity-Related Expression of Heat Shock Protein-16.2 in *Caenorhabditis elegans*. *Bull Math Biol* **80**, 2669–2697 (2018).

70. M. O. Casanueva, A. Burga, B. Lehner, Fitness Trade-Offs and Environmentally Induced Mutation Buffering in Isogenic *C. elegans*. *Science* **335**, 82–85 (2012).

71. H. J. E. Beaumont, J. Gallie, C. Kost, G. C. Ferguson, P. B. Rainey, Experimental evolution of bet hedging. *Nature* **462**, 90–93 (2009).
72. M. J. De Rosa, *et al.*, The flight response impairs cytoprotective mechanisms by activating the insulin pathway. *Nature* **573**, 135–138 (2019).
73. G. Kao, *et al.*, ASNA-1 Positively Regulates Insulin Secretion in *C. elegans* and Mammalian Cells. *Cell* **128**, 577–587 (2007).
74. A. Suzuki, H. Nakauchi, H. Taniguchi, Glucagon-like peptide 1 (1–37) converts intestinal epithelial cells into insulin-producing cells. *Proceedings of the National Academy of Sciences* **100**, 5034–5039 (2003).
75. C. Talchai, S. Xuan, T. Kitamura, R. A. DePinho, D. Accili, Generation of functional insulin-producing cells in the gut by Foxo1 ablation. *Nat Genet* **44**, 406–412, S1 (2012).
76. R. A. Kellogg, S. Tay, Noise facilitates transcriptional control under dynamic inputs. *Cell* **160**, 381–392 (2015).
77. S. Zambrano, I. De Toma, A. Piffer, M. E. Bianchi, A. Agresti, NF-κB oscillations translate into functionally related patterns of gene expression. *Elife* **5**, e09100 (2016).
78. M. Heltberg, R. A. Kellogg, S. Krishna, S. Tay, M. H. Jensen, Noise Induces Hopping between NF-κB Entrainment Modes. *Cell Syst* **3**, 532-539.e3 (2016).
79. E. Batchelor, A. Loewer, G. Lahav, The ups and downs of p53: Understanding protein dynamics in single cells. *Nat Rev Cancer* **9**, 371–377 (2009).
80. A. Hafner, *et al.*, Quantifying the Central Dogma in the p53 Pathway in Live Single Cells. *Cell Systems* **10**, 495-505.e4 (2020).
81. H. Venkatachalapathy, Z. Yang, S. M. Azarin, C. A. Sarkar, E. Batchelor, Pulsed stimuli entrain p53 to synchronize single cells and modulate cell-fate determination. [Preprint] (2023). Available at: https://www.biorxiv.org/content/10.1101/2023.10.24.563786v2 [Accessed 17 May 2024].
82. Y. Jiramongkol, E. W.-F. Lam, FOXO transcription factor family in cancer and metastasis. *Cancer Metastasis Rev* **39**, 681–709 (2020).
83. A. R. Gomes, J. J. Brosens, E. W.-F. Lam, Resist or die: FOXO transcription factors determine the cellular response to chemotherapy. *Cell Cycle* **7**, 3133–3136 (2008).
84. S. Yao, L. Y.-N. Fan, E. W.-F. Lam, The FOXO3-FOXM1 axis: A key cancer drug target and a modulator of cancer drug resistance. *Seminars in Cancer Biology* **50**, 77–89 (2018).
85. A. A. Cohen, *et al.*, Dynamic Proteomics of Individual Cancer Cells in Response to a Drug. *Science* **322**, 1511–1516 (2008).
86. P. E. Kloeden, E. Platen, "Stochastic Differential Equations" in *Numerical Solution of Stochastic Differential Equations*, Applications of Mathematics., P. E. Kloeden, E. Platen, Eds. (Springer, 1992), pp. 103–160.

4

Chapter 5

General discussion

In this thesis we studied the impact of environmental factors on developing animals. For this we made use of the model organism *C. elegans*, where we used fluorescent time-lapse microscopy to track individual animals trapped inside microchambers.

In **Chapter 2**, we tracked animals for the entire duration of post-embryonic development, under various environmental conditions that resulted in different overall developmental rates. We varied temperature, diet, and food availability, and also examined mutants that perturbed developmental timing. We measured or manually annotated the timing of key developmental events for individual animals, namely molting, hypodermal stem cell divisions, and peaks of oscillatory *wrt-2* expression. Of particular interest was the apparent variability in developmental timing between the isogenic animals.

In **Chapter 3** we studied the dynamics of insulin signaling in individual animals under stress. In particular, we tracked the main output of insulin signaling, nuclear localization of the transcription factor DAF-16/FOXO over time. We tested the response to various stresses, such as starvation, osmotic stress, and heat stress and measured the ratio between nuclear and cytoplasmic DAF-16::GFP. We also measured the growth of animals under mild stresses, to see how it related to DAF-16 activity.

In **Chapter 4** we developed a mathematical model, consisting of a set of coupled stochastic differential equation based on known interactions in the IIS pathway. We used this model to reproduce the dynamics of DAF-16/FOXO that we found in **Chapter 3**, and to predict new dynamics of DAF-16/FOXO under heat stress, which we tested experimentally. We next theorized about a possible synchronization mechanism through ILP-mediated cell coupling. Using insights from the synchronization model, we predicted that when DAF-16/FOXO is constitutively active in a subset of cells, the remaining cells should have a reduced pulse frequency, which we also tested experimentally.

Here, I will summarize our key findings and discuss them, as well as give an outlook. I will also assess the societal impact of the findings presented in this thesis.

Development during small deviations from the optimum: temporal scaling in *C. elegans*

In **Chapter 2**, we measured the overall post-embryonic developmental rate, i.e. the time animals required to reach adulthood, and the timing of distinct developmental events in individual animals. Despite the fact animals in these experiments were isogenic, there was variability in the timing of individual events, namely molting, seam cell divisions, and peaks of *wrt-2* expression. We showed that the timing of these events was the same relative to the total time of development within each individual, a phenomenon called temporal scaling. This remained true for various temperatures, at which the animals grew at different overall developmental rates. However, this did not work for *lin-42/Period* mutant animals, or animals on a different diet, namely HB101 instead of OP50 (both are strains of *E. coli*). In this case, however, temporal scaling still worked when we divided the timing of events into "epochs", defined as consecutive periods in which the timing of all developmental events was impacted by the same distinct change in developmental rate.

The natural environment of animals is constantly fluctuating, in terms of temperature, food availability, diet, etc. These factors influence the overall rate of development in animals: for example, lower concentrations of food result in slower overall growth in *C. elegans* (1). We have shown that *C. elegans* has a remarkable capability to ensure that the timing of individual developmental events is retained despite fluctuating environmental factors. For instance, when changing food availability or temperature mid-development, the order of some developmental events was changed (**Chapter 2**), but the animals were otherwise healthy and, in the case of changing temperature, continued development as normal. This provides a valuable insight into how animals in general might ensure correct development in the wild. Not only now, but also in the future: in a time of changing climate, not only will the global average temperature rise, but extremes of temperature are also likely to become more common and thereby affect many animal populations across the world (2–4). Understanding how animals develop under changing, non-optimal temperatures, or extremes of temperature (stress) is paramount to grasping the impact of climate change.

While spatial patterns during development are generally well understood (5), this is much less the case for temporal patterns such as timing of cell divisions, formations of tissues, etc., especially during post-embryonic development into an adult animal. *C. elegans* allows study of post-embryonic development due to the fact that it is transparent and has a relatively simple body plan, but a constraining factor has historically been the fact that it is challenging to track individual animals over time, while at the same time measuring cellular dynamics. By using microchambers to trap individual animals and performing time-lapse microscopy, a setup called "WormHostel", we managed to overcome this challenge. Time-lapse microscopy of individual

animals can thus provide valuable, novel insights into post-embryonic development, as it also allows for the study of inter-individual variability and timing of key events. Other model organisms are also used for studying development, for example the fruit fly *Drosophila Melanogaster* or the zebrafish *Danio rerio*. Much fruit fly research focuses on the fruit fly embryo, which are not motile. Flies, however, also go through three larval stages where they do move, and therefore pose the same challenge to be studied as *C. elegans*. Zebrafish have traditionally been used to study embryonal development, with post-embryonal development again being challenging due to movement of the animal. While some progress has been made with imaging larval and adult zebrafish, this still requires intubation and anesthetization of the fish, which can affect developmental processes (6). In both cases, immobilizing animals mechanically or pharmacologically means feeding becomes impossible, and may therefore affect developmental processes. In this case, a WormHostel-like setup could provide a solution, allowing studying of cellular dynamics during (larval, and adult) development and relating them to the organ- or whole-body level without drug-induced immobilization, such as formation of the heart in fruit flies, or vertebrate-specific processes in zebrafish (6, 7)("FlyHostel"? "FishHostel"?).

We used a simple, phenomenological model to interpret the temporal scaling data. It would be interesting, however, to also develop a more detailed model that tries to explain the mechanism that gives rise to robust temporal scaling. While there is evidence that suggests body size controls developmental timing in *C. elegans* (1, 8), our result that *lin-42* mutant animals stop growing but continue developing (**Chapter 2**) contradicts this. It would therefore be interesting to design a model that attempts to combine the coupling between size and development with non-size related mechanisms of timing, such as oscillating gene clocks, whose time scale is set by protein degradation rate (9, 10). This could allow us to pin-point the exact mechanism that ensures temporal scaling, for example by generating predictions on situations where temporal scaling should break down.

A limitation of our study of post-embryonic development, in the case of temporal scaling but also for worms under stress, is the fact that we use body length as a proxy for body size. While body length is generally a good proxy for size, for designing better mathematical models to understand post-embryonic growth, it would be more accurate to measure body volume. This is possible, by measuring the area of the cross-section of the animal's body coupled with the assumption of cylindrical symmetry (1). A challenge here is that there are no free fluorescent channels in the WormHostel setup to use for body markers, and measurements of body area would therefore have to be done manually for every time point, which would not be feasible due to the large amounts of data. A solution would be to employ a machine learning approach

to automatically detect the outline of worms inside the chamber. This would bring the added benefit of automating an important part of measurements when studying development.

Development during environmental stress: insulin signaling and DAF-16/FOXO pulses

Despite insulin being very widely studied, including in *C. elegans* (11), almost nothing was known about the dynamics of its main output, the nuclear translocation of DAF-16/FOXO. The classic view of the insulin signaling pathway is that it is either "on" or "off", depending on the level of stress (11). In this view, DAF-16/FOXO is either cytoplasmic, or nuclear, respectively. Our results show that this is not the case at all, and that DAF-16/FOXO localization in animals under a constant stress is highly dynamic, with DAF-16::GFP shuttling between the nucleus and cytoplasm in pulses that last on the order of hours.

We further found that the dynamics of DAF-16/FOXO depends on the stress type: starvation lead to stochastic oscillations, osmotic stress induced randomly times pulses, and heat stress caused an initial accumulation of DAF-16::GFP in the nucleus, before returning mostly to the cytoplasm, with a baseline level of presence in the nucleus afterwards. We further found that the dynamics depend on the magnitude of stress, in the case of osmotic and heat stress: for increasing salt concentration the duration, but not the frequency of pulses increased, while for increasing temperature, the amplitude of the initial pulse and baseline increased. This suggests that perhaps DAF-16 encodes information about the type and magnitude of stress. This could then drive the expression of only a subset of stress-specific genes. Other transcription factors are known to work in this manner, for example p53 in mammals encodes information on the type (gamma or UV) and doses of irradiation in its dynamics (dosage-dependent number of pulses versus sustained non-pulsatile activation), while targets of Msn-2 in yeast are sensitive to frequency and amplitude of Msn-2 nuclear localization pulses (12–14). In future experiments, it would be interesting to experimentally control DAF-16 pulses and measure the effect on DAF-16 target genes, to see whether they are sensitive to the frequency or amplitude of DAF-16 pulses. While optogenetic control of signaling pathways in *C. elegans* is possible, these methods often make use of short wavelength (blue) light (15–17), which worms tend to avoid, which therefore might interfere with the stress response. A solution would be to use red light-induced optogenetic control to force nuclear localization of DAF-16, either directly or through inactivation of DAF-2 (18), or alternatively, to use sequences of heat pulses to control DAF-16 nuclear localization dynamics as an alternative to optogenetics (**Chapter 4, SI**).

DAF-16/FOXO dynamics is likely a key part of the functioning of insulin signaling, most likely in *C. elegans* but possibly also in higher organisms including humans, and future research will have to keep this in mind when designing experiments and formulating theories. Past research on insulin signaling in *C. elegans* will have to be reinterpreted in light of the knowledge that

DAF-16/FOXO is highly pulsatile. For example, studies that look at a population of starving worms invariably tend to report that a small fraction of animals still retain cytoplasmic localization, even after multiple hours of starvation (19, 20). This makes sense in light of DAF-16 dynamics during starvation. When animals undergo stochastically timed DAF-16 pulses during starvation, observations at a single time point will always (given enough individuals are imaged) include a few animals that happen to be in the cytoplasmic phase of pulsing.

Another aspect of insulin signaling that was so far unexplored, is the coupling between DAF-16/FOXO activity at the single-cell level and the whole-body level. Most studies look at FOXO dynamics in cell cultures (21–23), missing the context of a living animal. What our investigations revealed is that, firstly, DAF-16 pulses are strikingly synchronized in time across the ~200 µm long body of the animals. Using high-time resolution imaging we showed that this delay is on the order of ~3 minutes between the two ends of the intestine (~100 µm distance). Secondly, we show that pulses of nuclear DAF-16/FOXO result directly in temporary arrest in body growth. While it was previously known that starved mutant animals lacking active DAF-16/FOXO show continued cell division and development but without growth (24), this direct link between DAF-16/FOXO translocation and body growth was so far unknown. Third, stochasticity appears to be an integral part of DAF-16/FOXO pulses, as DAF-16 dynamics vary greatly between individuals under starvation, low to intermediate osmotic stress, and low to intermediate heat stress. Interestingly, animals with more, or longer-lasting pulses grew slower than those with little DAF-16 pulse activity, at least in the case of osmotic stress (**Chapter 3**). It's an intriguing possibility that stochasticity is a "feature and not a bug" in the functioning of the IIS pathway, and evolved to enable bet-hedging strategies under stress (25). Future research should focus on whether the same level of synchronization, and the arrest in growth, occurs for FOXO pulses in human cells in a more realistic biological context, such as human intestinal organoids.

If DAF-16 pulses cause a transient arrest in growth, an interesting question is then whether temporal scaling is preserved in the case of stress. The fact that changing conditions mid-development, for example by letting food run out, causes a perturbation in event order (**Chapter 2)** suggests that it might not. But it is still worth probing to see whether this occurs in a predictable manner, for example under conditions with stochastic pulses, such as osmotic stress, where animals repeatedly arrest and resume growth.

Mathematical modeling of the insulin signaling pathway

With the mathematical model presented in **Chapter 4**, we have identified a basic mathematical structure that is capable of the generating DAF-16/FOXO pulses that strongly resemble those we observed experimentally. This model now raises key questions on what molecular

components of the IIS form the core pulse-generating feedback loop at the center of our model. This model explains synchronized DAF-16/FOXO pulse dynamics either by a combination of intra- and extracellular feedback, or through a fully extracellular (ILP-mediated) feedback loop. Where on this spectrum does the *in vivo C. elegans* IIS system lie? In future experiments, this can be systematically tested by a series of time-lapse experiments in strains of *C. elegans* where components of the IIS have been knocked out, such as AKT-1/2, PDK-1 and AGE-1. As AKT/PKB and DAF-16/FOXO are promising targets of chemotherapeutic agents in treating various cancers (26–29), figuring out the exact role of these IIS components in generating pulses is important for creating a more quantitative model, thereby increasing the clinical relevance of our proposed mechanism.

While in experiments we observed randomly timed DAF-16 pulses (osmotic stress), and stochastic oscillations (starvation), our model suggests that there exists a region in parameter space with robust, sustained oscillations. Specifically, we would expect this in cases where animals are confronted with a constant, low concentration of food. Does *C. elegans* IIS indeed display such robust oscillations, and if so, what could be their function? Preliminary results we obtained indicate that this is indeed the case: we observed rare instances where animals hatched in absence of *E. coli* food, but in the accidental presence of a second, non-viable *C. elegans* egg. Here, animals appeared to feed on the egg remains, but with low apparent nutritional value, as animals grew slowly, while indeed showing DAF-16 translocation oscillations that were strikingly robust (**Chapter 3**). This is an interesting phenomenon, as it suggests robust DAF-16/FOXO oscillations may be an aspect of the low-nutrient response of *C. elegans*. Our setup, however, does not allow for a systematic way to test this, as we cannot control food levels, as the sample is inaccessible once it is sealed. One way to address this would be to make use of microfluidics. Alternative time-lapse setups exists that are coupled to microfluidics, allowing inflow of precisely calibrated concentration of *E. coli* food (30), which could be combined with a WormHostel-like tracking of DAF-16::GFP localization in individual animals over time. Especially interesting would be the relation to growth: we now can only measure growth arrest conditions (no food), but cannot measure low-food conditions, where growth does not arrest but proceeds at a slower rate (1). Our serendipitous findings with non-viable eggs suggest that DAF-16 dynamics might play a role in this regime, too, potentially via robust oscillations. Robust oscillations could be a way to respond to varying concentrations of low food availability, with the frequency of pulses (and therefore the relative duration of growth arrest VS growth) increasing with decreasing food availability. It's also possible that other types of stress that we have not tested would elicit a robust oscillatory DAF-16/FOXO response. This could be explored by screening more types of stress, such as oxidative stress, or heavy metal stress (31, 32).

We performed experiments to validate predictions generated by our model. Strikingly, DAF-16 nuclear localization displays hysteresis during heat stress: DAF-16::GFP at 31°C was cytoplasmic when the temperature was upshifted from 20°C, but was predominantly nuclear at 31°C when shifting the temperature down from 33°C. This is a property that likely could not have been anticipated without the use of a mathematical model. Furthermore, as we showed in **Chapter 3**, nuclear DAF-16 leads to growth arrest. This means that a small change of only 2°C in temperature can already severely impede growth in *C. elegans*, which potentially extends other ectotherm (cold-blooded) animals in general. Coming back to the example of climate change, the fact that even a small change in temperature can apparently make a significant difference in stress response, and growth, does not bode well for the survival of ectotherm animals. And given that ectotherms are a vital part of many ecosystems, it's bad news for life on Earth in general. This, again, underscores the need to better understand stress response in animals, and of course the importance of combating climate change.

Some of the experiments we performed to validate the synchronization model also raised new questions. For example, in the case of animals with intestinal DAF-2 depletion (and therefore, permanent nuclear DAF-16/FOXO in the intestine) synchronization between adjacent cells was sometimes broken (**Chapter 4**). Although our model could partly explain this phenomenon, it does not address the spatial aspects, such as the fact that some tissues display almost permanent nuclear DAF-16/FOXO localization in all animals, while cells in other tissues continued pulsing, albeit often with complex patterns of local desynchronization. A possible way to address this would be to explicitly take space, and diffusion of ILPs into account. In real biological systems, molecules take time to diffuse from one cell to another. A modification to our model would therefore be to model individual cells as "point sources" producing and secreting ILPs into a 3D environment, which could be described using partial differential equations (PDEs).

A further advantage of a PDE model would be that it allows the generation of hypotheses relating pulse generation and synchronization to animal size during development. In this case, to simplify such a model, the body of *C. elegans* could be approximated as a 1D line. A PDE model could be used to predict, firstly, whether pulsing is expected in older/larger animals, and secondly, whether these pulses are then still tightly synchronized. Here, we postulate that as animals increase in size, the observed body-wide synchronization of pulses could make way for other phenomena such as travelling waves, depending on whether diffusion of ILPs becomes limiting for communicating IIS state from one part of the body to another. Combining this with experiments where animals are exposed to stress at systematically varying sizes, i.e. different stages during larval development, and measuring DAF-16::GFP localization dynamics would allow us to further constrain possible mechanisms of synchronization.

Conclusion

In summary, I discussed some of the key findings presented in this thesis. Fluorescent time-lapse microscopy of individual *C. elegans* animals provides insights into how animals manage to survive in an ever-changing, and often harsh environment. During development, developmental events need to be executed at precise times and in a specific order. We found that the timing of developmental events in *C. elegans* follows temporal scaling, meaning that the timing of individual events is the same for animals with different overall rates of development, when the timing of events is divided by the total development time. During stressful environmental conditions, we found that *C. elegans* insulin signaling displays highly dynamic and stochastic dynamics of DAF-16/FOXO nuclear localization. We also found that these pulses cause a transient arrest in growth. In conclusion, *C. elegans* remains a useful model organism to understand how developing animals deal with a fluctuating environment.

Epilogue: On the need for fundamental scientific research in times of crisis

"… the individual looks his own short life span too squarely in the eye and feels no strong incentives to build on enduring institutions, designed for the ages. He wants to pick the fruit from the tree he has planted himself, and therefore no longer likes to plant those trees which require regular care over centuries, trees that are destined to overshade long successions of generations."
-Friedrich Nietzsche (33)

Climate change, lack of housing, the rise of anti-democratic forces in Western countries, increasing wealth inequality: we live in a time of ongoing or upcoming crises. Crises that impact the lives of many millions of people, and that will require the concentrated effort of the brightest minds, and huge amounts of resources and finances to tackle. In such a time, how can we justify doing fundamental science, an endeavor that requires substantial amounts of money, and that does not directly contribute to solving such crises? As an example: four million euros could be used to fund research on the origins of life in The Netherlands for one year (34), or it could be used to provide free breakfast to children at over 100 Dutch primary schools for the same amount of time (35).

One argument is the fact that fundamental scientific research does often end up producing knowledge and technologies that benefit society. For example, Emanuelle Charpentier and Jennifer Doudna did fundamental work on the bacterial genome, and in doing so helped develop CRISPR-CAS, which has many possible practical applications, and for which they received the 2020 Nobel Prize in chemistry (36). In this view, research that at this time does not seem to have a direct application may end up producing solutions to current and future

crises, and are therefore "trees which require regular care over centuries". In a time where all processes in society seem to be speeding up, science is the domain where deep, slow-paced, ponderous thought that leads to results only in the long term is still somewhat possible (though even in science this is changing). Of course, the possible applications of fundamental science are always uncertain, and it is unclear on which timescale it may "pay off" its investment.

Another argument, however, is that fundamental science is a way for us to come to understand ourselves. This is especially true for biology, which amongst the sciences occupies a special place. Unlike the abstract realms of physics or mathematics, the objects of biological study are not distant concepts, but constitute the fundaments of our own mode of existence (37). Exploring the fundamental processes of organisms sheds a light, however small or indirect, on what it means to be human. This motivation also underpins the research laid out in this thesis, and is, in my opinion, infinitely more valuable than the financial costs required to get there.

5

References

1.   S. Uppaluri, C. P. Brangwynne, A size threshold governs *Caenorhabditis elegans* developmental progression. *Proc. Biol. Sci.* **282**, 20151283 (2015).

2.   M. J. Islam, A. Kunzmann, M. J. Slater, Responses of aquaculture fish to climate change-induced extreme temperatures: A review. *J. World Aquac. Soc.* **53**, 314–366 (2022).

3.   J. A. Harvey, R. Heinen, R. Gols, M. P. Thakur, Climate change-mediated temperature extremes and insects: From outbreaks to breakdowns. *Glob. Change Biol.* **26**, 6685–6701 (2020).

4.   P. Thornton, G. Nelson, D. Mayberry, M. Herrero, Increases in extreme heat stress in domesticated livestock species during the twenty-first century. *Glob. Change Biol.* **27**, 5762–5772 (2021).

5.   D. M. Umulis, H. G. Othmer, Mechanisms of scaling in pattern formation. *Dev. Camb. Engl.* **140**, 4830–4843 (2013).

6.   D. Castranova, *et al.*, Long-term imaging of living adult zebrafish. *Development* **149**, dev199667 (2022).

7.   C. Q. Lischik, L. Adelmann, J. Wittbrodt, Enhanced in vivo-imaging in medaka by optimized anaesthesia, fluorescent protein selection and removal of pigmentation. *PLOS ONE* **14**, e0212956 (2019).

8.   L. Byerly, R. C. Cassada, R. L. Russell, The life cycle of the nematode *Caenorhabditis elegans*. I. Wild-type growth and reproduction. *Dev. Biol.* **51**, 23–33 (1976).

9.   M. Matsuda, *et al.*, Species-specific segmentation clock periods are due to differential biochemical reaction speeds. *Science* **369**, 1450–1455 (2020).

10.   T. Rayon, *et al.*, Species-specific pace of development is associated with differences in protein stability. *Science* **369**, eaba7667 (2020).

11.   C. T. Murphy, P. J. Hu, "Insulin/insulin-like growth factor signaling in *C. elegans*" in *WormBook: The Online Review of C. Elegans Biology [Internet]*, (WormBook, 2018).

12.   J. E. Purvis, *et al.*, p53 Dynamics Control Cell Fate. *Science* **336**, 1440–1444 (2012).

13.   E. Batchelor, A. Loewer, C. Mock, G. Lahav, Stimulus-dependent dynamics of p53 in single cells. *Mol. Syst. Biol.* **7**, 488 (2011).

14.   N. Hao, E. K. O'Shea, Signal-dependent dynamics of transcription factor translocation controls gene expression. *Nat. Struct. Mol. Biol.* **19**, 31–39 (2012).

15.   L.-E. Fielmich, *et al.*, Optogenetic dissection of mitotic spindle positioning in vivo. *eLife* **7**, e38198 (2018).

16.   M. Endo, *et al.*, Optogenetic activation of axon guidance receptors controls direction of neurite outgrowth. *Sci. Rep.* **6**, 23976 (2016).

17.   S. De Henau, M. Pagès-Gallego, W.-J. Pannekoek, T. B. Dansen, Mitochondria-Derived H_2O_2 Promotes Symmetry Breaking of the *C. elegans* Zygote. *Dev. Cell* **53**, 263-271.e6 (2020).

18.   S. Oda, E. Sato-Ebine, A. Nakamura, K. D. Kimura, K. Aoki, Optogenetic control of cell signaling with red/far-red light-responsive optogenetic tools in *Caenorhabditis elegans*. [Preprint] (2022). Available at: https://www.biorxiv.org/content/10.1101/2022.08.12.503710v1 [Accessed 31 May 2024].

19.   D. Weinkove, J. R. Halstead, D. Gems, N. Divecha, Long-term starvation and ageing induce AGE-1/PI 3-kinase-dependent translocation of DAF-16/FOXO to the cytoplasm. *BMC Biol.* **4**, 1 (2006).

20.   X.-X. Lin, *et al.*, DAF-16/FOXO and HLH-30/TFEB function as combinatorial transcription factors to promote stress resistance and longevity. *Nat. Commun.* **9**, 4400 (2018).

21.   G. J. P. L. Kops, *et al.*, Forkhead transcription factor FOXO3a protects quiescent cells from oxidative stress. *Nature* **419**, 316–321 (2002).

22.   S. Nemoto, M. M. Fergusson, T. Finkel, Nutrient Availability Regulates SIRT1 Through a Forkhead-Dependent Pathway. *Science* **306**, 2105–2108 (2004).

23.   H. Tran, *et al.*, DNA Repair Pathway Stimulated by the Forkhead Transcription Factor FOXO3a Through the Gadd45 Protein. *Science* **296**, 530–534 (2002).

24.   L. R. Baugh, P. W. Sternberg, DAF-16/FOXO regulates transcription of cki-1/Cip/Kip and repression of lin-4 during *C. elegans* L1 arrest. *Curr. Biol. CB* **16**, 780–785 (2006).

25.   H. J. E. Beaumont, J. Gallie, C. Kost, G. C. Ferguson, P. B. Rainey, Experimental evolution of bet hedging. *Nature* **462**, 90–93 (2009).

26.   J. Brognard, A. S. Clark, Y. Ni, P. A. Dennis, Akt/Protein Kinase B Is Constitutively Active in Non-Small Cell Lung Cancer Cells and Promotes Cellular Survival and Resistance to Chemotherapy and Radiation. *Cancer Res.* **61**, 3986–3997 (2001).

27.   M. Iida, P. M. Harari, D. L. Wheeler, M. Toulany, Targeting AKT/PKB to improve treatment outcomes for solid tumors. *Mutat. Res. Mol. Mech. Mutagen.* **819–820**, 111690 (2020).

28.   A. R. Gomes, J. J. Brosens, E. W.-F. Lam, Resist or die: FOXO transcription factors determine the cellular response to chemotherapy. *Cell Cycle* **7**, 3133–3136 (2008).

29.   S. Yao, L. Y.-N. Fan, E. W.-F. Lam, The FOXO3-FOXM1 axis: A key cancer drug target and a modulator of cancer drug resistance. *Semin. Cancer Biol.* **50**, 77–89 (2018).

30.   S. Berger, S. Spiri, A. deMello, A. Hajnal, Microfluidic-based imaging of complete *C. elegans* larval development. [Preprint] (2021). Available at: http://biorxiv.org/lookup/doi/10.1101/2021.03.31.437890 [Accessed 25 June 2024].

31.   S. T. Henderson, T. E. Johnson, daf-16 integrates developmental and environmental inputs to mediate aging in the nematode *Caenorhabditis elegans*.

32.   A. Keshet, *et al.*, PMK-1 p38 MAPK promotes cadmium stress resistance, the expression of SKN-1/Nrf and DAF-16 target genes, and protein biosynthesis in *Caenorhabditis elegans*. *Mol. Genet. Genomics* **292**, 1341–1361 (2017).

33.   F. W. Nietzsche, "Section One: Of First and Last Things, Aphorism # 22" in *Human, All Too Human*, 9e Ed., (Cambridge University Press).

34.   M. Oostveen, T. Mudde, Overheid geeft 'enorme smak geld' aan wetenschappers: 174 miljoen euro. *Volkskrant* (2024). Available at: https://www.volkskrant.nl/wetenschap/overheid-geeft-enorme-smak-geld-aan-wetenschappers-174-miljoen-euro~bf323392/ [Accessed 13 June 2024].

35.   C. en W. Ministerie van Onderwijs, M. van S. Z. en Werkgelegenheid, Gratis schoolontbijt op 500 basisscholen met veel kwetsbare leerlingen - Nieuwsbericht - Rijksoverheid.nl. (2022). Available at: https://www.rijksoverheid.nl/actueel/nieuws/2022/10/04/gratis-schoolontbijt-op-500-basisscholen-met-veel-kwetsbare-leerlingen [Accessed 13 June 2024].

36.   The Nobel Prize in Chemistry 2020. *NobelPrize.org*. Available at: https://www.nobelprize.org/prizes/chemistry/2020/summary/ [Accessed 31 May 2024].

37.   S. R. a.k.a. Meltdown Your Books, i0 xen0, *Where Does a Body Begin? Biology's function in Contemporary Capitalism* (Becoming).

5

Summary

Introduction

Animals go through post-embryonic development in fluctuating environments where conditions such as food availability, temperature and osmotic pressure constantly shift. To survive, grow, and reproduce, they must adapt to both mild deviations from optimal conditions and extreme stresses that threaten cellular integrity. This thesis explores two fundamental questions: how do developing animals adjust to environmental variation? And how do they cope with extreme stress that disrupts normal cellular function?

Development requires precise coordination of cell divisions, tissue formation, and gene expression, all of which are influenced by environmental factors. Changes in temperature, nutrition, and other external conditions can alter developmental timing, necessitating compensatory mechanisms to maintain proper organismal growth. The regulatory networks underlying this coordination, however, remain poorly understood.

When environmental stress becomes severe, animals activate specialized stress response pathways. One of these pathways is insulin signaling, which is crucial for responding to a wide array of stresses such as temperature, starvation and osmotic stress. It is highly conserved across evolution, as many components of the insulin signaling pathway are shared across the animal kingdom. The transcription factor DAF-16/FOXO plays a central role in insulin signaling, translocating to the nucleus to regulate gene expression of stress response genes during stress. However, maintaining stress responses comes at a cost, diverting resources from growth and reproduction. Thus, animals must carefully regulate when and how strongly these pathways are activated, meaning when and how DAF-16/FOXO translocates to the nucleus. How the dynamics of DAF-16/FOXO translocation unfold in real time, particularly in a stressful and unpredictable environment, remains an open question.

To investigate these processes, we use the nematode *C. elegans*, an ideal model due to its transparency, rapid development, and well-characterized genetic pathways. Using fluorescent time-lapse microscopy, we track developmental gene expression and DAF-16/FOXO dynamics in individual animals under controlled environmental conditions. This approach bridges the gap between cellular-level responses and whole-body developmental coordination.

By combining experimental observations with quantitative analysis and mathematical modeling, this work aims to explore the principles governing environment-dependent development and stress adaptation. Understanding these mechanisms has broad implications,

from developmental biology to human health, where insulin signaling and FOXO play critical roles in aging, metabolism, and disease.

Objectives

Characterizing developmental timing variability and the effects of environmental conditions: understanding how the timing of key cellular events differs among genetically identical individuals, and how factors such as temperature, diet, and genotype influence developmental timing and whether these changes occur in distinct phases (**Chapter 2**).

Exploring the role of insulin signaling and DAF-16/FOXO dynamics: examining how nuclear translocation of DAF-16/FOXO responds to environmental stress in real-time and whether its dynamics influence overall growth and development (**Chapter 3**).

Developing a mathematical model of DAF-16/FOXO dynamics: constructing a theoretical framework to explain the generation and synchronization of DAF-16/FOXO activity across cells and predicting new experimental outcomes (**Chapter 4**).

Method

Fluorescent time-lapse microscopy and quantitative data analysis: *C. elegans* eggs were placed in hydrogel microchambers. Upon hatching, animals were trapped, allowing us to track individual animals over multiple days. This allowed for precise measurement of developmental event timing, DAF-16/FOXO nuclear localization dynamics at the single-cell level, and the identification of variability between individuals. Custom-written software in Python was used to process and quantify the microscopy data.

Mathematical/computational modeling: A system of stochastic differential equations was formulated to describe the feedback mechanisms governing DAF-16/FOXO pulse dynamics and synchronization. Model predictions were tested experimentally, allowing for iterative refinement of the theoretical framework.

Results

Developmental timing varies among individual *C. elegans* animals but follows temporal scaling, meaning that individual events occur at consistent relative timings when adjusted for total development duration. Environmental factors such as temperature and diet influence timing shifts in discrete developmental epochs, where all events change at a similar rate (**Chapter 2**).

Under stress, DAF-16/FOXO exhibits stochastic nuclear translocation pulses, which are synchronized across the cells of the entire body of *C. elegans*. DAF-16/FOXO pulses correlate negatively with growth rate, influencing whether animals continue growing or enter developmental arrest (**Chapter 3**).

A mathematical model explains the generation of DAF-16/FOXO pulses through insulin signaling feedback, where secreted insulin-like peptides (ILPs) regulate synchronization across cells. The model successfully predicts new experimental outcomes, such as hysteresis in nuclear localization during heat stress, and the impact of disrupting insulin signaling in specific tissues (**Chapter 4**).

Conclusions

The findings presented in this thesis suggest that *C. elegans* developmental timing is governed by relative scaling principles rather than fixed time schedules. Despite variability, a common regulatory framework ensures coordinated development. Insulin signaling plays a key role in synchronizing growth across cells under stress, with potential implications for understanding similar mechanisms in more complex organisms.

Recommendations

Future research should explore:

- A more mechanistically detailed model of temporal scaling that incorporates size-dependent and oscillatory mechanisms to explain the robustness of temporal scaling.
- FOXO dynamics and cell-to-cell synchronization in groups of mammalian cells, e.g. human organoids, to ascertain the relevance of FOXO pulses in a human health context.
- Mutations which decrease the level of cell-to-cell synchronization of DAF-16/FOXO pulses to discover the molecular mechanisms that govern synchronization.
- An automated method to measure worm body volume from time-lapse images to enable high-throughput measurement and analysis of growth versus DAF-16/FOXO activity over time.
- A more detailed, mechanistic, mathematical model of DAF-16/FOXO pulses and their synchronization, to test hypotheses regarding specific components of insulin signaling

Samenvatting

Inleiding

Tijdens hun ontwikkeling tot volwassen dier, hebben dieren te maken met een omgeving die voortdurend fluctueert, bijvoorbeeld in de beschikbaarheid van voedsel, in de temperatuur en in de osmolariteit (bijv. zoutconcentratie). Om te kunnen overleven, te groeien en om zich uiteindelijk voort te kunnen planten, moeten dieren zich aanpassen aan zowel kleine afwijkingen van optimale omstandigheden, als extreme stress die de gezondheid van cellen bedreigt. In deze dissertatie worden twee fundamentele vragen onderzocht: hoe passen dieren hun post-embryonale ontwikkeling aan in een veranderende omgeving? En hoe gaan ze om met extreme omgevingsstress die de normale cellulaire functie verstoort?

Dierlijke ontwikkeling vereist nauwkeurige coördinatie van celdelingen, weefselvorming en genexpressie, die allemaal beïnvloed worden door omgevingsfactoren. Veranderingen in temperatuur, voeding en andere externe omstandigheden kunnen de timing van ontwikkeling veranderen. Hierdoor zijn compensatiemechanismen nodig om de juiste groei van het organisme te behouden die uiteindelijk resulteert in een gezonde volwassene. Onze kennis van dit soort mechanismen is vooralsnog gebrekkig.

Wanneer de externe omstandigheden erg ver afwijken van het optimum en de normale cellulaire functie in gevaar komt, is er sprake van omgevingsstress. In dit geval activeren dieren gespecialiseerde biochemische reactiepaden, ofwel stressresponspaden. Eén van deze reactiepaden is insulinesignalering, die cruciaal is bij de reactie op een breed scala aan stresssituaties zoals verhongering, hittestress en osmotische stress. Insulinesignalering is evolutionair gezien in hoge mate geconserveerd, aangezien veel componenten ervan worden gevonden door het hele dierenrijk. De transcriptiefactor DAF-16/FOXO speelt een centrale rol in insulinesignalering, omdat het tijdens stress verplaatst naar de celkern en daar specifieke stressresponsgenen activeert door aan het DNA te binden. Het in stand houden van de stressrespons gaat echter ten koste van de groei en voortplanting. Dieren moeten dus zorgvuldig regelen wanneer en hoe sterk de stressresponspaden worden geactiveerd, oftewel wanneer en hoe DAF-16/FOXO naar de celkern wordt verplaatst. Hoe de dynamiek van DAF-16/FOXO translocatie zich in "real-time" ontvouwt, vooral in een stressvolle en onvoorspelbare omgeving, blijft een open vraag.

Om deze processen te onderzoeken gebruiken we de nematode *C. elegans*. *C. elegans* is een veelgebruikt modelorganisme omdat het een relatief snelle post-embryonale ontwikkeling heeft, de genetica goed gekarakteriseerd is, en het doorzichtig is (wat ons in staat stelt

processen binnen de cellen te bestuderen). Met behulp van time-lapse microscopie, waarbij we tevens specifieke eiwitten volgen door middel van fluorescentie, bestuderen we de ontwikkelingsgenen en de dynamiek van DAF-16/FOXO in individuele dieren. Hierbij controleren we de omgevingsomstandigheden zoals temperatuur, voedselbeschikbaarheid en zoutconcentratie. Met deze aanpak kunnen we processen op cellulair niveau koppelen aan die op het niveau van het gehele lichaam.

Door experimentele observaties te combineren met kwantitatieve analyse en wiskundige modellen, is het doel van het werk in deze dissertatie om de omgevingsafhankelijke ontwikkeling en stressadaptatie in *C. elegans* te onderzoeken. Beter inzicht in deze mechanismen heeft brede implicaties, van ontwikkelingsbiologie tot menselijke gezondheid, waar insulinesignalering en FOXO een belangrijke rol spelen bij veroudering, metabolisme en ziekte.

Doelstellingen

Het karakteriseren van variabiliteit in ontwikkelingstiming en de effecten van omgevingsfactoren: begrijpen hoe de timing van cruciale ontwikkelingsgebeurtenissen verschilt tussen genetisch identieke individuen en hoe factoren zoals temperatuur, dieet en genotype de ontwikkelingstiming beïnvloeden en of deze veranderingen in afzonderlijke fasen optreden (**Hoofdstuk 2**).

Onderzoeken van de rol van insulinesignalering en DAF-16/FOXO dynamica: onderzoeken hoe nucleaire translocatie van DAF-16/FOXO afhangt van omgevingsstress in real-time en of de translocatiedynamica de algehele groei en ontwikkeling van *C. elegans* beïnvloedt (**Hoofdstuk 3**).

Het ontwikkelen van een wiskundig model van DAF-16/FOXO dynamica: het opstellen van een theoretisch raamwerk om de generatie en de synchronisatie van DAF-16/FOXO pulsen in verschillende cellen te verklaren en nieuwe experimentele resultaten te voorspellen (**Hoofdstuk 4**).

Methode

Fluorescente time-lapse microscopie en kwantitatieve data-analyse: individuele *C. elegans* eieren werden in hydrogel microkamers geplaatst. Na het uitkomen zaten ze vast in de kamers, waardoor we individuele dieren gedurende meerdere dagen konden volgen. Dit maakte precieze metingen mogelijk van de timing van ontwikkelingsgebeurtenissen, de dynamiek van DAF-16/FOXO-celkernlokalisatie op enkel-celniveau en de meting van variabiliteit tussen

individuen. Zelfgeschreven software in Python werd gebruikt om de microscopiegegevens te verwerken en te kwantificeren.

Wiskundige/computationele modellering: een systeem van stochastische differentiaalvergelijkingen werd geformuleerd om de feedbackmechanismen te beschrijven die de DAF-16/FOXO pulsdynamica en synchronisatie bepalen. De modelvoorspellingen werden experimenteel getest, waardoor het theoretische raamwerk iteratief verfijnd kon worden.

Resultaten

De ontwikkelingstiming varieert tussen individuele C. elegans-dieren, maar volgt temporele schaalverhoudingen, wat betekent dat individuele gebeurtenissen op consistente relatieve tijdstippen plaatsvinden wanneer ze worden aangepast aan de totale ontwikkelingsduur. Omgevingsfactoren zoals temperatuur en dieet beïnvloeden de timing in discrete ontwikkelingsfasen, waarbij alle gebeurtenissen in een vergelijkbaar tempo veranderen **(Hoofdstuk 2).**

Tijdens stress vertoont DAF-16/FOXO stochastische nucleaire translocatiepulsen, die gesynchroniseerd zijn over de cellen van het hele lichaam van *C. elegans*. DAF-16/FOXO pulsen correleren negatief met de groeisnelheid en beïnvloeden of dieren doorgroeien of in een ontwikkelingsstilstand raken (**Hoofdstuk 3**).

Het wiskundig model biedt een verklaring voor hoe DAF-16/FOXO pulsen worden gegenereerd en gesynchroniseerd via insuline signaleringsfeedback, waarbij afgescheiden insulineachtige peptiden ("ILP's") de synchronisatie tussen cellen reguleren. Het model voorspelt met succes nieuwe experimentele resultaten, zoals hysterese in DAF-16/FOXO nucleaire lokalisatie tijdens hittestress en de impact van het verstoren van insulinesignalering in specifieke weefsels (**Hoofdstuk 4**).

Conclusies

De bevindingen in dit proefschrift suggereren dat de timing van de ontwikkeling bij *C. elegans* wordt bepaald door relatieve schalingsprincipes in plaats van vaste tijdschema's. Ondanks variabiliteit zorgt een gemeenschappelijk regelgevend kader voor een gecoördineerde ontwikkeling. Insulinesignalering speelt een sleutelrol in het synchroniseren van groei in cellen onder stress, met mogelijke implicaties voor het begrijpen van vergelijkbare mechanismen in meer complexe organismen.

Aanbevelingen

Toekomstig onderzoek moet zich richten op:

- Een meer mechanistisch gedetailleerd model van temporele schaalverhoudingen dat grootte-afhankelijke en oscillerende mechanismen integreert om de robuustheid van temporele schaalverhoudingen te verklaren.

- FOXO-dynamica en cel-cel synchronisatie in groepen zoogdiercellen, bijvoorbeeld menselijke organoïden, om de relevantie van FOXO-pulsen in een menselijke gezondheidscontext vast te stellen.

- Mutaties die de mate van cel-cel synchronisatie van DAF-16/FOXO pulsen verlagen om de moleculaire mechanismen te ontdekken die de synchronisatie bepalen.

- Een geautomatiseerde methode om het lichaamsvolume van wormen te meten uit time-lapse beelden om high-throughput metingen en analyses van groei versus DAF-16/FOXO activiteit in de tijd mogelijk te maken.

- Een meer gedetailleerd, mechanistisch, wiskundig model van DAF-16/FOXO pulsen en hun synchronisatie, om hypotheses over specifieke componenten van insulinesignalering te testen.

Acknowledgements

The acknowledgements: the most important "unimportant" part of a PhD thesis. Perhaps simply the most important, as it is certainly the part that is most read. It feels strange to condense the countless interactions and support I received over the past few years into just a few words. In truth, it's not really possible to do it justice. But here's an attempt.

First of all, I would like to thank my supervisor, **Jeroen**, for giving me the opportunity to do a PhD in his lab. Your guidance was always there when needed, while also allowing me the freedom to explore my own ideas. I appreciated that you always had interesting stories about pretty much any topic imaginable. Lunch-time discussions often revolved around a particular book you had read, or a program you had watched, which I enjoyed a lot.

I am also grateful to our collaborators in Spain, especially **María Olmedo**. The *C. elegans* strains you provided, as well as the feedback you gave during the many DAF-16 meetings were invaluable. It was great finally meeting you in person during the International *C. elegans* Meeting in Glasgow.

Further, I would like to thank the members of my thesis committee, **Pieter Rein**, **María**, and **Maria**. Special thanks to prof. dr. **Roeland Merks** for being my promotor, and guiding me through the graduation procedure at Leiden University.

During my time at AMOLF I was fortunate to meet many wonderful people. **Joleen**, we were office mates at the start of my PhD, and our conversations about our common love for cats, video games, and sometimes even more philosophical topics, were always a pleasure. **Olga**, thank you for teaching me the experimental *C. elegans* skills that I used throughout my PhD. **Timo**, our discussions on the DAF-16 project were invaluable and I truly appreciated your insights on the biological side of things. **Yvonne**, without your expertise and support, the work I did in the lab would have been much more difficult. We had many nice chats in the lab, especially during the project on temporal scaling. But besides this, we of course had a lot of fun during many (online) DnD sessions. **Rutger**, your dedication and work ethic were inspiring, and I always enjoyed our conversations during coffee breaks and AMOLF events. **Pascal**, besides sharing an office, we shared some great moments at concerts and festivals thanks to our similar music tastes. Hopefully many more will follow! **Kasper**, we had many interesting discussions, often on the topic of politics. I could not persuade you to vote for any of the 'correct' parties, but I remain hopeful :). And thanks to both Pascal and Kasper for being my paranymphs! **Max**, I could always bother you with philosophical discussions in which you

happily obliged me, both at AMOLF and during conferences. **Xuan**, we shared the same path from the TU Delft to AMOLF; good luck in your further scientific career! **Gouri**, I enjoyed our conversations and meetings on the *C. elegans* machine learning project. **Ananya**, thank you for carrying out additional experiments for the DAF-16 project, I wish you lots of luck in the remainder of your PhD!

I would also like to extend my gratitude to the students I supervised, **Madelon**, **Anastasia**, and **Noor**. Unfortunately, due to the lockdown, I did not get to see you in real life very often. However, you all managed to deliver great work in the end, working much more independently than the average Bachelor/Master student. Many thanks to the technical and administrative staff at AMOLF. No WormHostel-related technical problem remained a problem for too long thanks to skilled technicians such as **Hinco**, **Marko**, **Marco**, and of course, **Marco**. And finally, to everyone else at AMOLF I crossed paths with, including, but not only, Jente, Amber, Dhawal, Kathi, Jack, Chi, Jack, Marcel, Age, Nebojša, Parisa and many more - thank you!

I would further like to thank some people outside academia, who provided essential support during the past years. **Thomas**, besides being friends for a long time, our bouldering sessions were vital for keeping up morale in the final part of my PhD. **Sarah**, our many conversations on (the frustrations of) academia were likewise much needed catharsis during this period. And, of course, thank you for drawing the wonderful cover image of this thesis! **Koen**, our lockdown walks were pivotal in staying sane during the work-from-home period.

Meagan, thank you for always being there for me, during my PhD and of course at every other moment. There are not enough words to describe my gratitude, I would simply not have made it without your support.

Finally, I would like to thank my parents and my sisters (**anne**, **baba**, **Amine** abla ve **Dilek** abla), who were always there as a bedrock during all of my studies and during my PhD.

Curriculum vitae

Burak Demirbas was born in Vlaardingen, the Netherlands, on 27 February 1995. He was brought up in Maassluis and completed his secondary education at Lentiz Reviuslyceum (2007–2013). He then pursued a Bachelor's degree in Applied Physics at Delft University of Technology (2013–2016), alongside a double degree in Philosophy at Erasmus University Rotterdam (2015–2017).

He continued with a Master's in Applied Physics at Delft (2017–2019), where he focused on biophysics and quantitative biology. His Master's thesis on the topic of bacteriophage-host interaction dynamics was supervised by Dr. Bertus Beaumont. In 2019 he started his PhD at AMOLF under the supervision of Dr. Jeroen van Zon, on the topic of stress response and developmental biology in *C. elegans*, which resulted in the work presented here.

List of publications

-Filina, O., **Demirbas, B.**, Haagmans, R., & van Zon, J. S. (2022). Temporal scaling in C. elegans larval development. Proceedings of the National Academy of Sciences, 119(11), e2123110119.

-**Demirbas, B.**, Filina, O., Louisse, T., Goos, Y., Sánchez-Romero, M. A., Olmedo, M., & van Zon, J. (2023). Control of C. elegans growth arrest by stochastic, yet synchronized DAF-16/FOXO nuclear translocation pulses. bioRxiv, 2023-07.

-**Demirbas, B.** & van Zon, J. A collective model of stress-specific, synchronized DAF-16/FOXO pulses in insulin signaling. In preparation.